ARRAY SIGNAL PROCESSING TECHNIQUES FOR BROADBAND BEAMFORMING

HUIPING DUAN

NANYANG TECHNOLOGICAL UNIVERSITY

2007

ARRAY SIGNAL PROCESSING TECHNIQUES FOR BROADBAND BEAMFORMING

HUIPING DUAN

School of Electrical & Electronic Engineering

A thesis submitted to the Nanyang Technological University

in fulfillment of the requirement for the degree of

Doctor of Philosophy

2007

Acknowledgement

I would like to express my most sincere gratitude to my supervisor Dr. Ng Boon Poh for his advise, support and encouragement. Dr. Ng has supported me not only by financially providing the scholarship but also academically offering illuminating instructions and thoughtful suggestions for my research. His patience and kindness are deeply appreciated.

I would also like to thank Dr. Chong Meng Samson See for his suggestions on my research.

Many thanks go to all my friends for their encouragement. Besides, I would like to acknowledge all the technicians in the Information System Research Laboratory for their help. I am grateful to Nanyang Technological University and the DSO National Laboratories of Singapore for the facilities and financial support they provide.

I wish to express my most heartfelt thanks to my parents and parents-in-law for their love and support. I want to say thanks to my brother and my sister-in-law for their encouragement and the care they provide to my parents. My pretty niece should be thanked for all the happiness her cute words have brought to me. Finally, special thanks go to my husband for his understanding and encouragement.

Contents

List of Figures

List of Tables

Abbreviations

DOA	Direction Of Arrival
EM	Electromagnetic
FBW	Fractional Bandwidth
FFT	Fast Fourier Transform
FIB	Frequency Invariant Beamformer
FIBP	Frequency Invariant Beampattern
FIR	Finite Impulse Response
GSC	Generalized Sidelobe Canceller
IFFT	Inverse Fast Fourier Transform
IIR	Infinite Impulse Response
INR	Interference-to-Noise Ratio
LCMV	Linearly Constrained Minimum Variance
LMS	Least Mean Square
MRA	Minimum Redundancy Array
NRA	Nonredundant Array
RGN	Recursive Gauss-Newton

SINR	Signal-to-Interference-plus-Noise Ratio
SIR	Signal-to-Interference Ratio
SNR	Signal-to-Noise Ratio
SOCP	Second-Order Cone Programming
SRV	Spatial Response Variation
TDL	Tapped Delay Line
ULA	Uniform Linear Array

Notations

$[\cdot]^T$	Transpose of $[\cdot]$
$[\cdot]^*$	Complex conjugate of $[\cdot]$
$[\cdot]^H$	Complex conjugate transpose of $[\cdot]$
$[\cdot]^{-1}$	Inverse of $[\cdot]$
$\lvert \cdot \rvert$	Absolute value
$\lVert \cdot \rVert$	Euclidean norm
$\otimes$	Kronecker product
$\circledast$	Linear convolution
$\boldsymbol{e}_i$	ith column of the identity matrix
j	Imaginary unit, $j = \sqrt{-1}$
$\mathrm{E}[\cdot]$	Mathematical expectation of $[\cdot]$
$\boldsymbol{I}$	Identity matrix
$\mathrm{Re}[\cdot]$	Real part of $[\cdot]$
$\mathbb{R}^n$	$n \times 1$ column vectors with real entries
$\mathbb{Z}^+$	Positive integers
$\mathbf{0}$	Column vector with all-zero entries

$\mathbf{1}$	Column vector with all-one entries

Summary

The content of this thesis comprises the original research work on the investigations of broadband beamforming techniques, including the design of broadband beamforming structures and algorithms, the performance analysis of broadband beamformers using nonuniform array geometries and the development of broadband pattern synthesis approaches.

In the Frost beamformer, the optimum weights are obtained by minimizing the output power while maintaining a chosen frequency response in the look direction. In this thesis, to optimize the interference and noise suppression performance of the Frost beamformer, three constrained optimization methods are developed to design the look-direction response, which is subsequently used to compute the optimum weight vector of the beamformer. The improved performance relative to the beamformer with the distortionless constraint is illustrated.

To suppress broadband interferences effectively, conventional broadband beamformers are designed by connecting each sensor with a group of tapped delay lines (TDLs), or finite impulse response (FIR) filter. As the operating bandwidth increases, high-order FIR filters and hence large numbers of weights are required to achieve satisfactory performance. A type of new broadband beamforming structure using TDL-form infinite impulse response (IIR) filters is designed in this thesis. Adaptive algorithms are presented to compute the feedforward and feedback weights in the IIR beamformers. The advantages of the proposed beamformers, including the improved steady-state signal-to-interference-plus-noise ratio (SINR), easier stability monitoring and less sensitivity to the coefficient quantization error, are demonstrated.

In addition, studies are carried out on using the minimum redundancy array (MRA) and nonredundant array (NRA) for broadband beamforming in this thesis. The linearly constrained minimum variance (LCMV) beamformer with the ideal continuous-time, infinite-length filters is assumed for the study. Approximate formulations for the 3-dB beamwidths are obtained to measure the spatial resolutions of the broadband MRA and NRA. The accuracy of the derived formulations is assessed by numerical studies. Several original properties about the interference suppression performance of the MRA compared with that of the uniform linear array (ULA) are obtained by mathematical proofs and graphic illustrations. They can provide important guidance for the application of MRA in broadband beamforming.

Besides the investigations of the broadband adaptive beamforming, some studies on broadband pattern synthesis are conducted. The spatial response variation (SRV) is defined to measure the fluctuations of the array spatial responses within the desired frequency band. Applying the SRV constraint directly in the optimization formulations to produce the frequency invariant beampattern (FIBP) is studied. It is found that by using the SRV constraint, broadband pattern synthesis problems can be formulated in an efficient way. The examples of designing the single-beam FIBP and multi-beam forming network are demonstrated to show the effect of applying the SRV constraint in broadband pattern synthesis.

Chapter 1

Introduction

1.1 Background

Sensor or antenna arrays have been widely used in radar, radio astronomy, sonar, communications, seismology and many other applications for transmitting or receiving wave energy. Array signal processing, which involves manipulating signals induced on array elements to extract useful information, has been studied extensively. Beamforming is one of the important research topics in array signal processing. In this thesis, we discuss beamforming in the receiving arrays. Beamforming is implemented by combining the data collected from array elements in some forms of weighting and summation. It performs spatial or spatial-temporal filtering to estimate the signal arriving from the desired direction but contaminated by the noise and interferences from other directions.

According to the methods to choose the weights, beamformers can be classified as the data-independent or statistically optimum types. Designing the data independent beamformer is normally referred to as pattern synthesis. The weights are chosen to make the array response to approximate a desired response or meet requirements for pattern specifications. The statistical information of the array data is used for obtaining the weights in the statistically optimum beamformer. Data independent beamformers have been extensively used due to the superiority of their robustness and simplicity while statistically optimum beamformers can adapt to the changes of the environment and achieve near perfect interference suppression performance.

Much effort has been devoted to using sensor arrays to receive and process narrowband signals. Literatures [1–5] and the references therein can be referred to about the well-known narrowband beamforming and direction of arrival (DOA) estimation methods.

In recent years, the requirement for high data rates and bandwidths promotes the rapid development of broadband systems. In some applications, the signals of interest cover a wide frequency range themselves, like the speech signals processed by microphone arrays. The narrowband beamformer with a desired spatial response for a particular frequency is implemented by applying one complex weight after each array element. Studies show that narrowband weighting schemes cause varied mainlobe shape and sidelobe/null locations at different frequencies so they will degrade the performance of the broadband systems. Various broadband beamforming techniques have been developed to process broadband signals to achieve satisfactory performance.

1.2 Overview of Broadband Beamforming Techniques

i) Broadband Time-Domain Beamformer

References [6, 7] use the tapped delay line (TDL) rather than the single complex weight after each array element in beamformers to process the broadband signals. Using the time-domain filter in each channel tends to increase the degrees of freedom of the array system.

They provide frequency-dependent weighting for the data collected by array elements. Reference [7] presents the Frost beamformer with the optimum weight vector obtained by the linearly constrained minimum variance (LCMV) optimization criterion and proposes the constrained least-mean-square (LMS) algorithm for adjusting the weights iteratively. An alternative implementation, the generalized sidelobe canceller (GSC), is presented in [8] to compute the weight vector with the unconstrained adaptive algorithm.

The relationships between the LCMV and GSC beamformers and their applications have been investigated. Reference [9] presents a geometric interpretation to the relationship between the two beamformers. The equivalence of the LCMV and GSC beamforming is proved in [10, 11]. In addition, [12, 13] and some other literatures have discussed the applications and performance of these two broadband beamformers in speech processing. The nulling performance of the broadband time-domain beamformer varying with the number of taps, the tap spacing, the array geometry, the interference bandwidth and the interference power has been examined in [14–18].

As the signal bandwidth increases, larger numbers of coefficients are required to achieve satisfactory interference suppression performance in the broadband time-domain processors. To reduce the number of weights, the computational complexity and increase the convergence rate, broadband beamformers using the infinite impulse response (IIR) filters [19–22] and subband techniques [23, 24] have been investigated.

To achieve some special performance like the robustness and the desired interference and noise suppression performance in different applications, some variations of the Frost beamformer and the GSC beamformer have been designed [25–33].

ii) Broadband Frequency-Domain Beamformer

In narrowband systems, signals are usually modelled by sinusoidal waves. Broadband signals can be considered as multiple superposed narrowband components. The amplitude and phase of each narrowband wave determine the frequency spectrum of the broadband signal. A natural extension from narrowband to broadband processing is to decompose the broadband signals by the Fourier transform into multiple narrowband signals. Then the well-studied narrowband beamforming techniques are applied for each frequency bin. Finally, all the narrowband beamforming outputs are combined together by the inverse Fourier transform to get the output of the broadband beamformer. This is the basic idea behind the frequency-domain broadband beamformer. The study in [34] indicates that the frequency-domain method is insensitive to the sampling rate. Reference [35] points out that the frequency-domain beamforming adopts the modular parallel structure so it is less sensitive to the coefficient quantization. References [36–38] explore the relationships between the time-domain and the frequency-domain processors. Their studies show that the frequency-domain implementation does not offer improvement in array bandwidth performance relative to the time-domain implementation. Their optimum performance are the same only when the signals in various frequency bins are independent. Due to the use of the fast Fourier transform (FFT), the parallel processing for each frequency bin and the different step size to adjust the weights in each narrowband processor, the frequency-domain realization of the broadband beamformer shows faster weight updating speed.

In addition, based on the coherent signal-subspace (CSS) method [39] which is originally proposed for broadband DOA estimation, some broadband beamformers [40, 41] are implemented by performing the frequency independent beamforming after preprocessing the signals in the frequency domain with the focusing transformation.

iii) Design of Various Constraints

To prevent the cancellation of the desired signal caused by mismatched signal arrivals, beamformers with the broad beamwidth in the look direction are desired. One important way is to use the derivative constraints. In [42], the first-order, second-order and nth-order derivative constraints are derived in the form of linear equations. By imposing these derivative constraints as well as the gain constraint in the LCMV optimization, the optimum weight vector can produce flat spatial response around the look direction of the broadband beamformer, at the cost of reduced array gain. This type of derivative constraints is derived by the sufficient condition for the flat power response of the beamformer. Studies in [43, 44] show that they are phase-center dependent. The poor choice of the location of the phase center coordinate origin can result in undesirable beampatterns. To solve this problem, some phase-independent derivative constraints are derived in [45–48]. These constraints are the sufficient and necessary conditions for the maximally flat spatial power response of the beamformer so they are independent of the phase center. However, relative to the linear-form constraints in [42], the constrained optimization problems become complicated because these phase-independent constraints involve quadratic equations. Recently, in [49], a set of presteering derivative constraints are derived by computing the partial derivative of the power response with respect to the presteering delay. Presteering derivative constraints are capable of not only preventing the directional mismatches but also being robust against the position calibration errors and the quantization errors in the presteered front end.

Besides, to achieve robust performance, some other constraints, such as the quadratic constraint and multiple linear constraints, are designed. In [50], minimizing the output power subject to multiple linear equality constraints and a quadratic inequality constraint on the array gain against uncorrelated noise, implemented by a scaled projection algorithm, is proposed so that the beamformer is robust to array errors.

In [51], the soft constraint controlling the mean square error between the desired and actual responses in the signal direction is investigated. It is designed as a quadratic inequality which purposely permits the signal distortion in order to achieve the improved interference cancellation performance. In [52], the constraint in the optimization is formulated by restricting the mean square deviation between the beamformer response and the desired unity response in the look direction over the specified spatial region smaller than a threshold. By varying the range of the spatial region, the width of the main beam can be controlled to enhance the robustness of the beamformer.

iv) Broadband Pattern Synthesis

Array pattern synthesis is to design array geometries and/or weights for the data-independent beamformers to achieve the desired radiation patterns. For the narrowband array, the well-known Dolph-Chebyshev pattern [53] has the minimum mainlobe width for a given sidelobe level, with the weights computed analytically for the uniform linear array (ULA). For the array with more general geometry and arbitrary element responses, the quadratic programming method [54], semidefinite programming method [55], numerical methods based on the adaptive array theory [56, 57], iterative methods [58–60], support vector machine method [61], and so on, are developed to synthesize the narrowband beampattern. For the broadband array, the typical beamforming structure employs a digital filter instead of a single complex weight after each sensor. The beampattern is a function of both direction and frequency. The two-dimensional Fourier transform [62], weighted Chebyshev approximation [63], eigenfilters [64], second-order cone programming (SOCP) [65–68], vector space projections [69], and some other approaches [70–72], have been proposed to synthesize broadband beampatterns. References [73, 74] are examples designing broadband beamformers with specified nulls.

For the linear array, the beamwidth of the beampattern decreases as the frequency increases. In applications using microphone arrays for audio teleconferencing, this will filter out the high frequency component of the signal incident within the mainlobe but not in the look direction, resulting in distortion. Therefore, an important problem for broadband beamforming is to generate the beampattern with a constant beamwidth. In some other applications, it is desirable that the spatial response in the whole field of view remains constant with respect to the frequency within the frequency range of interest. Some beamforming techniques for achieving constant beamwidth have been proposed [75], for example, harmonic nesting, elemental lowpass filtering, and multi-beamforming. In [76], the asymptotic theory of unequally-spaced arrays is used to derive the relationship between the beampattern characteristics and the functional requirements on sensor spacings and weightings. The theory for the far-field frequency invariant beamformer (FIB) presented in [77] provides a deep insight into this issue, including the intrinsic structure of the beamformer and the frequency responses for the filters in each channel. In [78], single-rate and multi-rate methods are proposed to determine the coefficients of the primary filter based on the dilation property for the one-dimensional FIB. In [79], IIR filters and the multirate technique are used. The beampatterns generated by the methods proposed in [77–79] possess the frequency invariant property in all the directions. In [68], the SOCP method is used and the frequency invariant spatial response within the mainlobe region is achieved by minimizing the mean square error between the synthesized and the desired mainlobe responses. In [80], the authors design two-dimensional fan filters by the spectral transformation and the window method for the ULA. The patterns of the beams generated by these fan filters in the beamspace adaptive array show good frequency invariance in both the mainlobe region and the sidelobe region so that the interferences are not distorted and hence are suppressed as expected. Reference [81] extends the work of [80] to two-dimensional and three-dimensional broadband arrays. In [82], the fan filters are applied in the GSC beamformer. The designs in [80–83] are only applicable to uniformly spaced arrays. In [84], the concentric ring array with the frequency invariant beampattern (FIBP) is studied with each sensor connected to only one single weight. In [85], the author studies the rectangular array with a single real weight following behind each array element to generate the FIBP. Recently, in [86, 87], the FIBP is designed by the stochastic approach for the superdirective array.

Besides the FIB, in many applications, the beampattern is synthesized according to the desired response or the required beampattern specifications. These synthesis problems are always formulated as some forms of optimization problems. In [64, 88], the cost functions using the weighted least-squares, the total least-squares, the maximum energy, the nonlinear optimization and eigenfilter techniques, are presented to design broadband beamformers. In [63, 65, 68], broadband pattern synthesis is formulated as the SOCP or quadratic programming problems. The interior-point method is used to solve for the weights in these optimization problems. Some toolboxes, like SeDuMi [89], can be used to solve these problems conveniently [90].

1.3 Motivations and Contributions

First, the look-direction response is directly related with the linear constraint in the broadband LCMV beamformer under the assumption of exact presteering delays. The constraint for the distortionless response is normally used but it does not ensure optimum output signal-to-interference-plus-noise ratio (SINR). This motivates us to choose some optimization criteria appropriately to design the constraint vector, hence the look-direction response, so that the interference and noise suppression performance of the broadband beamformer can be improved.

Second, as the signal bandwidth increases, high-order filters are required in broadband time-domain beamformers for achieving satisfactory interference suppression performance. Large numbers of weighting coefficients in high-order filters lead to huge computational complexity and long convergence time in adaptive algorithms. Therefore, one of the motivations for our study is to propose more efficient designs, in terms of either the beamforming structure or the algorithms, to provide better broadband nulling performance with less number of coefficients.

Third, the nonuniform linear array has been studied in narrowband beamforming or DOA estimation to achieve improved spatial resolution. There is rare study of using them in broadband beamformers. Analyzing the spatial resolution and the interference suppression performance of the broadband beamformer using arrays with the nonuniform geometry attracts our interest.

Fourth, the beampattern with a constant beamwidth or even with the spatial response in the whole field of view being constant with respect to the frequency is desired in some applications like the microphone or loudspeaker arrays. Existing optimization formulations for broadband array synthesis do not have the flexibility of controlling the extent of frequency invariance. Designing appropriate constraints in the optimization to restrict the fluctuations of the spatial responses within the frequency range can be a simple scheme to produce the FIBP.

The contributions of this thesis are listed as follows:

i) Designing the Amplitude/Phase Response of the Frost Beamformer

The LCMV optimization criterion is used in the Frost beamformer. The constraint is designed to get a certain look-direction response. Normally the unit gain constraint is used to get the distortionless response for the desired signal. In this thesis, several optimization criteria are developed to design the look-direction response, which is subsequently used in the constraint to compute the optimum weight vector of the beamformer [91]. Improved interference and noise suppression performance relative to the beamformer using the distortionless constraint is demonstrated by simulation examples.

ii) Broadband Beamformers Using TDL-Form IIR Filters

For broadband beamformers using finite impulse response (FIR) filters, large numbers of coefficients are required to retain the desired SINR performance as the operating bandwidth increases. Motivated by the desire to reduce the number of weights, research has been carried out to explore beamformers using IIR filters. However, some potential problems in the IIR filters, such as the stability monitoring and sensitivity to quantization errors, make the implementation of the IIR beamformers difficult. In this thesis, a type of new broadband beamformers using IIR filters is proposed to solve these problems [92,93]. Both the Frost-based and the GSC-based broadband beamformers utilizing the TDL-form IIR filters are designed. The combined LMS and combined recursive Gauss-Newton (RGN) algorithms are developed to compute the feedforward and feedback weights in the Frost-based implementation. In the GSC-based structure, the unconstrained RGN algorithm is customized for the TDL-form IIR filters in the adaptive beamforming part. Similar to the beamformer using direct-form IIR filters, the new IIR beamformers can achieve better SINR performance than the FIR beamformer for a given number of coefficients. Moreover, the new structures facilitate stability monitoring. The sensitivity to the coefficient quantization error is much smaller than the beamformer using direct-form IIR filters.

iii) Performance Analysis of Broadband Beamformers Using the Minimum Redundancy Array (MRA) and Nonredundant Array (NRA)

The MRA and NRA have been investigated in narrowband systems for the capability of improving the resolution for a given number of array elements. However, to the best of our knowledge, there is rare study of using them in broadband beamformers. In some broadband applications, like microphone arrays, great attention is paid to the resource and resolution issues. Therefore, the performance of using MRA and NRA in broadband beamformers is worth studying. In this thesis, the expressions of the ideal filter response vector and the output power of the broadband LCMV beamformer are obtained by the frequency-domain optimization. Approximate formulations for the 3-dB beamwidth are derived to measure the spatial resolution of the broadband beamformers using MRA and NRA [94]. The accuracy of the derived formulations is assessed by numerical studies. The beamwidths of MRA and NRA are compared with that of the ULA. These formulations can avoid the onerous procedure for finding the half-power point each time when the array performance need to be evaluated. The influences of various parameters on the array resolution can be easily observed by the formulations. In addition, several original properties about the broadband interference suppression performance of the MRA compared with that of the ULA are revealed by mathematical proofs and graphic illustrations [95]. They can provide important guidance for the application of MRA in broadband beamforming.

iv) Applications of the Spatial Response Variation (SRV) Constraint in Broadband Pattern Synthesis

Existing optimization formulations for synthesizing broadband array beampatterns do not have the capability of controlling the extent of the frequency invariance. In this thesis, the SRV is defined to measure the fluctuations of the array spatial responses within the desired frequency band. Applying the SRV constraint directly in the optimization formulations to produce the FIBP is studied. It is found that by using the SRV constraint, the broadband pattern synthesis problems can be formulated in an efficient way [96]. The examples of designing the single-beam FIBP and multi-beam forming network are demonstrated to show the effect of applying the SRV constraint in broadband pattern synthesis.

1.4 Thesis Outline

The outline of the thesis is as follows:

In Chapter 2, we briefly introduce the array fundamentals, including the coordinate systems usually used in array signal processing, the wave propagation model applied as the theoretical foundation of the array steering vector models and the array geometries designed for various applications. In addition, the Frost beamformer and the broadband GSC beamformer are introduced in detail because they are backgrounds closely related with our work in subsequent chapters. Finally, some simulation examples are included to demonstrate the influences of the environment and the design on the broadband beamforming performance.

Next, in Chapter 3, we present three new optimization criteria to design the look-direction response for the Frost beamformer. The formulations for the norm-constrained, frequency-response-constrained and amplitude-response-constrained optimization criteria are described and solved to generate the new constraint vector, which is different from the distortionless constraint. The weight vectors of the beamformer are obtained by solving the optimization problem under the new constraints. Simulation examples are illustrated to show the performance improvement of the new methods relative to the beamformer using the distortionless constraint. The proposed methods are compared too with each other by analysis and simulations.

In Chapter 4, the broadband beamforming structure using TDL-form IIR filters is proposed. The constrained LMS algorithm for updating the feedforward weight vector and the unconstrained LMS algorithm for adjusting the feedback weight vector are developed. Simulation examples are used to demonstrate the performance improvement of the new IIR beamformer relative to the FIR beamformer. Comparisons of the computational load are also demonstrated.

In Chapter 5, to improve the convergence rate of the combined LMS algorithm designed in Chapter 4, the combined RGN algorithm is developed in this chapter for the Frost-based beamformer using TDL-form IIR filters. The GSC-based implementation is presented as an extension of the Frost-based implementation, with the unconstrained RGN algorithm developed for updating the weight vectors. In addition, the second-order tap-to-tap IIR sections are introduced to allow the existence of complex poles. The convergence rate and the steady-state performance are compared between the Frost-based IIR beamformer using the combined LMS algorithm and that using the combined RGN algorithm. Simulation examples are also included to demonstrate the performance improvement of the proposed IIR beamformer relative to the existing IIR and FIR beamformers.

In Chapter 6, the formulations for the optimum frequency responses of the ideal continuous-time, infinite-length filters in the broadband LCMV beamformer are derived by the frequency-domain optimization. After obtaining the expression of the array output power and finding the half-power point, approximate formulations for the 3-dB beamwidth are achieved to measure the spatial resolutions of the beamformer. By these formulations, the beamwidths of MRA and NRA are compared with that of the ULA. Moreover, the accuracy of the derived formulations is assessed by numerical studies for various scenarios.

In Chapter 7, based on the frequency-domain optimization problem formulated in Chapter 6, the expressions of the ideal filter responses and the output power spectrum of the broadband beamformer using MRA under different scenarios are derived. Several properties about the broadband interference suppression performance of the LCMV beamformer using MRA are obtained based on mathematical proofs and graphic illustrations.

Chapter 8 defines the SRV to measure the variation of the spatial responses over the desired frequency range. Applying the SRV constraint in the optimization formulations for broadband pattern synthesis is studied to control the frequency invariance of the beampattern. It is indicated that using the SRV constraint can reduce the number of constraints in the optimization formulations, at the cost of certain performance degradation. Examples of synthesizing the single-beam FIBP and constructing the multi-beam forming network are presented to show the effect of applying the SRV constraint in broadband pattern synthesis.

Finally, Chapter 9 concludes the thesis and proposes some suggestions for the possible future research.

Chapter 2

Array Fundamentals and Beamforming Background

2.1 Introduction

In this chapter, some array fundamentals and beamforming background are introduced as foundations for the studies in subsequent chapters. The algorithms and performance of some existing broadband time-domain beamformers, which are closely related with the work in this thesis, are described.

This chapter is organized as follows: Section 2.2 introduces some array fundamentals, including the coordinate system, wave propagation model and array geometry. In Section 2.3, the narrowband and broadband signal models, beamforming structures and beampatterns are compared. Section 2.4 describes the algorithms in the broadband LCMV beamformer and the broadband GSC implementation in detail. The influences of the operating bandwidth and the filter length on the performance of the broadband time-domain beamformer are examined.

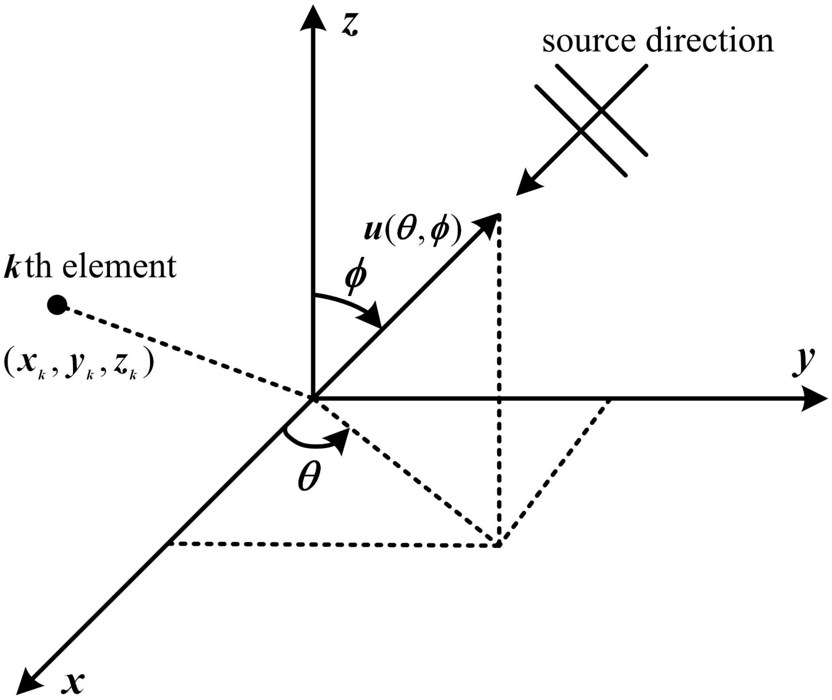

Figure 2.1. Coordinate system.

2.2 Array Fundamentals

2.2.1 Coordinate System and Wave Propagation Model

Cartesian and spherical coordinate systems are frequently used in array systems to describe the positions of the array elements or spatial points in the radiation field of the propagating waves. Figure 2.1 shows the coordinate system of interest, where θ and ϕ are the azimuth and polar angles describing the direction of the propagating wave. The cartesian coordinate (x, y, z) and the spherical coordinate (r, θ, ϕ) can be transformed by the following formula:

$$\begin{aligned} x &= r\sin\phi\cos\theta \\ y &= r\sin\phi\sin\theta \\ z &= r\cos\phi \end{aligned} \tag{2.1}$$

or on the contrary:

$$\begin{aligned} r &= \sqrt{x^2+y^2+z^2} \\ \theta &= \arccos\left(\frac{x}{\sqrt{x^2+y^2}}\right) = \arcsin\left(\frac{y}{\sqrt{x^2+y^2}}\right) \\ \phi &= \arccos\left(\frac{z}{\sqrt{x^2+y^2+z^2}}\right) \end{aligned} \tag{2.2}$$

At a spatial position $\boldsymbol{r}_k = [x_k \;\; y_k \;\; z_k]^T$, the time varying field of an electromagnetic (EM) or acoustic wave at time t can be expressed as:

$$s(t, \boldsymbol{r}_k) = s(t - \boldsymbol{\alpha}^T \boldsymbol{r}_k) \tag{2.3}$$

where the superscript T denotes the transpose. $\boldsymbol{\alpha}$ is the slowness vector defined as:

$$\boldsymbol{\alpha} = -\frac{1}{c}\left[\sin\phi\cos\theta \;\; \sin\phi\sin\theta \;\; \cos\phi\right]^T = -\frac{1}{c}\boldsymbol{u}(\theta,\phi), \tag{2.4}$$

where $\boldsymbol{u}(\theta,\phi)$ is the unit vector in the direction (θ,ϕ). The slowness vector points in the direction of the propagating wave with the magnitude equivalent to $1/c$. c represents the signal propagation velocity.

In this thesis, we make the assumption that the array elements are located in the far field of the directional sources. Therefore, the propagating wave incident on the array has the plane wavefront rather than the spherical wavefront. The plane wavefront means that at any time instant t, $s(t, \boldsymbol{r}_k)$ has the same value for all points in the plane $\boldsymbol{\alpha}^T \boldsymbol{r}_k =$ constant.

2.2.2 Array Geometry

Array geometry is the geometrical form in which the array elements are placed according to the application scenario or the pattern to be synthesized. The linear array, circular

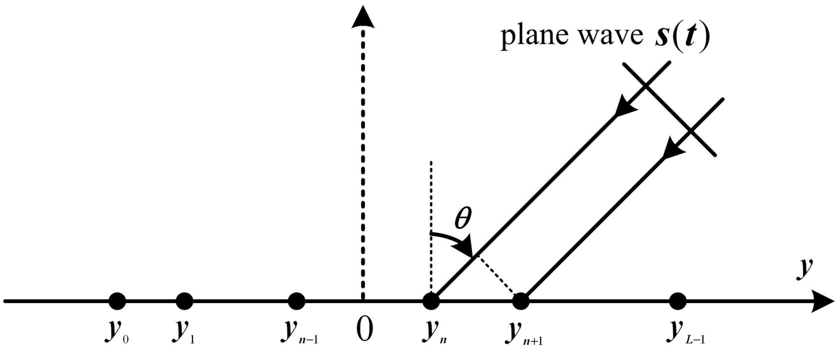

Figure 2.2. Linear array geometry.

array and rectangular planar array are common geometries of interest. The linear array is simple and useful so it has been studied extensively. It can only resolve one-dimensional angles and has the cone-shaped ambiguity. The circular array and the rectangular array can see two-dimensional angles and the ambiguity is above or below the plane of the array. Detailed descriptions for the array geometry can be found in [4, 97].

Our studies in this thesis are focused on the simplest array geometry, the linear array. In this type of geometry, the array elements are deployed along a straight line with the uniform or nonuniform inter-element spacing. We assume that L elements are placed on the y-axis as shown in Figure 2.2. The coordinates of the array elements satisfy $x_k = 0$ and $z_k = 0$. The source direction θ is measured from the broadside of the array so its value is within $[-90°, 90°]$. The time delay of the wavefront arriving at the kth element relative to the origin is calculated by

$$\tau_k(\theta) = \frac{y_k}{c} \sin\theta \tag{2.5}$$

In this thesis, we assume that all the array elements are identical, omnidirectional and there is no mutual coupling. For the ULA, if the beamformer works at a single frequency, the responses caused by the array elements are similar to the responses on the taps of the

FIR filters in the mathematical form. Therefore, previously investigated theories about FIR filtering can be transplanted to narrowband beamforming in the ULA.

Besides, two types of nonuniform linear arrays, the MRA and NRA, are studied in this thesis. Nonuniform spacing may lead to performance improvement, like increasing the resolution and resolving the ambiguity problem. In [98–100], procedures for searching the sensor placement for the MRA and NRA are addressed. The coarray presents all the spatial lags that can be obtained for the given placement of array elements. Reducing the redundancy involves spreading out the coarray and thereby increasing the number of distinct separations that can be obtained. The geometries of MRA are designed by minimizing the redundancy of spatial correlation lags. If there is no missing lags, it belongs to the restricted MRA, otherwise it is an unrestricted MRA. The NRA has the structure with the minimum missing lags and no redundant lags. MRA and NRA with three or four sensors have the same sensor placement, without duplications for nonzero lags and without missing lags. The ULA with L sensors generates correlation estimates at L different spatial lags with redundancy. MRA and NRA with the same number of sensors can generate correlation estimates at more spatial lags. This corresponds to prolonged array apertures and leads to better spatial resolutions for a given number of array elements.

For the ULA, MRA and NRA with five elements in the narrowband scenario, with the sensor positions chosen to be $\{0, 1, 2, 6, 9\}d$ for the MRA and $\{0, 1, 4, 9, 11\}d$ for the NRA. d is the unit spacing equal to half the wavelength. Tables 2.1 - 2.3 demonstrate the positions of array elements and the spatial lags in the coarrays. More than one mark appears when the spatial lag has redundancies. Figure 2.3 shows their beampatterns when all the weights equal 0.2. The beampatterns for the MRA and NRA have much narrower beamwidth but higher sidelobe level than the ULA.

Table 2.1: FIVE-ELEMENT ULA AND ITS COARRAY

Spatial Positions or Lags (d)	0	1	2	3	4
Positions of Array Elements	×	×	×	×	×
Spatial Lags in the Coarray	×	×	×	×	×
	×	×	×	×	
	×	×	×		
	×	×			
	×				

Table 2.2: FIVE-ELEMENT MRA AND ITS COARRAY

Spatial Positions or Lags (d)	0	1	2	3	4	5	6	7	8	9
Positions of Array Elements	×	×	×				×			×
Spatial Lags in the Coarray	×	×	×	×	×	×	×	×	×	×
	×	×								
	×									
	×									
	×									

Table 2.3: FIVE-ELEMENT NRA AND ITS COARRAY

Spatial Positions or Lags (d)	0	1	2	3	4	5	6	7	8	9	10	11
Positions of Array Elements	×	×			×					×		×
Spatial Lags in the Coarray	×	×		×	×	×		×	×	×	×	×
	×											
	×											
	×											
	×											

2.3 Signal Models and Beamforming

Narrowband and broadband beamforming involves different signal models, beamforming structures and beampatterns.

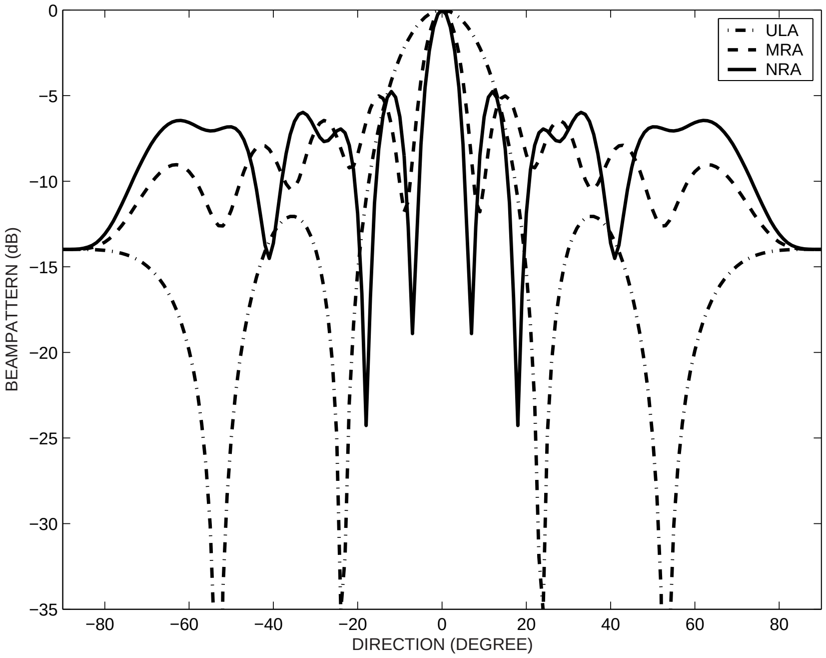

Figure 2.3. Beampatterns of the ULA, MRA and NRA with five elements.

2.3.1 Narrowband Signal Model and Beamforming

i) Narrowband Signal Model

Under the narrowband assumption, the maximum time delay for a signal to traverse the whole array is much smaller than its correlation time (the reciprocal of the bandwidth). Therefore, the variation of the signal envelope over the array aperture is negligible. At the time instant t and the spatial position $\boldsymbol{r}_k$, the narrowband signal is usually modelled as:

$$s(t, \boldsymbol{r}_k) = A(t)e^{j(2\pi f_0 t - \boldsymbol{k}^T \boldsymbol{r}_k)} \tag{2.6}$$

where j is the imaginary unit and equivalent to $\sqrt{-1}$. $A(t)$ represents the complex modulating function. f_0 denotes the carrier frequency. $\boldsymbol{k}$ is referred to as the wavenumber vector and defined as:

$$\boldsymbol{k} = 2\pi f_0 \boldsymbol{\alpha} \tag{2.7}$$

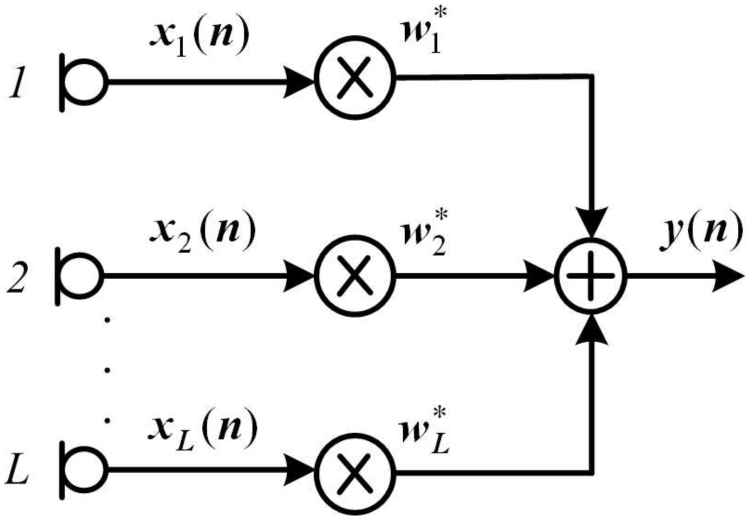

Figure 2.4. Narrowband beamforming structure.

where $\boldsymbol{\alpha}$ is the slowness vector defined in (2.4). The amplitude of $\boldsymbol{k}$ is equal to the wavenumber $2\pi/\lambda$. The direction of $\boldsymbol{k}$ is the same as that of the propagating wave.

ii) Narrowband Beamforming Structure and Beampattern

Figure 2.4 shows a typical narrowband beamforming structure. The weights of this beamformer are complex scalars. The output of the beamformer is computed by:

$$y(n) = \sum_{i=1}^{L} w_i^* x_i(n) = \boldsymbol{w}^H \boldsymbol{x}(n) \tag{2.8}$$

where the superscript $*$ represents the complex conjugate. $\boldsymbol{x}(n)$ is the $L \times 1$ vector consisting of the discrete samples from each array element:

$$\boldsymbol{x}(n) = [x_1(n) \;\; x_2(n) \;\; \cdots \;\; x_L(n)]^T \tag{2.9}$$

$\boldsymbol{w}$ is the $L \times 1$ weight vector:

$$\boldsymbol{w} = [w_1 \;\; w_2 \;\; \cdots \;\; w_L]^T \tag{2.10}$$

The value of the weight vector can be fixed or adaptively adjusted according to the type of the beamformer. Literatures [1–3, 5] can be referred to for the design of narrowband beamforming algorithms.

According to the narrowband signal model (2.6), the response of each array element to the incident plane wave $A(t)e^{j2\pi f_0 t}$ constitutes the following vector:

$$\boldsymbol{a}(\boldsymbol{\alpha}) = [e^{-j2\pi f_0 \boldsymbol{\alpha}^T \boldsymbol{r}_1} \;\; e^{-j2\pi f_0 \boldsymbol{\alpha}^T \boldsymbol{r}_2} \;\; \cdots \;\; e^{-j2\pi f_0 \boldsymbol{\alpha}^T \boldsymbol{r}_L}]^T \tag{2.11}$$

$\boldsymbol{a}(\boldsymbol{\alpha})$ is called the array steering vector. Under the assumption of the linear array geometry, the steering vector is re-expressed as:

$$\boldsymbol{a}(\theta) = [e^{j2\pi f_0 \tau_1(\theta)} \;\; e^{j2\pi f_0 \tau_2(\theta)} \;\; \cdots \;\; e^{j2\pi f_0 \tau_L(\theta)}]^T \tag{2.12}$$

where $\tau_k(\theta)$ is given by (2.5). The spatial response of the beamformer for the narrowband signal coming from θ is given by:

$$H(\theta) = \boldsymbol{w}^H \boldsymbol{a}(\theta) \tag{2.13}$$

It is a function of the incident angle. The beampattern is defined as the norm square of the spatial response (2.13).

2.3.2 Broadband Signal Model and Beamforming

i) Broadband Signal Model

The broadband signal occupies a certain frequency band. For the deterministic signal, it

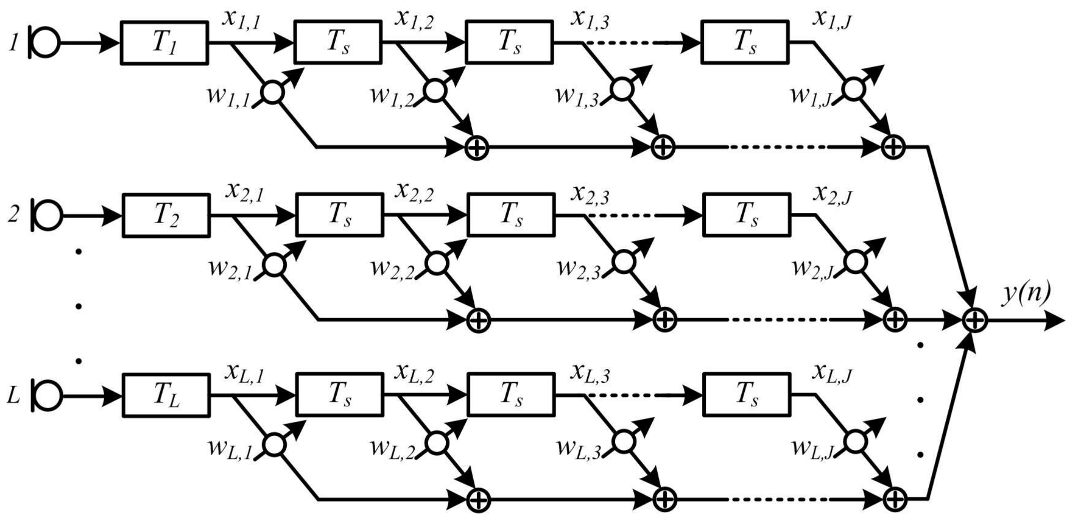

Figure 2.5. Time-domain broadband beamforming structure.

can be modelled as the superposition of multiple narrowband signals:

$$s(t, \boldsymbol{r}_k) = \int_{f \in F} A(f) e^{j\phi(f)} e^{j2\pi f(t - \boldsymbol{\alpha}^T \boldsymbol{r}_k)} df \tag{2.14}$$

where F represents the frequency band of the broadband signal. $A(f)$ and $\phi(f)$ are the amplitude spectrum and phase spectrum. For the random signal, a convenient way to represent the signal at the time instant t and the spatial position $\boldsymbol{r}_k$ is:

$$s(t, \boldsymbol{r}_k) = \int_{\tau} s(t - \tau) h(\tau, \boldsymbol{r}_k) d\tau \tag{2.15}$$

where $s(t)$ is the random signal with a broad power spectrum density. $h(t, \boldsymbol{r}_k)$ denotes the kth-channel impulse response of the array.

ii) Broadband Beamforming Structure and Beampattern

Unlike narrowband signals which only need one-dimensional processing in the spatial domain, for broadband signals, both spatial and temporal samples are required for the two-dimensional processing. Figure 2.5 shows a general time-domain broadband beamforming structure implemented in the element space. The array consists of L sensors. Presteering delays $T_1, \cdots, T_L$ are followed behind each element to steer the look direction of the array to the specified direction. It should be noted that some specially designed broadband beamformers can work without the presteering delays [101]. Moreover, transversal filters with J taps are connected after presteering delays in each channel. The real-valued weight vector is expressed as:

$$\boldsymbol{w} = [w_{1,1} \quad \cdots \quad w_{L,1} \quad \cdots \quad w_{1,J} \quad \cdots \quad w_{L,J}]^T \tag{2.16}$$

The data at all taps correspondingly form an $LJ \times 1$ vector:

$$\boldsymbol{x}(n) = [x_{1,1}(n) \quad \cdots \quad x_{L,1}(n) \quad \cdots \quad x_{1,J}(n) \quad \cdots \quad x_{L,J}(n)]^T \tag{2.17}$$

where $x_{i,k}(n)$ is the sampled data variable:

$$\begin{gathered} x_{i,k}(n) = x_i[n-(k-1)], \\ i = 1, 2, \cdots, L; \quad k = 1, 2, \cdots, J \end{gathered} \tag{2.18}$$

where $x_i(n)$ is the presteered data from the ith sensor. The output of the beamformer is the weighted sum of $x_{i,k}(n)$:

$$y(n) = \boldsymbol{w}^T \boldsymbol{x}(n) = \sum_{i=1}^{L} \sum_{k=1}^{J} w_{i,k} x_i[n-(k-1)] \tag{2.19}$$

We would like to highlight that the weights of the broadband beamformers presented in this thesis are real but not complex like in the narrowband processors. Therefore, all the algorithms for the broadband beamformers are described by the operations on the real signals and real beamforming weights.

According to the beamforming structure shown in Figure 2.5, the spatial response of this beamformer can be expressed as a function of both frequency and direction [5] as follows:

$$H(f,\theta) = \boldsymbol{s}^T(f,\theta)\cdot\boldsymbol{T}(f)\cdot\sum_{k=1}^{J}\boldsymbol{w}_k e^{-j2\pi f(k-1)T_s} \tag{2.20}$$

where

$$\boldsymbol{w}_k = [w_{1,k}\ \ w_{2,k}\ \ \cdots\ \ w_{L,k}]^T \tag{2.21}$$

$\boldsymbol{T}(f)$ is an $L\times L$ diagonal matrix to carry out presteering, which is defined as follows:

$$\boldsymbol{T}(f) = \begin{pmatrix} e^{-j2\pi fT_1} & 0 & \cdots & 0 \\ 0 & e^{-j2\pi fT_2} & \cdots & 0 \\ \vdots & \vdots & \ddots & \vdots \\ 0 & 0 & \cdots & e^{-j2\pi fT_L} \end{pmatrix} \tag{2.22}$$

where T_i is the presteering delay behind the ith sensor. $\boldsymbol{s}(f,\theta)$ is an $L\times 1$ column vector:

$$\boldsymbol{s}(f,\theta) = [e^{j2\pi f\tau_1(\theta)}\ \ e^{j2\pi f\tau_2(\theta)}\ \ \cdots\ \ e^{j2\pi f\tau_L(\theta)}]^T \tag{2.23}$$

Under exact presteering delays,

$$\boldsymbol{s}^T(f,\theta_0)\boldsymbol{T}(f) = \varphi(f)[1\ \ 1\ \ \cdots\ \ 1] \tag{2.24}$$

where θ_0 represents the look direction. $\varphi(f) = e^{-j2\pi fT_0}$ corresponds to a bulk delay T_0. Therefore, the look-direction response is:

$$H(f,\theta_0) = \varphi(f)\sum_{k=1}^{J} f_k e^{-j2\pi f(k-1)T_s} \tag{2.25}$$

where

$$f_k = \boldsymbol{c}^T \boldsymbol{w}_k, \quad k = 1, 2, \cdots, J \tag{2.26}$$

and $\boldsymbol{c}$ is an $L \times 1$ vector given by

$$\boldsymbol{c} = [1 \;\; 1 \;\; \cdots \;\; 1]^T \tag{2.27}$$

If there is no presteering delays, the spatial response of the beamformer is written in another form:

$$H(f, \theta) = \boldsymbol{w}^T \boldsymbol{a}(f, \theta) \tag{2.28}$$

where $\boldsymbol{a}(f, \theta)$ can be considered as the steering vector of the broadband beamformer:

$$\boldsymbol{a}(f, \theta) = \boldsymbol{e}(f) \otimes \boldsymbol{s}(f, \theta) \tag{2.29}$$

where $\otimes$ represents the Kronecker product and

$$\boldsymbol{e}(f) = [1 \;\; e^{-j2\pi f T_s} \;\; \cdots \;\; e^{-j2\pi f (J-1) T_s}]^T \tag{2.30}$$

As shown by (2.20) and (2.28), the spatial response of the broadband beamformer is a function of both the direction and the frequency. Figure 2.6 shows an example of two-dimensional beampatterns of a broadband time-domain beamformer. We observe that the mainlobe width and the sidelobe position vary significantly with the frequency.

Another important broadband beamforming structure is the frequency-domain implementation shown in Figure 2.7. FFT is used to decompose the array data into N narrowband frequency components. Narrowband processing with the complex-valued weight vector is performed in each frequency bin. IFFT is used to obtain the time-domain signal as the beamformer output. The narrowband beamformer introduced in Section 2.3.1 can be

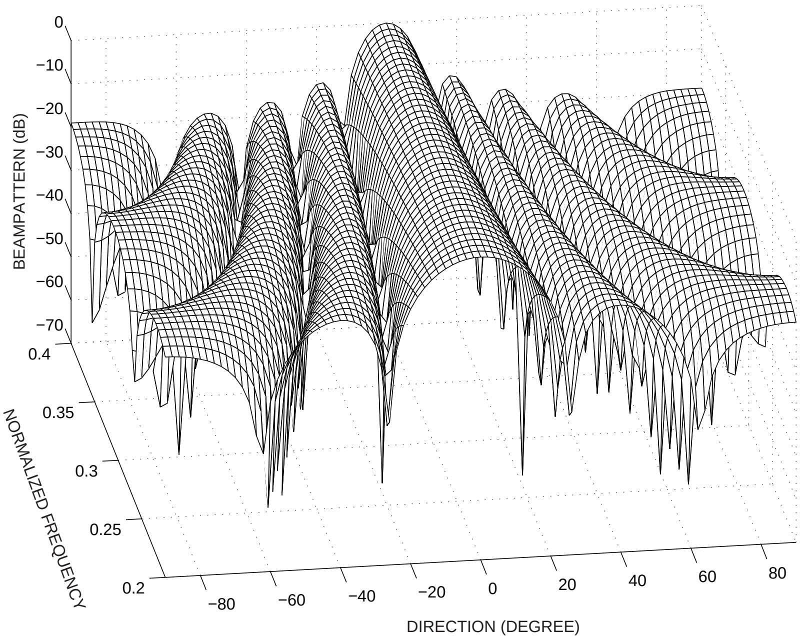

Figure 2.6. Two-dimensional beampattern of a broadband time-domain beamformer.

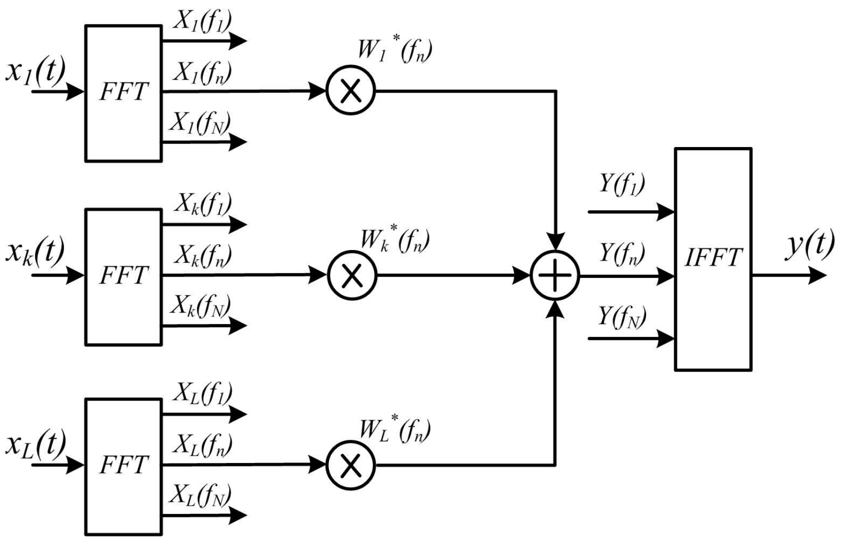

Figure 2.7. Frequency-domain broadband beamforming structure.

referred to for the data model and the beamforming in each frequency bin.

2.4 Broadband Time-Domain Beamformers

2.4.1 Broadband LCMV Beamformer

The Frost beamformer presented in [7] is one of the earliest broadband time-domain beamformers with the beamforming structure shown by Figure 2.5. The optimum weight vector of the Frost beamformer is computed by the LCMV optimization criterion, which is designed to minimize the mean output power subject to certain linear constraints. Under the assumption of accurate presteering delays, the signal coming from the look direction is completely in phase at each element. The look-direction response of the beamformer is specified by the linear constraint. The optimization formulation is given by:

$$\begin{aligned} &\min_{\boldsymbol{w}} \ \boldsymbol{w}^T \boldsymbol{R}_{\boldsymbol{xx}} \boldsymbol{w} \\ &\text{subject to } \boldsymbol{C}^T \boldsymbol{w} = \boldsymbol{f} \end{aligned} \tag{2.31}$$

where $\boldsymbol{R}_{\boldsymbol{xx}}$ is the correlation matrix. $\boldsymbol{C}$ is the constraint matrix:

$$\boldsymbol{C} = \begin{pmatrix} \mathbf{1}_L & \mathbf{0}_L & \cdots & \mathbf{0}_L \\ \mathbf{0}_L & \mathbf{1}_L & \cdots & \mathbf{0}_L \\ \vdots & \vdots & \ddots & \vdots \\ \mathbf{0}_L & \cdots & \cdots & \mathbf{1}_L \end{pmatrix} \tag{2.32}$$

where $\mathbf{1}_L$ and $\mathbf{0}_L$ are all-one and all-zero column vectors with the dimension L. The J-dimensional constraint vector $\boldsymbol{f}$ is the specified impulse response in the look direction. If the distortionless response is required in the look direction, the constraint vector $\boldsymbol{f}$ is:

$$\boldsymbol{f} = [0 \ \cdots \ 0 \ 1 \ 0 \ \cdots \ 0]^T \tag{2.33}$$

The position of 1 in the vector $\boldsymbol{f}$ can be optimized.

The Lagrangian η associated with the problem (2.31) can be defined as:

$$\eta = \frac{1}{2}\boldsymbol{w}^T\boldsymbol{R}_{\boldsymbol{xx}}\boldsymbol{w} + \boldsymbol{\lambda}^T(\boldsymbol{C}^T\boldsymbol{w} - \boldsymbol{f}) \tag{2.34}$$

where $\boldsymbol{\lambda}$ is the Lagrange multiplier. The gradient of η relative to $\boldsymbol{w}$ is:

$$\nabla\eta = \boldsymbol{R}_{\boldsymbol{xx}}\boldsymbol{w} + \boldsymbol{C}\boldsymbol{\lambda} \tag{2.35}$$

For the convex optimization problem (2.31), the optimum solution is achieved by solving the equation $\nabla\eta = 0$. Thus, the optimum weight vector is given by:

$$\boldsymbol{w} = -\boldsymbol{R}_{\boldsymbol{xx}}^{-1}\boldsymbol{C}\boldsymbol{\lambda} \tag{2.36}$$

Substituting this expression into the constraint in (2.31), the Lagrange multiplier is solved as:

$$\boldsymbol{\lambda} = -(\boldsymbol{C}^T\boldsymbol{R}_{\boldsymbol{xx}}^{-1}\boldsymbol{C})^{-1}\boldsymbol{f} \tag{2.37}$$

Finally, the optimum weight vector of the optimization formulation (2.31) is obtained as:

$$\boldsymbol{w}_{opt} = \boldsymbol{R}_{\boldsymbol{xx}}^{-1}\boldsymbol{C}(\boldsymbol{C}^T\boldsymbol{R}_{\boldsymbol{xx}}^{-1}\boldsymbol{C})^{-1}\boldsymbol{f} \tag{2.38}$$

In [7], a gradient-descent adaptive algorithm, the constrained LMS algorithm, is designed to adjust the weight vector iteratively. The weight at the $(n+1)$th iteration is updated by:

$$\begin{aligned}\boldsymbol{w}(n+1) &= \boldsymbol{w}(n) - \mu\nabla\eta(n) \\ &= \boldsymbol{w}(n) - \mu[\boldsymbol{R}_{\boldsymbol{xx}}\boldsymbol{w}(n) + \boldsymbol{C}\boldsymbol{\lambda}(n)] \end{aligned} \tag{2.39}$$

where μ is the step size. By substituting this iterative formulation into the constraint, the following expression is obtained:

$$\begin{aligned} \boldsymbol{f} &= \boldsymbol{C}^T \boldsymbol{w}(n+1) \\ &= \boldsymbol{C}^T \boldsymbol{w}(n) - \mu \boldsymbol{C}^T \boldsymbol{R}_{\boldsymbol{xx}} \boldsymbol{w}(n) - \mu \boldsymbol{C}^T \boldsymbol{C} \boldsymbol{\lambda}(n) \end{aligned} \tag{2.40}$$

By (2.40), $\boldsymbol{\lambda}(n)$ can be solved for and substituted into (2.39) to derive $\boldsymbol{w}(n+1)$. With $\boldsymbol{R}_{\boldsymbol{xx}}$ estimated by $\boldsymbol{x}(n)\boldsymbol{x}^T(n)$, the following iterative formulation is achieved:

$$\begin{cases} \boldsymbol{w}(0) = \boldsymbol{g} \\ \boldsymbol{w}(n+1) = \boldsymbol{P}[\boldsymbol{w}(n) - \mu y(n)\boldsymbol{x}(n)] + \boldsymbol{g} \end{cases} \tag{2.41}$$

where

$$\boldsymbol{g} = \boldsymbol{C}(\boldsymbol{C}^T\boldsymbol{C})^{-1}\boldsymbol{f} \tag{2.42}$$

$$\boldsymbol{P} = \boldsymbol{I} - \boldsymbol{C}(\boldsymbol{C}^T\boldsymbol{C})^{-1}\boldsymbol{C}^T \tag{2.43}$$

where $\boldsymbol{I}$ represents $LJ \times LJ$ identity matrix. It is easy to prove that $\boldsymbol{C}^T\boldsymbol{w}(0) = \boldsymbol{f}$.

Due to the simple form of the matrix $\boldsymbol{C}$, the iterative formulation for $\boldsymbol{w}$ can be simplified to the following expression:

$$\begin{aligned} w_{i,k}(n+1) = w_{i,k}(n) - \mu y(n)x_{i,k}(n) - \frac{1}{L}\sum_{l=1}^{L}\Big[w_{l,k}(n) - \mu y(n)x_{l,k}(n)\Big] + \frac{f_k}{L} \\ i = 1, \cdots, L; \quad k = 1, \cdots, J \end{aligned} \tag{2.44}$$

2.4.2 Broadband GSC Beamformer

An alternative implementation of the broadband LCMV beamformer is the broadband GSC proposed in [8], with the structure shown in Figure 2.8. Similar to the element-space structure shown in Figure 2.5, presteering delays $T_1, \cdots, T_L$ follow behind the array

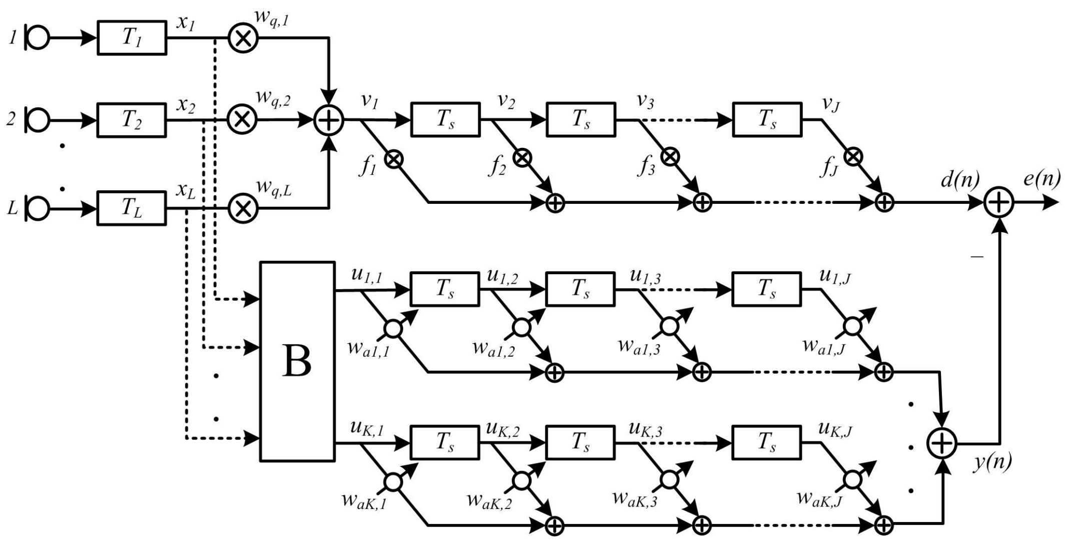

Figure 2.8. GSC beamforming structure.

elements in the GSC beamformer to align the signals coming from the look direction. The GSC beamforming structure consists of two branches. The upper branch uses the quiescent weight vector $\boldsymbol{w}_q$ to form a fixed beam and the fixed coefficient vector $\boldsymbol{f}$ to generate the frequency response in the look direction. The $K \times L$ blocking matrix $\boldsymbol{B}$ in the lower branch is used to prevent the leakage of the desired signal to the adaptive filters. The multichannel filters after the blocking matrix adopt adaptive weights.

The array signal after steering delays is expressed by an $L \times 1$ vector $\check{\boldsymbol{x}}(n)$:

$$\check{\boldsymbol{x}}(n) = [x_1(n) \;\; x_2(n) \;\; \cdots \;\; x_L(n)]^T \tag{2.45}$$

The fixed weight vector $\boldsymbol{w}_q$, the filter coefficient vector $\boldsymbol{f}$, the adaptive weight vector $\boldsymbol{w}_a$ are respectively defined as:

$$\boldsymbol{w}_q = [w_{q,1} \;\; w_{q,2} \;\; \cdots \;\; w_{q,L}]^T \tag{2.46}$$

$$\boldsymbol{f} = [f_1 \;\; f_2 \;\; \cdots \;\; f_J]^T \tag{2.47}$$

$$\boldsymbol{w}_a = [w_{a1,1} \quad \cdots \quad w_{aK,1} \quad \cdots \quad w_{a1,J} \quad \cdots \quad w_{aK,J}]^T \tag{2.48}$$

The output of the beamformer is:

$$e(n) = d(n) - y(n) \tag{2.49}$$

where $d(n)$ and $y(n)$ are the outputs of the upper and lower branches, respectively, with

$$d(n) = \boldsymbol{f}^T \boldsymbol{v}(n) \tag{2.50}$$

$$y(n) = \boldsymbol{w}_a^T \boldsymbol{u}(n) \tag{2.51}$$

where $\boldsymbol{v}(n)$ is the sampled data of the fixed beamformer output:

$$\boldsymbol{v}(n) = \Big[v(n) \;\; v(n-1) \;\; \cdots \;\; v[n-(J-1)] \Big]^T \tag{2.52}$$

$$v(n) = \boldsymbol{w}_q^T \check{\boldsymbol{x}}(n) \tag{2.53}$$

and

$$\boldsymbol{u}(n) = \Big[\boldsymbol{u}_1^T(n) \;\; \boldsymbol{u}_2^T(n) \;\; \cdots \;\; \boldsymbol{u}_J^T(n) \Big]^T \tag{2.54}$$

$$\boldsymbol{u}_k(n) = [u_{1,k}(n) \;\; u_{2,k}(n) \;\; \cdots \;\; u_{K,k}(n)]^T \tag{2.55}$$

$$u_{i,k}(n) = u_i[n-(k-1)] \tag{2.56}$$

The relation between $\check{\boldsymbol{x}}(n)$ and $\boldsymbol{u}_1(n)$ is:

$$\boldsymbol{u}_1(n) = \boldsymbol{B} \check{\boldsymbol{x}}(n) \tag{2.57}$$

where $\boldsymbol{B}$ is the $K \times L$ blocking matrix which can be evaluated according to various objectives like those presented in [8, 26, 29]. For example, a simple form of the blocking matrix $\boldsymbol{B}$ with the dimension $(L-1) \times L$ is used in [8]:

$$\boldsymbol{B} = \begin{pmatrix} 1 & -1 & 0 & \cdots & 0 & 0 \\ 0 & 1 & -1 & \cdots & 0 & 0 \\ \vdots & \vdots & \vdots & \ddots & \vdots & \vdots \\ 0 & 0 & 0 & \cdots & 1 & -1 \end{pmatrix} \tag{2.58}$$

The $LJ \times 1$ vectors $\boldsymbol{x}(n)$, $\tilde{\boldsymbol{w}}_q$ and the $KJ \times LJ$ matrix $\tilde{\boldsymbol{B}}$ are respectively defined as follows:

$$\boldsymbol{x}(n) = \left[\check{\boldsymbol{x}}^T(n) \ \ \check{\boldsymbol{x}}^T(n-1) \ \ \cdots \ \ \check{\boldsymbol{x}}^T[n-(J-1)] \right]^T \tag{2.59}$$

$$\tilde{\boldsymbol{w}}_q = \begin{pmatrix} \boldsymbol{w}_q & \boldsymbol{0}_L & \cdots & \boldsymbol{0}_L \\ \boldsymbol{0}_L & \boldsymbol{w}_q & \cdots & \boldsymbol{0}_L \\ \vdots & \vdots & \ddots & \vdots \\ \boldsymbol{0}_L & \cdots & \cdots & \boldsymbol{w}_q \end{pmatrix}_{LJ \times J} \cdot \boldsymbol{f} \tag{2.60}$$

$$\tilde{\boldsymbol{B}} = \begin{pmatrix} \boldsymbol{B} & \boldsymbol{0}_{K \times L} & \cdots & \boldsymbol{0}_{K \times L} \\ \boldsymbol{0}_{K \times L} & \boldsymbol{B} & \cdots & \boldsymbol{0}_{K \times L} \\ \vdots & \vdots & \ddots & \vdots \\ \boldsymbol{0}_{K \times L} & \cdots & \cdots & \boldsymbol{B} \end{pmatrix}_{KJ \times LJ} \tag{2.61}$$

In the GSC beamformer, the optimum weight vector in the lower branch is obtained by minimizing the mean output power without constraints:

$$\min_{\boldsymbol{w}_a} \mathrm{E}[e^2(n)] \tag{2.62}$$

According to the above described formulations, we obtain:

$$\mathrm{E}[e^2(n)] = \mathrm{E}\left\{ [\tilde{\boldsymbol{w}}_q{}^T \boldsymbol{x}(n) - \boldsymbol{w}_a^T \tilde{\boldsymbol{B}} \boldsymbol{x}(n)]^2 \right\}$$

$$= \tilde{\boldsymbol{w}}_q{}^T \boldsymbol{R}_{\boldsymbol{xx}} \tilde{\boldsymbol{w}}_q - \tilde{\boldsymbol{w}}_q{}^T \boldsymbol{R}_{\boldsymbol{xx}} \tilde{\boldsymbol{B}}^T \boldsymbol{w}_a - \boldsymbol{w}_a^T \tilde{\boldsymbol{B}} \boldsymbol{R}_{\boldsymbol{xx}} \tilde{\boldsymbol{w}}_q + \boldsymbol{w}_a^T \tilde{\boldsymbol{B}} \boldsymbol{R}_{\boldsymbol{xx}} \tilde{\boldsymbol{B}}^T \boldsymbol{w}_a \tag{2.63}$$

where $\boldsymbol{R}_{\boldsymbol{xx}} = \mathrm{E}[\boldsymbol{x}(n)\boldsymbol{x}^T(n)]$. The optimum weight vector $\boldsymbol{w}_{aopt}$ can be found by solving $\nabla \mathrm{E}[e^2(n)] = 2\tilde{\boldsymbol{B}} \boldsymbol{R}_{\boldsymbol{xx}} \tilde{\boldsymbol{B}}^T \boldsymbol{w}_a - 2\tilde{\boldsymbol{B}} \boldsymbol{R}_{\boldsymbol{xx}} \tilde{\boldsymbol{w}}_q = \boldsymbol{0}$. Therefore, the optimum weight vector in the lower branch of the GSC beamformer is given by:

$$\boldsymbol{w}_{aopt} = (\tilde{\boldsymbol{B}} \boldsymbol{R}_{\boldsymbol{xx}} \tilde{\boldsymbol{B}}^T)^{-1} \tilde{\boldsymbol{B}} \boldsymbol{R}_{\boldsymbol{xx}} \tilde{\boldsymbol{w}}_q \tag{2.64}$$

2.4.3 Influences of Bandwidth and Filter Length

Studies show that the performance of an adaptive array will deteriorate rapidly as the operating bandwidth increases. We use simulations to demonstrate the influences of the bandwidth and the filter length on the system performance.

The time-domain element-space beamformer with exact presteering delays is assumed. The LCMV optimization criterion with the distortionless constraint is adopted to compute the optimum weight vector, as expressed by (2.38). The performance of the beamformer is observed by the output signal-to-interference ratio (SIR) and SINR. Before the simulation, the formulation of the ideal correlation matrix of the broadband array is derived as follows.

The directional sources with flat spectra within the same frequency range are assumed. In addition, we assume the desired signal and the interferences are uncorrelated with each other. The noise is temporally and spatially white with zero mean. All the directional sources and the noise are stationary random processes. The continuous-time array data is modelled as:

$$\boldsymbol{x}(t) = \boldsymbol{s}(t) + \sum_{k=1}^{K} \boldsymbol{u}_k(t) + \boldsymbol{n}(t) \tag{2.65}$$

where $\boldsymbol{x}(t)$ is an $LJ \times 1$ vector:

$$\boldsymbol{x}(t) = \Big[x_1(t) \ \cdots \ x_L(t) \ \cdots \ x_1[t-(J-1)T_s] \ \cdots \ x_L[t-(J-1)T_s]\Big]^T \tag{2.66}$$

$\boldsymbol{s}(t)$, $\boldsymbol{u}_k(t)$ and $\boldsymbol{n}(t)$ are the desired signal component, the jammer component and the noise component in $\boldsymbol{x}(t)$. The space-time correlation matrix is:

$$\boldsymbol{R_{xx}} = \mathrm{E}[\boldsymbol{x}(t)\boldsymbol{x}^T(t)] \tag{2.67}$$

According to the assumptions, it can be written as:

$$\boldsymbol{R_{xx}} = \boldsymbol{R_{ss}} + \sum_{k=1}^{K} \boldsymbol{R_{u_k u_k}} + \boldsymbol{R_{nn}} \tag{2.68}$$

where $\boldsymbol{R_{nn}} = \sigma_n^2 \boldsymbol{I}$. $\boldsymbol{I}$ represents the $LJ \times LJ$ identity matrix. σ_n^2 is the power of the noise. In (2.68), adding the space-time correlation matrices of the desired signal and the interferences without cross-correlation terms implies that all the directional sources are uncorrelated. Due to the assumption that both the interferences and the signal of interest have flat temporal spectra, the entries of $\boldsymbol{R_{ss}}$ and $\boldsymbol{R_{u_k u_k}}$ can be computed by the same formulation with different parameters like the power and the incident direction. They can be calculated by the inverse Fourier transform of the cross spectrum matrix with the time lag specified as zero. The computation of $\boldsymbol{R_{ss}}$ is derived as follows:

$$\boldsymbol{R_{ss}} = \int_{f \in F} \boldsymbol{S}(f)df \tag{2.69}$$

where F represents the frequency band of the desired signal. For the real signal, the spectrum is symmetric and assumed to be nonzero within $F = [-f_u, -f_l] \cup [f_l, f_u]$. The total bandwidth is $2B = 2(f_u - f_l)$. Therefore, the spectral density of the signal is expressed by:

$$S(f) = \begin{cases} \frac{\sigma_s^2}{2B}, \ f \in F \\ 0, \quad \text{otherwise} \end{cases} \tag{2.70}$$

where σ_s^2 is the signal power. The cross spectrum matrix $\boldsymbol{S}(f)$ is expressed by [5]:

$$\boldsymbol{S}(f) = S(f)\boldsymbol{a}(f,\theta)\boldsymbol{a}^H(f,\theta) \tag{2.71}$$

where $\boldsymbol{a}(f,\theta)$ represents the $LJ \times 1$ stacked steering vector of the broadband beamformer. It is given by:

$$\boldsymbol{a}(f,\theta) = \boldsymbol{e}(f) \otimes \boldsymbol{s}(f,\theta) \tag{2.72}$$

where

$$\boldsymbol{e}(f) = [1 \ \ e^{-j2\pi f T_s} \ \ \cdots \ \ e^{-j2\pi f(J-1)T_s}]^T \tag{2.73}$$

$$\boldsymbol{s}(f,\theta) = [e^{j2\pi f \tau_1(\theta)} \ \ e^{j2\pi f \tau_2(\theta)} \ \ \cdots \ \ e^{j2\pi f \tau_L(\theta)}]^T \tag{2.74}$$

The (m,n)th element of $\boldsymbol{S}(f)$ is $S(f)e^{j2\pi f \varsigma_{m,n}}$, where

$$\begin{aligned} \varsigma_{m,n} &= [\tau_{i_1}(\theta) - k_1 T_s] - [\tau_{i_2}(\theta) - k_2 T_s] \\ & m = k_1 L + i_1; n = k_2 L + i_2; i_1 = 1,2,\cdots,L; \\ & k_1 = 0,1,\cdots,J-1; i_2 = 1,2,\cdots,L; k_2 = 0,1,\cdots,J-1. \end{aligned} \tag{2.75}$$

The integral of $S(f)e^{j2\pi f \varsigma_{m,n}}$ within $f \in F$ can be computed in the following closed-form expression:

$$\begin{aligned} [\boldsymbol{R_{ss}}]_{m,n} &= \int_{f\in F} \frac{\sigma_s^2}{2B} e^{j2\pi f \varsigma_{m,n}} df \\ &= \frac{\sigma_s^2}{2B}\left[\frac{e^{-j2\pi f_l \varsigma_{m,n}} - e^{-j2\pi f_u \varsigma_{m,n}}}{j2\pi\varsigma_{m,n}} + \frac{e^{j2\pi f_u \varsigma_{m,n}} - e^{j2\pi f_l \varsigma_{m,n}}}{j2\pi\varsigma_{m,n}}\right] \\ &= \frac{\sigma_s^2}{2B}\left[\frac{\sin(2\pi f_u \varsigma_{m,n})}{\pi\varsigma_{m,n}} - \frac{\sin(2\pi f_l \varsigma_{m,n})}{\pi\varsigma_{m,n}}\right] \end{aligned}$$

$$= \frac{\sigma_s^2}{B}\left[f_u \text{sinc}(2f_u \varsigma_{m,n}) - f_l \text{sinc}(2f_l \varsigma_{m,n})\right] \tag{2.76}$$

where sinc$(\alpha) = \sin(\pi\alpha)/(\pi\alpha)$. $[\boldsymbol{R_{ss}}]_{m,n}$ is the (m,n)th element of $\boldsymbol{R_{ss}}$. By the above calculation, the correlation matrix $\boldsymbol{R_{ss}}$ for the desired signal is obtained. With the same method, the correlation matrix for all the interferences can be achieved. Then we can get the overall correlation matrix $\boldsymbol{R_{xx}}$ of the array snapshot data.

To reduce the influences brought by many factors in real implementations, the ideal correlation matrix derived above is used in the following simulations. The output SINR and SIR for evaluating the performance of the beamformer are computed as follows:

$$\text{SINR} = 10\log_{10}\left(\frac{\boldsymbol{w}^T\boldsymbol{R_{ss}}\boldsymbol{w}}{\sum_{k=1}^{K}\boldsymbol{w}^T\boldsymbol{R}_{\boldsymbol{u}_k\boldsymbol{u}_k}\boldsymbol{w} + \boldsymbol{w}^T\boldsymbol{R_{nn}}\boldsymbol{w}}\right) \quad \text{dB} \tag{2.77}$$

$$\text{SIR} = 10\log_{10}\left(\frac{\boldsymbol{w}^T\boldsymbol{R_{ss}}\boldsymbol{w}}{\sum_{k=1}^{K}\boldsymbol{w}^T\boldsymbol{R}_{\boldsymbol{u}_k\boldsymbol{u}_k}\boldsymbol{w}}\right) \quad \text{dB} \tag{2.78}$$

An equally-spaced linear array with 7 elements is used. The input SIR and signal-to-noise ratio (SNR) are chosen to be -20dB and 30dB at each element. Figure 2.9 shows the output SINR at different interference directions when the signal and interference bandwidths vary from 0.1 to 0.4, with the gap 0.1. The length of the filters in each channel is assumed to be 11. We observe that the output SINR decreases significantly as the interference bandwidth increases. In addition, the output SIR curves are demonstrated in Figure 2.10 to provide a direct observation for the nulling performance under different bandwidths.

In another example, we fix the bandwidth to be 0.3 and increase the number of taps from 1 to 50. The curves of the output SIR and SINR are demonstrated in Figure 2.11. This figure shows that by increasing the order of the FIR filters in the array processor, we can

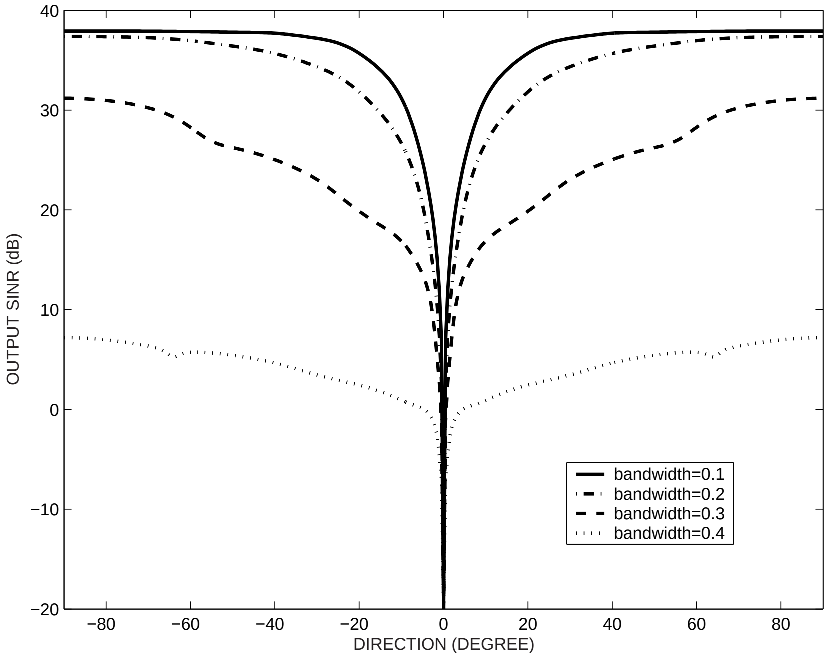

Figure 2.9. Output SINR curves for varied bandwidth.

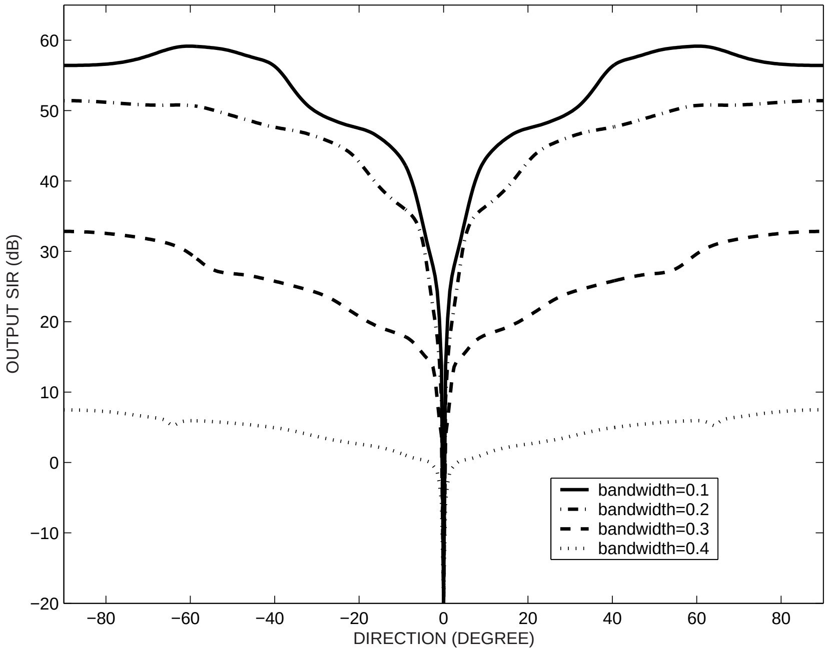

Figure 2.10. Output SIR curves for varied bandwidth.

achieve a better output SINR. However, when the number of taps is larger than a certain value, the performance improvement does not change significantly any more.

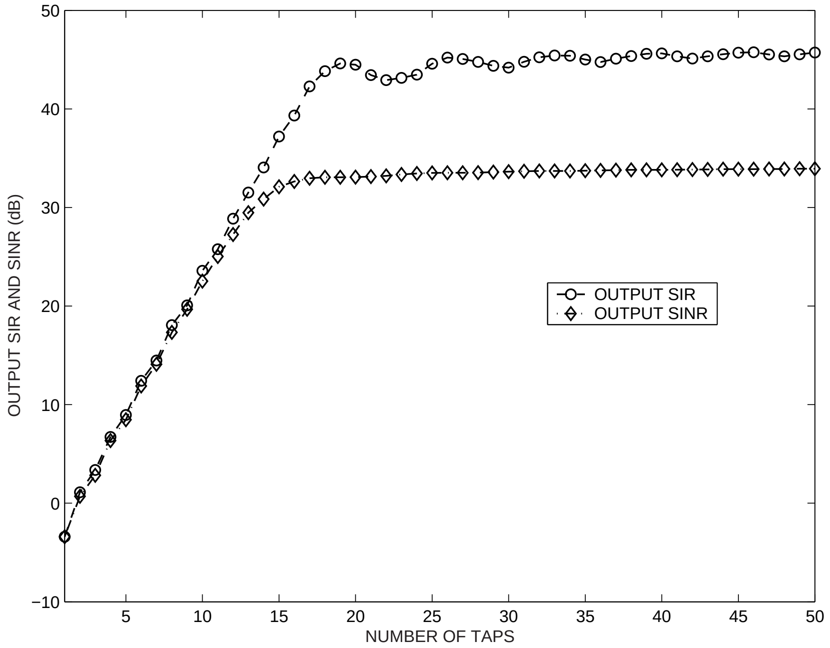

Figure 2.11. Output SIR and SINR curves for increased number of taps.

2.5 Conclusion

In this chapter, the array fundamentals, including the coordinate system, wave propagation model and array geometry, are introduced. The narrowband and broadband beamforming techniques are compared by the signal models, beamforming structures and beampatterns. The algorithms of the broadband LCMV and GSC beamformers are described as the basis for the studies in the next few chapters. Moreover, the influences of the operating bandwidth and the filter length on the performance of the broadband time-domain beamformer are described.

Chapter 3

Designing the Amplitude/Phase Response of the Frost Beamformer

3.1 Introduction

Based on the classical broadband beamformer proposed by Frost [7], numerous algorithms and implementations have been presented [12, 42, 45, 47, 101–105]. By designing various constraints, such as the linear gain constraint [7], the derivative constraint [42, 45, 104], and the response constraint [101], in the algorithms, spatial responses with different characteristics can be obtained. The phase center problem occurring in the derivative constrained beamformers has been discussed in some literatures [45, 47, 104, 105]. However, in the past studies, less attention has been paid on the optimization of the broadband beamformer by designing the amplitude and phase responses for the look-direction signal.

In [51], the soft response constraint is used to achieve the improved interference suppression performance by allowing signal distortion. In the Frost beamformer [7], the optimum weights are obtained by minimizing the output power while maintaining a chosen frequency response in the look direction. Due to the assumption of exact presteering, the constraint vector corresponds to the impulse response in the look direction. In this chapter, to optimize the interference and noise suppression performance of the Frost beamformer, three constrained optimization methods are developed to design the look-direction impulse response, which is subsequently used to compute the optimum weight vector of the beamformer. In the first method, the optimum output power derived by the original constrained optimization in [7] is maximized under a norm constraint. The second method is to minimize the optimum output power while restricting the mean square deviation between the desired and designed look-direction frequency responses to be not larger than a specified threshold. In the third method, the optimum output power is minimized under a constraint by which the mean square deviation between the desired and designed look-direction amplitude responses is confined within a specified limit. As the new methods introduce distortion to the look-direction signal, equalization is applied in the beamformer for signal recovery. Simulation results demonstrate that all these methods have significantly better performance than the normally used distortionless beamformer. The differences between these methods are also analyzed.

This chapter is organized as follows: In Section 3.2, the proposed methods to optimize the beamformer are described. In Section 3.3, simulation examples are presented to show the performance of the new methods.

3.2 Optimization Methods

The structure and the algorithm for the Frost beamformer have been introduced in Sections 2.3.2 and 2.4.1. All definitions for the mathematical expressions in these two sections are inherited in this chapter with one exception: The constraint vector is represented by $\boldsymbol{b}$ instead of $\boldsymbol{f}$ to avoid the confusion with the frequency f.

The optimum weight vector $\boldsymbol{w}_{opt}$ for the Frost beamformer is given by (2.38), which is repeated here for the convenience of narration:

$$\boldsymbol{w}_{opt} = \boldsymbol{R}_{\boldsymbol{xx}}^{-1}\boldsymbol{C}(\boldsymbol{C}^T\boldsymbol{R}_{\boldsymbol{xx}}^{-1}\boldsymbol{C})^{-1}\boldsymbol{b} \tag{3.1}$$

By simple derivations, under the specified constraint vector $\boldsymbol{b}$, the optimum output power of the Frost beamformer is given by:

$$\rho = \boldsymbol{w}_{opt}^T\boldsymbol{R}_{\boldsymbol{xx}}\boldsymbol{w}_{opt} = \boldsymbol{b}^T(\boldsymbol{C}^T\boldsymbol{R}_{\boldsymbol{xx}}^{-1}\boldsymbol{C})^{-1}\boldsymbol{b} \tag{3.2}$$

Based on this expression, three methods are proposed to design the optimized constraint vector $\boldsymbol{b}$ to improve the SINR of the beamformer.

3.2.1 Norm Constraint

The norm-constraint method is expressed as follows:

$$\begin{aligned} &\max_{\boldsymbol{b}} \ \boldsymbol{b}^T(\boldsymbol{C}^T\boldsymbol{R}_{\boldsymbol{xx}}^{-1}\boldsymbol{C})^{-1}\boldsymbol{b} \\ &\text{subject to } ||\boldsymbol{b}|| = 1 \end{aligned} \tag{3.3}$$

In this method, the norm of the constraint vector $\boldsymbol{b}$ is constrained to be unity. This constraint alone can not guarantee the gain in the look direction. As there is no response constraint to preserve the desired signal from the look direction, maximizing the optimum output power can avoid desired signal cancellation. Formulation (3.3) can be understood as maximizing the total output power while suppressing the interferences and noise. This results in the increase of the output SINR. Clearly, the optimized constraint vector $\boldsymbol{b}_{opt}$ is the eigenvector of $(\boldsymbol{C}^T\boldsymbol{R}_{\boldsymbol{xx}}^{-1}\boldsymbol{C})^{-1}$ corresponding to the maximum eigenvalue.

With the solved $\boldsymbol{b}_{opt}$, the new optimum weight vector of the beamformer is computed by:

$$\boldsymbol{w}_{opt} = \boldsymbol{R}_{\boldsymbol{xx}}^{-1}\boldsymbol{C}(\boldsymbol{C}^T\boldsymbol{R}_{\boldsymbol{xx}}^{-1}\boldsymbol{C})^{-1}\boldsymbol{b}_{opt} \tag{3.4}$$

In the norm-constraint method, (3.4) can be simplified to be:

$$\boldsymbol{w}_{opt} = \lambda_{max}\boldsymbol{R}_{\boldsymbol{xx}}^{-1}\boldsymbol{C}\boldsymbol{b}_{opt} \tag{3.5}$$

where λ_{max} is the maximum eigenvalue of $(\boldsymbol{C}^T\boldsymbol{R}_{\boldsymbol{xx}}^{-1}\boldsymbol{C})^{-1}$. Because $\boldsymbol{b}_{opt}$ does not correspond to the distortionless response, an equalizer has to be used after beamforming to recover the desired signal. The equalization filter has the following desired frequency response:

$$H_{eq}(f) = \begin{cases} \left[\boldsymbol{b}_{opt}^T\boldsymbol{e}(f)\right]^{-1}, & f \in [f_l, f_u] \\ 0, & \text{otherwise} \end{cases} \tag{3.6}$$

where

$$\boldsymbol{e}(f) = [1 \;\; e^{-j2\pi f T_s} \;\; \cdots \;\; e^{-j2\pi f (J-1) T_s}]^T \tag{3.7}$$

As $\boldsymbol{b}_{opt}$ is obtained to avoid signal cancellation, $\boldsymbol{b}_{opt}^T\boldsymbol{e}(f)$ will not be zero or very small and hence there is no problem for the inverse operation.

3.2.2 Frequency Response Constraint

In the Frost beamformer, the constraint vector is exactly the impulse response in the look direction. In this section, we design the constraint vector as follows so that $\boldsymbol{b}_{opt}$ can offer an approximately desired frequency response in the look direction and maximize the output SINR at the same time.

$$\begin{aligned} &\min_{\boldsymbol{b}} \ \boldsymbol{b}^T(\boldsymbol{C}^T\boldsymbol{R}_{\boldsymbol{xx}}^{-1}\boldsymbol{C})^{-1}\boldsymbol{b} \\ &\text{subject to } \frac{1}{B}\int_{f_l}^{f_u}\left|\boldsymbol{b}^T\boldsymbol{e}(f)-\boldsymbol{b}_d^T\boldsymbol{e}(f)\right|^2 df \leq \varepsilon \end{aligned} \tag{3.8}$$

where f_l and f_u represent the lower and upper frequencies of the signals, respectively. B is the bandwidth. $\boldsymbol{b}_d$ is the desired impulse response that might be chosen to be the distortionless response $\boldsymbol{e}_i$ or designed beforehand according to some prior knowledge, such as the signal frequency range and the desired frequency response. ε is a small positive number to specify the upper limit for the mean square deviation between the actual and the desired look-direction frequency responses.

Formulation (3.8) is a quadratic inequality constrained optimization problem. The constraint can be expanded as:

$$(\boldsymbol{b}-\boldsymbol{b}_d)^T\boldsymbol{Q}(\boldsymbol{b}-\boldsymbol{b}_d) \leq \varepsilon \tag{3.9}$$

where $\boldsymbol{Q}$ is a symmetric matrix:

$$\boldsymbol{Q} = \text{Re}\Big[\frac{1}{B}\int_{f_l}^{f_u}\boldsymbol{e}(f)\boldsymbol{e}^H(f)df\Big] \tag{3.10}$$

where Re$[\cdot]$ represents the real part of each complex entry. Using the method presented in [106] for the similar optimization problem, the Lagrangian for (3.8) is defined as:

$$\eta = \boldsymbol{b}^T(\boldsymbol{C}^T\boldsymbol{R}_{\boldsymbol{xx}}^{-1}\boldsymbol{C})^{-1}\boldsymbol{b} + \lambda[(\boldsymbol{b}-\boldsymbol{b}_d)^T\boldsymbol{Q}(\boldsymbol{b}-\boldsymbol{b}_d)-\varepsilon] \tag{3.11}$$

where λ is the Lagrange multiplier. The optimum $\boldsymbol{b}_{opt}$ to minimize the Lagrangian is obtained by solving $\frac{\partial \eta}{\partial \boldsymbol{b}} = \mathbf{0}$. By some mathematical derivations, we get:

$$\frac{\partial \eta}{\partial \boldsymbol{b}} = 2(\boldsymbol{C}^T \boldsymbol{R}_{\boldsymbol{xx}}^{-1} \boldsymbol{C})^{-1} \boldsymbol{b} + 2\lambda(\boldsymbol{Q}\boldsymbol{b} - \boldsymbol{Q}\boldsymbol{b}_d) = \mathbf{0} \tag{3.12}$$

therefore,

$$\boldsymbol{b}_{opt} = \lambda[(\boldsymbol{C}^T \boldsymbol{R}_{\boldsymbol{xx}}^{-1} \boldsymbol{C})^{-1} + \lambda \boldsymbol{Q}]^{-1} \boldsymbol{Q}\boldsymbol{b}_d \tag{3.13}$$

Let $\boldsymbol{M} = (\boldsymbol{C}^T \boldsymbol{R}_{\boldsymbol{xx}}^{-1} \boldsymbol{C})^{-1}$, then:

$$\begin{aligned} \left.\frac{\partial \eta}{\partial \lambda}\right|_{\boldsymbol{b}=\boldsymbol{b}_{opt}} &= -\lambda \boldsymbol{b}_d^T \boldsymbol{Q}(\boldsymbol{M} + \lambda \boldsymbol{Q})^{-1} \boldsymbol{M} (\boldsymbol{M} + \lambda \boldsymbol{Q})^{-1} \boldsymbol{Q}\boldsymbol{b}_d \\ &\quad -\lambda \boldsymbol{b}_d^T \boldsymbol{Q}(\boldsymbol{M} + \lambda \boldsymbol{Q})^{-1} \boldsymbol{Q}\boldsymbol{b}_d + \boldsymbol{b}_d^T \boldsymbol{Q}\boldsymbol{b}_d - \varepsilon \end{aligned} \tag{3.14}$$

Using the eigendecomposition $\boldsymbol{M}^{-\frac{1}{2}} \boldsymbol{Q} \boldsymbol{M}^{-\frac{1}{2}} = \boldsymbol{U}\boldsymbol{D}\boldsymbol{U}^T$ and letting $\boldsymbol{z} = \boldsymbol{U}^T \boldsymbol{M}^{-\frac{1}{2}} \boldsymbol{Q}\boldsymbol{b}_d$, (3.14) can be transformed into:

$$\begin{aligned} \left.\frac{\partial \eta}{\partial \lambda}\right|_{\boldsymbol{b}=\boldsymbol{b}_{opt}} &= -\lambda \boldsymbol{z}^T (\boldsymbol{I} + \lambda \boldsymbol{D})^{-1} (\boldsymbol{I} + \lambda \boldsymbol{D})^{-1} \boldsymbol{z} \\ &\quad -\lambda \boldsymbol{z}^T (\boldsymbol{I} + \lambda \boldsymbol{D})^{-1} \boldsymbol{z} + \boldsymbol{b}_d^T \boldsymbol{Q}\boldsymbol{b}_d - \varepsilon \\ &= -\lambda \boldsymbol{z}^T (2\boldsymbol{I} + \lambda \boldsymbol{D})(\boldsymbol{I} + \lambda \boldsymbol{D})^{-2} \boldsymbol{z} + \boldsymbol{b}_d^T \boldsymbol{Q}\boldsymbol{b}_d - \varepsilon \end{aligned} \tag{3.15}$$

The optimum Lagrange multiplier λ is the root of $\left.\frac{\partial \eta}{\partial \lambda}\right|_{\boldsymbol{b}=\boldsymbol{b}_{opt}} = 0$. Any root finding method, such as the Newton's method, can be used to solve it.

Similar to the first method, after obtaining $\boldsymbol{b}_{opt}$, the weight vector can be computed by (3.4).

The norm-constraint method causes larger distortion for the desired signal because it does not impose direct constraint on the look-direction response. In comparisons, if $\boldsymbol{b}_d$ corresponds to the distortionless or approximately distortionless response, and ε is small enough, the frequency-response-constraint method produces a response with smaller distortion in the look direction. This will be demonstrated by simulation results in Section 3.3. If the ripple of the look-direction response is small enough, equalization becomes unnecessary for some applications. According to the analysis in [51], if the amplitude of the frequency response of the equalization filter is approximately constant, equalization does not have a large effect on the SINR.

By adjusting ε, we can achieve a tradeoff between the signal distortion and the output SINR performance. This point will be shown by simulation examples in Section 3.3.

3.2.3 Amplitude Response Constraint

In many applications, we only care about the amplitude response of the desired signal. Constraining the frequency response actually imposes both amplitude constraint and phase constraint in the optimization problem. Phase response constraint wastes the degree of freedom. Therefore we consider the following amplitude constrained optimization method:

$$\begin{aligned} &\min_{\boldsymbol{b}} \ \boldsymbol{b}^T(\boldsymbol{C}^T\boldsymbol{R}_{\boldsymbol{xx}}^{-1}\boldsymbol{C})^{-1}\boldsymbol{b} \\ &\text{subject to } \frac{1}{B}\int_{f_l}^{f_u}\Big||\boldsymbol{b}^T\boldsymbol{e}(f)| - |\boldsymbol{b}_d^T\boldsymbol{e}(f)|\Big|^2 df \le \varepsilon \end{aligned} \tag{3.16}$$

where ε is a small positive number to specify the upper limit for the mean square deviation between the actual and the desired look-direction amplitude responses. This is a nonconvex optimization problem. Similar amplitude constrained optimization problem has been investigated in [55, 107, 108] for the narrowband array synthesis problem. Referring to the methods presented in [107, 108], an iterative procedure is designed to solve this nonconvex optimization problem.

It is easily shown that (3.16) is equivalent to the following expression:

$$\begin{aligned} &\min_{\boldsymbol{b}} \ \boldsymbol{b}^T(\boldsymbol{C}^T\boldsymbol{R}_{\boldsymbol{xx}}^{-1}\boldsymbol{C})^{-1}\boldsymbol{b} \\ &\text{subject to } \frac{1}{B}\int_{f_l}^{f_u}\left|\boldsymbol{b}^T\boldsymbol{e}(f) - \boldsymbol{b}_d^T\boldsymbol{e}(f)e^{-j[\phi_d(f)-\phi(f)]}\right|^2 df \le \varepsilon \end{aligned} \tag{3.17}$$

where $\phi_d(f)$ is the phase response of $\boldsymbol{b}_d^T\boldsymbol{e}(f)$ while $\phi(f)$ is the phase response of $\boldsymbol{b}^T\boldsymbol{e}(f)$. The constraint in the above optimization problem can be expanded as follows:

$$\boldsymbol{b}^T\boldsymbol{Q}\boldsymbol{b} - 2\boldsymbol{b}^T\boldsymbol{P}\boldsymbol{b}_d + \boldsymbol{b}_d^T\boldsymbol{Q}\boldsymbol{b}_d \le \varepsilon \tag{3.18}$$

where

$$\boldsymbol{Q} = \mathrm{Re}\left[\frac{1}{B}\int_{f_l}^{f_u}\boldsymbol{e}(f)\boldsymbol{e}^H(f)df\right] \tag{3.19}$$

$$\boldsymbol{P} = \mathrm{Re}\left[\frac{1}{B}\int_{f_l}^{f_u}\boldsymbol{e}(f)\boldsymbol{e}^H(f)e^{-j[\phi_d(f)-\phi(f)]}df\right] \tag{3.20}$$

If $\phi(f)$ is fixed, the above constrained optimization becomes a convex optimization problem which can be solved with the method described in Section 3.2.2:

$$\boldsymbol{b}_{opt} = \lambda(\boldsymbol{M} + \lambda\boldsymbol{Q})^{-1}\boldsymbol{P}\boldsymbol{b}_d \tag{3.21}$$

where $\boldsymbol{M} = (\boldsymbol{C}^T\boldsymbol{R}_{\boldsymbol{xx}}^{-1}\boldsymbol{C})^{-1}$. Performing the eigendecomposition $\boldsymbol{M}^{-\frac{1}{2}}\boldsymbol{Q}\boldsymbol{M}^{-\frac{1}{2}} = \boldsymbol{U}\boldsymbol{D}\boldsymbol{U}^T$ and letting $\boldsymbol{z} = \boldsymbol{U}^T\boldsymbol{M}^{-\frac{1}{2}}\boldsymbol{P}\boldsymbol{b}_d$, we can solve for λ as the root of the following equation, by the Newton's method:

$$-\lambda\boldsymbol{z}^T(2\boldsymbol{I} + \lambda\boldsymbol{D})(\boldsymbol{I} + \lambda\boldsymbol{D})^{-2}\boldsymbol{z} + \boldsymbol{b}_d^T\boldsymbol{Q}\boldsymbol{b}_d - \varepsilon = 0 \tag{3.22}$$

Here, we design an iterative procedure to solve (3.16). In each step, the phase response $\phi(f)$ is estimated and fixed, then the convex optimization technique is applied to obtain the optimum weight. The iteration steps are described as follows:

Step 1: Compute $\phi_d(f)$, and initialize the phase response $\phi(f)$ within $[f_l, f_u]$.

Step 2: Compute λ by (3.22) and $\boldsymbol{b}_{opt}$ by (3.21).

Step 3: Compute the phase response $\phi(f)$ of $\boldsymbol{b}^T\boldsymbol{e}(f)$, with $\boldsymbol{b} = \boldsymbol{b}_{opt}$.

Step 4: Repeat Step 2 - Step 4 until the change of $\boldsymbol{b}_{opt}$ in two successive iterations is no larger than the specified threshold.

Step 5: Compute $\boldsymbol{w}_{opt}$ by (3.4).

This method can provide a better interference and noise suppression performance than the frequency-response-constraint method because less degree of freedom is used in the constraint. Simulations indicate that this iterative procedure can always converge, but not necessarily converge to a global optimum point.

3.3 Simulation Examples

In this section, simulation examples are presented to demonstrate the performance of the three methods described in Section 3.2.

A ULA with 4 sensors and 6 taps in each channel is applied. The temporal sampling frequency is chosen to be no smaller than twice the highest frequency for the band of interest, so the normalized frequency will not exceed 0.5. The normalized frequency range of all the directional sources is assumed to be $[0.2, 0.4]$. The look direction is the broadside direction. One interference comes from 40°. The input SIR is -20dB and SNR is 30dB. Both the desired signal and the interference are assumed to have flat spectrum. For the frequency-response-constraint and the amplitude-response-constraint methods, we assume that $\boldsymbol{b}_d$ is chosen to be the distortionless impulse response $\boldsymbol{e}_1$. In addition, ε for both

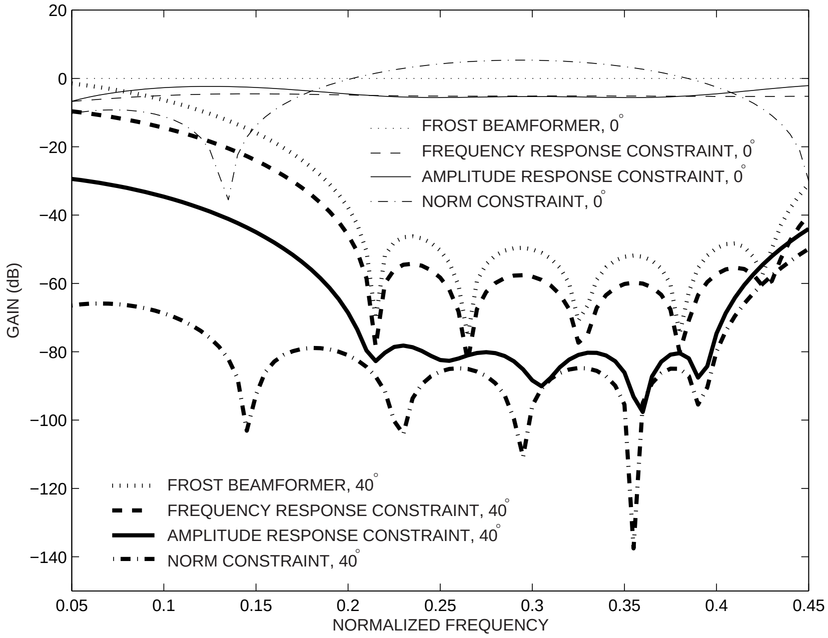

Figure 3.1. Norm squared frequency responses in the look direction and the interference direction before equalization.

methods are chosen to be 0.2. The Frost beamformer with the distortionless response constraint $\boldsymbol{e}_1$ is compared with the new methods. In our simulations, a 51-tap FIR filter is designed as the equalizer according to (3.6) by the least squares criterion for removing the distortion in the new methods.

Figures 3.1 and 3.2 are the norm squared frequency responses in the look direction and the interference direction before and after equalization, respectively. We find that the three new methods have better interference suppression performance relative to the Frost beamformer within the frequency range. Among the three methods, the amplitude-response-constraint method and the frequency-response-constraint method have a flatter look-direction response than the norm-constraint method while the norm-constraint method has the best interference suppression performance among the three new methods.

Figure 3.3 shows the beampatterns averaged over the frequency band after equalization. It can be seen that all the three new methods have deeper nulls in the interference direction

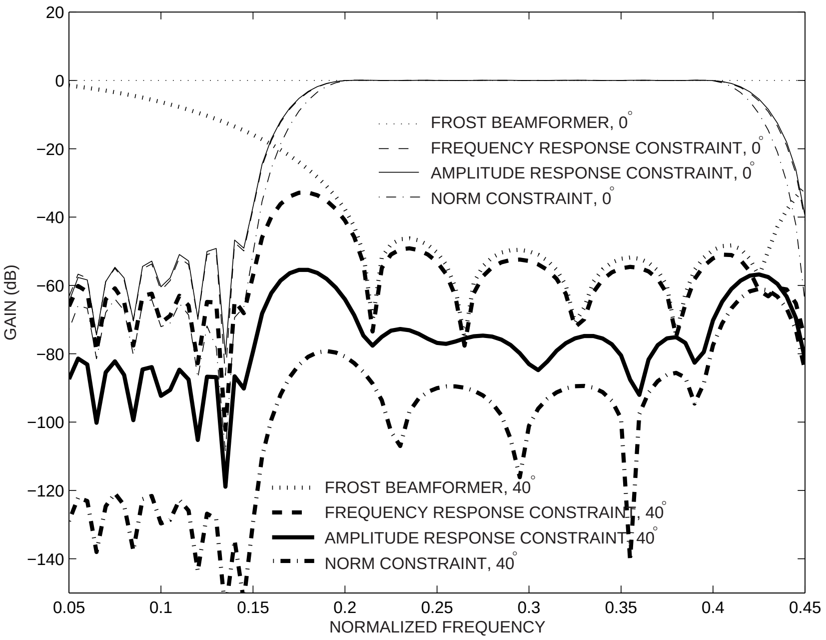

Figure 3.2. Norm squared frequency responses in the look direction and the interference direction after equalization.

and lower sidelobe than the Frost beamformer. To observe the depth of the nulls in the interference direction more clearly, the beampatterns around the interference direction are shown in Figure 3.4.

Figure 3.5 shows the output SINR when the input noise power changes so that the input SNR varies from 0dB to 50dB, with a 5-dB step. From this figure, we can find that the improved SINR is obtained by the new methods, especially for the amplitude-response-constraint and the norm-constraint methods in the high-SNR cases. Also, the curves in this figure show that when the input SNR is large, the output SINR does not increase much in a linear way. In the narrowband minimum variance beamformer, for the low input SNR, the output SINR increases linearly while for the high input SNR, the output SINR levels off. That means, the output SINR does not increase any more when the input SNR is higher than a certain value. The studies in [109] have shown that this can be caused by using the finite-sample estimation of the correlation matrix in the presence

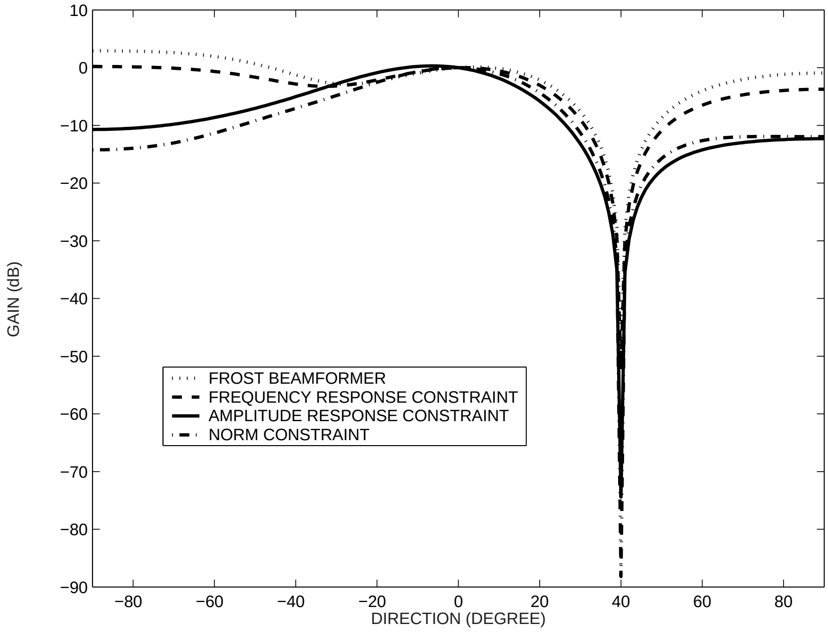

Figure 3.3. Beampatterns averaged over the frequency band $[0.2, 0.4]$.

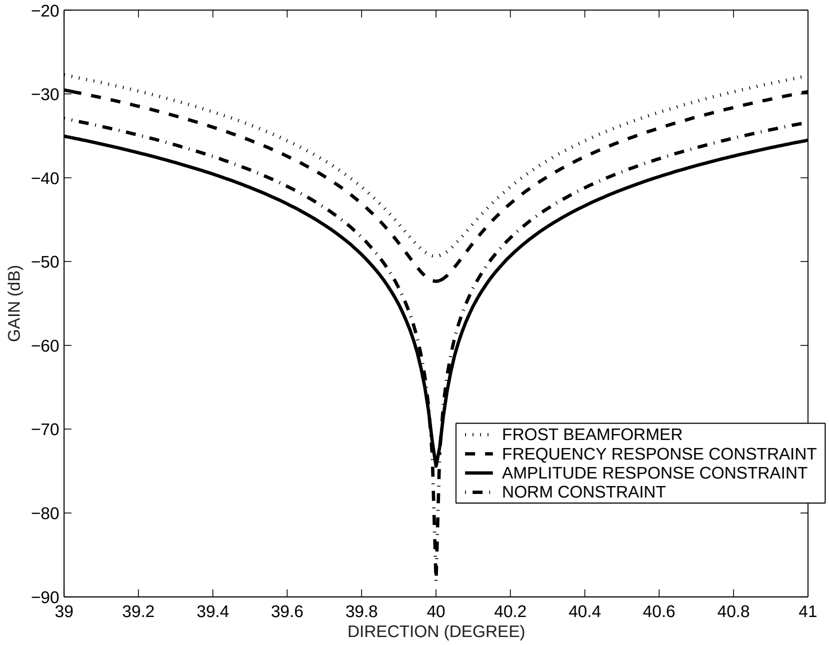

Figure 3.4. Averaged beampatterns around the interference direction.

of the desired signal. The proposed methods can achieve better output SINR than the Frost beamformer, but they still follow the above rule due to the finite sample size. The

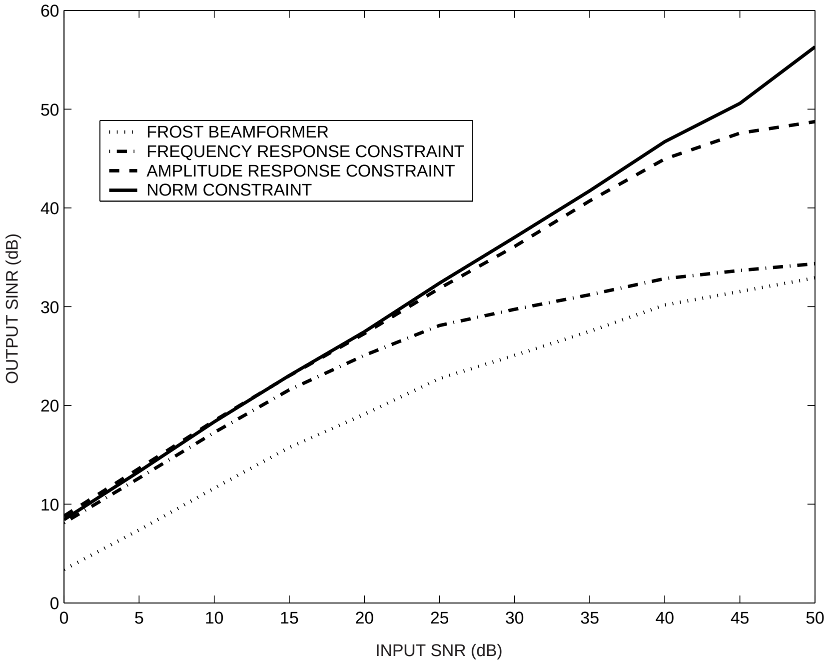

Figure 3.5. Output SINR versus the input SNR.

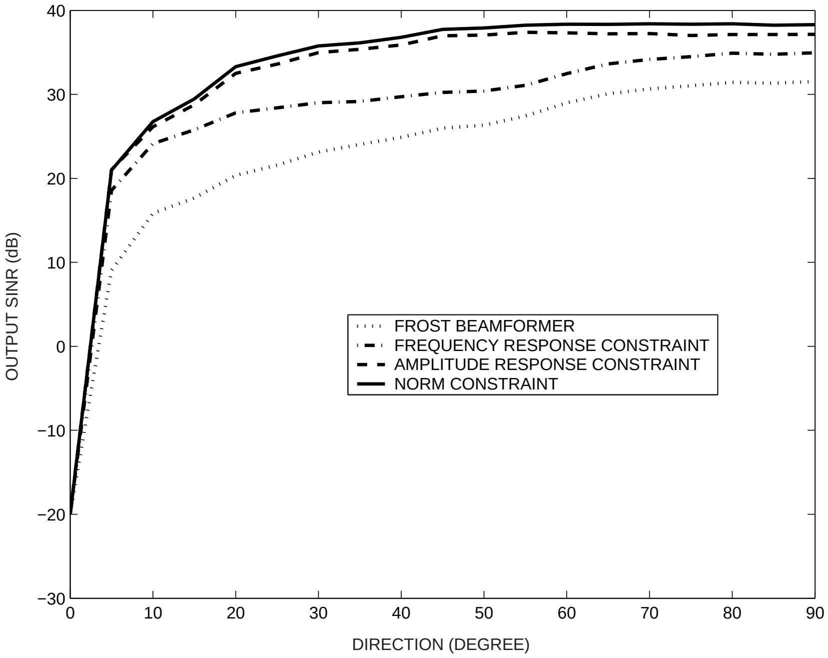

Figure 3.6. Output SINR versus the interference directions.

performance difference between these methods results in the different threshold of the input SNR above which the output SINR levels off. This can explain the phenomenon

Table 3.1: OUTPUT SINR (dB) VERSUS ε BEFORE EQUALIZATION

ε	0.001	0.01	0.1	0.25	0.5
Output SINR (dB) using the Frequency-Response-Constraint Method	25.1	25.5	26.3	26.8	27.2
Output SINR (dB) using the Amplitude-Response-Constraint Method	27.7	27.9	28.5	29.0	29.6

shown in Figure 3.5. Strict mathematical formulations for analyzing the output SINR of the proposed broadband minimum variance beamformer in terms of parameters such as the input SNR, finite sample size and so on are not easy to obtain. This can be studied in the future.

To prove that the new methods can provide better performance for suppressing the interference from any directions, Figure 3.6 demonstrates the output SINR when the interference direction changes from $0°$ to $90°$, with a $5°$ spacing. It can be seen that when the interference comes from any directions except the look direction, improved interference and noise suppression performance can be achieved by the new methods. Of course, we should note that the performance improvement of the new methods is paid by the cost of the increased processing complexity.

Furthermore, we perform simulations to observe the output SINR for the frequency-response-constraint method and the amplitude-response-constraint method under different choices of ε, $\varepsilon = \{0.001, 0.01, 0.1, 0.25, 0.5\}$. We provide the SINR before and after equalization in Tables 3.1 - 3.2, respectively, so that the effect of the equalization can be observed at the same time. We can see that the new methods can obtain increased SINR as the value of ε becomes high. In addition, we find that the equalization filter improves the SINR. It should be noted that this is not the general conclusion for carrying out equalization. In some cases, for example, using different $\boldsymbol{b}_d$, equalization causes a little performance degradation.

Table 3.2: OUTPUT SINR (dB) VERSUS ε AFTER EQUALIZATION

ε	0.001	0.01	0.1	0.25	0.5
Output SINR (dB) using the Frequency-Response-Constraint Method	27.3	27.8	29.1	30.0	30.8
Output SINR (dB) using the Amplitude-Response-Constraint Method	35.7	35.8	35.9	36.0	36.1

All the above simulation results show that among the three new methods, the amplitude-response-constraint method has better interference and noise suppression performance than the frequency-response-constraint method. This is obtained at the cost of an iterative procedure which involves higher computational complexity and does not necessarily converge to the global optimum point. The norm-constraint method has the best interference suppression performance but its look-direction response has larger fluctuations than the other two methods. Therefore, equalization is potentially required for this method. In conclusion, at the cost of higher computational complexity and the potentially required equalization, the new methods obtain better output SINR than the Frost beamformer using the distortionless constraint.

If both $\boldsymbol{b}$ and $\boldsymbol{b}_d$ are chosen to be the impulse response designed according to some prior knowledge, the new methods also show better performance than the Frost beamformer. The simulation results will not be included due to the similarity of the analysis.

3.4 Conclusion

In this chapter, three methods are investigated to optimize the Frost beamformer. With the proposed constrained optimization criteria, the look-direction response is designed to optimize the output SINR so that the performance of the beamformer is improved. Simulation results demonstrate that the new methods can achieve better SINR performance than the beamformer with the distortionless constraint. Furthermore, our computer studies show that when other constraints, for example, the derivative constraints, are imposed on the beamformer, with the original constrained optimization replaced by the new methods, we can also achieve improved performance.

Chapter 4

Broadband Beamformer using TDL-Form IIR Filters

4.1 Introduction

The Frost processor [7] and the GSC beamformer [8] are two types of traditional broadband beamformers using FIR filters. Investigations show that as the operating bandwidth increases, large numbers of taps are required to retain an acceptable SINR performance in the FIR beamformers [18]. However, too many adaptive weights will slow down the convergence rate and increase the computational complexity. Some methods have been proposed to solve this problem. Broadband beamspace adaptive array is designed in [80] so that the convergence rate can be faster. The partially adaptive method with subband processing proposed in [23] and the GSC employing frequency invariant filters in [82] can also increase the convergence speed and reduce the computational complexity. Motivated by the desire to reduce the number of weights, research has been carried out to explore beamformers using IIR filters. In [19], it is proven that the optimal frequency-dependent array weighting can be better approximated by IIR filters in broadband beamformers. Three types of pole-zero beamformers based on the GSC structure are proposed in [19] and [110]. Furthermore, in [20] and [21], the beamformers are designed to cancel the poles in the ideal filter transfer functions so that the required filter length is reduced. In [22], two-pole IIR filters are used together with FIR fan filters to generate auxiliary beams in the partially adaptive array. The coefficients of the IIR filters are synthesized rather than computed adaptively.

In this chapter, we propose a new broadband beamformer using TDL-form IIR filters. The unique feature of our work is that by replacing all the delay elements with tap-to-tap IIR sections under some structural restrictions, the Frost processor is naturally extended from the FIR beamformer to the IIR beamformer. Constrained and unconstrained LMS algorithms are designed to compute the feedforward and feedback weights of the new beamformer, respectively. The time-domain pole-zero beamformers proposed in [19] adopt direct-form IIR filters. Their stability is not easy to monitor. The frequency-domain beamformer in [19] and [110] applies parallel-form IIR filters [111]. The problem of stability monitoring is overcome but the frequency-domain implementation is not suitable for some applications due to its associated time delay. In the new beamformer with low-order tap-to-tap IIR sections, the stability is much easier to monitor. Moreover, relative to the frequency-domain implementation, the latency of the time-domain implementation is typically smaller. Simulation results in Section 4.5 will show that the new IIR beamformer can achieve a better SINR performance than the Frost beamformer with the same number of coefficients. The reduction of the number of weights and computational load brought by the new beamformer to obtain the specified interference suppression performance will also be illustrated.

This chapter is organized as follows: In Section 4.2, the new beamforming structure is

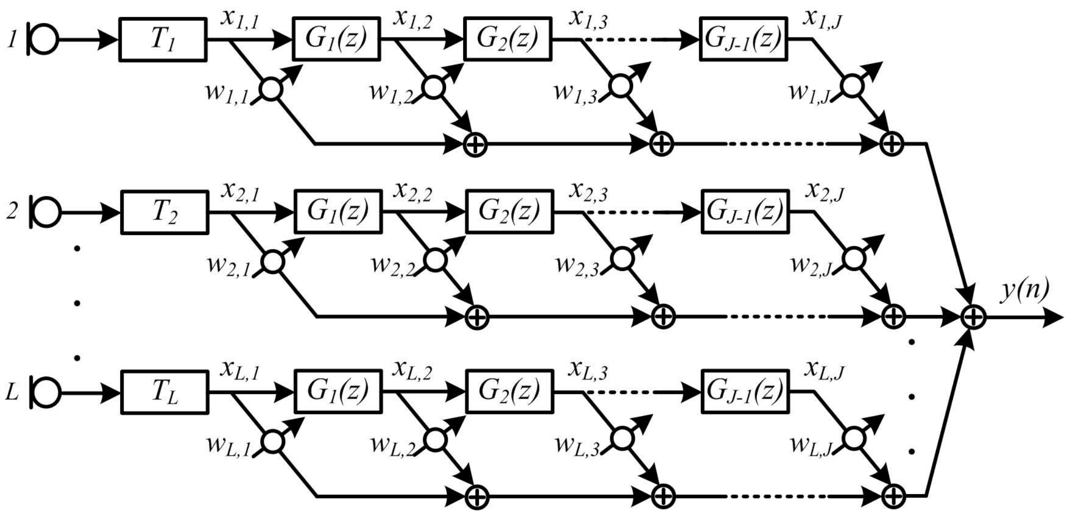

Figure 4.1. Frost-based beamforming structure using TDL-form IIR filters.

presented and the expression of the array response is given. In Section 4.3, the combined LMS algorithm to compute the weights is described. Section 4.4 derives the derivative constraints for the new IIR beamformer. In Section 4.5, simulation results and analysis are presented to demonstrate the improved performance.

4.2 Beamforming Structure and Array Response

The beamforming structure using TDL-form IIR filters is shown in Figure 4.1. By designing the tap-to-tap filter transfer functions $G_k(z)$, poles are introduced into the new beamformer. Here all the transfer functions are constrained to be the first-order form defined as follows:

$$G_k(z) = \frac{z^{-1}}{1 - a_k z^{-1}}, \quad k = 1, 2, \cdots, J-1 \tag{4.1}$$

where $J-1$ is the number of first-order IIR filters behind each sensor. The structure of the first-order section $G_k(z)$ is shown by Figure 4.2. Because the IIR sections in each channel are cascaded like tapped delay lines, we call the filter in each channel the TDL-form IIR filter. Another structural restriction is that the IIR sections after the kth tap of each channel have the identical transfer function $G_k(z)$. Compared with the Frost processor shown by Figure 2.5, all the delay elements are replaced by tap-to-tap IIR sections in this new beamforming structure. If all the feedback coefficients are fixed as zeros, $G_k(z)$ will be equivalent to z^{-1} and the new structure will be completely reduced to the Frost processor. Therefore, the new beamformer can be regarded as an extension of the conventional Frost processor.

The beamforming structure shown in Figure 4.1 can be expressed by the following state-space model:

$$\begin{aligned} \boldsymbol{x}(n+1) &= \boldsymbol{A}\boldsymbol{x}(n) + \boldsymbol{B}\boldsymbol{u}(n) \\ y(n) &= \boldsymbol{c}^T\boldsymbol{x}(n) + \boldsymbol{d}^T\boldsymbol{u}(n) \end{aligned} \tag{4.2}$$

where

$$\boldsymbol{x}(n) = [x_{12}(n) \ \cdots \ x_{L2}(n) \ \cdots \ x_{1J}(n) \ \cdots \ x_{LJ}(n)]^T \tag{4.3}$$

$$\boldsymbol{u}(n) = [x_{11}(n) \ x_{21}(n) \ \cdots \ x_{L1}(n)]^T \tag{4.4}$$

$$\boldsymbol{A} = \begin{pmatrix} a_1\mathrm{I} & \mathbf{0} & \mathbf{0} & \cdots & \mathbf{0} \\ \mathrm{I} & a_2\mathrm{I} & \mathbf{0} & \cdots & \mathbf{0} \\ \mathbf{0} & \mathrm{I} & a_3\mathrm{I} & \cdots & \mathbf{0} \\ \vdots & \vdots & \ddots & \ddots & \vdots \\ \mathbf{0} & \mathbf{0} & \cdots & \mathrm{I} & a_{J-1}\mathrm{I} \end{pmatrix} \tag{4.5}$$

$$\boldsymbol{B} = [\mathrm{I} \ \mathbf{0} \ \cdots \ \mathbf{0}]^T \tag{4.6}$$

$$\boldsymbol{c} = [w_{12} \ \cdots \ w_{L2} \ \cdots \ w_{1J} \ \cdots \ w_{LJ}]^T \tag{4.7}$$

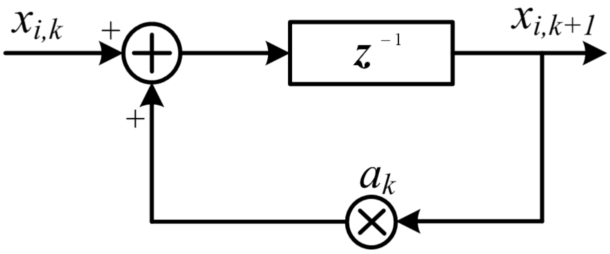

Figure 4.2. Structure of the first-order IIR section.

$$\boldsymbol{d} = [w_{11} \;\; w_{21} \;\; \cdots \;\; w_{L1}]^T \tag{4.8}$$

In the definitions of $L(J-1) \times L(J-1)$ matrix $\boldsymbol{A}$ and $L(J-1) \times L$ matrix $\boldsymbol{B}$, I represents the $L \times L$ identity matrix and **0** is the $L \times L$ all-zero matrix.

The array response of the proposed beamformer can be written as follows:

$$H(f, \theta) = \boldsymbol{S}^T(f, \theta) \cdot \boldsymbol{T}(f) \cdot \boldsymbol{W} \cdot \boldsymbol{G}(f) \tag{4.9}$$

where $\boldsymbol{S}(f, \theta)$ is the $L \times 1$ steering vector of the array,

$$\boldsymbol{S}(f, \theta) = [e^{j2\pi f \tau_1(\theta)} \;\; e^{j2\pi f \tau_2(\theta)} \;\; \cdots \;\; e^{j2\pi f \tau_L(\theta)}]^T \tag{4.10}$$

where $\tau_i(\theta)$ is the propagation delay of the plane wave impinging on the ith sensor relative to the phase center. $\boldsymbol{T}(f)$ is an $L \times L$ diagonal matrix to carry out presteering, which is defined as follows:

$$\boldsymbol{T}(f) = \begin{pmatrix} e^{j2\pi f T_1} & 0 & \cdots & 0 \\ 0 & e^{j2\pi f T_2} & \cdots & 0 \\ \vdots & \vdots & \ddots & \vdots \\ 0 & 0 & \cdots & e^{j2\pi f T_L} \end{pmatrix} \tag{4.11}$$

where T_i is the presteering delay behind the ith sensor. $\boldsymbol{W}$ is the $L \times J$ feedforward weighting matrix:

$$\boldsymbol{W} = \begin{pmatrix} w_{1,1} & w_{1,2} & \cdots & w_{1,J} \\ w_{2,1} & w_{2,2} & \cdots & w_{2,J} \\ \vdots & \vdots & \ddots & \vdots \\ w_{L,1} & w_{L,2} & \cdots & w_{L,J} \end{pmatrix} \tag{4.12}$$

where $w_{i,k}$ denotes the adjustable weight of the kth feedforward tap following behind the ith sensor. $\boldsymbol{G}(f)$ is the $J \times 1$ vector:

$$\boldsymbol{G}(f) = \begin{pmatrix} 1 \\ G_1(f) \\ G_1(f) \cdot G_2(f) \\ \vdots \\ G_1(f) \cdot G_2(f) \cdots G_{J-1}(f) \end{pmatrix} \tag{4.13}$$

where $G_k(f)$ is the frequency response of the kth tap-to-tap IIR filter.

Similar to [19], the new beamformer also applies common poles for all channels. But due to the special structure for implementing the feedback paths, the new beamformer has different algorithm and demonstrates the advantage of easily controlled stability that will be addressed later. Note that if the proposed beamformer is implemented as a GSC structure, the poles in different channels after the blocking matrix can be further extended to be independent.

4.3 Combined LMS Algorithm

In this section, we derive the weighting update algorithm using the constrained and unconstrained optimization techniques.

In the array response of the beamformer, $w_{i,k}$ and a_k are coefficients which can be adjusted to obtain a minimum output power while the desired signal is maintained to be undistorted. Because the desired signal from the look direction appears exactly in phase at the outputs of the steering delays, the frequency response for the desired signal can be written as:

$$H_s(f) = \sum_{i=1}^{L} w_{i,1} + G_1(f) \cdot \sum_{i=1}^{L} w_{i,2} + \cdots + G_1(f) \cdot G_2(f) \cdots G_{J-1}(f) \cdot \sum_{i=1}^{L} w_{i,J} \quad (4.14)$$

To ensure the desired signal to be free of distortion, $w_{i,k}$ should satisfy the following constraint:

$$\boldsymbol{C}^T \boldsymbol{w} = \boldsymbol{f} \quad (4.15)$$

where $\boldsymbol{C}$ is a constraint matrix with dimension $LJ \times J$,

$$\boldsymbol{C} = \begin{pmatrix} \mathbf{1}_L & \mathbf{0}_L & \cdots & \mathbf{0}_L \\ \mathbf{0}_L & \mathbf{1}_L & \cdots & \mathbf{0}_L \\ \vdots & \vdots & \ddots & \vdots \\ \mathbf{0}_L & \cdots & \cdots & \mathbf{1}_L \end{pmatrix} \quad (4.16)$$

where $\mathbf{1}_L$ and $\mathbf{0}_L$ are column vectors containing L ones and zeros, respectively. $\boldsymbol{f}$ is a $J \times 1$ constant vector $[1 \ \ 0 \ \ \cdots \ \ 0]^T$, and $\boldsymbol{w}$ is the $LJ \times 1$ feedforward weighting vector:

$$\boldsymbol{w} = [w_{1,1} \ \cdots \ w_{L,1} \ \cdots \ w_{1,J} \ \cdots \ w_{L,J}]^T \quad (4.17)$$

Therefore, the following constrained optimization can be used to adjust the feedforward weighting vector $\boldsymbol{w}$:

$$\begin{gathered} \min_{\boldsymbol{w}} \ \boldsymbol{w}^T \boldsymbol{R}_{\boldsymbol{xx}} \boldsymbol{w} \\ \text{subject to } \boldsymbol{C}^T \boldsymbol{w} = \boldsymbol{f} \end{gathered} \quad (4.18)$$

where $\boldsymbol{R}_{\boldsymbol{xx}}$ is the estimated correlation matrix of the vector $\boldsymbol{x}(n)$. $\boldsymbol{x}(n)$ is an $LJ \times 1$

column vector:

$$\boldsymbol{x}(n) = [x_{1,1}(n) \quad \cdots \quad x_{L,1}(n) \quad \cdots \quad x_{1,J}(n) \quad \cdots \quad x_{L,J}(n)]^T \tag{4.19}$$

It should be noted that the entries of $\boldsymbol{x}(n)$ are the tap variables rather than the data samples. They satisfy the following relations according to (4.1):

$$\begin{cases} x_{i,1}(n) : \text{presteered snapshot data from the } i\text{th sensor.} \\ x_{i,k}(n) = x_{i,k-1}(n-1) + a_{k-1}x_{i,k}(n-1) \\ \qquad\qquad i = 1, 2, \cdots, L; \quad k = 2, 3, \cdots, J \end{cases} \tag{4.20}$$

The constrained LMS algorithm is used to adjust the feedforward weighting vector iteratively [7],

$$\begin{cases} \boldsymbol{w}(0) = \boldsymbol{g} \\ \boldsymbol{w}(n+1) = \boldsymbol{P}[\boldsymbol{w}(n) - \mu_{\boldsymbol{w}} y(n)\boldsymbol{x}(n)] + \boldsymbol{g} \end{cases} \tag{4.21}$$

where $\mu_{\boldsymbol{w}}$ is the step size, $\boldsymbol{P}$ is a projection matrix and $\boldsymbol{g}$ is a quiescent solution vector,

$$\boldsymbol{P} = \boldsymbol{I}_{LJ} - \boldsymbol{C}(\boldsymbol{C}^T\boldsymbol{C})^{-1}\boldsymbol{C}^T \tag{4.22}$$

$$\boldsymbol{g} = \boldsymbol{C}(\boldsymbol{C}^T\boldsymbol{C})^{-1}\boldsymbol{f} \tag{4.23}$$

Because matrix $\boldsymbol{C}$ has a simple form, the iterative formulation for $\boldsymbol{w}$ can be simplified to such a form:

$$\begin{aligned} w_{i,k}(n+1) = {} & w_{i,k}(n) - \mu_{\boldsymbol{w}} y(n) x_{i,k}(n) - \\ & \frac{1}{L}\sum_{m=1}^{L}\Big[w_{m,k}(n) - \mu_{\boldsymbol{w}} y(n) x_{m,k}(n)\Big] + \frac{f_k}{L} \\ & i = 1, \cdots, L; \quad k = 1, \cdots, J \end{aligned} \tag{4.24}$$

We define $\boldsymbol{a}$ as a $(J-1)\times 1$ column vector containing all the feedback coefficients,

$$\boldsymbol{a} = [a_1 \;\; a_2 \;\; \cdots \;\; a_{J-1}]^T \tag{4.25}$$

Because the constraint equation (4.15) can guarantee the desired signal is passed without distortion whatever the feedback coefficients are, we use the unconstrained optimization approach to compute $\boldsymbol{a}$,

$$\min_{\boldsymbol{a}} \mathrm{E}[y^2(n)] \tag{4.26}$$

Using LMS algorithm, the update equation can be written as follows:

$$\boldsymbol{a}(n+1) = \boldsymbol{a}(n) - \mu_{\boldsymbol{a}} \boldsymbol{\nabla}_{\boldsymbol{a}}(n) \tag{4.27}$$

where $\mu_{\boldsymbol{a}}$ is the step size and $\boldsymbol{\nabla}_{\boldsymbol{a}}(n)$ is the instantaneous estimate of the gradient of $\frac{1}{2}\mathrm{E}[y^2(n)]$ relative to $\boldsymbol{a}$:

$$\begin{aligned} \boldsymbol{\nabla}_{\boldsymbol{a}}(n) &= y(n)\frac{\partial y(n)}{\partial \boldsymbol{a}} \\ &= y(n)\sum_{i=1}^{L}\sum_{k=1}^{J} w_{i,k}\frac{\partial x_{i,k}(n)}{\partial \boldsymbol{a}} \end{aligned} \tag{4.28}$$

Assuming $\boldsymbol{v}_{i,k}(n) = \dfrac{\partial x_{i,k}(n)}{\partial \boldsymbol{a}}$, we can calculate $\boldsymbol{v}_{i,k}(n)$ by differentiating (4.20):

$$\begin{cases} \boldsymbol{v}_{i,1}(n) = \boldsymbol{0} \\ \boldsymbol{v}_{i,k}(n) = \boldsymbol{v}_{i,k-1}(n-1) + \boldsymbol{e}_{k-1}\cdot x_{i,k}(n-1) + a_{k-1}\cdot \boldsymbol{v}_{i,k}(n-1) \\ \qquad\qquad i = 1,2,\cdots,L; \quad k = 2,3,\cdots,J \end{cases} \tag{4.29}$$

where $\boldsymbol{e}_{k-1}$ is the $(k-1)$th column vector of a $(J-1)\times(J-1)$ identity matrix. $\boldsymbol{v}_{i,k}(n)$ is a $(J-1)\times 1$ vector. We can easily deduce that the $\{k, k+1, \cdots, J-1\}$th entries of $\boldsymbol{v}_{i,k}(n)$ are zeros because $x_{i,k}(n)$ is irrelevant to $\{a_k, a_{k+1}, \cdots, a_{J-1}\}$.

The algorithms for the feedforward and the feedback weight vectors are actually combined together in implementations. Therefore, the whole algorithm for the IIR beamformer is named the combined LMS algorithm.

The step size $\mu_{\boldsymbol{w}}$ and $\mu_{\boldsymbol{a}}$ should be sufficiently small so that the iteration process works well. Moreover, if the poles of IIR filters move outside the unit circle and remain there for a significant length of time during the adaptive learning process, the filter will become unstable. We must constrain all the poles to be always inside the unit circle. In our proposed beamformer, the feedback coefficients define the poles of the IIR filters directly, therefore, it is easy to monitor the stability of this IIR beamformer. For this purpose, we need to judge if the absolute values of the feedback coefficients are less than one,

$$|a_k| < 1, \quad k = 1, 2, \cdots, J-1 \tag{4.30}$$

In simulations, we adopt the simplest rescue mechanism following the stability monitoring: the feedback coefficients breaking (4.30) are not updated in the current iteration.

4.4 Derivative Constraints

Literatures [42–49, 112] have discussed extensively on the techniques to design robust broadband beamformers. The new beamforming structure described in Section 4.3 only imposes the gain constraint on the feedforward weight vector. Similar to the Frost beamformer, it is sensitive to the steering error and the mismatched arrival. To counteract such errors, in this section, we try to impose the derivative constraint on the weights to obtain a broadened beamwidth in the look direction. The derivation is similar to that proposed in [42].

4.4.1 First-Order Derivative

The power response of the new IIR beamformer is given by:

$$\rho(f,\theta) = H^*(f,\theta)\cdot H(f,\theta) \tag{4.31}$$

The first-order derivative of the power response relative to the angle θ in the look direction θ_0 is derived as follows:

$$\left.\frac{\partial\rho(f,\theta)}{\partial\theta}\right|_{\theta=\theta_0} = 2\mathrm{Re}\Big\{\Big[j2\pi f\boldsymbol{s}_0^T\boldsymbol{\Lambda}_\theta(\theta_0)\boldsymbol{W}\boldsymbol{G}\Big]^*\cdot\Big[\boldsymbol{s}_0^T\boldsymbol{W}\boldsymbol{G}\Big]\Big\} \tag{4.32}$$

where

$$\boldsymbol{s}_0 = [1\ \ 1\ \ \cdots\ \ 1]^T \tag{4.33}$$

$$\boldsymbol{\Lambda}_\theta(\theta_0) = \begin{pmatrix} \left.\frac{\partial\tau_1(\theta)}{\partial\theta}\right|_{\theta_0} & 0 & \cdots & 0 \\ 0 & \left.\frac{\partial\tau_2(\theta)}{\partial\theta}\right|_{\theta_0} & \cdots & 0 \\ \vdots & \vdots & \ddots & \vdots \\ 0 & 0 & \cdots & \left.\frac{\partial\tau_L(\theta)}{\partial\theta}\right|_{\theta_0} \end{pmatrix} \tag{4.34}$$

According to the gain constraint $\boldsymbol{s}_0^T\boldsymbol{W} = h^T = [1\ \ 0\ \ \cdots\ \ 0]$, we know that $\boldsymbol{s}_0^T\boldsymbol{W}\boldsymbol{G} = 1$. Hence,

$$\left.\frac{\partial\rho(f,\theta)}{\partial\theta}\right|_{\theta=\theta_0} = 2\mathrm{Re}\Big\{j2\pi f\boldsymbol{s}_0^T\boldsymbol{\Lambda}_\theta(\theta_0)\boldsymbol{W}\boldsymbol{G}\Big\} \tag{4.35}$$

It is obvious that the following equation is the sufficient condition for $\left.\frac{\partial\rho(f,\theta)}{\partial\theta}\right|_{\theta=\theta_0} = 0$:

$$\boldsymbol{s}_0^T\boldsymbol{\Lambda}_\theta(\theta_0)\boldsymbol{W} = \boldsymbol{0}_J^T \tag{4.36}$$

where $\boldsymbol{0}_J$ represents a $J\times 1$ all-zero column vector.

4.4.2 Second-Order Derivative

The second-order derivative of the power response relative to the angle θ is derived as follows:

$$\begin{aligned}
\frac{\partial^2 \rho(f,\theta)}{\partial \theta^2}\bigg|_{\theta=\theta_0} &= 2\mathrm{Re}\Big\{\Big[(j2\pi f)^2 \boldsymbol{s}_0^T \boldsymbol{\Lambda}_\theta^2(\theta_0)\boldsymbol{W}\boldsymbol{G} + j2\pi f \boldsymbol{s}_0^T \frac{\partial \boldsymbol{\Lambda}_\theta(\theta_0)}{\partial \theta}\boldsymbol{W}\boldsymbol{G}\Big]\cdot\Big[\boldsymbol{s}_0^T\boldsymbol{W}\boldsymbol{G}\Big]^*\Big\} + \\
&\quad 2\Big|j2\pi f \boldsymbol{s}_0^T \boldsymbol{\Lambda}_\theta(\theta_0)\boldsymbol{W}\boldsymbol{G}\Big|^2 \\
&= 2\mathrm{Re}\Big\{(j2\pi f)^2 \boldsymbol{s}_0^T \boldsymbol{\Lambda}_\theta^2(\theta_0)\boldsymbol{W}\boldsymbol{G} + j2\pi f \boldsymbol{s}_0^T \frac{\partial \boldsymbol{\Lambda}_\theta(\theta_0)}{\partial \theta}\boldsymbol{W}\boldsymbol{G}\Big\} + \\
&\quad 2\Big|j2\pi f \boldsymbol{s}_0^T \boldsymbol{\Lambda}_\theta(\theta_0)\boldsymbol{W}\boldsymbol{G}\Big|^2 \qquad (4.37)
\end{aligned}$$

Obviously, the sufficient condition for $\frac{\partial^2 \rho(f,\theta)}{\partial \theta^2}\Big|_{\theta=\theta_0} = 0$ is:

$$\begin{cases}
\boldsymbol{s}_0^T \frac{\partial \boldsymbol{\Lambda}_\theta(\theta_0)}{\partial \theta}\boldsymbol{W} = \mathbf{0}_J^T \\
\boldsymbol{s}_0^T \boldsymbol{\Lambda}_\theta(\theta_0)\boldsymbol{W} = \mathbf{0}_J^T \\
\boldsymbol{s}_0^T \boldsymbol{\Lambda}_\theta^2(\theta_0)\boldsymbol{W} = \mathbf{0}_J^T
\end{cases} \qquad (4.38)$$

where

$$\frac{\partial \boldsymbol{\Lambda}_\theta(\theta_0)}{\partial \theta} = \begin{pmatrix}
\frac{\partial^2 \tau_1(\theta)}{\partial \theta^2}\Big|_{\theta_0} & 0 & \cdots & 0 \\
0 & \frac{\partial^2 \tau_2(\theta)}{\partial \theta^2}\Big|_{\theta_0} & \cdots & 0 \\
\vdots & \vdots & \ddots & \vdots \\
0 & 0 & \cdots & \frac{\partial^2 \tau_L(\theta)}{\partial \theta^2}\Big|_{\theta_0}
\end{pmatrix} \qquad (4.39)$$

$$\boldsymbol{\Lambda}_\theta^2(\theta_0) = \begin{pmatrix}
\left(\frac{\partial \tau_1(\theta)}{\partial \theta}\Big|_{\theta_0}\right)^2 & 0 & \cdots & 0 \\
0 & \left(\frac{\partial \tau_2(\theta)}{\partial \theta}\Big|_{\theta_0}\right)^2 & \cdots & 0 \\
\vdots & \vdots & \ddots & \vdots \\
0 & 0 & \cdots & \left(\frac{\partial \tau_L(\theta)}{\partial \theta}\Big|_{\theta_0}\right)^2
\end{pmatrix} \qquad (4.40)$$

The design of the new IIR beamformer has no special requirements for the array geometries although only the azimuth angle θ is considered in the above derivation. If both the azimuth angle and the polar angle are involved, the derivatives with respect to the polar angle and the hybrid derivatives with respect to the azimuth angle and the polar angle should be derived as well to find the sufficient condition for the maximally flat power response. We observe that our result is consistent with that derived for the FIR beamformer in [42]. All these derivative constraints are only related with the feedforward coefficients in the IIR beamformers, so we only need to impose these constraint equations in (4.18). The simulation results in Section 4.5 will demonstrate the effectiveness of the derivative constraint in the new IIR beamformer.

This example implies that in the new IIR beamforming structure, although the feedback paths are introduced, some of the existing research achievements in FIR beamformers, for example, using the derivative constraint to obtain broadened beamwidth, can still be applied easily.

4.5 Simulation Examples

In this section, simulation examples are presented by comparing the new IIR beamformer with the Frost beamformer to demonstrate the improved performance.

4.5.1 Convergence Curves and Beampatterns

In this simulation, we assume a two-element array with sensors spaced by d, which is chosen to be one half of the wavelength of the highest frequency. Behind each array element, three feedforward coefficients are adopted in the new IIR beamformer. According to the

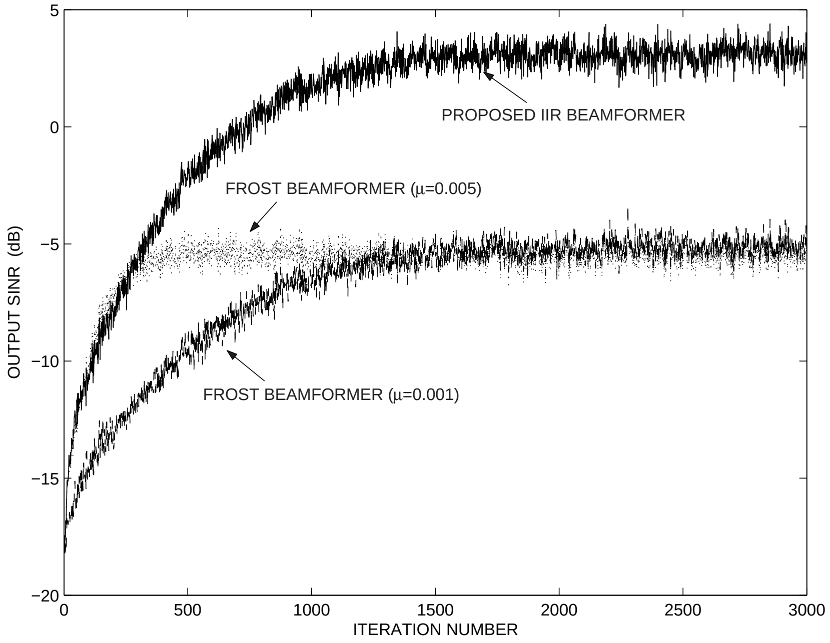

Figure 4.3. Output SINR convergence curves.

structure shown in Figure 4.1, this beamformer has two feedback coefficients in all. For the Frost beamformer to be comparable (with the same number of coefficients), 4 feed-forward coefficients are assumed to follow behind each sensor and the constrained LMS algorithm is used to adjust its coefficients. One interference with bandwidth 0.25 and center frequency 0.25 coming from $40°$ and the desired signal with the same bandwidth and center frequency coming from the broadside direction impinge on the array. The sampling frequency is chosen to be 1. The input SIR is -20dB and SNR is 30dB. The step size is chosen as 0.005 for the new IIR beamformer (both $\mu_{\boldsymbol{w}}$ and $\mu_{\boldsymbol{a}}$) and 0.001 for the Frost beamformer so that they can converge at the same time. The Frost beamformer using the step size 0.005 is also simulated for comparisons. According to the adaptive filtering theory, the Frost beamformer using the step size 0.005 has a faster convergence rate but a worse steady-state performance than that using the step size 0.001.

Figure 4.3 shows the output SINR convergence curves for the two beamformers in 3000

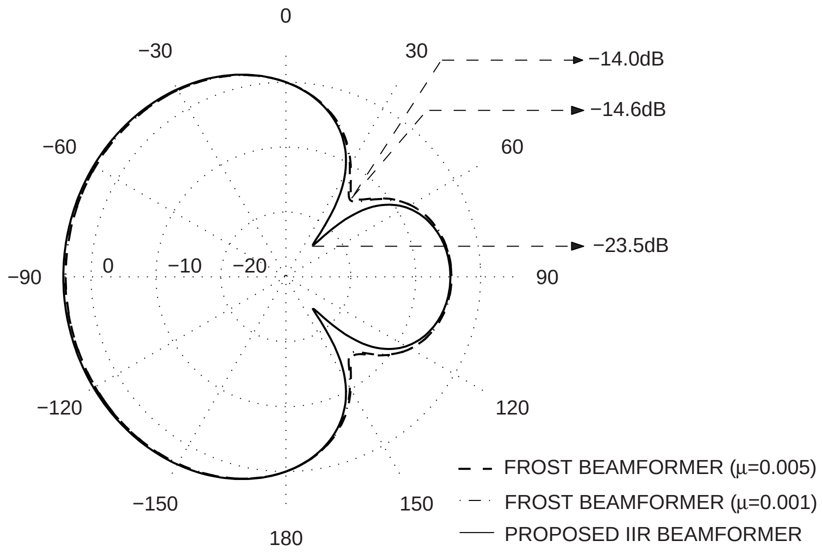

Figure 4.4. Averaged beampatterns.

iterations averaged over 500 trials. Figure 4.4 compares the beampatterns averaged over the frequency band in the steady state.

The simulation results in Figures 4.3 - 4.4 show that the new IIR beamformer achieves a better steady-state SINR than the Frost beamformer with the same number of coefficients and the interference suppression performance is improved by about 9dB.

4.5.2 Computational Load

In this part, we compare the number of weights and computational load for achieving the specified interference suppression performance. The scenario in Section 4.5.1 is used again and the desired SIR improvement is set as 23.5dB. As shown in Figure 4.4, the proposed IIR beamformer has obtained this performance with parameters described previously. Based on the criterion that the required number of taps and iterations are as small as possible, sufficient simulations are performed and the data in the second column of Table 4.1 for the Frost beamformer is acquired. Comparing the two beamformers, we find

Table 4.1: COMPUTATIONAL LOAD

Type of Beamformer	Frost Beamformer	Proposed IIR Beamformer
Number of Weights	16 (L=2, J=8)	8 (L=2, J=3)
Multiplications per Iteration	41	35
Additions per Iteration	63	43
SIR Improvement in 1500 Iterations	16.5dB	23.5dB
SIR Improvement in 6000 Iterations	23.5dB	23.5dB

that the Frost beamformer needs 16 weights and 6000 iterations while the proposed IIR beamformer requires 8 weights and 1500 iterations to converge and achieve the specified SIR improvement. Because the numbers of arithmetic operations in each iteration for the two beamformers are approximately the same, the total amount of computation required by the Frost beamformer in 6000 iterations is about 4 times of that required by the new IIR beamformer in 1500 iterations. In the above comparison, the Frost beamformer requires more taps to achieve the specified interference suppression performance, so it has a higher-dimensional Hessian matrix with a larger eigenvalue spread. This results in a slower convergence rate and consequently a larger total computational load. Therefore, the new IIR beamformer is preferred in applications which desire both fast convergence rate and good steady-state performance.

4.5.3 Broadened Beamwidth

This simulation aims to verify the effectiveness of the derivative constraints imposed on the proposed IIR beamformer. An equally-spaced linear array with 7 elements is used. Four taps are following behind each element. Therefore, there are 31 weights in total. The noise is assumed to be white both temporally and spatially. The signal power and the noise power are 0dB and -30dB, respectively. The step size is chosen to be 0.01. The output power of the beamformer after 3000 iterations is estimated with the signal direction varying from $-90°$ to $90°$. Figure 4.5 shows the output power curves obtained by

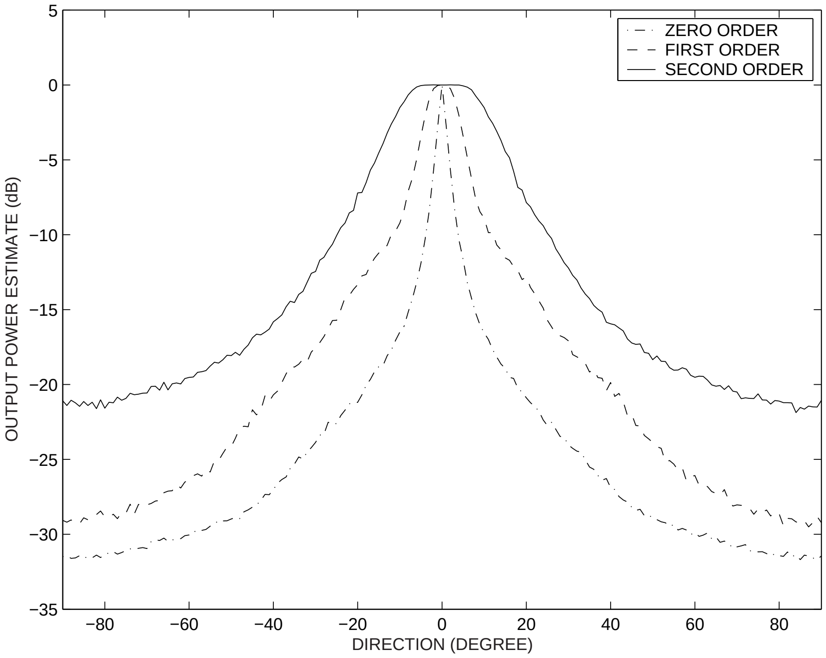

Figure 4.5. Output power curves in the presence of the 0dB broadband signal and -30dB white noise. The first order, second-order and third order represent the highest order of the derivative constraints adopted in the algorithm.

the algorithm using the gain constraint, the gain constraint plus the first-order derivative constraint and the gain constraint plus the first-order derivative constraint and the second-order derivative constraint. The highest order of the derivative constraints is indicated in the figures to represent the three cases. We observe that the width of the mainlobe becomes wider as the highest order of the derivative constraint increases. This proves that the derivative constraints derived in Section 4.4 can effectively broaden the beamwidth of the new IIR beamformer.

4.6 Conclusion

A new broadband beamformer using TDL-form IIR filters is proposed in this chapter. The new beamforming structure is constructed by replacing all the delay elements of the

Frost beamformer with tap-to-tap IIR sections under some structural restrictions. It can be regarded as a natural extension of the Frost beamformer. The combined LMS algorithm is designed to compute the feedforward and feedback weights. Because only first-order IIR filters are involved, the stability of the new beamformer can be monitored easily. It is demonstrated that the proposed IIR beamformer can achieve improved SINR relative to the Frost beamformer with the same number of coefficients. Comparisons show that the new beamformer requires less number of weights and computational load to obtain the specified interference suppression performance. Due to the nonlinear relation between the output of the beamformer and the input data, a drawback of the IIR beamformer is that we can not solve for the optimization formulation with the closed-form solution, like what has been done for the FIR beamformer. This is the main obstacle for obtaining a deeper insight and analysis for the IIR beamformer. Relative to the FIR beamformer, a well-known drawback of the IIR beamformer is the possible instability of the adaptation process and the local minima in the performance surface.

Chapter 5

Broadband IIR Beamformers using RGN-Type Algorithms

5.1 Introduction

In this chapter, further investigations are carried out on beamforming using TDL-form IIR filters. In the beamformer described in Chapter 4, the poles are restricted on the real axis for the real input. Here we present the second-order IIR sections so that the complex poles are allowed for the real signals. To improve the convergence performance of the combined LMS algorithm, the combined RGN algorithm is designed to compute the feedforward and feedback weights in the Frost-based IIR beamformer. The GSC-based implementation with the unconstrained RGN algorithm is developed. Our analyses show that the proposed beamformers have certain attractive properties. First, similar to the beamformer using direct-form IIR filters, the new IIR beamformers can achieve better SINR performance than the FIR beamformer with the same number of coefficients. Second, the new structures facilitate the stability monitoring. Third, the sensitivity to the

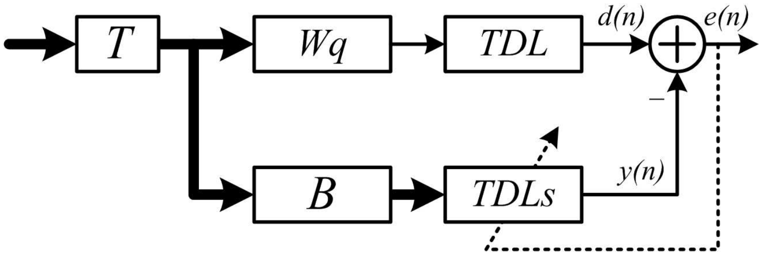

Figure 5.1. Broadband GSC beamforming structure in a simplified form.

coefficient quantization error is much smaller than the beamformer using direct-form IIR filters.

This chapter is organized as follows: In Section 5.2, the background on the conventional FIR beamformer and the beamformer using direct-form IIR filters are introduced briefly. In Section 5.3, the combined RGN algorithm is designed for the Frost-based IIR beamformer. The beamformer using second-order IIR sections is presented. In Section 5.4, the GSC-based implementation is described. In Section 5.5, we consider the problem of convergence and stability. In Section 5.6, the difference between the Frost-based and GSC-based implementations and the probable extension are discussed. In Section 5.7, simulation examples are included to compare the performance of the beamformers using TDL-form IIR filters with that of the existing FIR and IIR beamformers.

5.2 Background

Instead of using the structure shown by Figure 2.8 in Section 2.4.2, Figure 5.1 presents the GSC beamforming structure [8] in a simplified form. $\boldsymbol{T}$ denotes the presteering delays. The blocking matrix $\boldsymbol{B}$ is designed to prevent the signal of interest from entering the lower branch. The quiescent weight vector $\boldsymbol{w}_q$ and the TDL in the upper branch determine the look-direction response. Unconstrained adaptive filtering algorithms can be employed to

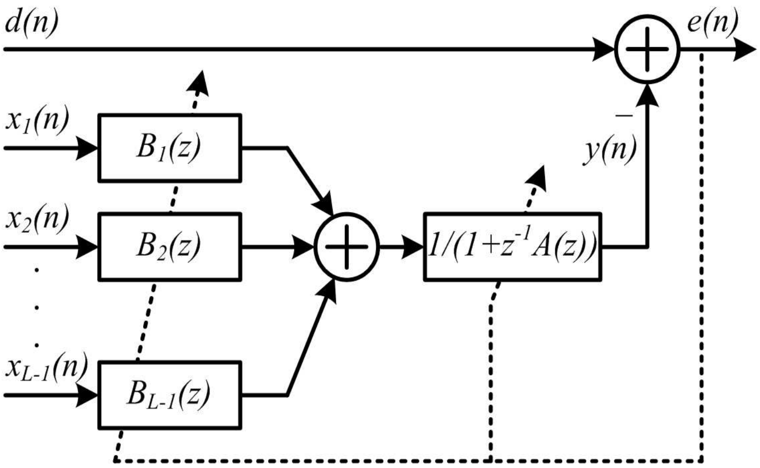

Figure 5.2. Beamforming structure using direct-form IIR filters.

compute the weights in the groups of the TDLs in the lower branch.

Figure 5.2 shows the beamforming structure using the output-error adaptive IIR filtering proposed in [19]. This beamformer adopts the GSC implementation (we omit the preprocessing part of the GSC for generating $d(n)$ and $x_i(n), i = 1, 2, \cdots, L-1$ in Figure 5.2) while a direct-form IIR filter is introduced. The lower branch comprises $L-1$ all-zero filters with transfer functions $B_i(z)$ followed by a common all-pole IIR filter $1/(1+z^{-1}A(z))$. The RGN algorithm [113] is used to compute the weights in [19].

5.3 Frost-Based Implementation

5.3.1 Combined RGN Algorithm

The combined LMS algorithm presented in Chapter 4 has low computational complexity but it has slow convergence rate which is unbearable in some applications. Therefore, the combined RGN algorithm is developed for the Frost-based IIR beamformer.

For the processor shown in Figure 4.1 on Page 59, the beamformer output is:

$$y(n) = \boldsymbol{w}^T \boldsymbol{x}(n) \tag{5.1}$$

where $\boldsymbol{w}$ is the $LJ \times 1$ feedforward weighting vector:

$$\boldsymbol{w} = [w_{1,1} \ \cdots \ w_{L,1} \ \cdots \ w_{1,J} \ \cdots \ w_{L,J}]^T \tag{5.2}$$

and $\boldsymbol{x}(n)$ is the $LJ \times 1$ tap data vector:

$$\boldsymbol{x}(n) = [x_{1,1}(n) \ \cdots \ x_{L,1}(n) \ \cdots \ x_{1,J}(n) \ \cdots \ x_{L,J}(n)]^T \tag{5.3}$$

Similar to [7], to reject the interference and noise but preserve the desired signal, the following constrained optimization criterion is used to find the feedforward coefficient vector $\boldsymbol{w}$:

$$\begin{gathered} \min_{\boldsymbol{w}} \ \boldsymbol{w}^T \boldsymbol{R}_{\boldsymbol{xx}} \boldsymbol{w} \\ \text{subject to } \boldsymbol{C}^T \boldsymbol{w} = \boldsymbol{f} \end{gathered} \tag{5.4}$$

where $\boldsymbol{R}_{\boldsymbol{xx}}$ is the estimated correlation matrix. $\boldsymbol{C}$ is a constraint matrix with dimension $LJ \times J$,

$$\boldsymbol{C} = \begin{pmatrix} \mathbf{1}_L & \mathbf{0}_L & \cdots & \mathbf{0}_L \\ \mathbf{0}_L & \mathbf{1}_L & \cdots & \mathbf{0}_L \\ \vdots & \vdots & \ddots & \vdots \\ \mathbf{0}_L & \cdots & \cdots & \mathbf{1}_L \end{pmatrix} \tag{5.5}$$

where $\mathbf{1}_L$ and $\mathbf{0}_L$ are column vectors containing L ones and zeros, respectively. $\boldsymbol{f}$ is a $J \times 1$ constant vector:

$$\boldsymbol{f} = [1 \ \ 0 \ \ \cdots \ \ 0]^T \tag{5.6}$$

The transfer function of the first-order tap-to-tap IIR section is again designed as:

$$G_k(z) = \frac{z^{-1}}{1 - a_k z^{-1}}, \quad k = 1, 2, \cdots, J-1 \tag{5.7}$$

where $z = e^{j2\pi f T_s}$ and a_k is the feedback coefficient. Therefore, the tap variable $x_{i,k}(n)$ in $\boldsymbol{x}(n)$ is related with the feedback coefficients as follows:

$$\begin{cases} x_{i,1}(n) : \text{presteered snapshot data from the } i\text{th sensor.} \\ x_{i,k}(n) = x_{i,k-1}(n-1) + a_{k-1} x_{i,k}(n-1) \\ \qquad\qquad i = 1, 2, \cdots, L; \quad k = 2, 3, \cdots, J \end{cases} \tag{5.8}$$

The constrained RGN algorithm is designed to adjust the feedforward weight vector $\boldsymbol{w}(n)$ as follows.

For the linearly constrained optimization problem expressed by (5.4), the Lagrangian can be defined as:

$$\eta = (1/2)\boldsymbol{w}^T \boldsymbol{R}_{\boldsymbol{xx}} \boldsymbol{w} + \boldsymbol{\lambda}^T (\boldsymbol{C}^T \boldsymbol{w} - \boldsymbol{f}) \tag{5.9}$$

At the time instant n, the gradient of η relative to $\boldsymbol{w}$ is:

$$\boldsymbol{\nabla}_{\boldsymbol{w}}(n) = \boldsymbol{R}_{\boldsymbol{xx}}(n)\boldsymbol{w}(n-1) + \boldsymbol{C\lambda} \tag{5.10}$$

The iteration formula for obtaining $\boldsymbol{w}(n)$ is:

$$\begin{aligned} \boldsymbol{w}(n) &= \boldsymbol{w}(n-1) - \mu_{\boldsymbol{w}} \boldsymbol{R}_{\boldsymbol{xx}}^{-1}(n) \boldsymbol{\nabla}_{\boldsymbol{w}}(n) \\ &= (1 - \mu_{\boldsymbol{w}})\boldsymbol{w}(n-1) - \mu_{\boldsymbol{w}} \boldsymbol{R}_{\boldsymbol{xx}}^{-1}(n) \boldsymbol{C\lambda} \end{aligned} \tag{5.11}$$

where $\mu_{\boldsymbol{w}}$ is the step size. By setting:

$$\begin{aligned} \boldsymbol{f} &= \boldsymbol{C}^T\boldsymbol{w}(n) \\ &= (1-\mu_{\boldsymbol{w}})\boldsymbol{C}^T\boldsymbol{w}(n-1) - \mu_{\boldsymbol{w}}\boldsymbol{C}^T\boldsymbol{R}_{\boldsymbol{xx}}^{-1}(n)\boldsymbol{C}\boldsymbol{\lambda} \end{aligned} \tag{5.12}$$

we can solve for $\boldsymbol{\lambda}$ and substitute it into (5.11), then the following update equation for the weight vector $\boldsymbol{w}$ can be derived:

$$\boldsymbol{w}(n) = (1-\mu_{\boldsymbol{w}})\boldsymbol{P}\boldsymbol{w}(n-1) + \boldsymbol{g} \tag{5.13}$$

where

$$\boldsymbol{P} = \boldsymbol{I} - \boldsymbol{R}_{\boldsymbol{xx}}^{-1}(n)\boldsymbol{C}[\boldsymbol{C}^T\boldsymbol{R}_{\boldsymbol{xx}}^{-1}(n)\boldsymbol{C}]^{-1}\boldsymbol{C}^T \tag{5.14}$$

and

$$\boldsymbol{g} = \boldsymbol{R}_{\boldsymbol{xx}}^{-1}(n)\boldsymbol{C}[\boldsymbol{C}^T\boldsymbol{R}_{\boldsymbol{xx}}^{-1}(n)\boldsymbol{C}]^{-1}\boldsymbol{f} \tag{5.15}$$

where $\boldsymbol{R}_{\boldsymbol{xx}}(n)$ is the Hessian matrix estimated by:

$$\boldsymbol{R}_{\boldsymbol{xx}}(n) = (1-\mu_{\boldsymbol{w}})\boldsymbol{R}_{\boldsymbol{xx}}(n-1) + \mu_{\boldsymbol{w}}\boldsymbol{x}(n)\boldsymbol{x}^T(n) \tag{5.16}$$

where $1-\mu_{\boldsymbol{w}}$ is the forgetting factor [19]. $\boldsymbol{\Phi}(n) = \boldsymbol{R}_{\boldsymbol{xx}}^{-1}(n)$ is defined for the notational convenience. Using the matrix inversion lemma, the update equation for $\boldsymbol{\Phi}(n)$ can be derived as follows:

$$\boldsymbol{\Phi}(n) = \frac{1}{1-\mu_{\boldsymbol{w}}}[\boldsymbol{\Phi}(n-1) - \frac{\mu_{\boldsymbol{w}}}{\beta_{\boldsymbol{w}}}\boldsymbol{\Phi}(n-1)\boldsymbol{x}(n)\boldsymbol{x}^T(n)\boldsymbol{\Phi}(n-1)] \tag{5.17}$$

where $\beta_{\boldsymbol{w}} = 1-\mu_{\boldsymbol{w}} + \mu_{\boldsymbol{w}}\boldsymbol{x}^T(n)\boldsymbol{\Phi}(n-1)\boldsymbol{x}(n)$. Equations (5.14) and (5.15) are then re-expressed as:

$$\boldsymbol{P} = \boldsymbol{I} - \boldsymbol{\Phi}(n)\boldsymbol{C}[\boldsymbol{C}^T\boldsymbol{\Phi}(n)\boldsymbol{C}]^{-1}\boldsymbol{C}^T \tag{5.18}$$

Table 5.1: CONSTRAINED RGN ALGORITHM FOR THE FEEDFORWARD WEIGHT VECTOR

---

1. Initialize: $n = 0$

$\boldsymbol{x}(0) = \mathbf{0}, \quad \boldsymbol{\Phi}(0) = \delta_1^{-1}\boldsymbol{I}_{LJ}$

$\boldsymbol{w}(0) = \boldsymbol{\Phi}(0)\boldsymbol{C}[\boldsymbol{C}^T\boldsymbol{\Phi}(0)\boldsymbol{C}]^{-1}\boldsymbol{f}$

2. $n = n + 1$, compute $\boldsymbol{x}(n)$ using (5.8).

3. Update:

$\boldsymbol{\Phi}(n) = \frac{1}{1-\mu_{\boldsymbol{w}}}[\boldsymbol{\Phi}(n-1) - \frac{\mu_{\boldsymbol{w}}}{\beta_{\boldsymbol{w}}}\boldsymbol{\Phi}(n-1)\boldsymbol{x}(n)\boldsymbol{x}^T(n)\boldsymbol{\Phi}(n-1)]$

where $\beta_{\boldsymbol{w}} = 1 - \mu_{\boldsymbol{w}} + \mu_{\boldsymbol{w}}\boldsymbol{x}^T(n)\boldsymbol{\Phi}(n-1)\boldsymbol{x}(n)$

4. Update:

$\boldsymbol{w}(n) = (1 - \mu_{\boldsymbol{w}})\boldsymbol{P}\boldsymbol{w}(n-1) + \boldsymbol{g}$

where $\boldsymbol{P} = \boldsymbol{I} - \boldsymbol{\Phi}(n)\boldsymbol{C}[\boldsymbol{C}^T\boldsymbol{\Phi}(n)\boldsymbol{C}]^{-1}\boldsymbol{C}^T$

and $\boldsymbol{g} = \boldsymbol{\Phi}(n)\boldsymbol{C}[\boldsymbol{C}^T\boldsymbol{\Phi}(n)\boldsymbol{C}]^{-1}\boldsymbol{f}$

5. Repeat step 2 to step 4 until convergence or the end of the input data.

---

and

$$\boldsymbol{g} = \boldsymbol{\Phi}(n)\boldsymbol{C}[\boldsymbol{C}^T\boldsymbol{\Phi}(n)\boldsymbol{C}]^{-1}\boldsymbol{f} \tag{5.19}$$

The iteration procedure for updating $\boldsymbol{w}(n)$ is listed in Table 5.1.

In Table 5.1, the weight vector $\boldsymbol{w}$ is initialized to be $\boldsymbol{w}(0) = \boldsymbol{\Phi}(0)\boldsymbol{C}[\boldsymbol{C}^T\boldsymbol{\Phi}(0)\boldsymbol{C}]^{-1}\boldsymbol{f}$, which satisfies the constraint in (5.4). $\boldsymbol{I}_{LJ}$ denotes the $LJ \times LJ$ identity matrix. δ_1 is a positive real constant. When updating the tap variables in $\boldsymbol{x}(n)$ by (5.8), the latest feedback coefficient vector $\boldsymbol{a}(n-1)$ is used. $\boldsymbol{P}$ and $\boldsymbol{g}$ are different from the constraint matrix and the constraint vector defined in the constrained LMS algorithm in [7] and the combined LMS algorithm in Chapter 4.

$\boldsymbol{a}$ is defined as a $(J-1) \times 1$ column vector containing all the feedback coefficients in

(5.7),

$$\boldsymbol{a} = [a_1 \ \ a_2 \ \ \cdots \ \ a_{J-1}]^T \tag{5.20}$$

Because the constraint in (5.4) can guarantee the desired signal to be passed without distortion whatever the feedback coefficients are, the unconstrained optimization approach can be used to compute $\boldsymbol{a}$,

$$\min_{\boldsymbol{a}} \ \ \mathrm{E}[y^2(n)] \tag{5.21}$$

The instantaneous estimate of the gradient of $(1/2)\mathrm{E}[y^2(n)]$ relative to $\boldsymbol{a}$ is:

$$\boldsymbol{\nabla}_{\boldsymbol{a}}(n) = y(n)\sum_{i=1}^{L}\sum_{k=1}^{J} w_{i,k}\frac{\partial x_{i,k}(n)}{\partial \boldsymbol{a}} \tag{5.22}$$

Assuming $\boldsymbol{v}_{i,k}(n) = (\partial x_{i,k}(n))/(\partial \boldsymbol{a})$, we can calculate the $(J-1)$-dimensional vector $\boldsymbol{v}_{i,k}(n)$ by differentiating (5.8):

$$\begin{cases} \boldsymbol{v}_{i,1}(n) = \boldsymbol{0} \\ \boldsymbol{v}_{i,k}(n) = \boldsymbol{v}_{i,k-1}(n-1) + \boldsymbol{e}_{k-1}x_{i,k}(n-1) + a_{k-1}\boldsymbol{v}_{i,k}(n-1) \\ \qquad\qquad i = 1, 2, \cdots, L; \quad k = 2, 3, \cdots, J \end{cases} \tag{5.23}$$

where $\boldsymbol{e}_{k-1}$ represents the $(k-1)$th column of the $(J-1)\times(J-1)$ identity matrix. Let

$$\boldsymbol{V}(n) = [\boldsymbol{v}_{1,1}(n) \ \ \cdots \ \ \boldsymbol{v}_{L,1}(n) \ \ \cdots \ \ \boldsymbol{v}_{1,J}(n) \ \ \cdots \ \ \boldsymbol{v}_{L,J}(n)] \tag{5.24}$$

and

$$\boldsymbol{u}(n) = \boldsymbol{V}(n)\boldsymbol{w}(n-1) \tag{5.25}$$

then (5.22) can be rewritten as:

$$\boldsymbol{\nabla}_{\boldsymbol{a}}(n) = y(n)\boldsymbol{u}(n) \tag{5.26}$$

Table 5.2: UNCONSTRAINED RGN ALGORITHM FOR THE FEEDBACK WEIGHT VECTOR

1. Initialize: $n = 0$

$\boldsymbol{a}(0) = \mathbf{0}, \quad \boldsymbol{V}(0) = \mathbf{0}, \quad \boldsymbol{\Psi}(0) = \delta_2^{-1}\boldsymbol{I}_{J-1}$

2. $n = n + 1$, compute $\boldsymbol{u}(n)$ using (5.23) (5.24) and (5.25).

3. Update:

$\boldsymbol{\Psi}(n) = \frac{1}{1-\mu_{\boldsymbol{a}}}[\boldsymbol{\Psi}(n-1) - \frac{\mu_{\boldsymbol{a}}}{\beta_{\boldsymbol{a}}}\boldsymbol{\Psi}(n-1)\boldsymbol{u}(n)\boldsymbol{u}^T(n)\boldsymbol{\Psi}(n-1)]$

where $\beta_{\boldsymbol{a}} = 1 - \mu_{\boldsymbol{a}} + \mu_{\boldsymbol{a}}\boldsymbol{u}^T(n)\boldsymbol{\Psi}(n-1)\boldsymbol{u}(n)$

4. Update:

$y(n) = \boldsymbol{w}^T(n-1)\boldsymbol{x}(n)$

$\boldsymbol{a}(n) = \boldsymbol{a}(n-1) - \mu_{\boldsymbol{a}}\boldsymbol{\Psi}(n)y(n)\boldsymbol{u}(n)$

5. Stability test and treatment.

6. Repeat step 2 to step 5 until convergence or the end of the input data.

With the unconstrained RGN algorithm, $\boldsymbol{a}(n)$ is updated by:

$$\boldsymbol{a}(n) = \boldsymbol{a}(n-1) - \mu_{\boldsymbol{a}}\boldsymbol{R}_{\boldsymbol{uu}}^{-1}(n)\boldsymbol{\nabla}_{\boldsymbol{a}}(n) \tag{5.27}$$

where $\mu_{\boldsymbol{a}}$ is the step size. $\boldsymbol{R}_{\boldsymbol{uu}}(n)$ is the Hessian matrix estimated by:

$$\boldsymbol{R}_{\boldsymbol{uu}}(n) = (1 - \mu_{\boldsymbol{a}})\boldsymbol{R}_{\boldsymbol{uu}}(n-1) + \mu_{\boldsymbol{a}}\boldsymbol{u}(n)\boldsymbol{u}^T(n) \tag{5.28}$$

where $1 - \mu_{\boldsymbol{a}}$ is the forgetting factor. Let $\boldsymbol{\Psi}(n) = \boldsymbol{R}_{\boldsymbol{uu}}^{-1}(n)$, then the update equation for $\boldsymbol{\Psi}(n)$ can be derived by the matrix inversion lemma:

$$\boldsymbol{\Psi}(n) = \frac{1}{1-\mu_{\boldsymbol{a}}}[\boldsymbol{\Psi}(n-1) - \frac{\mu_{\boldsymbol{a}}}{\beta_{\boldsymbol{a}}}\boldsymbol{\Psi}(n-1)\boldsymbol{u}(n)\boldsymbol{u}^T(n)\boldsymbol{\Psi}(n-1)] \tag{5.29}$$

where $\beta_{\boldsymbol{a}} = 1 - \mu_{\boldsymbol{a}} + \mu_{\boldsymbol{a}}\boldsymbol{u}^T(n)\boldsymbol{\Psi}(n-1)\boldsymbol{u}(n)$.

The iterative algorithm for computing $\boldsymbol{a}(n)$ is listed in Table 5.2.

In Table 5.2, δ_2 is a real positive constant. $\boldsymbol{w}(n-1)$ is required for computing $\boldsymbol{u}(n)$ and $y(n)$. It is obtained by the iteration procedure listed in Table 5.1. Therefore, in practical implementations, the constrained RGN algorithm in Table 5.1 and the unconstrained RGN algorithm in Table 5.2 are naturally combined together. The whole algorithm is named the combined RGN algorithm. The updating procedure is summarized simply as follows:

1) Initialize $\boldsymbol{x}(0)$, $\boldsymbol{\Phi}(0)$, $\boldsymbol{w}(0)$, $\boldsymbol{a}(0)$, $\boldsymbol{V}(0)$, $\boldsymbol{\Psi}(0)$;

2) Compute $\boldsymbol{u}(1)$; Compute $\boldsymbol{x}(1)$;

3) Compute $\boldsymbol{\Psi}(1)$ and $\boldsymbol{\Phi}(1)$;

4) Compute $y(1)$, $\boldsymbol{a}(1)$;

5) Compute $\boldsymbol{w}(1)$;

6) stability test and treatment;

7) Increase all the time index by one, and repeat steps 2-7 until convergence or the end of the data.

5.3.2 Beamformer using Second-Order IIR Sections

In the case of using first-order IIR sections, if the input signals are real, the poles of the IIR filters are on the real axis. To allow complex poles for the real input, second-order IIR sections can be employed. The algorithms in Section 5.3.1 can be extended to the second-order case.

The transfer functions of the second-order tap-to-tap IIR sections are defined as follows:

$$G_k(z) = \frac{z^{-1}}{1 - a_{k,1}z^{-1} - a_{k,2}z^{-2}}, \quad k = 1, 2, \cdots, J-1 \tag{5.30}$$

The poles can be in the form of real or complex conjugate pairs. The feedback weight vector is defined as a $2(J-1) \times 1$ vector:

$$\boldsymbol{a} = [a_{1,1} \;\; a_{1,2} \;\; \cdots \;\; a_{J-1,1} \;\; a_{J-1,2}]^T \tag{5.31}$$

Therefore, the elements of the tap vector $\boldsymbol{x}(n)$ are obtained by the following expressions:

$$\begin{cases} x_{i,1}(n) : \text{presteered snapshot data from the } i\text{th sensor.} \\ x_{i,k}(n) = x_{i,k-1}(n-1) + a_{k-1,1}x_{i,k}(n-1) + a_{k-1,2}x_{i,k}(n-2) \\ \qquad\qquad i = 1, 2, \cdots, L; \quad k = 2, 3, \cdots, J \end{cases} \tag{5.32}$$

By differentiating (5.32), $\boldsymbol{v}_{i,k}(n) = (\partial x_{i,k}(n))/(\partial \boldsymbol{a})$ is computed as follows:

$$\begin{cases} \boldsymbol{v}_{i,1}(n) = \boldsymbol{0} \\ \boldsymbol{v}_{i,k}(n) = \boldsymbol{v}_{i,k-1}(n-1) + \boldsymbol{e}_{2k-3}x_{i,k}(n-1) + a_{k-1,1}\boldsymbol{v}_{i,k}(n-1) \\ \qquad\qquad +\boldsymbol{e}_{2k-2}x_{i,k}(n-2) + a_{k-1,2}\boldsymbol{v}_{i,k}(n-2) \\ \qquad\qquad i = 1, 2, \cdots, L; \quad k = 2, 3, \cdots, J \end{cases} \tag{5.33}$$

where $\boldsymbol{e}_m$ represents the mth column of the $2(J-1) \times 2(J-1)$ identity matrix.

After replacing (5.20), (5.8) and (5.23) by (5.31), (5.32) and (5.33), respectively, in the second-order case, the feedforward weight vector $\boldsymbol{w}(n)$ can be adjusted with the algorithm listed in Table 5.1, while the feedback weight vector $\boldsymbol{a}(n)$ can be updated with the algorithm listed in Table 5.2.

5.4 GSC-Based Implementation

In this section, the GSC-based implementation for the beamformer using TDL-form IIR filters is presented.

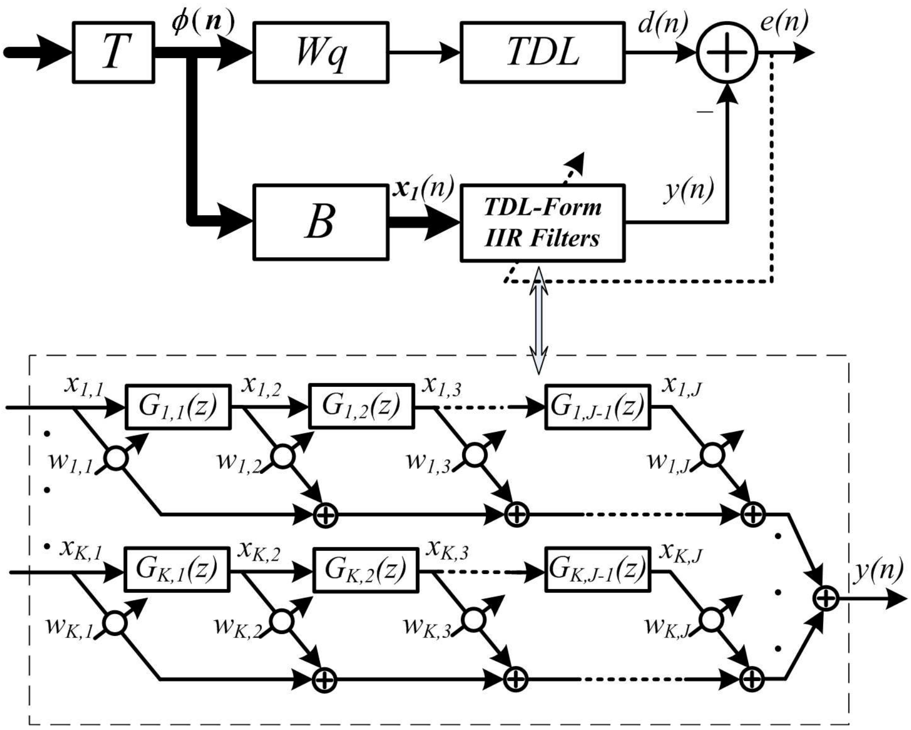

Figure 5.3. GSC-based beamforming structure using TDL-form IIR filters.

5.4.1 Beamforming Structure

Figure 5.3 shows the GSC implementation of the beamformer using TDL-form IIR filters. The feedforward weight vector $\boldsymbol{w}$ and the feedback weight vector $\boldsymbol{a}$ in the block of the TDL-form IIR filters are adapted by the output error $e(n)$ so that the interference and noise can be cancelled as completely as possible. In the beamformer in Figure 4.1, the tap-to-tap IIR sections in the same tap positions of different channels are restricted to have the same feedback coefficients so that the constraint is only imposed on the feedforward weights. In the GSC implementation, this restriction can be ignored because the unconstrained adaptive algorithm is used. $G_{m,k}(z)$ in Figure 5.3 can be equivalent to or different from $G_{n,k}(z)$ for $m \neq n$. That means, different channels can have either common poles or independent poles.

The introduction of the tap-to-tap feedbacks in the lower branch makes this beamformer different from the standard GSC beamformer and the beamformer using direct-form or parallel-form IIR filters.

For simplicity, in the following discussion, we assume that the quiescent weight $\boldsymbol{w}_q$ is an $L \times 1$ vector:

$$\boldsymbol{w}_q = (1/L)[1 \;\; 1 \;\; \cdots \;\; 1]^T \tag{5.34}$$

and the blocking matrix $\boldsymbol{B}$ has the dimension of $L \times (L-1)$:

$$\boldsymbol{B} = \begin{pmatrix} 1 & 0 & \cdots & 0 \\ -1 & 1 & \cdots & 0 \\ 0 & -1 & \cdots & 0 \\ \vdots & \vdots & \ddots & \vdots \\ 0 & 0 & \cdots & -1 \end{pmatrix} \tag{5.35}$$

As shown in Figure 5.3, $\boldsymbol{x}_1(n)$ is the $(L-1)$-dimensional input to the adaptive beamformer, and $\boldsymbol{\phi}(n)$ is the L-dimensional presteered snapshot data $\boldsymbol{\phi}(n) = [\phi_1(n) \;\; \phi_2(n) \;\; \cdots \;\; \phi_L(n)]^T$. They satisfy:

$$\boldsymbol{x}_1(n) = \boldsymbol{B}^T \boldsymbol{\phi}(n) \tag{5.36}$$

The output of the beamformer is:

$$e(n) = d(n) - y(n) = d(n) - \boldsymbol{w}^T \boldsymbol{x}(n) \tag{5.37}$$

where $\boldsymbol{w}$ is the $(L-1)J$-dimensional feedforward weight vector:

$$\boldsymbol{w} = [w_{1,1} \;\; \cdots \;\; w_{L-1,1} \;\; \cdots \;\; w_{1,J} \;\; \cdots \;\; w_{L-1,J}]^T \tag{5.38}$$

$\boldsymbol{x}(n)$ is the $(L-1)J \times 1$ tap data vector:

$$\boldsymbol{x}(n) = [x_{1,1}(n) \quad \cdots \quad x_{L-1,1}(n) \quad \cdots \quad x_{1,J}(n) \quad \cdots \quad x_{L-1,J}(n)]^T \tag{5.39}$$

The following transfer functions of the tap-to-tap IIR sections are assumed for the convenience of presenting the algorithms:

$$\begin{aligned} G_{i,k}(z) &= \frac{z^{-1}}{1-a_{i,k}z^{-1}} \\ i = 1, 2, \cdots, L-1&; \quad k = 1, 2, \cdots, J-1 \end{aligned} \tag{5.40}$$

5.4.2 Algorithms for Updating the Weights

When the beamformer uses common poles in different channels,

$$G_{m,k}(z) = G_{n,k}(z), \quad m \neq n, \quad k = 1, 2, \cdots, J-1 \tag{5.41}$$

That is to say, $a_{m,k} = a_{n,k}$ for $m \neq n$. To simplify the notations, $a_{i,k}$ is abbreviated to a_k. Therefore, the $(J-1)$-dimensional feedback weight vector $\boldsymbol{a}$ is defined as $\boldsymbol{a} = [a_1 \ a_2 \ \cdots \ a_{J-1}]^T$, which is the same as (5.20). The tap variable $x_{i,k}(n)$ satisfies:

$$\begin{cases} x_{i,1}(n) = \phi_i(n) - \phi_{i+1}(n) \\ x_{i,k}(n) = x_{i,k-1}(n-1) + a_{k-1}x_{i,k}(n-1) \\ \qquad\qquad i = 1, 2, \cdots, L-1; \quad k = 2, 3, \cdots, J \end{cases} \tag{5.42}$$

By differentiating (5.42), the $(J-1)\times 1$ vector $\boldsymbol{v}_{i,k}(n) = (\partial x_{i,k}(n))/(\partial \boldsymbol{a})$ is calculated as follows:

$$\begin{cases} \boldsymbol{v}_{i,1}(n) = \mathbf{0} \\ \boldsymbol{v}_{i,k}(n) = \boldsymbol{v}_{i,k-1}(n-1) + \boldsymbol{e}_{k-1} x_{i,k}(n-1) + a_{k-1}\boldsymbol{v}_{i,k}(n-1) \\ \qquad\qquad i = 1,2,\cdots,L-1; \quad k = 2,3,\cdots,J \end{cases} \tag{5.43}$$

where $\boldsymbol{e}_{k-1}$ is the $(k-1)$th column vector of the $(J-1)\times(J-1)$ identity matrix.

When the beamformer uses independent poles for different channels,

$$G_{m,k}(z) \neq G_{n,k}(z), \quad m \neq n, \quad k = 1,2,\cdots,J-1 \tag{5.44}$$

The $(L-1)(J-1)$-dimensional feedback weight vector $\boldsymbol{a}$ is defined as:

$$\boldsymbol{a} = [a_{1,1} \ \cdots \ a_{L-1,1} \ \cdots \ a_{1,J-1} \ \cdots \ a_{L-1,J-1}]^T \tag{5.45}$$

The tap variable $x_{i,k}(n)$ in (5.39) is given by:

$$\begin{cases} x_{i,1}(n) = \phi_i(n) - \phi_{i+1}(n) \\ x_{i,k}(n) = x_{i,k-1}(n-1) + a_{i,k-1} x_{i,k}(n-1) \\ \qquad\qquad i = 1,2,\cdots,L-1; \quad k = 2,3,\cdots,J \end{cases} \tag{5.46}$$

The $(L-1)(J-1)\times 1$ vector $\boldsymbol{v}_{i,k}(n) = (\partial x_{i,k}(n))/(\partial \boldsymbol{a})$ is calculated by differentiating (5.46):

$$\begin{cases} \boldsymbol{v}_{i,1}(n) = \mathbf{0} \\ \boldsymbol{v}_{i,k}(n) = \boldsymbol{v}_{i,k-1}(n-1) + \boldsymbol{e}_{(k-2)(L-1)+i} x_{i,k}(n-1) + a_{i,k-1}\boldsymbol{v}_{i,k}(n-1) \\ \qquad\qquad i = 1,2,\cdots,L-1; \quad k = 2,3,\cdots,J \end{cases} \tag{5.47}$$

where $\boldsymbol{e}_m$ is the mth column of the $(L-1)(J-1)\times(L-1)(J-1)$ identity matrix.

If there is only one channel in the lower branch, the case for using common poles and that for using independent poles become the same. For both cases, by minimizing the mean power of the output error $e(n)$, the optimum weight vector can be obtained. The optimization criterion is:

$$\min_{\boldsymbol{w},\boldsymbol{a}} \ \mathrm{E}[e^2(n)] \tag{5.48}$$

For convenience, the cost function is defined as $\eta = (1/2)\mathrm{E}[e^2(n)]$, then the gradients of η relative to $\boldsymbol{w}$ and $\boldsymbol{a}$ are estimated by:

$$\boldsymbol{\nabla}_{\boldsymbol{w}}(n) = -e(n)\boldsymbol{x}(n) \tag{5.49}$$

$$\boldsymbol{\nabla}_{\boldsymbol{a}}(n) = -e(n)\boldsymbol{u}(n) \tag{5.50}$$

where $\boldsymbol{u}(n) = \boldsymbol{V}(n)\boldsymbol{w}(n-1)$ and

$$\boldsymbol{V}(n) = [\boldsymbol{v}_{1,1}(n) \quad \cdots \quad \boldsymbol{v}_{L-1,1}(n) \quad \cdots \quad \boldsymbol{v}_{1,J}(n) \quad \cdots \quad \boldsymbol{v}_{L-1,J}(n)] \tag{5.51}$$

The unconstrained RGN algorithms for updating $\boldsymbol{w}(n)$ and $\boldsymbol{a}(n)$ are:

$$\boldsymbol{w}(n) = \boldsymbol{w}(n-1) - \mu_{\boldsymbol{w}}\boldsymbol{R}_{\boldsymbol{xx}}^{-1}(n)\boldsymbol{\nabla}_{\boldsymbol{w}}(n) \tag{5.52}$$

$$\boldsymbol{a}(n) = \boldsymbol{a}(n-1) - \mu_{\boldsymbol{a}}\boldsymbol{R}_{\boldsymbol{uu}}^{-1}(n)\boldsymbol{\nabla}_{\boldsymbol{a}}(n) \tag{5.53}$$

where $\mu_{\boldsymbol{w}}$ and $\mu_{\boldsymbol{a}}$ are the step sizes. $\boldsymbol{R}_{\boldsymbol{xx}}(n)$ and $\boldsymbol{R}_{\boldsymbol{uu}}(n)$ are Hessian matrices estimated by:

$$\boldsymbol{R}_{\boldsymbol{xx}}(n) = (1-\mu_{\boldsymbol{w}})\boldsymbol{R}_{\boldsymbol{xx}}(n-1) + \mu_{\boldsymbol{w}}\boldsymbol{x}(n)\boldsymbol{x}^T(n) \tag{5.54}$$

$$\boldsymbol{R}_{\boldsymbol{uu}}(n) = (1-\mu_{\boldsymbol{a}})\boldsymbol{R}_{\boldsymbol{uu}}(n-1) + \mu_{\boldsymbol{a}}\boldsymbol{u}(n)\boldsymbol{u}^T(n). \tag{5.55}$$

The matrix inversion lemma is used to compute the inverse $\boldsymbol{\Phi}(n) = \boldsymbol{R}_{\boldsymbol{xx}}^{-1}(n)$ and $\boldsymbol{\Psi}(n) =$

Table 5.3: UNCONSTRAINED RGN ALGORITHM FOR THE GSC-BASED IMPLEMENTATION

1. Initialize: $n = 0$

$\boldsymbol{w}(0) = \mathbf{0}, \quad \boldsymbol{a}(0) = \mathbf{0}, \quad \boldsymbol{V}(0) = \mathbf{0}, \quad \boldsymbol{x}(0) = \mathbf{0}$

$\boldsymbol{\Phi}(0) = \delta_1^{-1}\boldsymbol{I}_{(L-1)J}$

$\boldsymbol{\Psi}(0) = \delta_2^{-1}\boldsymbol{I}_{J-1}$ or $\boldsymbol{\Psi}(0) = \delta_2^{-1}\boldsymbol{I}_{(L-1)(J-1)}$

2. $n = n + 1$, compute $\boldsymbol{x}(n)$ and $\boldsymbol{u}(n)$ using (5.42) (5.43) or (5.46) (5.47).

3. Update:

$\boldsymbol{\Phi}(n) = \frac{1}{1-\mu_{\boldsymbol{w}}}[\boldsymbol{\Phi}(n-1) - \frac{\mu_{\boldsymbol{w}}}{\beta_{\boldsymbol{w}}}\boldsymbol{\Phi}(n-1)\boldsymbol{x}(n)\boldsymbol{x}^T(n)\boldsymbol{\Phi}(n-1)]$

$\boldsymbol{\Psi}(n) = \frac{1}{1-\mu_{\boldsymbol{a}}}[\boldsymbol{\Psi}(n-1) - \frac{\mu_{\boldsymbol{a}}}{\beta_{\boldsymbol{a}}}\boldsymbol{\Psi}(n-1)\boldsymbol{u}(n)\boldsymbol{u}^T(n)\boldsymbol{\Psi}(n-1)]$

where $\beta_{\boldsymbol{w}} = 1 - \mu_{\boldsymbol{w}} + \mu_{\boldsymbol{w}}\boldsymbol{x}^T(n)\boldsymbol{\Phi}(n-1)\boldsymbol{x}(n)$

and $\beta_{\boldsymbol{a}} = 1 - \mu_{\boldsymbol{a}} + \mu_{\boldsymbol{a}}\boldsymbol{u}^T(n)\boldsymbol{\Psi}(n-1)\boldsymbol{u}(n)$

4. Update:

$e(n) = d(n) - \boldsymbol{w}^T(n-1)\boldsymbol{x}(n)$

$\boldsymbol{w}(n) = \boldsymbol{w}(n-1) + \mu_{\boldsymbol{w}}\boldsymbol{\Phi}(n)e(n)\boldsymbol{x}(n)$

$\boldsymbol{a}(n) = \boldsymbol{a}(n-1) + \mu_{\boldsymbol{a}}\boldsymbol{\Psi}(n)e(n)\boldsymbol{u}(n)$

5. Stability test and treatment.

6. Repeat step 2 to step 5 until convergence or the end of the input data.

$\boldsymbol{R}_{\boldsymbol{uu}}^{-1}(n)$ in the iterations:

$$\boldsymbol{\Phi}(n) = \frac{1}{1-\mu_{\boldsymbol{w}}}[\boldsymbol{\Phi}(n-1) - \frac{\mu_{\boldsymbol{w}}}{\beta_{\boldsymbol{w}}}\boldsymbol{\Phi}(n-1)\boldsymbol{x}(n)\boldsymbol{x}^T(n)\boldsymbol{\Phi}(n-1)] \tag{5.56}$$

$$\boldsymbol{\Psi}(n) = \frac{1}{1-\mu_{\boldsymbol{a}}}[\boldsymbol{\Psi}(n-1) - \frac{\mu_{\boldsymbol{a}}}{\beta_{\boldsymbol{a}}}\boldsymbol{\Psi}(n-1)\boldsymbol{u}(n)\boldsymbol{u}^T(n)\boldsymbol{\Psi}(n-1)] \tag{5.57}$$

where $\beta_{\boldsymbol{w}} = 1-\mu_{\boldsymbol{w}}+\mu_{\boldsymbol{w}}\boldsymbol{x}^T(n)\boldsymbol{\Phi}(n-1)\boldsymbol{x}(n)$ and $\beta_{\boldsymbol{a}} = 1-\mu_{\boldsymbol{a}}+\mu_{\boldsymbol{a}}\boldsymbol{u}^T(n)\boldsymbol{\Psi}(n-1)\boldsymbol{u}(n)$.

The iteration procedure for computing $\boldsymbol{w}(n)$ and $\boldsymbol{a}(n)$ is listed in Table 5.3, where δ_1 and δ_2 are real positive constants.

5.5 Convergence and Stability

In (5.13) and (5.27), (5.52) and (5.53), the step sizes $\mu_{\boldsymbol{w}}$ and $\mu_{\boldsymbol{a}}$ control the convergence rate of the iterative procedure together. Finding the accurate upper bound for the step size parameters is difficult in IIR filtering algorithms. Large numbers of experiments are performed to investigate how to choose the step size. In all our experiments, $\mu_{\boldsymbol{w}}$ and $\mu_{\boldsymbol{a}}$ are chosen to be the same, and hence abbreviated to μ in the following narrations.

For the combined LMS algorithm presented in Chapter 4, experiments show that

$$0 < \mu < \frac{1}{M\sigma^2} \tag{5.58}$$

can be used as an approximate range to choose μ, where M is the summation of the length of the feedforward and feedback weight vectors $\boldsymbol{w}(n)$ and $\boldsymbol{a}(n)$. σ^2 represents the mean power of the data received on each sensor. A faster convergence can be achieved by increasing the step size but paid by the cost of the SINR degradation. These features are similar to the properties of the LMS algorithm in FIR filtering [114].

For the RGN algorithms listed in Tables 5.1 - 5.3, the step size is chosen in the range

$$0.01 \leq \mu \leq 0.1 \tag{5.59}$$

according to the typical evaluation as suggested by [111]. A faster convergence performance can be obtained relative to the combined LMS algorithm because the convergence rate of RGN algorithms is less dependent on the input power spectra.

The above criteria for choosing the step size will be demonstrated by simulation examples in Section 5.7. How to choose a proper combination of $\mu_{\boldsymbol{w}}$ and $\mu_{\boldsymbol{a}}$ to achieve fast convergence or good SINR needs further investigation.

When the IIR filters are employed in the beamformer, the problem of stability has to be considered. For the beamformer using direct-form IIR filters with a higher order, monitoring the poles requires high complexity. In the proposed beamformers, when the first-order tap-to-tap IIR sections are applied, the feedback coefficients define the poles directly. The criterion expressed by (4.30) is used to monitor the stability. When the second-order IIR sections are used, the monitoring criterion is still easy [111]:

$$\begin{cases} 1 - a_{k,1} - a_{k,2} > 0 \\ 1 + a_{k,1} - a_{k,2} > 0 \\ 1 + a_{k,2} > 0 \end{cases} \quad k = 1, 2, \cdots, J-1 \tag{5.60}$$

5.6 Difference and Extension

Two implementations are presented in the previous sections. The Frost-based implementation has a convenient mathematical formulation, with which some constraints, besides the gain constraint, can be imposed easily to get the desired spatial response. For example, we have proved in Chapter 4 that the derivative constraints proposed in [42] can be directly imposed on the Frost-based IIR beamformer to obtain a flat spatial response around the look direction. The GSC-based implementation has smaller computational complexity. Unconstrained adaptive algorithms can be easily applied to compute the weights. Therefore, the specific applications determine which implementation is to be chosen.

In Sections 5.3 and 5.4, the tap-to-tap IIR sections are designed with the specified transfer functions (5.7), (5.30) and (5.40). We would like to highlight that they can be extended to other forms. For example, the all-pass IIR filter with the transfer function like

$$G_k(z) = \frac{z^{-1} - a_k}{1 - a_k z^{-1}}, \quad k = 1, 2, \cdots, J-1 \tag{5.61}$$

can be used. New properties might be invoked. With new definitions of $G_k(z)$, the computations of the tap variables $x_{i,k}(n)$ and their derivatives $\boldsymbol{v}_{i,k}(n)$ relative to the feedback weight vector will be different from that described previously. However, the idea we have proposed to adjust the coefficients of this type of IIR beamformers is still applicable.

5.7 Simulation Examples

In this section, the proposed beamformers are evaluated by computer simulations. Because no assumptions about the array geometry are made before designing the beamforming structures and algorithms, the beamformers proposed in this chapter are applicable to any array geometries. In the following simulations, the ULA is used. Furthermore, the desired signal and the interferences are simulated as uncorrelated stationary random processes. Their spectra are nonzero within the same frequency band and zero elsewhere. Both the amplitude spectrum and the phase spectrum have random fluctuations. All sources are real-valued so their spectra are symmetric on the positive and negative frequencies. Besides, the gaussian distributed noise added to each sensor is both spatially and temporally white.

The SINR convergence curves are frequently used in the following simulations to measure the performance of different beamformers. Therefore, it is necessary to present the related formulations. The SINR at the nth iteration is calculated by:

$$\text{SINR}(n) = \frac{\overline{P_S(n)}}{\sum_{k=1}^{K} \overline{P_{I_k}(n)} + \overline{P_N(n)}} \tag{5.62}$$

where $\overline{(\cdot)}$ means the average of $(\cdot)$ over many Monte Carlo trials. K is the number of interferences. $P_S(n)$, $P_{I_k}(n)$ and $P_N(n)$ represent the output power for the desired signal, the kth interference and the noise at the nth iteration, respectively. In the Frost-based implementation,

$$P_S(n) = |\boldsymbol{w}^T(n)\boldsymbol{x}_S(n)|^2 \tag{5.63}$$

$$P_{I_k}(n) = |\boldsymbol{w}^T(n)\boldsymbol{x}_{I_k}(n)|^2 \tag{5.64}$$

$$P_N(n) = |\boldsymbol{w}^T(n)\boldsymbol{x}_N(n)|^2 \tag{5.65}$$

In the GSC-based implementation,

$$P_S(n) = |d_S(n) - \boldsymbol{w}^T(n)\boldsymbol{x}_S(n)|^2 \tag{5.66}$$

$$P_{I_k}(n) = |d_{I_k}(n) - \boldsymbol{w}^T(n)\boldsymbol{x}_{I_k}(n)|^2 \tag{5.67}$$

$$P_N(n) = |d_N(n) - \boldsymbol{w}^T(n)\boldsymbol{x}_N(n)|^2 \tag{5.68}$$

where $d_S(n)$, $d_{I_k}(n)$ and $d_N(n)$ are the desired signal, the kth interference and the noise components in $d(n)$. $\boldsymbol{w}(n)$ is the weight vector obtained at the nth iteration. For the FIR beamformer, $\boldsymbol{x}_S(n)$, $\boldsymbol{x}_{I_k}(n)$, $\boldsymbol{x}_N(n)$ are the simulated array snapshot data for the desired signal, the kth interference and the white noise, respectively. For the IIR beamformer, $\boldsymbol{x}_S(n)$, $\boldsymbol{x}_{I_k}(n)$, $\boldsymbol{x}_N(n)$ are parts of the tap data vector $\boldsymbol{x}(n)$, so they are related with the feedback coefficients. The update equations for $\boldsymbol{x}(n)$ presented in Sections 5.3 and 5.4 can be used to compute $\boldsymbol{x}_S(n)$, $\boldsymbol{x}_{I_k}(n)$ and $\boldsymbol{x}_N(n)$ at each iteration by replacing the input snapshot data with its signal, kth interference and noise components, respectively.

5.7.1 Compare the Beamformers using TDL-Form IIR filters

Compared with the combined LMS algorithm presented in Chapter 4, the combined RGN algorithm requires similar computational load for updating $\boldsymbol{w}(n)$, $\boldsymbol{a}(n)$, $\boldsymbol{x}(n)$, $\boldsymbol{u}(n)$ and $y(n)$ in each iteration, but extra computations on $\boldsymbol{P}$, $\boldsymbol{g}$, $\boldsymbol{\Phi}(n)$ and $\boldsymbol{\Psi}(n)$ are required in the combined RGN algorithm. The extra computational complexity incurred by the combined RGN algorithm wins improvement in the convergence rate and the steady-state SINR performance. The following simulation examples will show this point.

In the first group of simulations, the beamformers of interest include the Frost-based TDL-form IIR beamformer with the combined LMS algorithm, the Frost-based TDL-form IIR beamformer (using first-order IIR sections) with the combined RGN algorithm and the GSC-based TDL-form IIR beamformer (using common poles) with the unconstrained RGN algorithm. They are abbreviated to FROST-IIR-TDL-LMS, FROST-IIR-TDL-RGN and GSC-IIR-TDL-RGN, respectively.

A ULA with four sensors ($L = 4$) is used. The inter-sensor spacing is one half of the wavelength of the highest frequency. For each beamformer, 7 taps ($J = 7$) are used in each channel so that there are 34 coefficients in the two Frost-based beamformers and 27 coefficients in the GSC-based beamformer. The desired signal comes from the look direction $0°$. Three interferences come from $-60°$, $-20°$ and $40°$. The spectra for the desired signal and interferences are within $[0.2, 0.4]$. White Gaussian noise is imposed on each sensor. Two cases are simulated. In Case I, the powers for the desired signal, each interference and the noise are -20, -10 and -50dB, respectively. In Case II, they are 0, 10 and -30dB, respectively. Therefore, the two cases have the same input SIR and SNR. In experiments, δ_1 and δ_2 are chosen to be 1 in the initialization of the iterations.

The approximate number of iterations N_c for reaching convergence and the steady-state SINR are listed in Table 5.4 for evaluating the beamformers under different step sizes in the two cases. In some circumstances, after the N_cth iteration, the value of SINR still tends to increase, although in a very slow speed. Therefore, the data for N_c and SINR do not correspond to the true steady state. The superscript $*$ is labelled on the data in such cases in Table 5.4. A group of convergence curves averaged over 2000 trials in

Table 5.4: EVALUATION OF THE CONVERGENCE PERFORMANCE

Beamformer	Case	Step Size μ	Number of Iterations N_c for Reaching Convergence	Steady-Sate SINR (dB)
FROST-IIR-TDL-LMS	I	0.09	5000*	-0.1
	II	0.0009	5000*	-0.1
FROST-IIR-TDL-RGN	I	0.01	2000*	2.4
		0.05	600	-1.6
		0.1	200	-4.6
	II	0.01	2000*	2.6
		0.05	540	-1.5
		0.1	220	-4.6
GSC-IIR-TDL-RGN	I	0.01	1800	2.6
		0.05	230	-1.0
		0.1	100	-4.4
	II	0.01	1500	2.7
		0.05	220	-1.0
		0.1	60	-4.4

Case I is plotted in Figure 5.4. Two-dimensional beampatterns averaged over 100 trials at $n = 2000$ for the three beamformers are demonstrated in Figures 5.5-5.7.

For the FROST-IIR-TDL-LMS beamformer, the step sizes we use are very close to the upper bound indicated by (5.58). $M\sigma^2$ for Case I is equal to 10.54 while that for Case II is equal to 1054.0. The data in Table 5.4 show that with the same product $\mu M\sigma^2$ under the two cases, this beamformer has the same convergence performance.

For the FROST-IIR-TDL-RGN and GSC-IIR-TDL-RGN beamformers, their step sizes are chosen to be $\{0.01, 0.05, 0.1\}$ according to (5.59). From Table 5.4, we can see that the number of iterations for reaching convergence and the steady-state SINR are almost the same under the same step size for the two different cases.

Comparing the three beamformers, we find that the IIR beamformers using the RGN al-

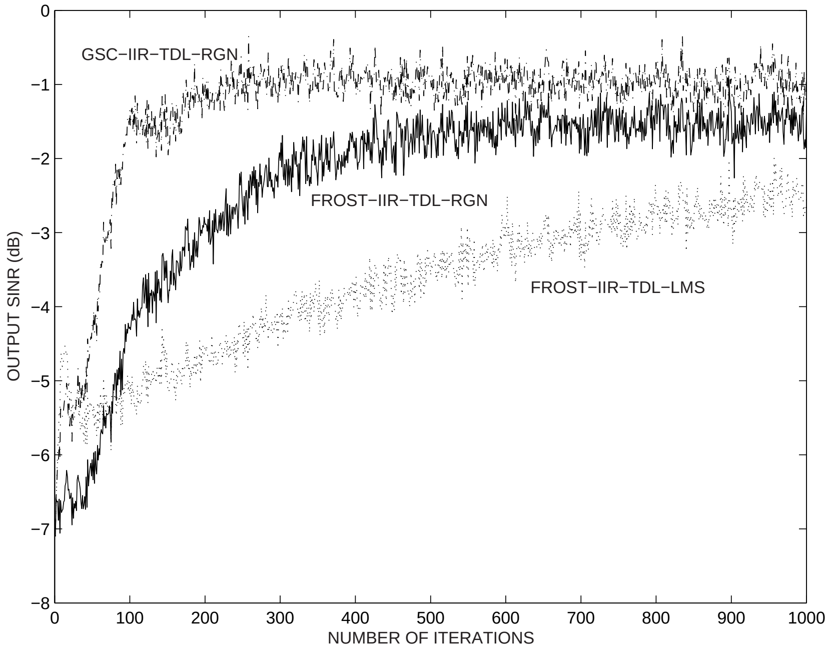

Figure 5.4. Output SINR convergence curves in 1000 iterations in Case I for the FROST-IIR-TDL-LMS ($\mu = 0.09$), FROST-IIR-TDL-RGN ($\mu = 0.05$) and GSC-IIR-TDL-RGN ($\mu = 0.05$) beamformers.

gorithm (the FROST-IIR-TDL-RGN and GSC-IIR-TDL-RGN beamformers) have faster convergence rate than that using the LMS algorithm (the FROST-IIR-TDL-LMS beamformer). The FROST-IIR-TDL-LMS beamformer shows very slow convergence rate especially when the number of sensors and taps are large. Therefore, the RGN algorithm is preferred in some applications even if it requires higher computational complexity in each iteration relative to the LMS algorithm.

From Table 5.4 and Figures 5.4, 5.6 and 5.7, we can see that the FROST-IIR-TDL-RGN and the GSC-IIR-TDL-RGN beamformers have different transient behavior but almost equivalent steady-state SINR and beampattern. This phenomenon is similar to that found in the FIR beamformers: A GSC beamformer using $L \times (L-1)$ blocking matrix followed by $(L-1) \times J$ tapped delay lines provides identical transient and steady-state performance with the equivalent Frost beamformer with $L \times J$ taps.

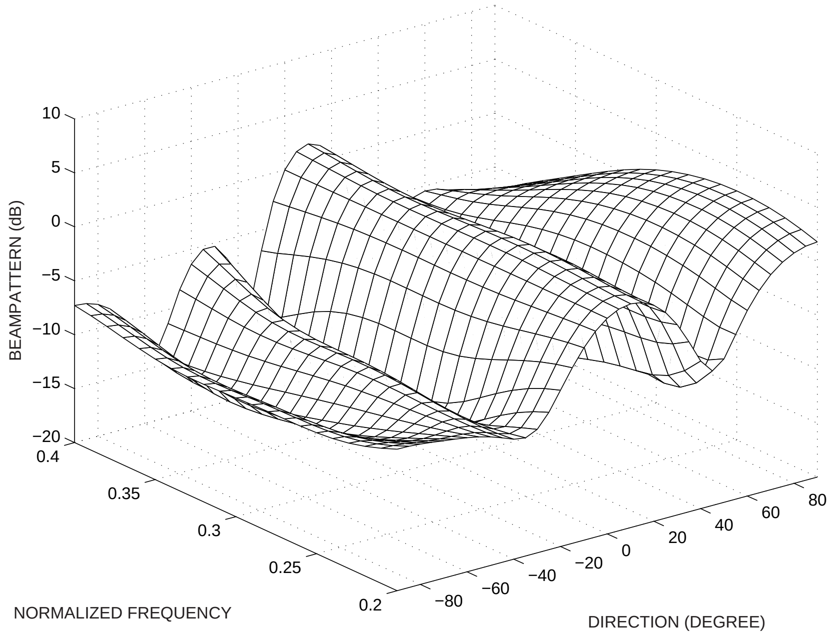

Figure 5.5. Two-dimensional beampattern in Case I for the FROST-IIR-TDL-LMS beamformer ($\mu = 0.09$) at $n = 2000$, averaged over 100 trials. The interferences are from $-60°$, $-20°$ and $40°$.

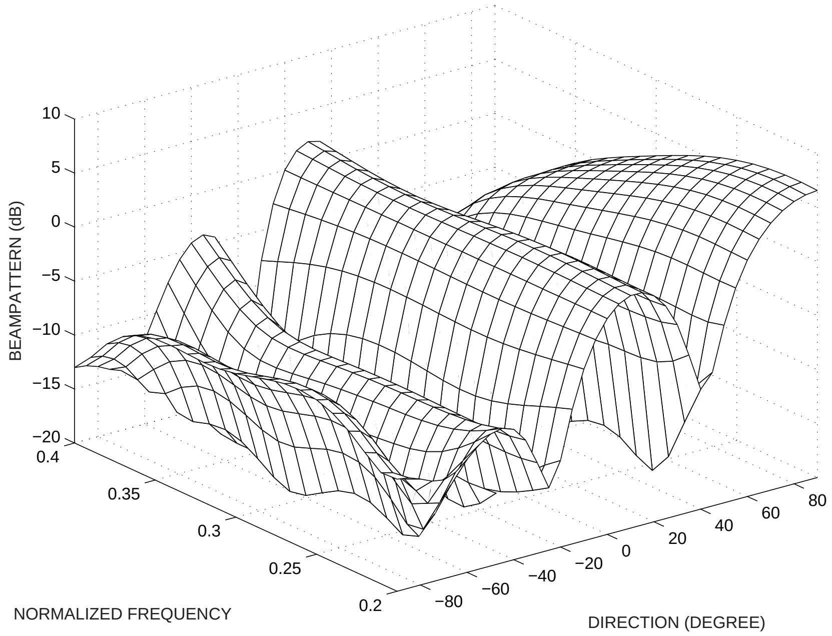

Figure 5.6. Two-dimensional beampattern in Case I for the FROST-IIR-TDL-RGN beamformer ($\mu = 0.01$) at $n = 2000$, averaged over 100 trials. The interferences are from $-60°$, $-20°$ and $40°$.

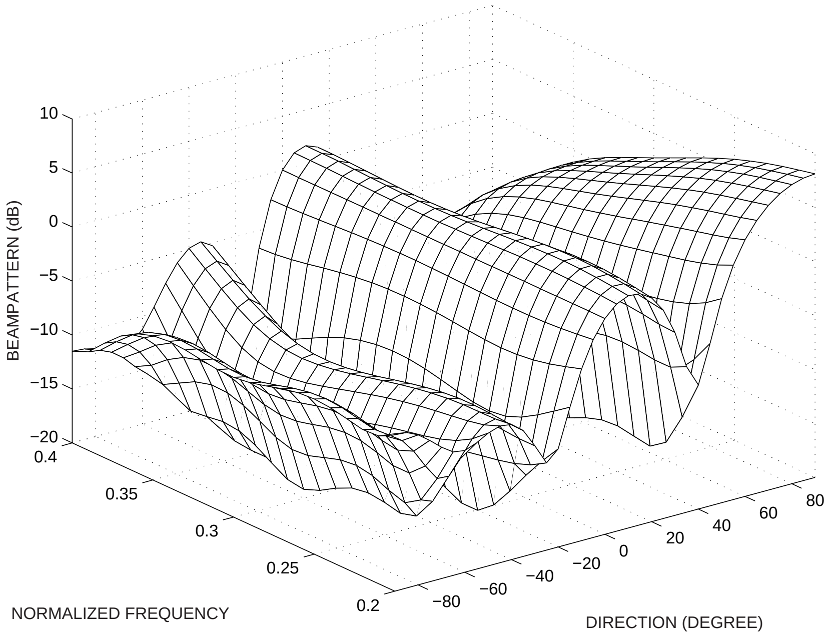

Figure 5.7. Two-dimensional beampattern in Case I for the GSC-IIR-TDL-RGN beamformer ($\mu = 0.01$) at $n = 2000$, averaged over 100 trials. The interferences are from -60°, -20° and 40°.

Another group of simulations is performed to compare the Frost-based beamformer using first-order and second-order IIR sections. They are abbreviated to FROST-IIR-FIRST-ORDER and FROST-IIR-SECOND-ORDER, respectively. A two-sensor array is used. The inter-sensor spacing is half the wavelength of the highest frequency. The desired signal comes from the look direction 0° and one interference comes from 40°. The frequency spectra for both of them are within $[0.05, 0.4]$. The input SIR is -20dB and SNR is 30dB. The FROST-IIR-FIRST-ORDER beamformer uses 5 taps and the FROST-IIR-SECOND-ORDER beamformer uses 4 taps, so both of them have 14 coefficients. Their step sizes are chosen to be 0.01. The convergence curves obtained by 1000 trials and the power responses averaged over 100 trials in the look direction and the interference direction are shown in Figures 5.8 and 5.9.

It can be seen that the FROST-IIR-SECOND-ORDER beamformer achieves better steady-state SINR. Its power response in the interference direction within the frequency band is deeper and flatter than that of the FROST-IIR-FIRST-ORDER beamformer. After averaging the power response over $[0.05, 0.4]$, the null depth in the interference direction is -24.0dB for the FROST-IIR-FIRST-ORDER beamformer and -27.5dB for the FROST-IIR-SECOND-ORDER beamformer. However, we can not draw a conclusive conclusion about the performance of the beamformers using first-order and second-order IIR sections by one example. Other simulations show that for the array with large number of sensors and taps, the FROST-IIR-SECOND-ORDER beamformer requires smaller $\mu_{\boldsymbol{a}}$ to achieve better interference suppression performance.

5.7.2 Compare with Existing Beamformers

In this simulation, the beamformers to be compared include: the FIR beamformer with the GSC structure [8] and RGN algorithm, the beamformer using direct-form output-error IIR filters [19] and the GSC-based TDL-form IIR beamformers using common poles and independent poles proposed in this chapter. They are abbreviated as GSC-FIR, GSC-IIR-GOOCH, GSC-IIR-TDL-COMMON and GSC-IIR-TDL-INDEPENDENT, respectively in the following descriptions and figures.

Two scenarios are simulated. Scenario I is as follows: Three sensors are used and there are two jammers from -60° and 40°. The desired signal comes from the look direction 0°. The input SNR is 30dB and the input SIR for each interference is -20dB. The frequency band of the desired signal and interferences is $[0.1, 0.4]$. All the beamformers are designed with the same number of coefficients. The numbers of taps in each channel of the lower branch are 7, 5, 5 and 4 for the GSC-FIR, GSC-IIR-GOOCH, GSC-IIR-TDL-COMMON and GSC-IIR-TDL-INDEPENDENT beamformers, respectively. The GSC-IIR-GOOCH beamformer uses a fourth-order all-pole direct-form IIR filter. There-

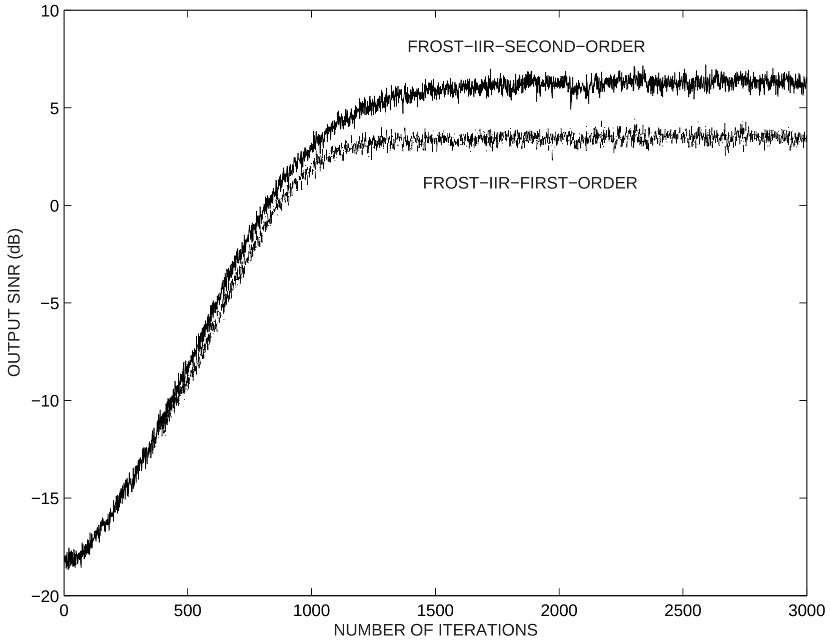

Figure 5.8. Output SINR convergence curves for the FROST-IIR-FIRST-ORDER and FROST-IIR-SECOND-ORDER beamformers. The step sizes for both beamformers are 0.01.

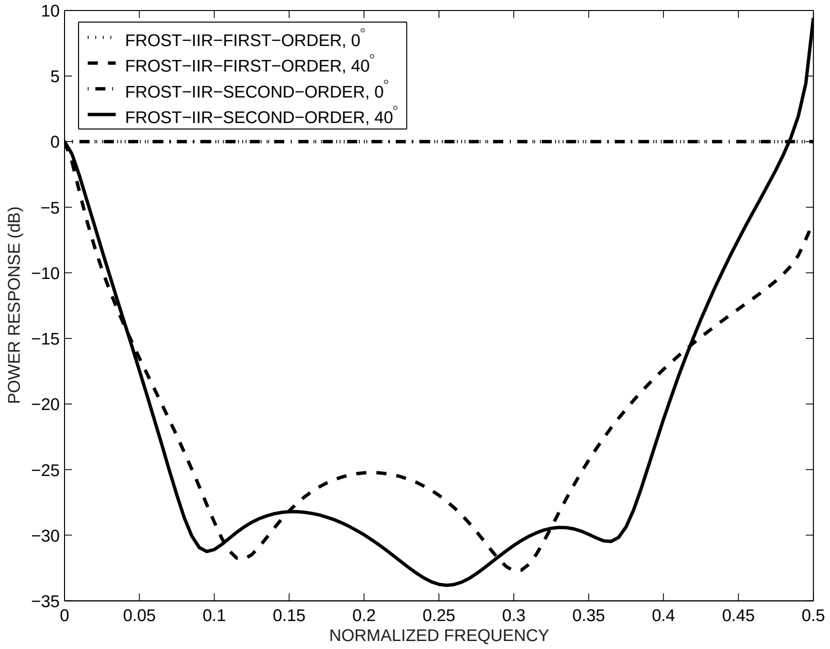

Figure 5.9. Power responses in the look direction 0° and the interference direction 40° at $n = 3000$. The frequency band is $[0.05, 0.4]$.

fore, both the GSC-IIR-GOOCH and the GSC-IIR-TDL-COMMON beamformers have 10 feedforward and 4 feedback coefficients. The GSC-IIR-TDL-INDEPENDENT beamformer has 8 feedforward and 6 feedback coefficients. Scenario II is as follows: The array has 4 sensors. The mean power, direction and frequency band of the desired signal and interferences are the same as scenario I. The numbers of taps in each channel of the lower branch are 9, 7, 7 and 5 for the GSC-FIR, GSC-IIR-GOOCH, GSC-IIR-TDL-COMMON and GSC-IIR-TDL-INDEPENDENT beamformers, respectively. The GSC-IIR-GOOCH beamformer uses a 6th-order all-pole direct-form IIR filter. Therefore, each beamformer has 27 coefficients. In addition, in both scenarios, the inter-sensor spacing of the uniform linear array is one half of the wavelength of the highest frequency. The temporal sampling frequency is 1. The step sizes for all the beamformers are chosen to be 0.01 for both scenarios (except an extra convergence curve provided by the GSC-FIR beamformer using the step size 0.004 in Scenario I for comparisons). δ_1 and δ_2 are chosen to be 1 in the initialization of all the beamformers. In both scenarios, the number of coefficients of the proposed GSC-IIR-TDL-COMMON beamformer is chosen to be the same with that of the existing GSC-IIR-GOOCH beamformer. The computational complexities of these two IIR-type beamformers are almost the same because both of them update the weights with the RGN algorithm.

The output SINR convergence curves averaged over 2000 trials and beampatterns averaged over the frequency band at $n = 3000$ (averaged over 100 trials) in Scenario I are shown in Figures 5.10 - 5.11 while those for Scenario II are shown in Figures 5.12 - 5.13.

From these figures, we can find that with the same number of coefficients and the same step size 0.01 (hence, the same forgetting factor), IIR beamformers achieve significantly improved SINR relative to the FIR beamformer at the steady state. Even if the GSC-FIR beamformer uses a smaller step size 0.004 and converges at almost the same time

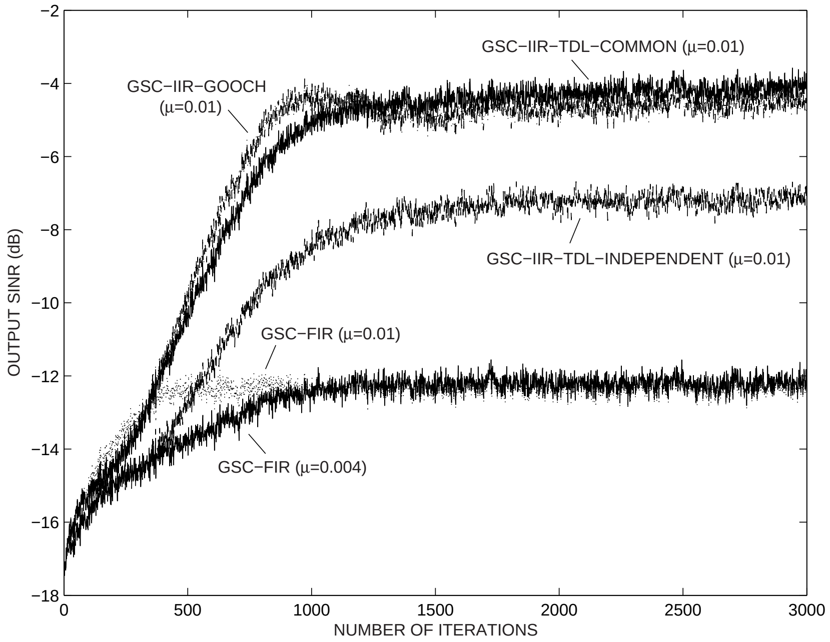

Figure 5.10. Output SINR convergence curves in Scenario I.

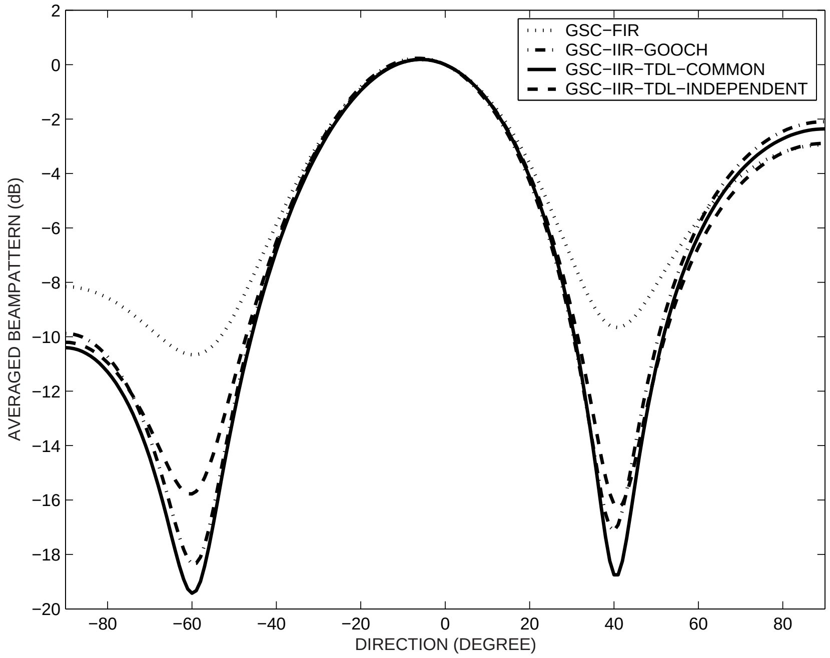

Figure 5.11. Beampatterns averaged over the frequency band $[0.1, 0.4]$ at $n = 3000$ in Scenario I. The interferences are from -60° and 40°. The step sizes for all the beamformers are 0.01.

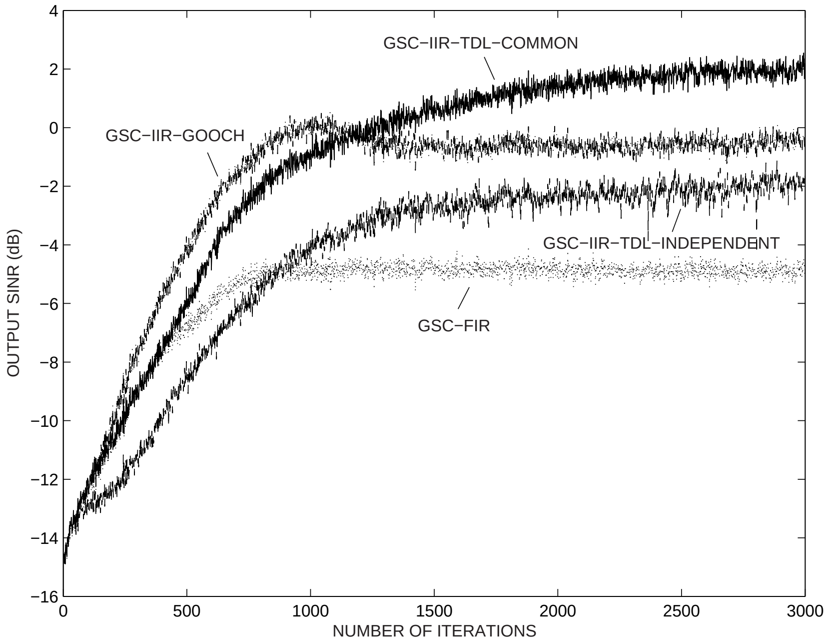

Figure 5.12. Output SINR convergence curves in Scenario II. The step sizes for all the beamformers are 0.01.

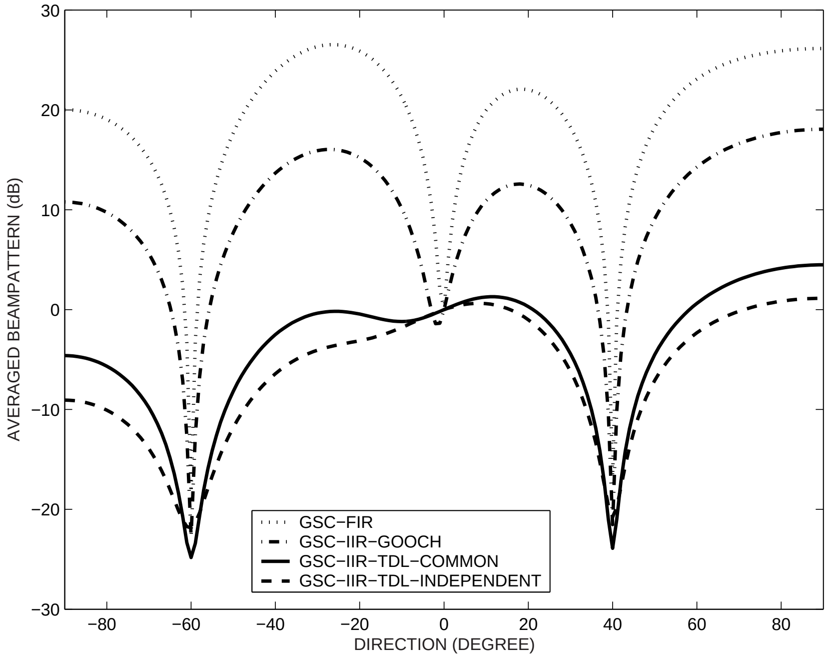

Figure 5.13. Beampatterns averaged over the frequency band $[0.1, 0.4]$ at $n = 3000$ in Scenario II. The interferences are from -60° and 40°. The step sizes for all the beamformers are 0.01.

with the IIR beamformers, its steady-state SINR performance is still worse than the IIR beamfomers. In Figure 5.10 for Scenario I, the performance of the GSC-IIR-TDL-COMMON beamformer is comparable with that of the GSC-IIR-GOOCH beamformer, in terms of both the convergence rate and the output SINR. In Figure 5.12 for Scenario II, although the SINR convergence curves of the GSC-IIR-TDL-COMMON and GSC-IIR-TDL-INDEPENDENT beamformers seem not to reach convergence after $n = 1000$, they have achieved better SINR than the GSC-IIR-GOOCH and GSC-FIR beamformers, respectively, after the latter two reach the steady state. A remarkable phenomenon shown in Figure 5.13 is that in Scenario II, the beampatterns for the GSC-FIR and GSC-IIR-GOOCH beamformers have abnormally high gains in the directions other than the look direction and interference directions. Such beampatterns are not favorable because sudden interferences from unknown directions will be magnified. The reason is ascribed to the poorly conditioned Hessian matrix and the induced large norm of the weight vector when the interference-to-noise-ratio (INR) is high and the dimension of the Hessian matrix is large. Imposing constraints on the weight norm can solve this problem, but the interference suppression performance will suffer degradation due to the reduction of the degrees of freedom. Also from Figure 5.13, we can see that this phenomenon is not so serious in the new IIR beamformers as that in the GSC-FIR and GSC-IIR-GOOCH beamformers.

In addition, one simulation is carried out to study the effect of the coefficient quantization. Other types of quantization are switched off in this example. All the coefficients of the beamformers are quantized in the “floor”-mode in each iteration. Scenario I is used to analyze the sensitivity to the coefficient quantization. Figure 5.14 shows the output SINR degradations (relative to the case of using infinite word length) at $n = 3000$ averaged over 200 independent trials, with the step sizes for all the beamformers chosen to be 0.01. The word length decreases from 16 bits to 12 bits.

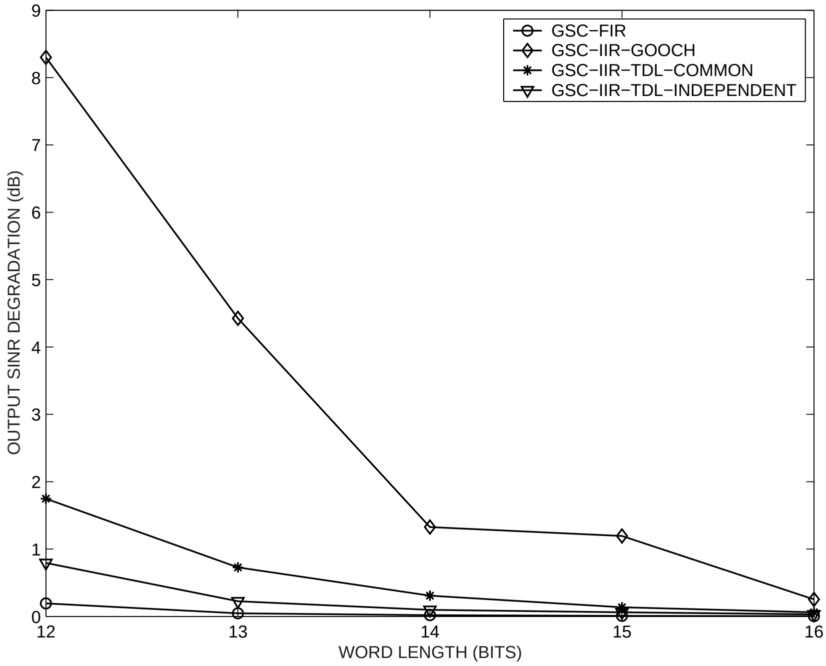

Figure 5.14. Output SINR degradations at $n = 3000$ under the finite word length in Scenario I.

From Figure 5.14, we find that all the IIR beamformers are more sensitive to the coefficient quantization than the FIR beamformer. The performance degradations of the proposed beamformers are much smaller than that of the GSC-IIR-GOOCH beamformer. That is to say, the proposed IIR beamformers are less sensitive to the coefficient quantization than the GSC-IIR-GOOCH beamformer. The beamformer using the parallel-form multichannel IIR filter in [19] is also less sensitive to the coefficient quantization than the beamformer using the direction-form IIR filter. That is a frequency-domain implementation as compared with the proposed time-domain one. From Figures 5.10 and 5.14, it can be seen that the GSC-IIR-TDL-INDEPENDENT beamformer has lower output SINR than the GSC-IIR-TDL-COMMON beamformer but it is less sensitive to the coefficient quantization error. The performance difference of these two beamformers depends much on the number of taps and the number of feedback coefficients, so we can not draw a general conclusion for any scenarios.

5.8 Conclusion

In this chapter, further investigations are performed for the broadband beamformer using TDL-form IIR filters. The combined RGN algorithm is designed for the Frost-based structure to compute the feedforward and feedback weights. Extension to the processor with second-order IIR sections is presented to allow complex poles for real signals. The unconstrained RGN algorithm is formulated for the GSC-based IIR beamformer. Analysis and simulation results are presented to demonstrate the advantages of the beamformers using TDL-form IIR filters: 1) The steady-state SINR performance is comparable to the GSC-IIR-GOOCH beamformer and much better than the GSC-FIR beamformer. 2) The stability can be monitored easily by checking the coefficients of the tap-to-tap IIR sections. 3) They are less sensitive to the coefficient quantization error than the GSC-IIR-GOOCH beamformer. The drawbacks of the IIR beamformer relative to the FIR beamformer have been presented in Section 4.6. Besides, in the proposed structure, the number of the feedback coefficients is implicitly restricted by the number of the feedforward coefficients. This may influence the modelling capability of the proposed IIR beamformer. Contrarily, the existing IIR beamformer has no such limitations.

Chapter 6

Spatial Resolutions of the Broadband MRA and NRA

6.1 Introduction

Just like in the narrowband array design, determining the spatial resolution of the broadband array is important for system design and performance evaluation.

The issue of spatial resolution for the narrowband array is addressed in literatures [98,100, 115–117]. Walach in [115] presents the formulation for the beamwidth of the narrowband adaptive array with the GSC configuration. In [118], the result of [115] is extended to the broadband array. The studies in both [115] and [118] are focused on the ULA.

The MRA and NRA are nonuniform linear arrays with the sensor placement configured by certain criteria to achieve the maximum resolution for a given number of elements. The configuration of MRA is developed by minimizing the number of redundant spacings while that of NRA is designed by minimizing the number of missing lags under the constraint of no redundancies. The references in [98, 100] can be referred to for the searching algorithms. The applications of MRA and NRA in narrowband systems have been investigated in some literatures. However, there is rare study for using MRA and NRA in broadband beamformers. In some broadband applications, like microphone arrays, great attention is paid on the resource and resolution problems. Therefore, the performance of using MRA and NRA in broadband beamformers is worth studying.

In [118], due to the existence of the blocking matrix, the computation and the resulting expression for the optimum response are complicated. They would get more intricate if the array geometry is not uniform and the look direction is not at broadside. Therefore, the generalization of [118] from ULA to arrays with more general geometries would not be easy if using the GSC model as in [118]. The GSC beamformer [8] is an alternative implementation of the LCMV beamformer but they take on different complexities for various problems. Our study shows that the LCMV structure is a favorable model for solving the problem addressed in this chapter.

In this chapter, by formulating the optimization problem in the frequency domain, the formulations for the optimum frequency responses of the temporal filters in the broadband LCMV beamformer are acquired. After obtaining the expression of the array output power and finding the half-power point, approximate formulations for the 3-dB beamwidth are achieved to measure the spatial resolution of the beamformer. With these formulations, the beamwidths of NRA and MRA are compared with that of ULA. Moreover, the accuracy of the derived formulations is assessed by numerical studies. These formulations can avoid the onerous procedure for finding the half-power point each time when the array performance need to be evaluated. The influences of various parameters on the array resolution can be easily observed by the formulations.

This chapter is organized as follows: In Section 6.2, the assumptions about the signal and array models are presented. In Section 6.3, the formulations for the beamwidth of the broadband NRA and MRA are derived in detail. In Section 6.4, the beamwidths of NRA and MRA are compared with that of ULA. The accuracy of the derived formulations is assessed.

6.2 Assumptions

The signal model is assumed to have the following features: 1) The source signal received by the array is a broadband stationary random process with power p_S and flat power spectral density $S_S(f), f \in F_S = [-f_c - B_S/2, -f_c + B_S/2] \cup [f_c - B_S/2, f_c + B_S/2]$. 2) The noise is spatially uncorrelated with power p_N and flat power spectral density $S_N(f), f \in F_N = [-f_c - B_N/2, -f_c + B_N/2] \cup [f_c - B_N/2, f_c + B_N/2]$. The spectrum of the noise is assumed to be wider than that of the source signal to reflect the situation in most real applications.

The array structure model is described as follows: 1) A linear array consists of L omnidirectional sensors located at $r_n d$, where r_n is a positive integer for $n = 1, 2, \cdots, L$ and d is a unit spacing chosen to avoid aliasing. 2) The ideal continuous-time, infinite-length filter is assumed in each channel, with the frequency response $H_n(f), n \in [1, L]$ obtained by the LCMV optimization criterion. 3) The look direction of the beamformer is assumed to be accurately steered to θ_0 by presteering delays $T_n, n \in [1, L]$. The array structure is shown in Figure 6.1.

The array output $y(t)$ is the filtered summation of the input $x_i(t)$:

$$y(t) = \sum_{i=1}^{L} h_i(t) \circledast x_i(t) \tag{6.1}$$

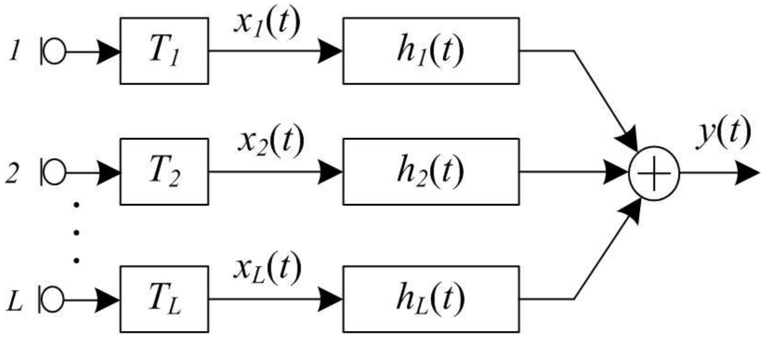

Figure 6.1. Broadband array structure.

where $\circledast$ represents linear convolution and $h_i(t)$ denotes the filter impulse response. The power spectral density of the array output can be computed by:

$$S_y(f) = \boldsymbol{H}^H(f)\boldsymbol{S}_{\boldsymbol{x}}(f)\boldsymbol{H}(f) \tag{6.2}$$

where the superscript H represents conjugate transpose and

$$\boldsymbol{H}(f) = [H_1(f) \;\; H_2(f) \;\; \cdots \;\; H_L(f)]^T \tag{6.3}$$

The frequency response $H_i(f)$ is the Fourier transform of $h_i(t)$. $\boldsymbol{S}_{\boldsymbol{x}}(f)$ is an $L \times L$ matrix composed of the cross power spectra of the signals on all sensors. It can be computed by:

$$\boldsymbol{S}_{\boldsymbol{x}}(f) = S_{_S}(f)\boldsymbol{\Lambda}(f)\boldsymbol{a}(f,\theta)\boldsymbol{a}^H(f,\theta)\boldsymbol{\Lambda}^H(f) + S_{_N}(f)\boldsymbol{I} \tag{6.4}$$

where $\boldsymbol{I}$ represents the $L \times L$ identity matrix and $\boldsymbol{\Lambda}(f)$ is an $L \times L$ diagonal matrix:

$$\boldsymbol{\Lambda}(f) = \text{diag}\Big\{[e^{-j2\pi f T_1} \;\; e^{-j2\pi f T_2} \;\; \cdots \;\; e^{-j2\pi f T_L}]\Big\} \tag{6.5}$$

$\boldsymbol{a}(f,\theta)$ is the source steering vector:

$$\boldsymbol{a}(f,\theta) = [e^{j2\pi f \tau_1(\theta)} \;\; e^{j2\pi f \tau_2(\theta)} \;\; \cdots \;\; e^{j2\pi f \tau_L(\theta)}]^T \tag{6.6}$$

where $\tau_n(\theta) = r_n d \sin\theta / c$ is the propagation delay of the plane wave to the nth sensor under propagation velocity c. θ is the signal direction relative to the broadside direction of the linear array.

6.3 Derivation of the Formulations

By the LCMV optimization criterion, the mean output power of the beamformer is minimized subject to certain linear constraints. The unit gain constraint is usually used to keep the desired signal undistorted. For the stationary random process, the mean power is equivalent to its mean-square value which can be computed by the power spectral density by:

$$E[|y(t)|^2] = \int_{f \in F_N} S_y(f) df \tag{6.7}$$

The constraint for the look-direction response is expressed by $\mathbf{1}^T \boldsymbol{H}(f) = 1$. $\mathbf{1}$ is an $L \times 1$ all-one vector. Accordingly, the LCMV optimization can be formulated by:

$$\begin{gathered} \min_{\boldsymbol{H}(f), f \in F_N} \int_{f \in F_N} S_y(f) df \\ \text{subject to } \mathbf{1}^T \boldsymbol{H}(f) = 1 \end{gathered} \tag{6.8}$$

Since the power spectral density $S_y(f)$ is always nonnegative, minimizing $S_y(f)$ for each $f \in F_N$ can ensure that $\int_{f \in F_N} S_y(f) df$ is minimized. Therefore, we reformulate the optimization in the frequency domain as follows:

$$\begin{gathered} \min_{\boldsymbol{H}(f), f \in F_N} S_y(f) \\ \text{subject to } \mathbf{1}^T \boldsymbol{H}(f) = 1 \end{gathered} \tag{6.9}$$

Solving (6.9) we get the optimum frequency response vector:

$$\boldsymbol{H}(f) = \frac{\boldsymbol{S}_{\boldsymbol{x}}^{-1}(f)\mathbf{1}}{\mathbf{1}^T\boldsymbol{S}_{\boldsymbol{x}}^{-1}(f)\mathbf{1}}, \quad \forall f \in F_{_N} \tag{6.10}$$

Substituting (6.10) into (6.2), the optimum output power spectrum is then given by:

$$S_y(f) = \frac{1}{\mathbf{1}^T\boldsymbol{S}_{\boldsymbol{x}}^{-1}(f)\mathbf{1}}, \quad \forall f \in F_{_N} \tag{6.11}$$

Defining $\boldsymbol{b}(f,\theta) = \boldsymbol{\Lambda}(f)\boldsymbol{a}(f,\theta)$, $\boldsymbol{S}_{\boldsymbol{x}}(f)$ in (6.4) can be re-expressed as:

$$\boldsymbol{S}_{\boldsymbol{x}}(f) = S_{_S}(f)\boldsymbol{b}(f,\theta)\boldsymbol{b}^H(f,\theta) + S_{_N}(f)\boldsymbol{I} \tag{6.12}$$

Under accurate presteering delays, $T_n = \tau_n(\theta_0)$ and the nth element of $\boldsymbol{b}(f,\theta)$ is $e^{j2\pi f r_n d(\sin\theta - \sin\theta_0)/c}$. By the matrix inversion lemma, the inverse of $\boldsymbol{S}_{\boldsymbol{x}}(f)$ can be computed by:

$$\boldsymbol{S}_{\boldsymbol{x}}^{-1}(f) = S_{_N}^{-1}(f)\Big[\boldsymbol{I} - \frac{\boldsymbol{b}(f,\theta)\boldsymbol{b}^H(f,\theta)S_{_S}(f)}{LS_{_S}(f) + S_{_N}(f)}\Big] \tag{6.13}$$

By (6.7) (6.11) and (6.13), the optimum output power can be derived as the following integral:

$$E[|y(t)|^2] = \int_{f\in F_N} \frac{S_{_N}^2(f) + LS_{_S}(f)S_{_N}(f)}{LS_{_N}(f) + [L^2 - |g(f,\theta)|^2]S_{_S}(f)} df \tag{6.14}$$

where

$$|g(f,\theta)|^2 = |\mathbf{1}^T\boldsymbol{b}(f,\theta)|^2 = L + 2\sum_{n=1}^{M-1} u_n \cos[n(\omega - \omega_0)] \tag{6.15}$$

where $\omega = 2\pi f d \sin\theta/c$ and $\omega_0 = 2\pi f d\sin\theta_0/c$. u_n is the multiplicity of the nonzero correlation lag n. $(M-1)$ is the maximum spatial correlation lag.

As in reference [118], we assume that the signal comes from a direction close to the look direction and make the following approximation:

$$\cos[n(\omega-\omega_0)] = 1-2\sin^2[n(\omega-\omega_0)/2] \approx 1-n^2(\omega-\omega_0)^2/2 \tag{6.16}$$

Substituting (6.16) into (6.15), we get:

$$|g(f,\theta)|^2 = L+2\sum_{n=1}^{M-1} u_n - (\omega-\omega_0)^2 \sum_{n=1}^{M-1} u_n n^2 \tag{6.17}$$

We note that $2\sum_{n=1}^{M-1} u_n$ is actually the total number of off-diagonal entries of $\boldsymbol{b}(f,\theta)\boldsymbol{b}^H(f,\theta)$ whatever the value of M, therefore, $2\sum_{n=1}^{M-1} u_n = L^2 - L$ can be obtained. Then (6.17) is re-expressed as:

$$|g(f,\theta)|^2 = L^2-(\omega-\omega_0)^2 \sum_{n=1}^{M-1} u_n n^2 \tag{6.18}$$

Thus, (6.14) can be simplified to be:

$$E[|y(t)|^2] = \int_{f\in F_N} \frac{S_N(f)/L+S_S(f)}{1+\alpha f^2} df \tag{6.19}$$

where

$$\alpha = [(2\pi d/c)(\sin\theta-\sin\theta_0)]^2 \Big[\sum_{n=1}^{M-1}(u_n n^2)/L\Big][S_S(f)/S_N(f)] \tag{6.20}$$

In real applications, $S_N(f)/L$ is far less than $S_S(f)$ and can be neglected in (6.19), so the integral region is approximated to be $f \in F_S$. Due to the assumption of flat power spectra, $S_S(f)$ and $S_N(f)$ are abbreviated to S_S and S_N and computed by $S_S = p_S/(2B_S)$ and $S_N = p_N/(2B_N)$. The integral in (6.19) can be computed analytically by:

$$\begin{aligned} E[|y(t)|^2] &= p_S/(B_S\sqrt{\alpha})\arctan[\sqrt{\alpha}(f_c+B_S/2)] \\ &\quad -p_S/(B_S\sqrt{\alpha})\arctan[\sqrt{\alpha}(f_c-B_S/2)] \end{aligned} \tag{6.21}$$

The maximum output power of the beamformer appears at the look direction and equals p_S (with the term p_N/L neglected). To find the half-power point, the equation $E[|y(t)|^2] = p_S/2$ needs to be solved. By the trigonometric formula for angle sum and $\tan(B_S\sqrt{\alpha}/2) \approx B_S\sqrt{\alpha}/2$ we can get:

$$\alpha(f_c^2 - B_S^2/4) \approx 1 \tag{6.22}$$

By substituting (6.20) into (6.22), the following expression is obtained:

$$|\sin\theta - \sin\theta_0| \approx K\frac{c}{2\pi d}\frac{\sqrt{p_N/p_S}\sqrt{B_S/B_N}}{\sqrt{f_c^2 - B_S^2/4}} \tag{6.23}$$

where K is a factor determined by the array geometry:

$$K = \sqrt{\frac{L}{\sum\limits_{n=1}^{M-1}(u_n n^2)}} \tag{6.24}$$

The solutions for (6.23) are the 3-dB angles denoted by θ_{3dB+} and θ_{3dB-}:

$$\begin{aligned} \theta_{3dB+} &= \arcsin(\sin\theta_0 + K\frac{c}{2\pi d}\frac{\sqrt{p_N/p_S}\sqrt{B_S/B_N}}{\sqrt{f_c^2-B_S^2/4}}) \\ \theta_{3dB-} &= \arcsin(\sin\theta_0 - K\frac{c}{2\pi d}\frac{\sqrt{p_N/p_S}\sqrt{B_S/B_N}}{\sqrt{f_c^2-B_S^2/4}}) \end{aligned} \tag{6.25}$$

With the definition for the half-power beamwidth in [119], the 3-dB beamwidth in radian is computed by:

$$\mathrm{BW} = \begin{cases} \theta_{3dB+} - \theta_{3dB-}, & 0^\circ \leq |\theta_0| \leq \theta_T \\ 2\arcsin(1 - K\frac{c}{2\pi d}\frac{\sqrt{p_N/p_S}\sqrt{B_S/B_N}}{\sqrt{f_c^2-B_S^2/4}}), & |\theta_0| = 90^\circ \end{cases} \tag{6.26}$$

where θ_T is the scan limit equivalent to $\arcsin(1 - K\frac{c}{2\pi d}\frac{\sqrt{p_N/p_S}\sqrt{B_S/B_N}}{\sqrt{f_c^2-B_S^2/4}})$. For $\theta_T < \theta_0 < 90^\circ$, there is only one half-power point for the beam. The beamwidth is not defined in this region.

Using Taylor series expansion for $\sin\theta$ in (6.23), $\theta_{3dB\pm}$ can be solved and BW is derived in another form:

$$\mathrm{BW} \approx \begin{cases} K\dfrac{c}{\pi d\cos\theta_0}\dfrac{\sqrt{p_N/p_S}\sqrt{B_S/B_N}}{\sqrt{f_c^2-B_S^2/4}}, & 0^\circ \le |\theta_0| \le \theta_T \\ 2\sqrt{K\dfrac{c}{\pi d}\dfrac{\sqrt{p_N/p_S}\sqrt{B_S/B_N}}{\sqrt{f_c^2-B_S^2/4}}}, & |\theta_0| = 90^\circ \end{cases} \tag{6.27}$$

From formulations (6.24)-(6.27), we can observe that the spatial resolution of the broadband adaptive beamformer is related with the array geometry, the signal and noise frequency band and the input SNR.

The approximations made during the above derivation cause errors. The accuracy of the formulations will be assessed in Section 6.4.

According to (6.24)-(6.27), the value of K should be determined before computing the beamwidth.

Three-element and four-element MRA and NRA have the same sensor placement. The correlation lags are $\{0,1,2\}$ for $L = 3$ and $\{0,1,2,3,4,5,6\}$ for $L = 4$, without duplications for nonzero lags and without missing lags. Therefore, we get $u_n = 1$ and $M-1 = L(L-1)/2$. Hence,

$$K_{NRA} = K_{MRA} = \sqrt{\frac{24}{(L-1)(L^2-L+1)(L^2-L+2)}} \tag{6.28}$$

For NRA and MRA with $L > 4$, the geometry can not be easily expressed in a general form, but $\sum\limits_{n=1}^{M-1}(u_n n^2)$ can be written as a function of sensor positions for the convenience of computation:

$$\sum_{n=1}^{M-1}(u_n n^2) = \sum_{m=1}^{L-1}\sum_{n=m+1}^{L}(r_m - r_n)^2 \tag{6.29}$$

Then K_{NRA}, K_{MRA} and hence the beamwidth can be computed easily.

Table 6.1: VALUES OF K FOR ULA, MRA and NRA

L	K_{ULA}	INTER-SENSOR SPACING OF MRA (d)	K_{MRA}	INTER-SENSOR SPACING OF NRA (d)	K_{NRA}
3	0.7071	$\cdot 1 \cdot 2 \cdot$	0.4629	$\cdot 1 \cdot 2 \cdot$	0.4629
4	0.4472	$\cdot 1 \cdot 3 \cdot 2 \cdot$	0.2097	$\cdot 1 \cdot 3 \cdot 2 \cdot$	0.2097
5	0.3162	$\cdot 1 \cdot 3 \cdot 3 \cdot 2 \cdot$	0.1304	$\cdot 1 \cdot 3 \cdot 5 \cdot 2 \cdot$	0.1031
6	0.2390	$\cdot 1 \cdot 5 \cdot 3 \cdot 2 \cdot 2 \cdot$	0.0841	$\cdot 1 \cdot 3 \cdot 6 \cdot 2 \cdot 5 \cdot$	0.0663
7	0.1890	$\cdot 1 \cdot 3 \cdot 6 \cdot 2 \cdot 3 \cdot 2 \cdot$	0.0600	$\cdot 1 \cdot 3 \cdot 6 \cdot 8 \cdot 5 \cdot 2 \cdot$	0.0390
8	0.1543	$\cdot 1 \cdot 3 \cdot 6 \cdot 6 \cdot 2 \cdot 3 \cdot 2 \cdot$	0.0413	$\cdot 1 \cdot 3 \cdot 5 \cdot 6 \cdot 7 \cdot 10 \cdot 2 \cdot$	0.0280
9	0.1291	$\cdot 1 \cdot 3 \cdot 6 \cdot 6 \cdot 6 \cdot 2 \cdot 3 \cdot 2 \cdot$	0.0310	$\cdot 1 \cdot 4 \cdot 7 \cdot 13 \cdot 2 \cdot 8 \cdot 6 \cdot 3 \cdot$	0.0206
10	0.1101	$\cdot 1 \cdot 2 \cdot 3 \cdot 7 \cdot 7 \cdot 7 \cdot 4 \cdot 4 \cdot 1 \cdot$	0.0231	$\cdot 1 \cdot 5 \cdot 4 \cdot 13 \cdot 3 \cdot 8 \cdot 7 \cdot 12 \cdot 2 \cdot$	0.0162

6.4 Numerical Studies

According to the assumptions in Section 6.2, we know that (6.24)-(6.27) are applicable to linear arrays with either uniform or nonuniform geometries. The difference of the spatial resolutions between NRA, MRA and ULA is caused by the different values of K. For an L-element ULA, the maximum correlation lag is equal to $L-1$. The correlation matrix for the ULA is Toeplitz. Therefore, u_n equals the number of entries on the nth diagonal of the $L \times L$ matrix. That is to say, $u_n = L - n$ and $M = L$, so we get:

$$K_{ULA} = \sqrt{\frac{L}{\sum_{n=1}^{L-1}[(L-n)n^2]}} = \sqrt{\frac{12}{L(L^2-1)}} \tag{6.30}$$

By substituting (6.30) into (6.27), the beamwidth for ULA can be computed. Obviously, if the look direction is at the broadside, the result obtained for ULA is consistent with that presented in [118].

The values of K are listed in TABLE 6.1 for $L \in [3, 10]$ for ULA, MRA and NRA. Two sets of geometries for MRA and NRA are selected from [100]. Figure 6.2 shows the beamwidths computed by formulation (6.27), with F_S chosen to be $[-0.4, -0.2] \cup [0.2, 0.4]$, $F_N = [-0.5, 0.5]$ and SNR $= 20$dB. The scenarios with the look direction

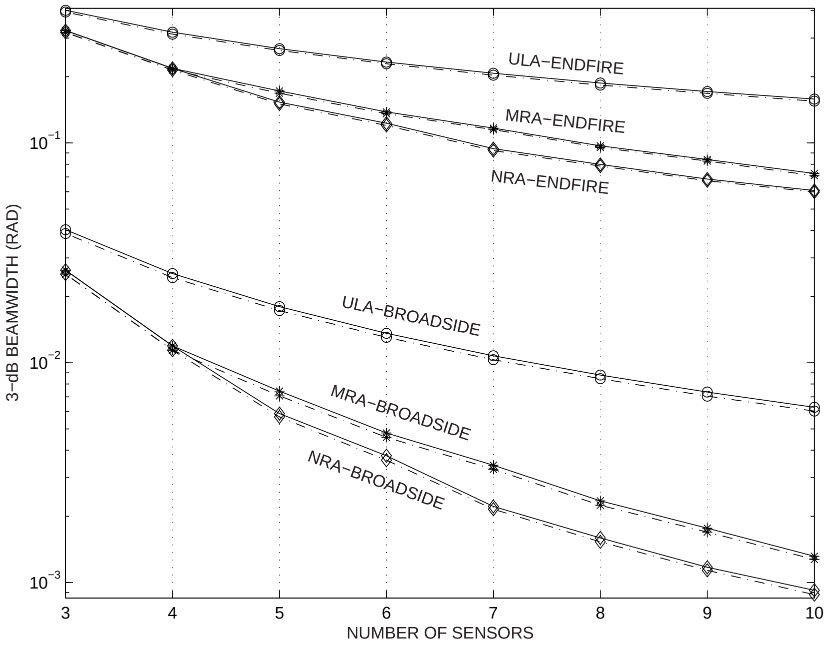

Figure 6.2. Beamwidths for the ULA, MRA and NRA. The solid lines are obtained by (6.27) while the dash-dot lines are obtained by finding the half-power point numerically.

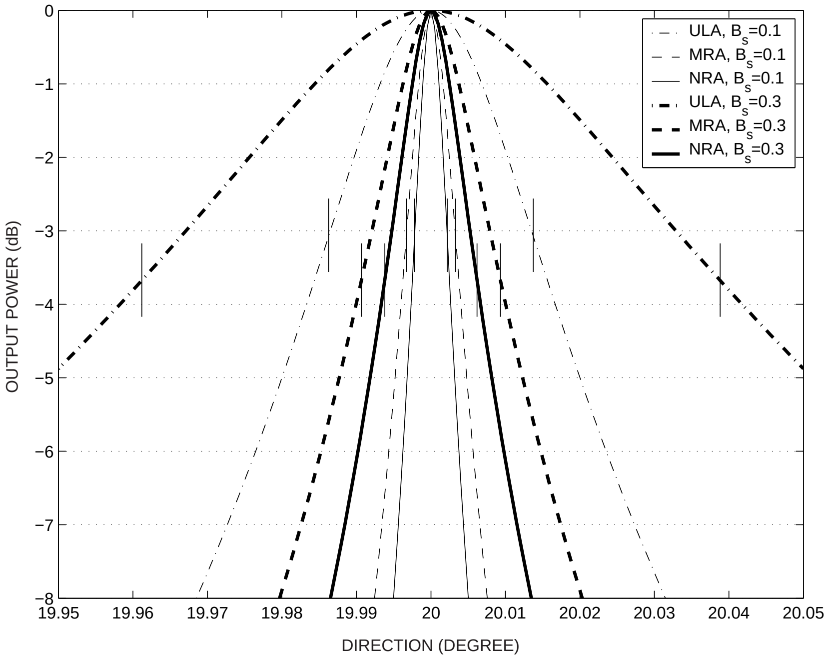

Figure 6.3. Output power for the nine-element ULA, MRA and NRA, with $\theta_0 = 20^\circ$. $\theta_{3dB\pm}$ computed by (6.25) are marked by vertical bars.

pointing to the broadside and endfire are demonstrated. The inter-element spacing is half the wavelength corresponding to the highest frequency. To assess the accuracy of the formulations, the beamwidths obtained by finding the half-power point numerically by (6.14) are also demonstrated. Figure 6.3 presents curves of the output power for the nine-element ULA, MRA and NRA, obtained by (6.14), with SNR $= 40$dB and $\theta_0 = 20°$. $\theta_{3dB\pm}$ computed by formulation (6.25) are marked.

From TABLE 6.1 and Figures 6.2-6.3, we have the following observations: The value of K decreases as the number of sensors increases. MRA and NRA have smaller K and much better resolution than ULA because they cover larger spatial apertures for the given number of array elements. The beamwidths for both MRA, NRA and ULA decrease as the number of sensors increases, the bandwidth of the signal reduces, or the look direction approaches the broadside of the array. In most of the examples demonstrated, the results obtained by the derived formulations match the numerical results satisfactorily. Our studies show that the smaller the signal fractional bandwidth, the higher the accuracy of the formulations. By investigating various scenarios, it is found that the error of the formulations is normally less than 10% for both MRA, NRA and ULA if the fractional bandwidth of the signal is not larger than 80% and SNR > 0dB ($L \geq 3$).

6.5 Conclusion

Approximate formulations for the 3-dB beamwidths of the broadband NRA and MRA are obtained in this chapter. Numerical studies are used to verify the accuracy of these formulations. The comparisons of the beamwidths between NRA, MRA and ULA show the superiority of the former two types of geometries in improving the spatial resolution. Due to the assumption of the ideal temporal filters, the beamwidth computed by our formulations is the lower bound for the realistic beamformers using digital filters with the finite order and finite temporal sampling interval.

Chapter 7

Broadband Interference Suppression Performance of MRA

7.1 Introduction

Connecting the FIR filter after each array element is the most common way to design the broadband beamformer. In real implementations, the signal sampling rate, the length of the digital filter and the interference bandwidth have influences on the performance of the beamformer. References [14,17,18] investigate the nulling performance affected by these factors. The array geometry is assumed to be the ULA in these studies.

By increasing the inter-element spacing [116] or designing nonuniform linear array geometries [98,100], the array aperture is enlarged for a given number of elements to improve the array resolution. The sensor placement of the MRA [98] is designed by minimizing the redundancy of spatial correlation lags. For the restricted MRA, no missing lags are allowed. Since MRA has better resolution than ULA, using MRA in broadband beamformers and investigating their broadband interference suppression performance attract our interest.

The narrowband interference cancellation performance of MRA has been investigated in [120–122]. However, their results can not be applied to broadband arrays directly because there are significant distinctions between narrowband and broadband array models. In narrowband arrays, sources are represented by monochromatic signals while in broadband arrays, the power spectra of sources may extend over certain frequency bands. In addition, the weights used in the narrowband beamformers are single complex scalar for each array element. Differently, broadband beamformers usually employ temporal filters in each channel to compensate for the dependence on the frequency.

In this chapter, we study the interference suppression performance of the broadband LCMV beamformer using the MRA configuration. The ideal continuous-time, infinite-length filter instead of the realistic finite-order digital filter is assumed in the beamformer. The expressions for the power spectrum of the beamformer output in different scenarios are derived to compute the mean output power. The broadband interference suppression performance of MRA is compared with that of ULA for the one- and two-interference cases. Some original properties are revealed based on mathematical proofs and graphic illustrations. Similar to the narrowband case, MRA can achieve better interference cancellation performance than ULA at directions close to the broadside of the array. A property which is different from the narrowband scenario is that, in broadband beamformers, MRA can outperform ULA at more directions as the fractional bandwidth (FBW) of the interference increases.

This chapter is organized as follows: In Section 7.2, the broadband signal and array structure models are introduced briefly. In Section 7.3, the formulations for the optimum output power of the broadband LCMV beamformer in different scenarios are derived. In Sections 7.4 and 7.5, the interference suppression performance of MRA is compared with that of ULA based on mathematical proofs and graphic illustrations for the one- and two-interference cases.

7.2 Broadband Signal and Array Models

The signal model is described as follows:

1) All the sources are real-valued, band-limited signals.

2) The desired signal comes from the broadside of the array. The frequency ranges of the desired signal and the interferences are the same or have a significant superposition so we can not depend on the temporal filter to separate them.

3) There are K interferences incident on the array. All are broadband stationary random processes. The kth interference comes from θ_k and its power is $p_{_{Ik}}$, $k \in [1, K]$. Their power spectral densities $S_{_{Ik}}(f)$ are nonzero at $f \in F_{_{Ik}} = [-f_c - B_{_{Ik}}/2, -f_c + B_{_{Ik}}/2] \cup [f_c - B_{_{Ik}}/2, f_c + B_{_{Ik}}/2]$. f_c is the center frequency. The total bandwidth of the kth interference is $2B_{_{Ik}}$. $S_{_{Ik}}(f)$ can be abbreviated to $S_{_{Ik}}$ and computed by $S_{_{Ik}} = p_{_{Ik}}/(2B_{_{Ik}})$ if the spectrum is flat. All the interferences are uncorrelated with each other and the desired signal.

4) The noise is spatially uncorrelated with power $p_{_N}$. Its power spectral density $S_{_N}(f)$ is nonzero at $f \in F_{_N} = [-f_c - B_{_N}/2, -f_c + B_{_N}/2] \cup [f_c - B_{_N}/2, f_c + B_{_N}/2]$. The total bandwidth of the noise is $2B_{_N}$. The spectrum of the noise is assumed to be wider than that of any directional sources to reflect the situation in most real applications. $S_{_N}(f)$ can be abbreviated to $S_{_N}$ and computed by $S_{_N} = p_{_N}/(2B_{_N})$ if the spectrum of noise is flat.

The array structure model is assumed to be as follows:

1) The sensor array is in the far field of the radiation sources.
2) L omnidirectional sensors are placed on a line and spaced by integer multiples of a unit spacing d. d is chosen to be half the wavelength corresponding to the highest frequency. The locations of elements are denoted by $r_n d$, $n \in [1, L]$.
3) The ideal continuous-time, infinite-length filter is assumed in each channel, with the frequency response $H_n(f), n \in [1, L]$ obtained by the LCMV optimization criterion.
4) The look direction of the array is at the broadside direction.

The beamforming structure discussed in this chapter is identical to Figure 6.1 except that the presteering delays should be removed due to the above assumption about the look direction. The expressions for the array output $y(t)$, the power spectral density $S_y(f)$ of the beamformer output, the frequency response vector $\boldsymbol{H}(f)$ of the temporal filters and the source steering vector $\boldsymbol{a}(f, \theta)$ given by (6.1), (6.2), (6.10) and (6.6) in Chapter 6 are retained in this chapter. However, the cross spectrum matrix $\boldsymbol{S_x}(f)$ used for calculating $S_y(f)$ should not be computed by (6.4) any more due to the assumptions about the signal models and the look direction. Detailed expressions for $\boldsymbol{S_x}(f)$ under different scenarios will be described in subsequent sections.

7.3 Formulations for the Optimum Output Power

According to the LCMV optimization criterion, the mean output power is minimized subject to certain linear constraints. Under the unit gain constraint which keeps the desired signal undistorted, the power of the desired signal is not changed. As a result, the SINR improvement of the beamformer is equal to the ratio of the input and output interference plus noise power. Because the desired signal is assumed to be uncorrelated with the interferences, it is feasible to remove the desired signal from the assumed input data to facilitate analysis. Consequently, the interference and noise suppression gain can be computed by the ratio of the input power p_{in} and output power p_{out} of the beamformer:

$$G = \frac{p_{in}}{p_{out}} = \frac{\sum_{k=1}^{K} p_{Ik} + p_{_N}}{p_y} \tag{7.1}$$

where $p_{_{Ik}}$ and $p_{_N}$ are the power of the kth incident interference and the input noise which have been defined in Section 7.2. p_y is the power of the beamformer output $y(t)$.

For the stationary random process, the mean power can be computed by the power spectral density by:

$$p_y = \mathrm{E}[y^2(t)] = \int_{F_{_N}} S_y(f)df \tag{7.2}$$

The region for the integral is $F_{_N}$ because we assume that the noise spectrum is wider than the spectra of any other sources.

The formulations for the optimum frequency response vector $\boldsymbol{H}(f)$ for the ideal temporal filters of the LCMV beamformer and the optimum output power spectrum $S_y(f)$ have been derived in Chapter 6. They are listed again as follows for the convenience of narration:

$$\boldsymbol{H}(f) = \frac{\boldsymbol{S}_{\boldsymbol{x}}^{-1}(f)\mathbf{1}}{\mathbf{1}^T\boldsymbol{S}_{\boldsymbol{x}}^{-1}(f)\mathbf{1}}, \quad \forall f \in F_{_N} \tag{7.3}$$

$$S_y(f) = \frac{1}{\mathbf{1}^T\boldsymbol{S}_{\boldsymbol{x}}^{-1}(f)\mathbf{1}}, \quad \forall f \in F_{_N} \tag{7.4}$$

Substituting (7.4) into (7.2), we obtain the output power of the beamformer under the optimum filter responses. Both the total output power p_y defined in (7.2) and the interference and noise suppression gain G defined in (7.1) can be utilized to compare the interference and noise suppression performance of MRA with that of ULA. The interference suppression performance can thereby be inferred since the power of interferences is generally much higher that of the noise.

7.3.1 One-Interference Case

For the one-interference case, the cross spectrum matrix $\boldsymbol{S_x}(f)$ can be expressed by:

$$\boldsymbol{S_x}(f) = S_{_{I1}}(f)\boldsymbol{a}(f,\theta_1)\boldsymbol{a}^H(f,\theta_1) + S_{_N}(f)\boldsymbol{I} \tag{7.5}$$

where $\boldsymbol{I}$ represents the $L \times L$ identity matrix. By the matrix inversion lemma [123], the inverse of the cross spectrum matrix is computed by:

$$\boldsymbol{S_x}^{-1}(f) = S_{_N}^{-1}(f)[\boldsymbol{I} - \kappa(f)\boldsymbol{a}(f,\theta_1)\boldsymbol{a}^H(f,\theta_1)] \tag{7.6}$$

where

$$\kappa(f) = \frac{S_{_{I1}}(f)}{S_{_N}(f) + LS_{_{I1}}(f)} \tag{7.7}$$

Using equations (7.2), (7.4) and (7.6), the output power of the beamformer is derived as:

$$p_y = \int_{F_N} \frac{S_{_N}^2(f) + LS_{_{I1}}(f)S_{_N}(f)}{LS_{_N}(f) + g(f,\theta_1)S_{_{I1}}(f)} df \tag{7.8}$$

where

$$g(f,\theta_1) = L^2 - |\mathbf{1}^T\boldsymbol{a}(f,\theta_1)|^2 \tag{7.9}$$

It can be proven that (7.8) is consistent with but much simpler in the form than the formulation derived in [118] for the GSC with the ULA configuration. This is in line with the fact that the GSC is an alternative implementation of the LCMV beamformer.

7.3.2 Two-Interference Case

For the two-interference case, the cross spectrum matrix $\boldsymbol{S_x}(f)$ can be written as:

$$\boldsymbol{S_x}(f) = \sum_{k=1}^{2} S_{Ik}(f)\boldsymbol{a}(f,\theta_k)\boldsymbol{a}^H(f,\theta_k) + S_N(f)\boldsymbol{I} \tag{7.10}$$

Using the matrix inversion lemma twice, the inverse of the cross spectrum matrix can be shown to be:

$$\begin{aligned}\boldsymbol{S_x}^{-1}(f) = S_N^{-1}(f)\{&\boldsymbol{I} - \kappa_1(f)\boldsymbol{a}(f,\theta_1)\boldsymbol{a}^H(f,\theta_1) - \kappa_2(f)\boldsymbol{a}(f,\theta_2)\boldsymbol{a}^H(f,\theta_2) + \\ &\kappa_{12}(f)\mathrm{Re}[\boldsymbol{a}(f,\theta_1)\boldsymbol{a}^H(f,\theta_1)\boldsymbol{a}(f,\theta_2)\boldsymbol{a}^H(f,\theta_2)]\}\end{aligned} \tag{7.11}$$

where

$$\begin{aligned}\kappa_1(f) &= \frac{LS_{I1}(f)S_{I2}(f) + S_N(f)S_{I1}(f)}{\chi(f)} \\ \kappa_2(f) &= \frac{LS_{I1}(f)S_{I2}(f) + S_N(f)S_{I2}(f)}{\chi(f)} \\ \kappa_{12}(f) &= \frac{2S_{I1}(f)S_{I2}(f)}{\chi(f)} \\ \chi(f) &= [S_N(f) + LS_{I1}(f)][S_N(f) + LS_{I2}(f)] - \\ &\quad S_{I1}(f)S_{I2}(f)|\boldsymbol{a}^H(f,\theta_1)\boldsymbol{a}(f,\theta_2)|^2\end{aligned} \tag{7.12}$$

Then the optimum output power of the beamformer can be derived as:

$$p_y = \int_{F_N} \frac{S_N^3(f) + LS_{I1}(f)S_N^2(f) + LS_{I2}(f)S_N^2(f) + \rho_n S_{I1}(f)S_{I2}(f)S_N(f)}{LS_N^2(f) + g_1 S_{I1}(f)S_N(f) + g_2 S_{I2}(f)S_N(f) + \rho_d S_{I1}(f)S_{I2}(f)} df \tag{7.13}$$

where g_1, g_2, ρ_n and ρ_d, for notational simplicity, are abbreviations of $g(f,\theta_1)$, $g(f,\theta_2)$, $\rho_n(f,\theta_1,\theta_2)$ and $\rho_d(f,\theta_1,\theta_2)$, respectively. They are calculated by the following expressions:

$$\begin{aligned} g_1 &= L^2 - |\mathbf{1}^T\boldsymbol{a}(f,\theta_1)|^2 \\ g_2 &= L^2 - |\mathbf{1}^T\boldsymbol{a}(f,\theta_2)|^2 \\ \rho_n &= L^2 - |\boldsymbol{a}^H(f,\theta_1)\boldsymbol{a}(f,\theta_2)|^2 \\ \rho_d &= L[g_1+g_2+\rho_n-2L^2]+2\mathrm{Re}[\mathbf{1}^T\boldsymbol{a}(f,\theta_1) \\ &\quad \boldsymbol{a}^H(f,\theta_1)\boldsymbol{a}(f,\theta_2)\boldsymbol{a}^H(f,\theta_2)\mathbf{1}] \end{aligned} \tag{7.14}$$

If $p_{_{I1}} = 0$ or $p_{_{I2}} = 0$ or $\theta_1 = \theta_2$, (7.13) reduces to the form of (7.8) for the one-interference case.

The expressions for the output power of the one- and two-interference cases derived in [122] for the narrowband array can be rewritten as:

$$p_y = \frac{p_{_N}^2 + Lp_{_{I1}}p_{_N}}{Lp_{_N} + g(f,\theta_1)p_{_{I1}}} \tag{7.15}$$

$$p_y = \frac{p_{_N}^3 + Lp_{_{I1}}p_{_N}^2 + Lp_{_{I2}}p_{_N}^2 + \rho_n p_{_{I1}}p_{_{I2}}p_{_N}}{Lp_{_N}^2 + g_1p_{_{I1}}p_{_N} + g_2p_{_{I2}}p_{_N} + \rho_d p_{_{I1}}p_{_{I2}}} \tag{7.16}$$

It can be seen that (7.8), (7.13) and (7.15), (7.16) are similar except for the additional manipulation of integral in (7.8) and (7.13). This agrees with the fact that the object studied by [122] is the narrowband interference with single frequency component while that studied in this chapter is the broadband interference with a group of frequency components. Therefore, our work can be considered as an extension of the study in [122].

Note that the formulations for the output power of the LCMV beamformer derived in this section are applicable to signals and noise with arbitrary color spectra.

7.4 Performance Analysis for the One-Interference Case

The FBW of a signal is defined as the ratio of the bandwidth to the center frequency, $B_f = B/f_c$, or computed by $B_f = 2(f_h - f_l)/(f_h + f_l)$, where f_h and f_l are the highest and lowest frequencies of the signal, respectively. FBW approaches 2 if $f_h \gg f_l$ and approaches 0 if the bandwidth of the signal is very small. Our analysis will show that the broadband interference suppression performance of the LCMV beamformer is always dependent on the value of FBW.

For the one-interference case, B_{I1}, $S_{I1}(f)$, p_{I1} and θ_1 are abbreviated to B_I, $S_I(f)$, p_I and θ, respectively in this section.

7.4.1 Three-Element Array

For ULA with three elements, $g(f,\theta)$ in (7.9) can be expressed by:

$$g_U(f,\theta) = 4[1 - u(f,\theta)][2 + u(f,\theta)] \tag{7.17}$$

where $u(f,\theta) = \cos(2\pi f d \sin\theta / c) = \cos(\pi \sin\theta f / f_u)$.

For MRA with three elements, the sensors are located at $\{0, 1d, 3d\}$, so $g(f,\theta)$ can be written as:

$$g_M(f,\theta) = 4[1 - u(f,\theta)][2u^2(f,\theta) + 3u(f,\theta) + 2] \tag{7.18}$$

The output power for ULA and MRA are respectively given by:

$$p_{yU} = \int_{F_N} \frac{S_N^2(f) + 3S_I(f)S_N(f)}{3S_N(f) + g_U(f,\theta)S_I(f)} df \tag{7.19}$$

$$p_{y_M} = \int_{F_N} \frac{S_N^2(f) + 3S_I(f)S_N(f)}{3S_N(f) + g_M(f,\theta)S_I(f)} df \tag{7.20}$$

Assuming flat spectra for the interference and noise, substituting (7.17) and (7.18) into (7.19) and (7.20), we get:

$$p_{y_U} = 2\int_{f_l}^{f_u} \frac{-b_1}{u^2(f,\theta) + u(f,\theta) - b_2} df + p_e \tag{7.21}$$

$$p_{y_M} = 2\int_{f_l}^{f_u} \frac{-b_1}{2u^3(f,\theta) + u^2(f,\theta) - u(f,\theta) - b_2} df + p_e \tag{7.22}$$

where $f_l = f_c - B_I/2$, $f_u = f_c + B_I/2$, $b_1 = (S_N^2 + 3S_IS_N)/(4S_I)$, $b_2 = 2 + 3S_N/(4S_I)$ and $p_e = (2B_N - 2B_I)S_N/3$. Let α_1 and α_2 denote the roots of the quadratic polynomial, the denominator of (7.21), with $\alpha_1 = (-1 + \sqrt{9 + 3S_N/S_I})/2 > 1$ and $\alpha_2 = (-1 - \sqrt{9 + 3S_N/S_I})/2 < -1$. Also, let β_1, β_2 and β_3 represent the roots of the cubic polynomial, the denominator of (7.22). According to the formulations calculating roots of cubic polynomials [124], we know that one of them is a positive real number and the other two are complex conjugate pair. In fact it can be shown that $\beta_1 > 1$, Re$(\beta_2) < 0$ and Re$(\beta_3) < 0$. The analytical expressions for the integrals of (7.21) and (7.22) are given by:

$$p_{y_U} = 2\sum_{k=1}^{2} c_k \arctan\left[\sqrt{\frac{\alpha_k + 1}{\alpha_k - 1}} \tan(\frac{af_u}{2})\right] - 2\sum_{k=1}^{2} c_k \arctan\left[\sqrt{\frac{\alpha_k + 1}{\alpha_k - 1}} \tan(\frac{af_l}{2})\right] + p_e \tag{7.23}$$

$$p_{y_M} = 2\sum_{k=1}^{3} d_k \arctan\left[\sqrt{\frac{\beta_k + 1}{\beta_k - 1}} \tan(\frac{af_u}{2})\right] - 2\sum_{k=1}^{3} d_k \arctan\left[\sqrt{\frac{\beta_k + 1}{\beta_k - 1}} \tan(\frac{af_l}{2})\right] + p_e \tag{7.24}$$

where

$$a = \frac{\pi}{f_u} \sin\theta \tag{7.25}$$

$$
\begin{aligned}
c_1 &= \frac{2b_1}{a(\alpha_1-\alpha_2)\sqrt{\alpha_1^2-1}} \\
c_2 &= \frac{-2b_1}{a(\alpha_2-\alpha_1)\sqrt{\alpha_2^2-1}}
\end{aligned}
\tag{7.26}
$$

$$
\begin{aligned}
d_1 &= \frac{b_1}{a(\beta_1-\beta_2)(\beta_1-\beta_3)\sqrt{\beta_1^2-1}} \\
d_2 &= \frac{-b_1}{a(\beta_2-\beta_1)(\beta_2-\beta_3)\sqrt{\beta_2^2-1}} \\
d_3 &= \frac{-b_1}{a(\beta_3-\beta_1)(\beta_3-\beta_2)\sqrt{\beta_3^2-1}}
\end{aligned}
\tag{7.27}
$$

By comparing (7.19), (7.21) with (7.20), (7.22), two important properties are obtained for the one-interference case.

Property 1: In three-element arrays, MRA achieves better broadband interference suppression performance than ULA if the interference comes from directions $\{\theta |\ |\theta| < \theta_t, \theta \neq 0^\circ\}$, where θ_t represents a critical value for the angle. θ_t is not smaller than 30°. The higher the FBW of the interference, the larger the value of θ_t.

Proof: According to (7.19) and (7.20), the array output power at angles $[-90^\circ, 0^\circ]$ and $[0^\circ, 90^\circ]$ are symmetric about the broadside. Therefore, by analyzing the performance in the region $[0^\circ, 90^\circ]$, we can get the knowledge about the whole field of view. Furthermore, at the broadside direction 0°, MRA and ULA always have the same output power $p_{_I} + p_{_N}/3$.

Firstly, we assume $B_f = 0$ and the unique frequency component of the interference is $f = f_u$, so $u(f_u, \theta) = \cos(\pi \sin\theta)$. The expression of the output power reduces to the form of narrowband arrays as shown by (7.15). By (7.15), (7.17) and (7.18), the difference of the output powers for ULA and MRA is derived as:

$$\begin{aligned}\Delta &= p_{y_U} - p_{y_M} \\ &= \frac{8p_I p_N (p_N + 3p_I) u(f_u,\theta)[1-u^2(f_u,\theta)]}{[3p_N + p_I g_U(f_u,\theta)][3p_N + p_I g_M(f_u,\theta)]}\end{aligned} \tag{7.28}$$

At $0°$ and $90°$, $|u(f_u,\theta)| = 1$ hence $\Delta = 0$. In the region $\theta \in (0°, 90°)$, since $u^2(f_u,\theta) < 1$, $g_U(f_u,\theta) > 0$ and $g_M(f_u,\theta) > 0$, by (7.28), we have $\Delta \gtreqless 0 \Leftrightarrow u(f_u,\theta) \gtreqless 0 \Leftrightarrow \theta \lesseqgtr 30°$. This implies that MRA achieves better interference suppression performance than ULA in the region $\theta \in (0°, 30°)$ while ULA performs better than MRA in the region $\theta \in (30°, 90°)$. Therefore, θ_t is equal to $30°$ if $B_f = 0$.

Secondly, we assume B_f is small but nonzero, and assume the positive frequency range of the interference can be represented by two frequency components f_1 and f_2. Without loss of generality, we can specify $f_2 < f_1$ so that $f_u = f_1$. The integrals in (7.19) and (7.20) can be approximated by summation so by (7.17) - (7.20), the difference of the output powers for ULA and MRA is expressed by:

$$\Delta = [\Delta(f_1) + \Delta(f_2)]B_I \tag{7.29}$$

where

$$\begin{aligned}\Delta(f_m) &= \frac{S_N^2(f_m) + 3S_I(f_m)S_N(f_m)}{3S_N(f_m) + g_U(f_m,\theta)S_I(f_m)} - \frac{S_N^2(f_m) + 3S_I(f_m)S_N(f_m)}{3S_N(f_m) + g_M(f_m,\theta)S_I(f_m)} \\ &= \frac{8S_I(f_m)S_N(f_m)[S_N(f_m) + 3S_I(f_m)]}{[3S_N(f_m) + g_U(f_m,\theta)S_I(f_m)]} \cdot \frac{u(f_m,\theta)[1-u^2(f_m,\theta)]}{[3S_N(f_m) + g_M(f_m,\theta)S_I(f_m)]} \\ & m = 1, 2.\end{aligned} \tag{7.30}$$

Similarly, in the region $\theta \in (0°, 90°)$, we can derive that $\Delta(f_1) \gtreqless 0 \Leftrightarrow u(f_1,\theta) \gtreqless 0 \Leftrightarrow \theta \lesseqgtr \theta_{t1}$ and $\Delta(f_2) \gtreqless 0 \Leftrightarrow u(f_2,\theta) \gtreqless 0 \Leftrightarrow \theta \lesseqgtr \theta_{t2}$. Since $u(f_1,\theta) = \cos(\pi \sin\theta)$ and

$u(f_2, \theta) = \cos(\pi f_2/f_1 \sin\theta)$, we know that $\theta_{t1} = 30^\circ$ and $\theta_{t2} = \arcsin[f_1/(2f_2)] > 30^\circ$. As a result, we derive that $\Delta > 0$ for $\theta \in (0^\circ, 30^\circ]$ and $\Delta < 0$ for $\theta \in [\theta_{t2}, 90^\circ)$. The direction θ_t at which $\Delta = 0$ should satisfy $30^\circ < \theta_t < \theta_{t2}$. So, compared with the case $B_f = 0$, θ_t becomes larger.

Analogically, we can deduce that, as the FBW of the interference is increased, θ_t becomes larger. The minimum value for θ_t is $\theta_t = 30^\circ$ when $B_f = 0$. Based on the symmetric feature, the exact description about the region in which MRA outperforms ULA in suppressing broadband interference is: $\{\theta|\ |\theta| < \theta_t, \theta \neq 0^\circ, \theta_t \geq 30^\circ\}$.

Obviously, this property does not require the assumption of the flat power spectra.

Property 2: In three-element arrays, if the FBW of the interference is larger than a certain critical value, B_{ft}, MRA achieves better interference suppression performance than ULA at all directions (except the broadside direction). For moderate and high interference-to-noise ratio (INR), B_{ft} is approximately equal to 121.5% under the assumption of flat power spectra.

Proof: If the interference comes from 0°, no interference suppression is achieved due to the look-direction constraint. Thus, the output powers of MRA and ULA are the same at the broadside direction. In addition, according to Property 1, if B_f keeps increasing, θ_t becomes larger. Therefore, we can deduce that θ_t is equal to 90° if the FBW of the interference is larger than a certain critical value, B_{ft}. $\theta_t = 90^\circ$ implies that at all directions except 0°, Δ is nonnegative and hence MRA achieves better interference suppression performance than ULA.

From the above conclusion, we know that the value of B_{ft} can be found by comparing the output power of MRA with that of ULA at $\theta = 90^\circ$.

If the input INR is moderate or very large, the output power for ULA (see (7.21)) and MRA (see (7.22)) can be approximated by:

$$p_{y_U} = 2\int_{f_l}^{f_u} \frac{-b}{\cos^2(af)+\cos(af)-2}df + p_e \tag{7.31}$$

$$p_{y_M} = 2\int_{f_l}^{f_u} \frac{-b}{2\cos^3(af)+\cos^2(af)-\cos(af)-2}df + p_e \tag{7.32}$$

where $b = (S_{_N}^2 + 3S_{_I}S_{_N})/(4S_{_I})$ and $a = (\pi/f_u)\sin\theta$ under the assumption of flat spectra. Equation (7.31) is computed analytically as:

$$\begin{aligned} p_{y_U} = & -\frac{2b}{3a}\cot\left(\frac{af_u}{2}\right) + \frac{4\sqrt{3}b}{9a}\arctan\left[\frac{\sqrt{3}}{3}\tan(\frac{af_u}{2})\right] \\ & + \frac{2b}{3a}\cot\left(\frac{af_l}{2}\right) - \frac{4\sqrt{3}b}{9a}\arctan\left[\frac{\sqrt{3}}{3}\tan(\frac{af_l}{2})\right] + p_e \end{aligned} \tag{7.33}$$

At $\theta = 90^\circ$, it is equivalent to:

$$p_{y_U} = \frac{2bf_u}{3\pi}\cot\left(\frac{\pi}{2}\frac{f_l}{f_u}\right) + \frac{4\sqrt{3}bf_u}{9\pi}\left\{\frac{\pi}{2} - \arctan\left[\frac{\sqrt{3}}{3}\tan(\frac{\pi}{2}\frac{f_l}{f_u})\right]\right\} + p_e \tag{7.34}$$

Equation (7.32) can also be computed analytically as:

$$p_{y_M} = 2[p(f_u) - p(f_l)] + p_e \tag{7.35}$$

where

$$\begin{aligned} p(f) = & -\frac{b}{7a}\cot\left(\frac{af}{2}\right) + \frac{b}{(2.841+0.178j)a}\arctan\left[0.435(1-j)\tan(\frac{af}{2})\right] + \\ & \frac{b}{(2.841-0.178j)a}\arctan\left[0.435(1+j)\tan(\frac{af}{2})\right] \end{aligned} \tag{7.36}$$

At $\theta = 90°$, (7.35) is equivalent to:

$$\begin{aligned} p_{y_M} = & \frac{2bf_u}{7\pi} \cot\left(\frac{\pi}{2}\frac{f_l}{f_u}\right) + \frac{2bf_u}{(2.841 + 0.178j)\pi}\Big\{\frac{\pi}{2} - \\ & \arctan\left[0.435(1-j)\tan(\frac{\pi}{2}\frac{f_l}{f_u})\right]\Big\} + \frac{2bf_u}{(2.841 - 0.178j)\pi} \\ & \Big\{\frac{\pi}{2} - \arctan\left[0.435(1+j)\tan(\frac{\pi}{2}\frac{f_l}{f_u})\right]\Big\} + p_e \end{aligned} \tag{7.37}$$

Let $x = \tan(\frac{\pi}{2}\frac{f_l}{f_u})$, then the difference of (7.34) and (7.37) is:

$$\begin{aligned} \Delta &= p_{y_U} - p_{y_M} \\ &= \{0.190/x - 0.497 - 0.385\arctan(x/\sqrt{3}) + \\ & \quad (0.351 - 0.022j)\arctan[0.435(1-j)x] + \\ & \quad (0.351 + 0.022j)\arctan[0.435(1+j)x]\}2bf_u/\pi \end{aligned} \tag{7.38}$$

Assuming $f_l \ll f_u$ (hence x is small), we may then make these approximations: $\arctan(x/\sqrt{3}) \approx x/\sqrt{3}$, $\arctan[0.435(1-j)x] \approx 0.435(1-j)x$ and $\arctan[0.435(1+j)x] \approx 0.435(1+j)x$, hence we get:

$$\Delta \approx (0.064x^2 - 0.497x + 0.190)2bf_u/(\pi x) \tag{7.39}$$

$\Delta \geq 0$ implies $x \in [0, 0.403] \cup [7.362, +\infty]$, which derives $f_l/f_u \leq 0.244$ and $f_l/f_u \geq 0.914$, respectively. Since $f_l/f_u = (1-B_f/2)/(1+B_f/2)$, we can obtain $B_f \geq 121.5\% \cup B_f \leq 8.99\%$ as the condition for $\Delta \geq 0$. Checking the two regions, we find that $B_f \leq 8.99\%$ should be neglected because it is in contradiction with the assumption of small x.

For the scenarios with very small input INR, the approximations in (7.31) and (7.32) will lead to errors. However, for moderate and large INR, the approximations have high accuracy and thus the lower bound 121.5% should have small variations. Therefore, we arrive at the conclusion that $B_{ft} \approx 121.5\%$ under the assumption of flat power spectra.

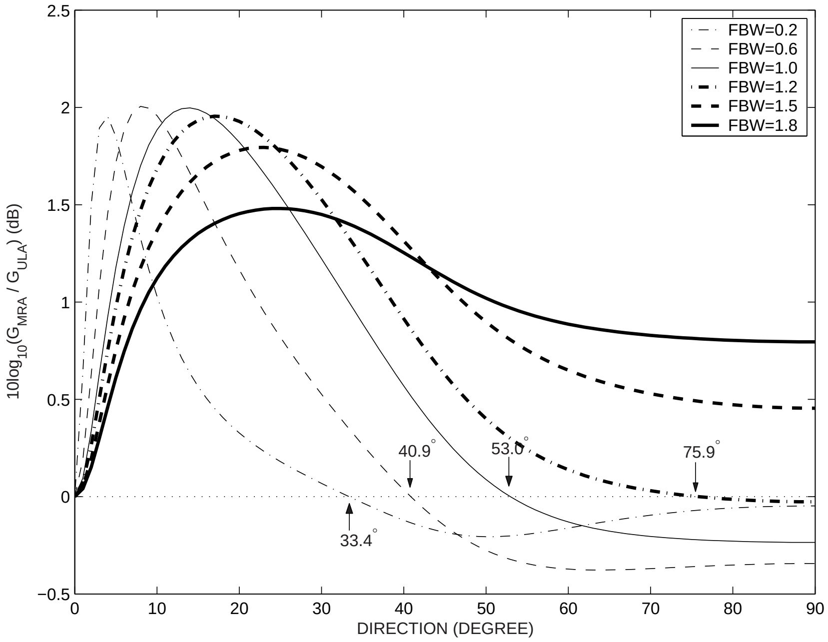

Figure 7.1. Ratio of the interference and noise suppression gain between MRA and ULA for different interference FBW, with INR $= 5$dB.

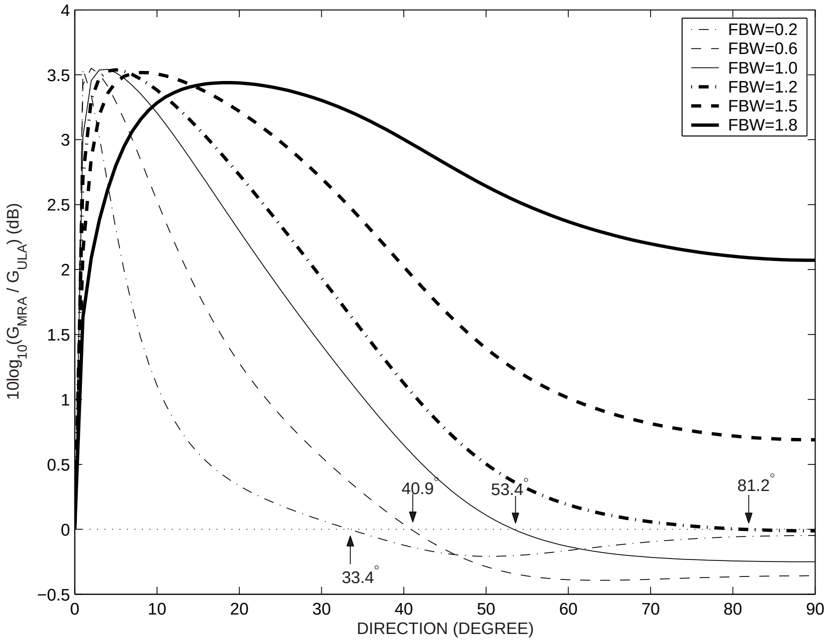

Figure 7.2. Ratio of the interference and noise suppression gain between MRA and ULA for different interference FBW, with INR $= 30$dB.

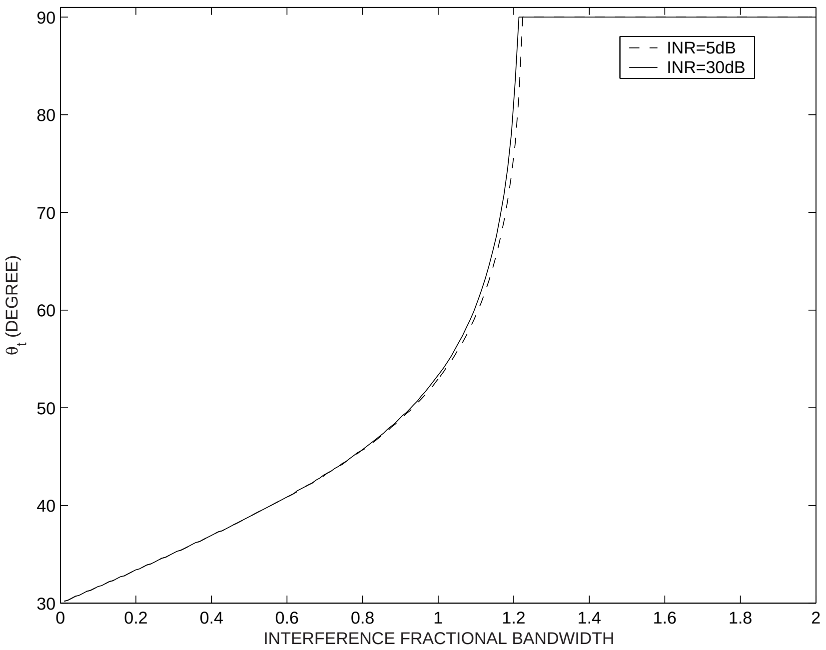

Figure 7.3. θ_t versus B_f for INR $= 5$dB and INR $= 30$dB.

Graphs are presented in Figures 7.1 - 7.3 to demonstrate these two properties. Flat spectra are assumed for both interference and noise. By formulations (7.23) and (7.24), the ratio of the interference and noise suppression gain between MRA and ULA, for various interference FBW, are obtained and shown in Figures 7.1 and 7.2 with the input INR chosen to be 5dB and 30dB, respectively. $10\log_{10}(G_{MRA}/G_{ULA}) > 0$dB implies that MRA has better interference suppression performance than ULA. The values for θ_t are labelled in the figures. The curves of θ_t versus B_f under INR $= 5$dB and INR $= 30$dB are plotted in Figure 7.3. θ_t is found by numerically searching within $(0°, 90°]$ for the angle at which $p_{y_U} - p_{y_M}$ is equal to zero. If $p_{y_U} - p_{y_M}$ is greater than zero for all the angles within $(0°, 90°]$, θ_t is set as $90°$. It can be seen that B_{ft} for INR $= 30$dB is 121.4% while B_{ft} for INR $= 5$dB is 122.4%. Therefore, the level of INR in the normal scenario has little influence on B_{ft}. θ_t is a monotonically nondecreasing function of B_f.

In addition, from Figures 7.1 and 7.2, we can see that for $B_f \in [0, B_{ft}]$ and $\theta \in [\theta_t, 90°]$, where ULA outperforms MRA, $|10\log_{10}(G_{MRA}/G_{ULA})|$ is close to 0dB. This implies similar interference and noise suppression gains of MRA and ULA.

7.4.2 L-Element Array

It is intractable to get an explicit analytical expression for the integral (7.8) for $L \geq 4$. Riemann sum can be adopted to obtain the approximate solution for the integral so that the output power for ULA and MRA and hence their interference and noise suppression gain can be acquired.

As discussed in Chapter 6, with the same number of array elements, MRA has larger aperture length and hence smaller beamwidth than ULA. This can explain the better interference suppression performance of MRA in the region close to the broadside direction. We use two examples, where flat spectra are assumed, to show the interference suppression performance of MRA and ULA when they have either the same number of elements or the same aperture length. An MRA with 3 sensors located at $\{0, 1d, 3d\}$ actually has an aperture length of $3d$ while an MRA with 4 sensors located at $\{0, 1d, 4d, 6d\}$ has an aperture length of $6d$. They are compared with ULA with $L = 3$ and $L = 4$ (same number of elements) and ULA with $L = 4$ and $L = 7$ (same aperture length), respectively. All related curves are shown in Figures 7.4 and 7.5 under different interference bandwidths.

From these figures, it can be seen that at directions close to the broadside of the array, the interference and noise suppression gain of MRA is similar to that of ULA with the same aperture length and better than that of ULA with the same number of elements. At other directions, MRA achieves better interference suppression performance than ULA with the same number of elements if the FBW of the interference is very large.

A group of sensor deployments for MRA with $L \in [3, 10]$ is selected from [100]. Figures

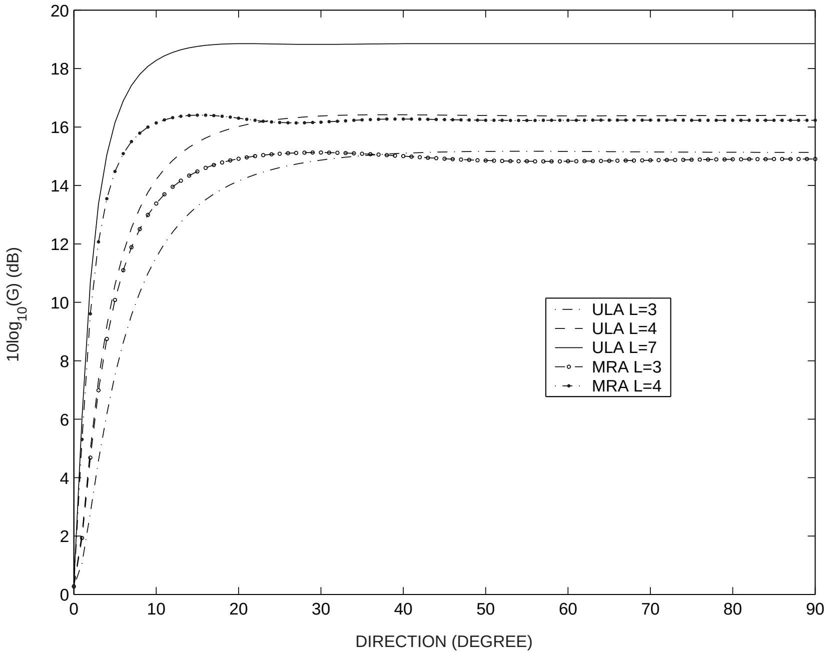

Figure 7.4. Interference and noise suppression gain of MRA and ULA with the same number of elements or same aperture length, with $B_f = 40\%$ and INR $= 10$dB.

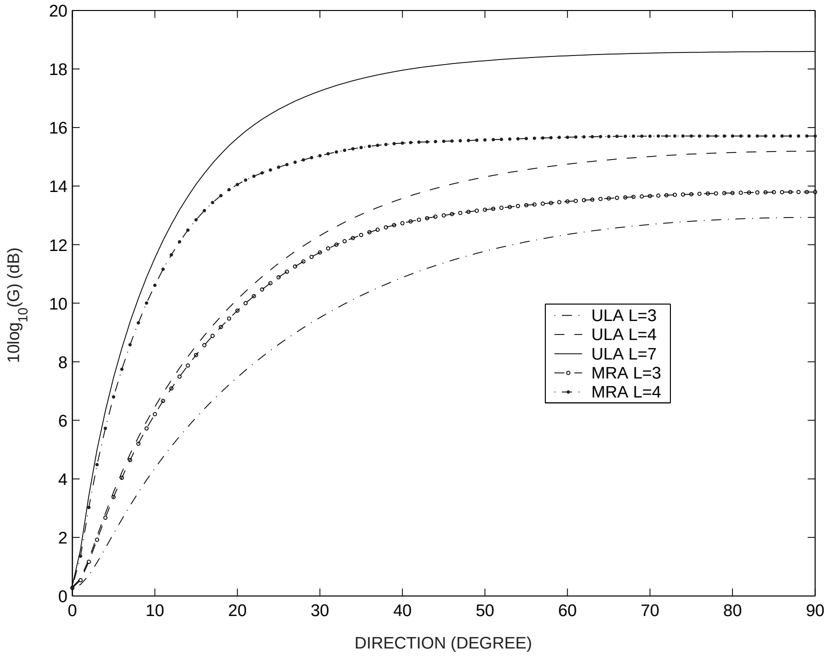

Figure 7.5. Interference and noise suppression gain of MRA and ULA with the same number of elements or same aperture length, with $B_f = 160\%$ and INR $= 10$dB.

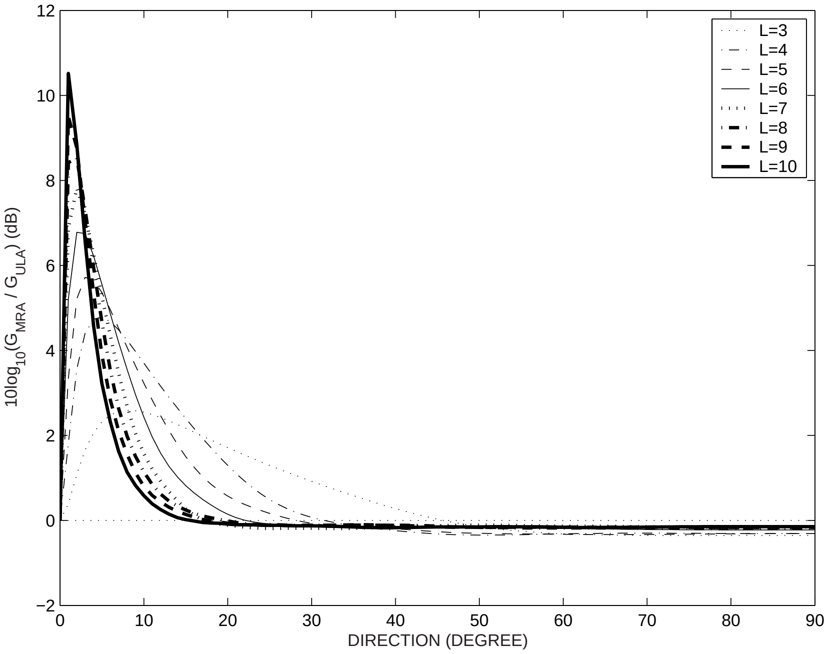

Figure 7.6. Ratio of the interference and noise suppression gain between MRA and ULA with various number of elements, with $B_f = 80\%$ and INR $= 10$dB.

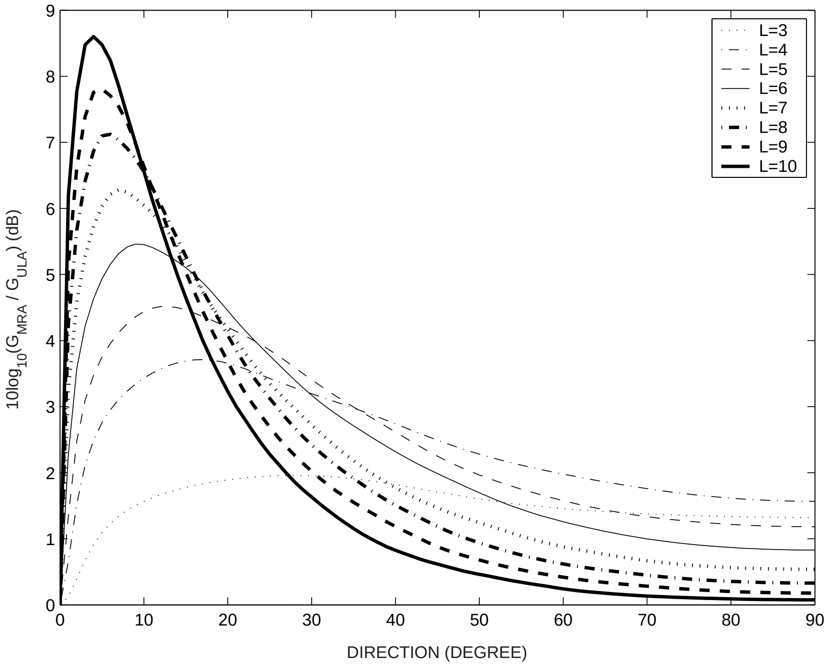

Figure 7.7. Ratio of the interference and noise suppression gain between MRA and ULA with various number of elements, with $B_f = 180\%$ and INR $= 10$dB.

7.6 and 7.7 show curves of $10\log_{10}(G_{MRA}/G_{ULA})$ for arrays with different number of sensors. Different interference FBWs are assumed in these two figures. Properties similar to the three-element array can be found:

1) For interference coming from directions close to the broadside of the array, MRA has better interference suppression performance than ULA with the same number of elements. Furthermore, at these directions, the superiority of MRA over ULA becomes more obvious as the number of sensors is increased.

2) The smaller the number of elements, the larger the angular region in which MRA outperforms ULA. In the region where ULA outperforms MRA, $|10\log_{10}(G_{MRA}/G_{ULA})|$ is close to 0dB so their interference and noise suppression gains are similar.

3) As the FBW of the interference is increased, the region where MRA outperforms ULA becomes larger. For very large FBW, MRA might achieve better interference suppression performance than ULA at all directions (except $0°$).

7.5 Performance Analysis for the Two-Interference Case

In the two-interference case, for ULA with three elements, the variables g_1, g_2, ρ_n and ρ_d in (7.14) can be written as:

$$\begin{aligned}
g_{1U} &= 4[1-u(f,\theta_1)][2+u(f,\theta_1)] \\
g_{2U} &= 4[1-u(f,\theta_2)][2+u(f,\theta_2)] \\
\rho_{nU} &= 4[1-v(f,\theta_1,\theta_2)][2+v(f,\theta_1,\theta_2)] \\
\rho_{dU} &= 8[1-u(f,\theta_1)][1-u(f,\theta_2)][1-v(f,\theta_1,\theta_2)]
\end{aligned} \tag{7.40}$$

where $u(f,\theta_1) = \cos(\pi \sin\theta_1 f/f_u)$, $u(f,\theta_2) = \cos(\pi \sin\theta_2 f/f_u)$ and $v(f,\theta_1,\theta_2) = \cos[\pi(\sin\theta_1 - \sin\theta_2) f/f_u]$.

For MRA with three elements, the variables g_1, g_2, ρ_n and ρ_d are given by:

$$\begin{aligned}
g_{1M} &= 4[1-u(f,\theta_1)][2u^2(f,\theta_1)+3u(f,\theta_1)+2] \\
g_{2M} &= 4[1-u(f,\theta_2)][2u^2(f,\theta_2)+3u(f,\theta_2)+2] \\
\rho_{nM} &= 4[1-v(f,\theta_1,\theta_2)][2v^2(f,\theta_1,\theta_2)+3v(f,\theta_1,\theta_2)+2] \\
\rho_{dM} &= 8[1-u(f,\theta_1)][1-u(f,\theta_2)][1-v(f,\theta_1,\theta_2)][3+2u(f,\theta_1)+2u(f,\theta_2) \\
&\quad +2v(f,\theta_1,\theta_2)]
\end{aligned} \tag{7.41}$$

Let $\gamma_1(f) = S_{I1}(f)/S_N(f)$ and $\gamma_2(f) = S_{I2}(f)/S_N(f)$. The output power (7.13) for ULA and MRA with three elements can be expressed in a simple form:

$$p_{yU} = \int_{F_N} \frac{1+3\gamma_1(f)+3\gamma_2(f)+\rho_{nU}\gamma_1(f)\gamma_2(f)}{3+g_{1U}\gamma_1(f)+g_{2U}\gamma_2(f)+\rho_{dU}\gamma_1(f)\gamma_2(f)} \cdot S_N(f)df \tag{7.42}$$

$$p_{yM} = \int_{F_N} \frac{1+3\gamma_1(f)+3\gamma_2(f)+\rho_{nM}\gamma_1(f)\gamma_2(f)}{3+g_{1M}\gamma_1(f)+g_{2M}\gamma_2(f)+\rho_{dM}\gamma_1(f)\gamma_2(f)} \cdot S_N(f)df \tag{7.43}$$

For the two-interference case, analytical solutions for the integrals for computing the output power are difficult to achieve. Numerical approximations have to be performed for computation.

Figures 7.8 - 7.10 demonstrate the contour plots of the ratio of the interference and noise suppression gain between MRA and ULA with three elements for the two-interference case, with p_{yU} and p_{yM} computed numerically by (7.42) and (7.43). The 0-dB contour patches, aside from those at the broadside, are plotted with thick lines to highlight the bound of the region where MRA outperforms ULA. The performance of MRA and ULA

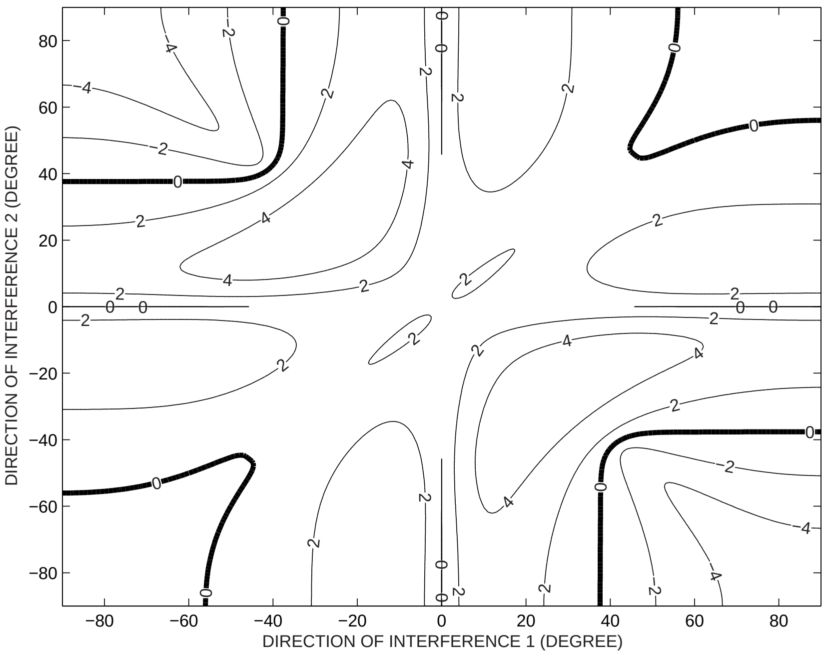

Figure 7.8. Contour plot of $10\log_{10}(G_{MRA}/G_{ULA})$ for three-element arrays, with $B_f = 80\%$ and $\text{INR}_1 = \text{INR}_2 = 10\text{dB}$.

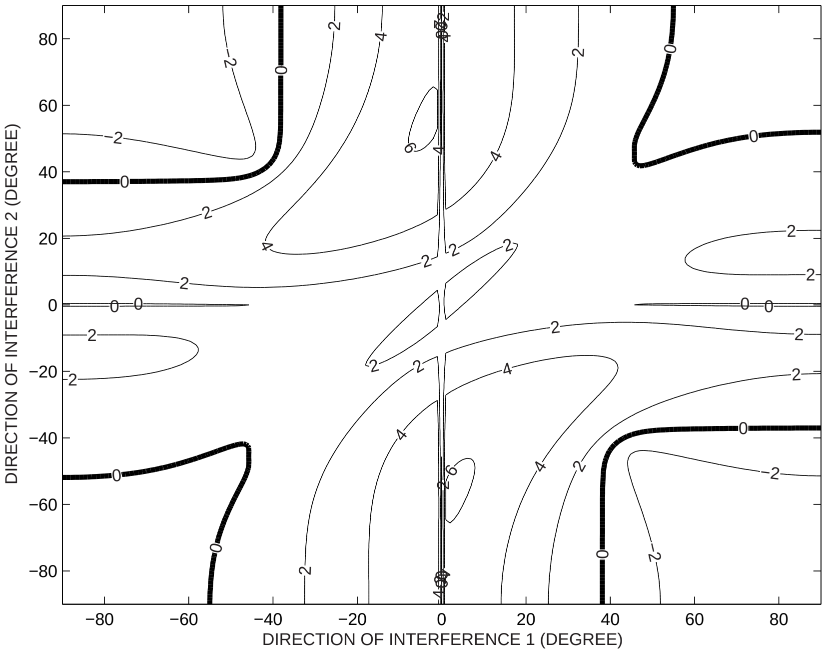

Figure 7.9. Contour plot of $10\log_{10}(G_{MRA}/G_{ULA})$ for three-element arrays, with $B_f = 80\%$, $\text{INR}_1 = 5\text{dB}$ and $\text{INR}_2 = 50\text{dB}$.

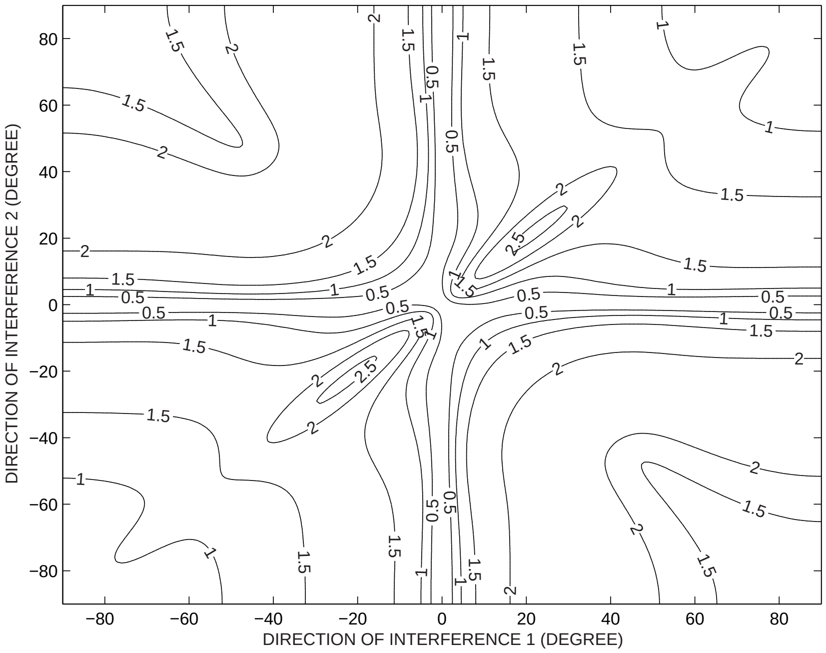

Figure 7.10. Contour plot of $10\log_{10}(G_{MRA}/G_{ULA})$ for three-element arrays, with $B_f = 160\%$ and $\text{INR}_1 = \text{INR}_2 = 10\text{dB}$.

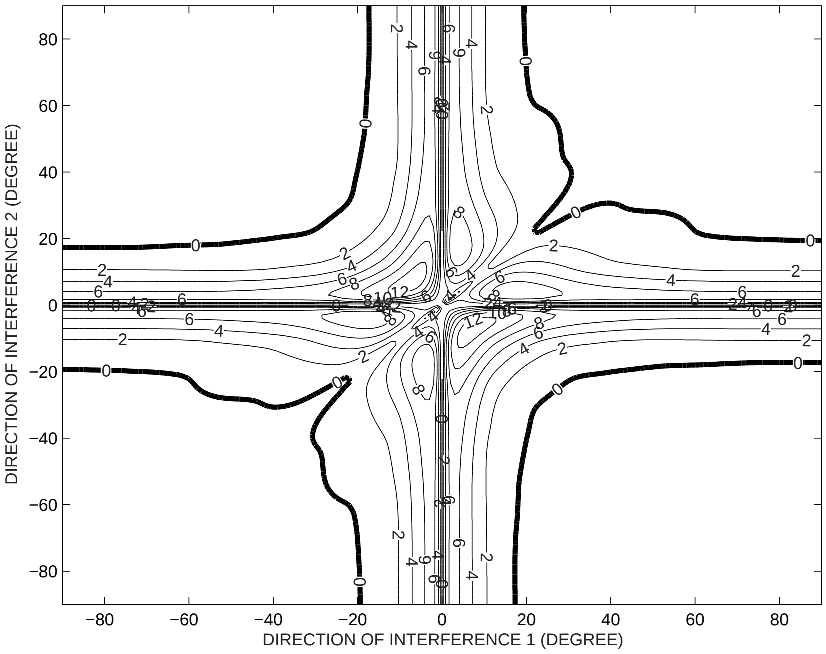

Figure 7.11. Contour plot of $10\log_{10}(G_{MRA}/G_{ULA})$ for six-element arrays, with $B_f = 80\%$ and $\text{INR}_1 = \text{INR}_2 = 10\text{dB}$.

are related with $(\sin\theta_1 - \sin\theta_2)$ according to the expressions of ρ_n and ρ_d shown in (7.40) and (7.41). Therefore, the contour plots are symmetric about the point $(0°, 0°)$ rather than the broadside direction. This is different from the one-interference case.

Figure 7.8 shows the result for assuming both interferences with INR $= 10$dB and $B_f = 80\%$. Figure 7.9 shows the result for assuming two interferences with distinct INR, 5dB and 50dB. We can find that the values of INR do not have significant influence on the position of 0-dB contour lines. Similar to the one-interference case, at angles around the broadside direction, MRA achieves better interference suppression performance than ULA. Figure 7.10 illustrates the contour lines for interferences with very large FBW, both 160%. It can be seen that at all directions, $10\log_{10}(G_{MRA}/G_{ULA})$ is larger than 0dB, i.e., MRA outperforms ULA for interferences coming from any directions if they have large FBW.

Figure 7.11 shows the contour lines of $10\log_{10}(G_{MRA}/G_{ULA})$ for six-element arrays, with p_y computed by (7.13) numerically. The sensors of MRA are located at $\{0, 1d, 6d, 9d, 11d, 13d\}$. We observe that in the region starting from the broadside to the marked 0-dB contour lines, MRA outperforms ULA. Outside this area, $10\log_{10}(G_{MRA}/G_{ULA})$ is very close to 0dB so no contour lines are shown.

7.6 Discussion and Conclusion

Performance analyses in Sections 7.4 and 7.5 are based on the assumption that the filters in the beamformer operate with the optimum frequency responses of the ideal continuous-time, infinite-length filters. In realistic implementations using finite-order digital filters, the degrees of freedom for suppressing interferences are limited by the design of temporal filters. As a result, the performance of the beamformer is dependent on the filter order and the signal sampling rate besides the array geometry and the interference bandwidth. Studies for the realistic systems need to consider more factors. If the frequency responses of the realistic digital filters approach the optimum responses of the ideal filters, the observed phenomena should be similar to what we present.

As indicated in literatures, relative to the ULA, the beampatterns of the MRA and NRA have higher sidelobe level. Some methods have been investigated to overcome this drawback in previous studies. Our research here is focused on their interference and noise suppression performance. In this chapter, the expressions for the power spectrum of the beamformer output in different scenarios are derived to compute the mean output power. Properties about the broadband interference suppression performance of MRA relative to ULA are obtained based on mathematical proofs and graphic illustrations. Our analyses show that due to the dependence on the FBW, the broadband interference suppression performance of the LCMV beamformer is different from the narrowband case. For interferences with small FBW, MRA can offer better cancellation performance at angles close to the broadside direction. As the FBW increases, the region of directions where MRA performs better than ULA becomes large. When the FBW is higher than a certain level, MRA might outperform ULA in all directions (except $0°$). Therefore, in applications involving interferences with extremely high FBW, using MRA instead of ULA can always achieve improved interference suppression performance.

In addition, the study in this chapter is focused on the one- and two-interference cases. As in [122], if the number of interferences is larger than two, the matrix inversion lemma can be used repeatedly to obtain the inverse of the cross spectrum matrix. Deriving the analytical formulations for the power spectrum of the beamformer output is possible but the complicated expressions are not easy to analyze.

Chapter 8

Applications of the SRV Constraint in Broadband Pattern Synthesis

8.1 Introduction

In applications using microphone and loudspeaker arrays for audio teleconferencing, the beampattern with a constant beamwidth over the frequency band of interest is desired. Some applications even want the spatial response in the whole field of view to remain constant with respect to the frequency. The theory for the far-field FIB is presented in [77]. Various methods, including the multi-rate and single-rate methods combining the FIR [78] or IIR filters [79], the fan filter for the uniformly spaced arrays [80–82], the designs for planar arrays like the concentric ring array and the rectangular array [84, 85, 125], and the minimum mean square error method [68], have been investigated to design the FIBP.

As the filter length in each channel increases, the frequency invariant property of the beampattern can become better. However, for the beamformer with a given filter length, existing methods do not have the capability of controlling the extent of the frequency invariance. In this chapter, the SRV is defined to measure the fluctuations of the array spatial responses over the desired frequency band. By constraining the average SRV in the specified angles to be smaller than a specified threshold, a desirable tradeoff between the sidelobe level and the frequency invariance of the beampattern can be obtained. By changing the spatial region specified in the SRV constraint, the frequency invariant feature can be obtained for any directions of interest, such as the mainlobe region or the whole field of view of the array. The designs in [77, 78] and [80] produce beampatterns with the frequency invariant feature in the whole spatial region while the study in [68] obtain the frequency invariance in the mainlobe region for the given desired response. Relative to these existing investigations, the method of applying the SRV constraint in the optimization formulations shows greater flexibility. Although the SRV is defined in a form which looks like the mean square error, it is completely different from the minimum mean square error method. This will be explained in detail in Section 8.3 when the definition of the SRV is presented. The study in this chapter is focused on applications requiring the frequency invariance in both the mainlobe and the sidelobe regions. A typical application is to use the fixed beamformer with the FIBP to construct the multi-beam forming network in the beamspace adaptive array. As indicated in [80], the frequency invariant property is required in the whole field of view to prevent the interferences coming from the sidelobe directions from being distorted because the distortion of the interferences in the output of the multi-beam forming network will result in severe performance degradation of the beamspace adaptive array.

Broadband beampattern is a function of both direction and frequency. The optimization problem for pattern synthesis is usually formulated over discrete frequencies and angles. The bandwidth and the number of frequency grids determine the accuracy and the complexity of the optimization problem [64, 65, 88]. Therefore, we have to choose the grid size properly to obtain a reasonable tradeoff. For applications with broad frequency band, when the frequency grid is decreased to be fine enough to achieve an acceptable performance, the optimization formulation includes large numbers of constraints. The numerical stability problem and infeasibility problem occurring in such optimizations can not be solved easily.

Since the SRV constraint can restrict the fluctuations of the spatial responses over the frequency band and thus enhance the correlation of the spatial responses at different frequencies significantly, we find that when the SRV constraint is used, the broadband pattern synthesis problems can be formulated in an efficient way: The constraints originally imposed on the whole frequency band of interest in the optimization formulations to realize the specifications of the beampatterns can be simplified to be on one reference frequency. This simplification results in significant reduction of the number of constraints and hence the complexity of the optimization problems.

This chapter is organized as follows: In Section 8.2, the mathematical formulations for the array model and the definition of the convex optimization problem are introduced. In Section 8.3, the definition of the SRV constraint and its applications in broadband pattern synthesis are presented. In Sections 8.4 and 8.5, the examples of using the SRV constraint to synthesize the single-beam FIBP and construct the multi-beam forming network are described with formulations and simulation results.

8.2 Background

For a broadband array with L sensors and J taps connected after each element, the beamforming output is the sum of all the LJ weighted tap signals. The $LJ \times 1$ real-valued weight vector $\boldsymbol{w}$ for the broadband array is defined as follows:

$$\boldsymbol{w} = [w_{1,1} \ \cdots \ w_{L,1} \ \cdots \ w_{1,J} \ \cdots \ w_{L,J}]^T \tag{8.1}$$

The two-dimensional spatial response is expressed by:

$$H(f,\theta) = \boldsymbol{w}^T \boldsymbol{s}(f,\theta) \tag{8.2}$$

The beampattern is defined as the norm square of the spatial response. $\boldsymbol{s}(f,\theta)$ is the $LJ \times 1$ steering vector which is written as:

$$\boldsymbol{s}(f,\theta) = \boldsymbol{s}_T(f) \otimes \boldsymbol{s}_\tau(f,\theta) \tag{8.3}$$

where

$$\boldsymbol{s}_T(f) = [1 \ e^{-j2\pi f T_s} \ \cdots \ e^{-j2\pi f (J-1) T_s}]^T \tag{8.4}$$

$$\boldsymbol{s}_\tau(f,\theta) = [e^{j2\pi f \tau_1(\theta)} \ e^{j2\pi f \tau_2(\theta)} \ \cdots \ e^{j2\pi f \tau_L(\theta)}]^T \tag{8.5}$$

where T_s is the sampling interval of the temporal filter in each channel. $\tau_i(\theta)$ is the propagation delay from the array origin to the ith sensor for the source coming from θ. Arbitrary element responses can be multiplied to the elements of $\boldsymbol{s}_\tau(f,\theta)$ if necessary.

In many array applications, the pattern synthesis problem is formulated as a convex optimization problem, defined in a standard form [126] as follows:

$$\begin{aligned} &\min_{\boldsymbol{x}} \ F_0(\boldsymbol{x}) \\ &\text{subject to } F_i(\boldsymbol{x}) \le 0, \ i = 1,2,\cdots,m \\ &\boldsymbol{a}_k^T \boldsymbol{x} = \boldsymbol{b}_k, \ k = 1,2,\cdots,p \end{aligned} \tag{8.6}$$

where $F_0, \cdots, F_m$ are convex functions. $m, p \in \mathbb{Z}^+$. $\boldsymbol{x} \in \mathbb{R}^n$ is the optimization variable.

$\boldsymbol{a}_k$ and $\boldsymbol{b}_k$ are vectors with appropriate dimensions defined according to specific problems.

8.3 Broadband Pattern Synthesis using the SRV Constraint

8.3.1 Definition of the SRV Constraint

The SRV in the direction θ is defined as follows:

$$\text{SRV}(\theta) = \frac{1}{B_\Omega} \int_{f \in \Omega} |\boldsymbol{w}^T \boldsymbol{s}(f, \theta) - \boldsymbol{w}^T \boldsymbol{s}(f_0, \theta)|^2 df \tag{8.7}$$

It represents the variation of the spatial responses within the frequency range Ω. B_Ω denotes the bandwidth of Ω. f_0 is the reference frequency selected within the frequency range. In the definition (8.7), the template for the desired response is not fixed but a function of the weight vector which is to be optimized. Therefore, the value of the SRV is the true fluctuation of the synthesized beampattern at different frequencies. However, in the mean square error method, the fixed template is used as the desired response, which has to be found before formulating the mean square error. The mean square error is not the fluctuation of the synthesized spatial responses at different frequencies, so it can not control the extent of the frequency invariance directly.

Expression (8.7) can be re-written as:

$$\text{SRV}(\theta) = \boldsymbol{w}^T \boldsymbol{C}(\theta) \boldsymbol{w} \tag{8.8}$$

where $\boldsymbol{C}(\theta)$ is an $LJ \times LJ$ matrix:

$$\boldsymbol{C}(\theta) = \frac{1}{B_\Omega} \int_{f \in \Omega} [\boldsymbol{s}(f, \theta) - \boldsymbol{s}(f_0, \theta)][\boldsymbol{s}(f, \theta) - \boldsymbol{s}(f_0, \theta)]^H df \tag{8.9}$$

Because $\boldsymbol{C}(\theta)$ is a Hermitian matrix with nonnegative real eigenvalues and the weight vector $\boldsymbol{w}$ is real-valued, it is easy to prove that:

$$\boldsymbol{w}^T\boldsymbol{C}^H(\theta)\boldsymbol{w} = [\boldsymbol{w}^T\boldsymbol{C}^*(\theta)\boldsymbol{w}]^T = \boldsymbol{w}^T\boldsymbol{C}^*(\theta)\boldsymbol{w} \tag{8.10}$$

Hence,

$$\boldsymbol{w}^T\boldsymbol{C}(\theta)\boldsymbol{w} = \boldsymbol{w}^T[\boldsymbol{C}(\theta) + \boldsymbol{C}^H(\theta)]\boldsymbol{w}/2 = \boldsymbol{w}^T\boldsymbol{C}_r(\theta)\boldsymbol{w} \tag{8.11}$$

where $\boldsymbol{C}_r(\theta)$ is the real part of $\boldsymbol{C}(\theta)$:

$$\boldsymbol{C}_r(\theta) = \frac{1}{B_\Omega}\int_{f\in\Omega} \mathrm{Re}\Big\{[\boldsymbol{s}(f,\theta) - \boldsymbol{s}(f_0,\theta)][\boldsymbol{s}(f,\theta) - \boldsymbol{s}(f_0,\theta)]^H\Big\}df \tag{8.12}$$

If the frequency range Ω is $[f_l, f_u]$, $B_\Omega = f_u - f_l$ and $f_c = (f_u + f_l)/2$, the entries in $\boldsymbol{C}_r(\theta)$ can be derived as the following analytical expression:

$$[\boldsymbol{C}_r(\theta)]_{m,n} = [\boldsymbol{C}_{r1}]_{m,n} - [\boldsymbol{C}_{r2}]_{m,n} - [\boldsymbol{C}_{r3}]_{m,n} + [\boldsymbol{C}_{r4}]_{m,n} \tag{8.13}$$

where

$$[\boldsymbol{C}_{r1}]_{m,n} = \frac{f_u}{B_\Omega}\mathrm{sinc}(2f_u\varsigma_{m,n}) - \frac{f_l}{B_\Omega}\mathrm{sinc}(2f_l\varsigma_{m,n}) \tag{8.14}$$

$$\begin{aligned}[\boldsymbol{C}_{r2}]_{m,n} = {} & \left[\frac{f_u}{B_\Omega}\mathrm{sinc}(2f_u\varsigma_m) - \frac{f_l}{B_\Omega}\mathrm{sinc}(2f_l\varsigma_m)\right]\cos(2\pi f_0\varsigma_n) \\ & +\mathrm{sinc}(B_\Omega\varsigma_m)\sin(2\pi f_c\varsigma_m)\sin(2\pi f_0\varsigma_n)\end{aligned} \tag{8.15}$$

$$[\boldsymbol{C}_{r3}]_{m,n} = [\boldsymbol{C}_{r2}]_{n,m} \tag{8.16}$$

$$[\boldsymbol{C}_{r4}]_{m,n} = \cos(2\pi f_0\varsigma_{m,n}) \tag{8.17}$$

$$\mathrm{sinc}(\alpha) = \frac{\sin(\pi\alpha)}{\pi\alpha} \tag{8.18}$$

$$\varsigma_{m,n} = \varsigma_m - \varsigma_n \tag{8.19}$$

$$\varsigma_m = \tau_{k_1}(\theta) - i_1 T_s, \;\; m = i_1 L + k_1; \;\; k_1 = 1, 2, \cdots, L; \;\; i_1 = 0, 1, \cdots, J-1 \tag{8.20}$$

$$\varsigma_n = \tau_{k_2}(\theta) - i_2 T_s, \;\; n = i_2 L + k_2; \;\; k_2 = 1, 2, \cdots, L; \;\; i_2 = 0, 1, \cdots, J-1 \tag{8.21}$$

The SRV averaged over the angles of interest is computed by:

$$\overline{\text{SRV}} = \frac{1}{B_{\Theta_{FI}}} \int_{\theta \in \Theta_{FI}} \text{SRV}(\theta) d\theta \tag{8.22}$$

or in the discrete form:

$$\overline{\text{SRV}} = \frac{1}{N} \sum_{i=1}^{N} \text{SRV}(\theta_i) \tag{8.23}$$

where Θ_{FI} denotes the set of directions in which the response variation is considered. $B_{\Theta_{FI}}$ represents the span of Θ_{FI}. θ_i, $i = 1, \cdots, N$, denote the angle grids in Θ_{FI}. According to (8.8), equations (8.22) and (8.23) can be re-expressed as:

$$\overline{\text{SRV}} = \boldsymbol{w}^T \overline{\boldsymbol{C}_r} \boldsymbol{w} \tag{8.24}$$

$\overline{\boldsymbol{C}_r}$ is given by:

$$\overline{\boldsymbol{C}_r} = \frac{1}{B_{\Theta_{FI}}} \int_{\theta \in \Theta_{FI}} \boldsymbol{C}_r(\theta) d\theta \tag{8.25}$$

or

$$\overline{\boldsymbol{C}_r} = \frac{1}{N} \sum_{i=1}^{N} \boldsymbol{C}_r(\theta_i) \tag{8.26}$$

When the average SRV is used as a constraint in the optimization, it is not necessary to use too small grid spacings for the angles due to the correlations between responses at neighbouring directions. If the value of $\overline{\text{SRV}}$ is used as a measure of the quality of the generated beampattern, the grid spacing should be small to get a true evaluation of the performance.

We design the SRV constraint

$$\boldsymbol{w}^T \overline{\boldsymbol{C}_r} \boldsymbol{w} \leq \gamma \tag{8.27}$$

for the broadband array, where γ is a small positive constant.

The SRV constraint is a quadratic inequality constraint. It can be re-expressed as:

$$\|\boldsymbol{L}^T \boldsymbol{w}\|^2 \leq \gamma \tag{8.28}$$

where $\boldsymbol{L} = \boldsymbol{U}\boldsymbol{D}^{\frac{1}{2}}$. $\boldsymbol{D}$ is a diagonal matrix including the nonzero eigenvalues of $\overline{\boldsymbol{C}_r}$. $\boldsymbol{U}$ consists of the corresponding eigenvectors. Therefore, introducing the quadratic inequality constraint (8.28) into the optimization problem will not change the structure and the characteristic of the convexity of the optimization.

8.3.2 Applications of the SRV Constraint

By constraining the average SRV to be less than a small value, we can restrict the synthesized beampattern at different frequencies to be similar to some extent. On the one hand, this motivates us to constrain the SRV in the optimization to obtain the FIBP. On the other hand, this implies that in optimization formulations for broadband pattern synthesis, the constraints imposed over the whole interested frequency band have redundancies and can be simplified.

To realize specifications without considering the frequency invariance, most broadband pattern synthesis formulations in the literatures can be generalized in the form as follows:

$$\begin{aligned} &\min_{\boldsymbol{w}} \; F_0\langle H(f,\theta)\rangle \\ \text{subject to } \; &F_i\langle H(f_m,\theta_n)\rangle \leq 0, \; f_m \in \Omega_{pb}, \; \theta_n \in \Theta_1 \\ &G_k\langle H(f_p,\theta_q)\rangle = 0, \; f_p \in \Omega_{pb}, \;\; \theta_q \in \Theta_2 \end{aligned} \tag{8.29}$$

where $m = 1, \cdots, N(\Omega_{pb})$, $n = 1, \cdots, N(\Theta_1)$ and $i = 1, \cdots, N(\Omega_{pb}) \cdot N(\Theta_1)$. $p = 1, \cdots, N(\Omega_{pb})$, $q = 1, \cdots, N(\Theta_2)$ and $k = 1, \cdots, N(\Omega_{pb}) \cdot N(\Theta_2)$. Ω_{pb} represents the desired frequency band. We assume that the band-pass filter is used before array processing to remove the frequency components outside Ω_{pb} [125]. $N(\cdot)$ represents the number of the discrete frequency or angle grids in the numerical treatment. Θ_1 and Θ_2 represent two groups of directional regions. $F_0\langle\cdot\rangle$, $F_i\langle\cdot\rangle$ and $G_k\langle\cdot\rangle$ denote convex functions.

To enhance the flexibility in controlling the frequency invariant feature of the broadband beampattern, the SRV constraint (8.28) is supplemented in (8.29) directly as follows:

$$\begin{aligned} &\min_{\boldsymbol{w}} \; F_0\langle H(f,\theta)\rangle \\ \text{subject to } \; &F_i\langle H(f_m,\theta_n)\rangle \le 0, \; f_m \in \Omega_{pb}, \; \theta_n \in \Theta_1 \\ &G_k\langle H(f_p,\theta_q)\rangle = 0, \; f_p \in \Omega_{pb}, \;\; \theta_q \in \Theta_2 \\ &\|\boldsymbol{L}^T\boldsymbol{w}\|^2 \le \gamma \end{aligned} \tag{8.30}$$

By choosing the value of the threshold γ, the extent of the frequency invariance of the beampattern can be controlled. It should be noted that the high frequency invariance is obtained at the cost of reduced degrees of freedom for realizing other specifications of the spatial response.

Since the SRV constraint can reduce the fluctuation of the spatial response over the frequency band and thus enhance the correlation of the spatial responses at different frequencies significantly, the constraints in (8.29) which are imposed on discrete frequencies over the whole interested frequency band can be reduced to be on only one reference frequency

f_0. The corresponding efficient optimization formulation is expressed as:

$$\begin{aligned} \min_{\boldsymbol{w}} \; & F_0\langle H(f,\theta)\rangle \\ \text{subject to } & F_i\langle H(f_0,\theta_i)\rangle \leq 0, \quad \theta_i \in \Theta_1 \\ & G_k\langle H(f_0,\theta_k)\rangle = 0, \; \theta_k \in \Theta_2 \\ & \|\boldsymbol{L}^T\boldsymbol{w}\|^2 \leq \gamma \end{aligned} \tag{8.31}$$

where $i = 1, \cdots, N(\Theta_1)$ and $k = 1, \cdots, N(\Theta_2)$.

We can compare the number of constraints in (8.29), (8.30) and (8.31) as follows. In (8.29), there are $M_1 = N(\Omega_{pb}) \cdot [N(\Theta_1) + N(\Theta_2)]$ constraints. Formulation (8.30) has $M_2 = M_1 + 1$ constraints. In (8.31), there are $M_3 = N(\Theta_1) + N(\Theta_2) + 1$ constraints. We know that $N(\Omega_{pb}) \gg 1$ for broadband applications. $N(\Theta_1) + N(\Theta_2)$ is the number of angle grids in the whole spatial region where the features of the spatial responses are to be specified, so it will be a large value, normally up to tens or hundreds. Therefore, we can draw the conclusion that $M_3 \ll M_1$. That is to say, the number of constraints is reduced significantly by the efficient formulation. Since most of the involved constraints are quadratic or second-order-cone constraints, the computational complexity of the optimization formulation will be reduced significantly with the decreased number of such constraints.

8.4 Example of Synthesizing Single-Beam FIBP

The MinMax optimization criterion can be used to synthesize beampatterns with the uniform sidelobe level. The specifications are described as follows: The look-direction response is the unity response. The peak sidelobe level is optimized to be the minimum. It is expressed by the following formulation:

$$\begin{aligned} &\min_{\boldsymbol{w}} \ \epsilon \\ \text{subject to } &\boldsymbol{w}^T\boldsymbol{s}(f_m,\theta_0) = 1, \quad f_m \in \Omega_{pb} \\ &|\boldsymbol{w}^T\boldsymbol{s}(f_m,\theta_n)| \leq \epsilon, \ f_m \in \Omega_{pb}, \ \theta_n \in \Theta_{sl} \\ &\|\boldsymbol{w}\| \leq \gamma_{\boldsymbol{w}} \end{aligned} \tag{8.32}$$

where Θ_{sl} represents the sidelobe region. θ_0 is the look direction. ϵ denotes the peak sidelobe level. The weight norm constraint $\|\boldsymbol{w}\| \leq \gamma_{\boldsymbol{w}}$ is used to improve the robustness of the beamformer against the random errors of the array characteristics. This is a convex optimization problem which we can solve by the interior point method. In this optimization, the look-direction response constraints and the sidelobe constraints are imposed on frequencies over the whole interested frequency band Ω_{pb}.

Based on the idea presented in Section 8.3.2, the direct application of the SRV constraint in the MinMax optimization (MinMax-SRV, for short) is formulated as:

$$\begin{aligned} &\min_{\boldsymbol{w}} \ \epsilon \\ \text{subject to } &\boldsymbol{w}^T\boldsymbol{s}(f_m,\theta_0) = 1, \quad f_m \in \Omega_{pb} \\ &|\boldsymbol{w}^T\boldsymbol{s}(f_m,\theta_n)| \leq \epsilon, \ f_m \in \Omega_{pb}, \ \theta_n \in \Theta_{sl} \\ &\|\boldsymbol{w}\| \leq \gamma_{\boldsymbol{w}} \\ &\|\boldsymbol{L}^T\boldsymbol{w}\|^2 \leq \gamma \end{aligned} \tag{8.33}$$

The efficient MinMax optimization using the SRV constraint (E-MinMax-SRV, for short) is formulated as:

$$\begin{aligned} &\min_{\boldsymbol{w}} \ \epsilon \\ \text{subject to } &\boldsymbol{w}^T\boldsymbol{s}(f_m,\theta_0)=1, \ \ f_m\in\Omega_{pb} \\ &|\boldsymbol{w}^T\boldsymbol{s}(f_0,\theta_n)|\leq\epsilon, \ \theta_n\in\Theta_{sl} \\ &\|\boldsymbol{w}\|\leq\gamma_{\boldsymbol{w}} \\ &\|\boldsymbol{L}^T\boldsymbol{w}\|^2\leq\gamma \end{aligned} \tag{8.34}$$

Assuming the frequency invariance is desired for the whole field of view, for both (8.33) and (8.34), Θ_{FI} is specified to be $[-90°,\theta_0)\cup(\theta_0,90°]$ for computing the matrix $\boldsymbol{L}$. The unity response constraint in the look direction is imposed on the whole frequency band to achieve the strict unity response in this example. If the requirement for the look-direction response is not so strict, the first set of constraints in (8.34) can be reduced to be $\boldsymbol{w}^T\boldsymbol{s}(f_0,\theta_0)=1$. In this case, θ_0 should be included in Θ_{FI} to guarantee the approximate unity response within Ω_{pb} in the look direction.

The number of constraints in (8.34) is significantly reduced relative to (8.32). The beampatterns synthesized by (8.33) and (8.34) possess the frequency invariant property over the operating band at specified directions if γ is small enough.

For the convenience of using the optimization tool SeDuMi [89], we assume M frequency grids within the passband represented by $f_m, m=1,2,\cdots,M$ and N direction grids in the sidelobe region represented by $\theta_n, n=1,2,\cdots,N$. The E-MinMax-SRV (8.34) is expressed in the following dual standard form of the second-order-cone programming (SOCP):

$$\begin{aligned} &\max_{\boldsymbol{y}} \ \boldsymbol{b}^T\boldsymbol{y} \\ &\text{subject to } \boldsymbol{c}-\boldsymbol{A}^T\boldsymbol{y}\in\kappa \end{aligned} \tag{8.35}$$

where κ represents a symmetric cone. $\boldsymbol{b}$ is a constant vector:

$$\boldsymbol{b}=[-1 \ \ 0 \ \ \cdots \ \ 0]^T \tag{8.36}$$

$\boldsymbol{y}$ includes the optimization variables ϵ and $\boldsymbol{w}$:

$$\boldsymbol{y} = [\epsilon \;\; \boldsymbol{w}^T]^T \tag{8.37}$$

$\boldsymbol{c}$ is defined as:

$$\boldsymbol{c} = [c_1 \;\; \cdots \;\; c_M \;\; \boldsymbol{c}_{M+1}^T \;\; \cdots \;\; \boldsymbol{c}_{M+N}^T \;\; \boldsymbol{c}_{M+N+1}^T \;\; \boldsymbol{c}_{M+N+2}^T]^T \tag{8.38}$$

and $\boldsymbol{A}^T$ is defined as:

$$\boldsymbol{A}^T = [\boldsymbol{A}_1 \;\; \cdots \;\; \boldsymbol{A}_M \;\; \boldsymbol{A}_{M+1} \;\; \cdots \;\; \boldsymbol{A}_{M+N} \;\; \boldsymbol{A}_{M+N+1} \;\; \boldsymbol{A}_{M+N+2}]^T \tag{8.39}$$

The elements in $\boldsymbol{c}$ and $\boldsymbol{A}^T$ are obtained by re-expressing the constraints in (8.34) as the zero-cone and quadratic-cone constraints as follows:

$$\begin{bmatrix} 1 \end{bmatrix} - \begin{bmatrix} 0 & \boldsymbol{s}^H(f_m, \theta_0) \end{bmatrix} \boldsymbol{y} = c_m - \boldsymbol{A}_m^T \boldsymbol{y} \in \{0\}^1 \tag{8.40}$$

$$\begin{bmatrix} 0 \\ 0 \end{bmatrix} - \begin{bmatrix} -1 & \mathbf{0}^T \\ 0 & -\boldsymbol{s}^H(f_0, \theta_n) \end{bmatrix} \boldsymbol{y} = \boldsymbol{c}_{M+n} - \boldsymbol{A}_{M+n}^T \boldsymbol{y} \in \{Q\}^2 \tag{8.41}$$

$$\begin{bmatrix} \gamma_{\boldsymbol{w}} \\ \mathbf{0} \end{bmatrix} - \begin{bmatrix} 0 & \mathbf{0}^T \\ \mathbf{0} & -\boldsymbol{I} \end{bmatrix} \boldsymbol{y} = \boldsymbol{c}_{M+N+1} - \boldsymbol{A}_{M+N+1}^T \boldsymbol{y} \in \{Q\}^{LJ+1} \tag{8.42}$$

$$\begin{bmatrix} \sqrt{\gamma} \\ \mathbf{0} \end{bmatrix} - \begin{bmatrix} 0 & \mathbf{0}^T \\ \mathbf{0} & -\boldsymbol{L}^T \end{bmatrix} \boldsymbol{y} = \boldsymbol{c}_{M+N+2} - \boldsymbol{A}_{M+N+2}^T \boldsymbol{y} \in \{Q\}^{r+1} \tag{8.43}$$

where $\boldsymbol{c}_i$ and $\boldsymbol{A}_i^T$ are equivalent to the constant vectors or matrices on the left side of equations (8.40)-(8.43). r is the number of columns of $\boldsymbol{L}$, equivalent to the rank of the matrix $\overline{\boldsymbol{C}}_r$. $\{0\}$ and $\{Q\}$ represent the zero cone and quadratic cone, respectively.

By (8.36) - (8.43), the software SeDuMi can be used to solve the convex conic optimization problem (8.34) easily. The parameter γ should be adjusted if the infeasibility is reported by the optimization tool. The MinMax (8.32) and MinMax-SRV (8.33) can be reformulated in the dual standard form of the SOCP in the same way.

Simulations on a uniform linear array with 15 sensors and 15 taps per element are performed. The normalized operating frequency band of the array is assumed to be $[0.2, 0.4]$. The sensor spacing is one half of the wavelength corresponding to the maximum frequency. The look direction is $0°$ and the sidelobe region is specified to be $[-90°, -15°] \cup [15°, 90°]$. The spacing of the frequency grid is chosen to be 0.01 and the angle spacing is chosen to be $5°$. During the computation of the matrix $\boldsymbol{L}$, Θ_{FI} is $[-90°, 0°) \cup (0°, 90°]$, with the grid spacing chosen to be $5°$. Figure 8.1 shows the beampatterns at 21 discrete frequencies within $[0.2, 0.4]$ synthesized by MinMax (8.32). Figures 8.2 and 8.3 demonstrate the beampatterns synthesized by MinMax-SRV (8.33) and E-MinMax-SRV (8.34), respectively, with the threshold γ in the SRV constraint chosen to be $4.0e-5$ and the reference frequency chosen to be $f_0 = f_l$. In the weight-norm constraint, $\gamma_{\boldsymbol{w}}$ is chosen to be 100.

Figure 8.3 proves that although the sidelobe constraints are imposed on only one reference frequency point, effective broadband beampatterns can be achieved by using the SRV constraint. Relative to the beampattern obtained by MinMax, the sidelobe levels in Figures 8.2 and 8.3 are a little higher but the frequency invariant property is much better in the whole field of view. It should be noted that f_0 can be selected according to the quality of the produced beampatterns.

Moreover, the peak sidelobe level for the beampatterns averaged over the frequency band, the number of constraints involved in the optimization, the CPU time spent in solving the optimization problem using SeDuMi and the value of the average SRV of the synthesized

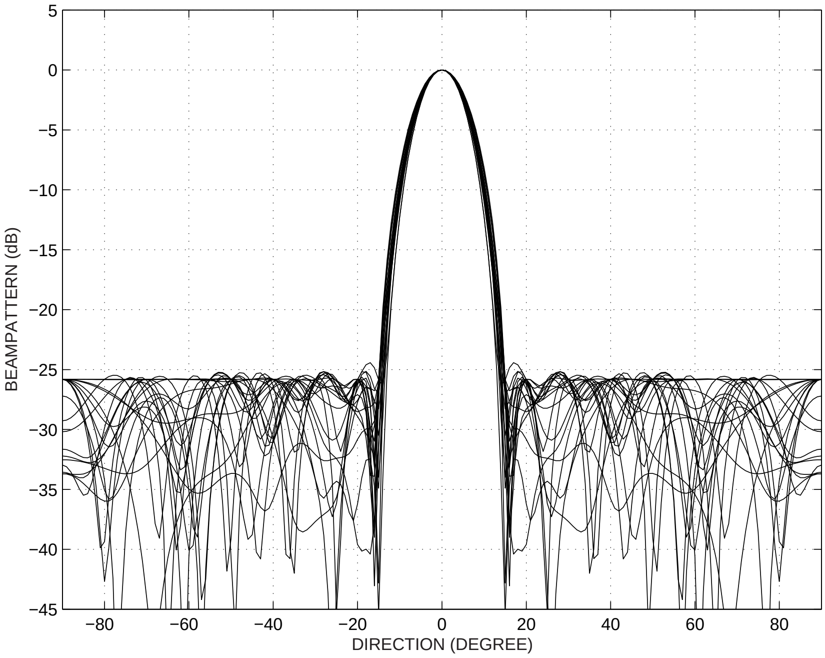

Figure 8.1. Beampatterns synthesized by MinMax at 21 discrete frequencies within $[0.2, 0.4]$.

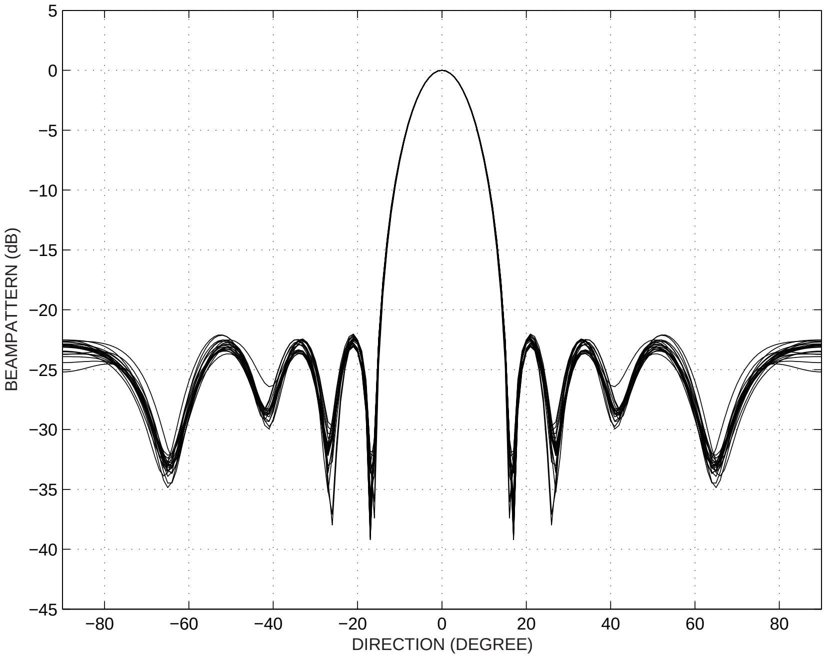

Figure 8.2. Beampatterns synthesized by MinMax-SRV at 21 discrete frequencies within $[0.2, 0.4]$, with $\gamma = 4.0e - 5$ and $f_0 = f_l$.

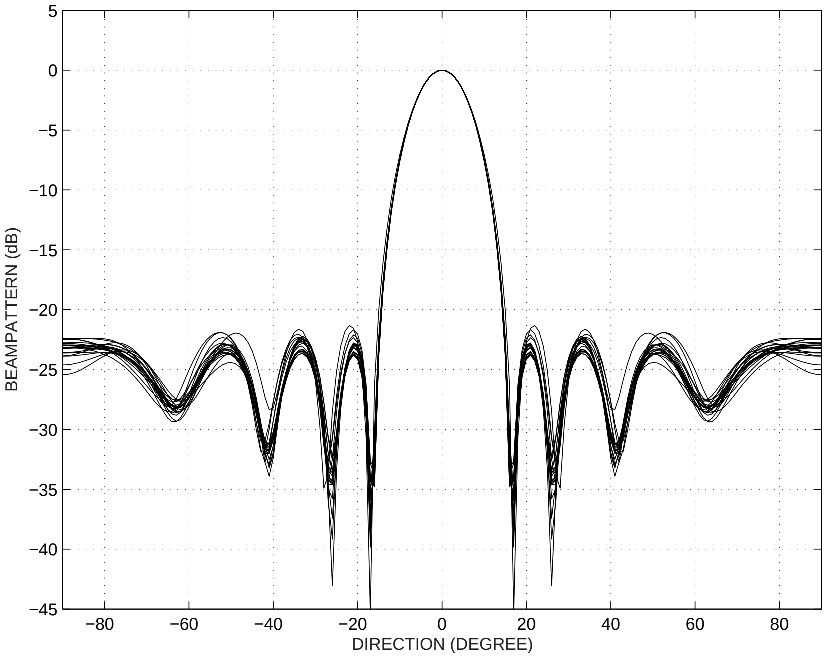

Figure 8.3. Beampatterns synthesized by E-MinMax-SRV at 21 discrete frequencies within $[0.2, 0.4]$, with $\gamma = 4.0e - 5$ and $f_0 = f_l$.

Table 8.1: COMPARISONS BETWEEN THE MINMAX, MINMAX-SRV AND E-MINMAX-SRV

Method	Averaged Peak Sidelobe Level (dB)	Number of Constraints	CPU Time (Seconds)	$\overline{\text{SRV}}$
MinMax	-26.9	694	26.4	2.8e-3
MinMax-SRV	-22.6	695	19.8	3.9e-5
E-MinMax-SRV	-22.8	55	2.9	3.9e-5

beampattern in the above example are listed in Table 8.1. We observe that both MinMax-SRV and E-MinMax-SRV generate beampatterns with smaller average SRV. Relative to MinMax, the number of constraints and the computational time of E-MinMax-SRV are reduced by about 10 times.

For the broadband uniform linear array with the broadside look direction, its directivity and white noise gain as the function of frequency are defined as follows [87]:

$$G_d(f) = \frac{\left|\sum_{m=0}^{L-1} H_m(f)\right|^2}{\sum_{m=0}^{L-1}\sum_{n=0}^{L-1} H_m(f)H_n^*(f)\text{sinc}[2(m-n)d/\lambda]} \tag{8.44}$$

$$G_w(f) = \frac{\left|\sum_{m=0}^{L-1} H_m(f)\right|^2}{\sum_{m=0}^{L-1}\sum_{n=0}^{L-1} H_m(f)H_n^*(f)} \tag{8.45}$$

where λ is the wavelength corresponding to the frequency f. sinc$(\alpha) = \sin(\pi\alpha)/(\pi\alpha)$. $H_m(f)$ and $H_n(f)$ represent the frequency response of the filter after the mth and nth sensors, respectively. Figures 8.4 and 8.5 demonstrate the directivity and the white noise gain curves of the beampatterns in the above example. We observe that MinMax-SRV and E-MinMax-SRV generate beampatterns with lower but much flatter directivity within the desired frequency band relative to MinMax. This, from another aspect, proves the improved frequency invariance due to the application of the SRV constraint in the optimizations for pattern synthesis. Moreover, MinMax, MinMax-SRV and E-MinMax-SRV generate beampatterns with similar white noise gain at frequencies higher than 0.32. For other lower frequencies, MinMax-SRV and E-MinMax-SRV have higher white noise gain than MinMax. At frequencies lower than 0.22, the white noise gain of MinMax decreases to the level below -30dB. This means high sensitivity of the beampattern to the array imperfections.

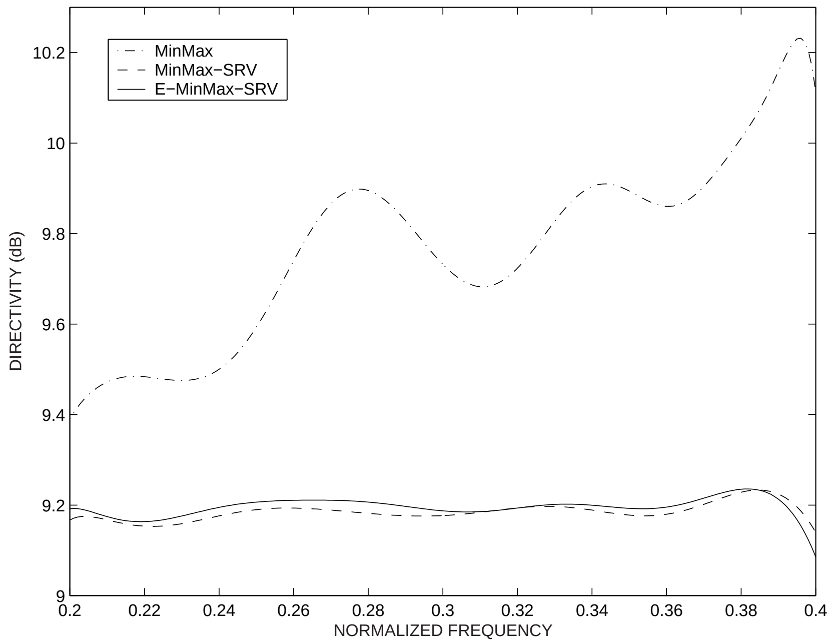

Figure 8.4. Directivity within the frequency range $[0.2, 0.4]$ for the beampatterns synthesized by MinMax, MinMax-SRV and E-MinMax-SRV.

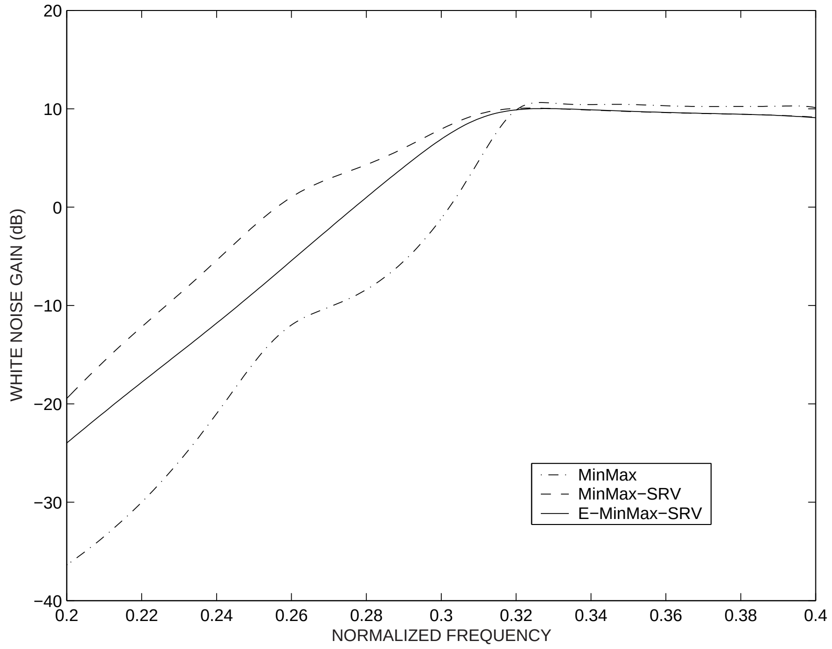

Figure 8.5. White noise gain within the frequency range $[0.2, 0.4]$ for the beampatterns synthesized by MinMax, MinMax-SRV and E-MinMax-SRV.

8.5 Example of Constructing Multi-Beam Forming Network

Beamspace adaptive arrays use a small number of adaptive weights and demonstrate better convergence performance than the conventional Griffiths-Jim beamformer. For broadband scenarios, the frequency invariance should be guaranteed for the beampattern of each beam such that the broadband interferences are not distorted in both the main beam and the auxiliary beams and hence can be suppressed. In [80], the fan filters are designed to construct the multi-beam forming network for the broadband beamspace adaptive array. Since the optimization using the SRV constraint can achieve the FIBP in the whole field of view, we utilize the proposed pattern synthesis method to construct the multi-beam forming network for the beamspace adaptive array.

Based on the idea of the efficient formulation (8.31), in the multi-beam forming network, the main beam pointing to the look direction θ_0 is designed by the following optimization:

$$\begin{aligned} &\min_{\boldsymbol{w}} \ \epsilon \\ \text{subject to } &\int_{\Omega_{pb}} |\boldsymbol{w}^T \boldsymbol{s}(f,\theta_0) - 1|^2 df \le 10^{\gamma_m/10} \\ &|\boldsymbol{w}^T \boldsymbol{s}(f_0,\theta)| \le \epsilon, \quad \theta \in \Theta_{sl} \\ &\|\boldsymbol{w}\| \le \gamma_{\boldsymbol{w}} \\ &\|\boldsymbol{L}^T \boldsymbol{w}\|^2 \le \gamma \end{aligned} \tag{8.46}$$

In this optimization formulation, the maximum sidelobe level is minimized. The response at θ_0 is constrained to be close to the unity response. γ_m is a small positive constant representing the amplitude of the ripple of the response in the look direction of the main beam. Θ_{FI} for the SRV constraint is specified to be the whole field of view to compute $\boldsymbol{L}$

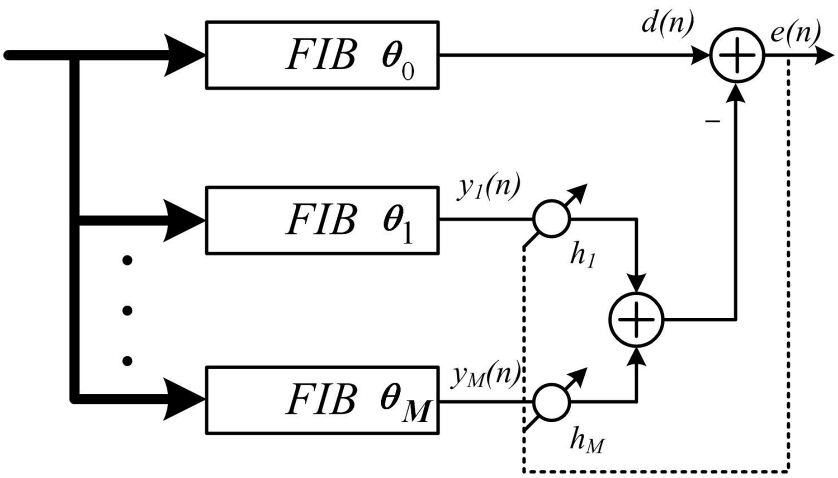

Figure 8.6. Broadband beamspace adaptive array using frequency invariant beamformers (FIBs), with the main beam pointing to θ_0 and the auxiliary beams pointing to $\theta_1, \cdots, \theta_M$.

so that the signals coming from any directions are not distorted in the main beam.

The auxiliary beams pointing to θ_i are designed as follows:

$$\begin{aligned} &\min_{\boldsymbol{w}} \ \epsilon \\ \text{subject to } &\int_{\Omega_{pb}} |\boldsymbol{w}^T \boldsymbol{s}(f,\theta_i) - 1|^2 df \leq 10^{\gamma_a/10} \\ &\int_{\Omega_{pb}} |\boldsymbol{w}^T \boldsymbol{s}(f,\theta_0) - \delta|^2 df \leq 10^{\gamma_m/10} \\ &|\boldsymbol{w}^T \boldsymbol{s}(f_0,\theta)| \leq \epsilon, \quad \theta \in \Theta_{sl} \\ &\|\boldsymbol{w}\| \leq \gamma_{\boldsymbol{w}} \\ &\|\boldsymbol{L}^T \boldsymbol{w}\|^2 \leq \gamma \end{aligned} \tag{8.47}$$

In this formulation, Θ_{FI} is also specified to be the whole field of view to compute $\boldsymbol{L}$. δ is a small positive constant to specify a very low gain in the main beam direction to suppress the signal coming from θ_0. γ_a and γ_m are small positive constants representing the amplitudes of the ripples of the response in the look direction of the auxiliary beams and the main beam, respectively. This optimization is carried out once for each auxiliary beam.

Figure 8.6 shows the beamspace adaptive array with the structure same as that presented in [80, 82] but with the multi-beam forming network constructed by the weight vectors computed by (8.46) and (8.47). The output of the main beam is $d(n)$. A group of adaptive weights h_i are multiplied to the outputs of the auxiliary beams $y_i(n)$. The output of the beamspace adaptive array is

$$e(n) = d(n) - \boldsymbol{h}^T \boldsymbol{y}(n) \tag{8.48}$$

where

$$\boldsymbol{h} = [h_1 \;\; h_2 \;\; \cdots \;\; h_M]^T \tag{8.49}$$

$$\boldsymbol{y}(n) = [y_1(n) \;\; y_2(n) \;\; \cdots \;\; y_M(n)]^T \tag{8.50}$$

The real-valued weight vector $\boldsymbol{h}$ is adjusted by the error signal $e(n)$ with adaptive algorithms.

A uniform linear array with 15 isotropic sensors is used. $L = 15$ and $J = 25$ are assumed to generate each beam in the multi-beam forming network. The desired signal comes from $0°$. Three interferences come from $-40°$, $-25°$ and $30°$. The frequency band for all the directional sources is assumed to be $\Omega_{pb} = [0.1, 0.3]$. The input SIR for each interference is chosen to be -25dB. Bandpassed white noise is added to each sensor, with the input SNR 30dB. Five sets of frequency invariant beampatterns are synthesized for the multi-beam forming network, with the main beam pointing to the look direction $0°$ and four auxiliary beams pointing to $\pm 53°$ and $\pm 24°$, respectively. The normalized LMS algorithm [114] is used to compute the adaptive weights. The step size is chosen to be 0.01. The fan-filter method proposed in [80] is simulated with the same parameters for the above scenario for comparison. In this method, the length of the prototype filter is chosen to be 5. According to [80], by choosing the beam directions to be $\{0°, \pm 24°, \pm 53°\}$, the look direction of each beam nearly coincides with the null directions of the other beams. In our proposed method, all the auxiliary beams are designed to have a null in the look direction of the main beam. The parameters in (8.46) and (8.47) to construct the multi-beam forming network are chosen to be $\gamma_m = \gamma_a = -40$dB, $\delta = 0.01$, $\gamma_{\boldsymbol{w}} = 100$ and $\gamma = 2.0e-5$. The sidelobe region Θ_{sl} is $[-90°, \theta_0 - 20°] \cup [\theta_0 + 20°, 90°]$ for (8.46) and $[-90°, \theta_i - 20°] \cup [\theta_i + 20°, 90°]$ for (8.47). Θ_{FI} is $[-90°, 90°]$. The grid spacing for both Θ_{sl} and Θ_{FI} is chosen to be $5°$.

Figures 8.7 and 8.8 show the beampatterns of the beamspace adaptive array after 3000 iterations, with the multi-beam forming network constructed by the fan-filter method [80] and the proposed method, respectively. The beampatterns averaged over the frequency range $[0.1, 0.3]$ are demonstrated in Figure 8.9. Figure 8.10 shows the output SINR convergence curves. All the results are obtained by averaging over 200 simulation trials. We observe that the beampattern of the beamspace adaptive array produced by the proposed method has better frequency invariance and deeper nulls than the fan-filter method. In the averaged beampatterns, the nulling depths in the directions of interferences obtained by the proposed method are -41.4dB, -41.6dB and -40.3dB while those obtained by the fan-filter method are -35.5dB, -37.8dB and -37.1dB. Moreover, the response in the look direction achieved by the proposed method is closer to the unity response than the fan-filter method. Relative to the fan-filter method, the proposed method obtains better output SINR in both the transient state and the steady state.

In the fan-filter method, the length of the prototype filter, which determines the shape of the beampattern, is restricted by the number of sensors, which affects the frequency invariance of the beampattern. This method does not provide the optimum tradeoff between the frequency invariance and the sidelobe level of the beampattern. The proposed method can accomplish this tradeoff for the given numbers of sensors and taps, so we achieve the

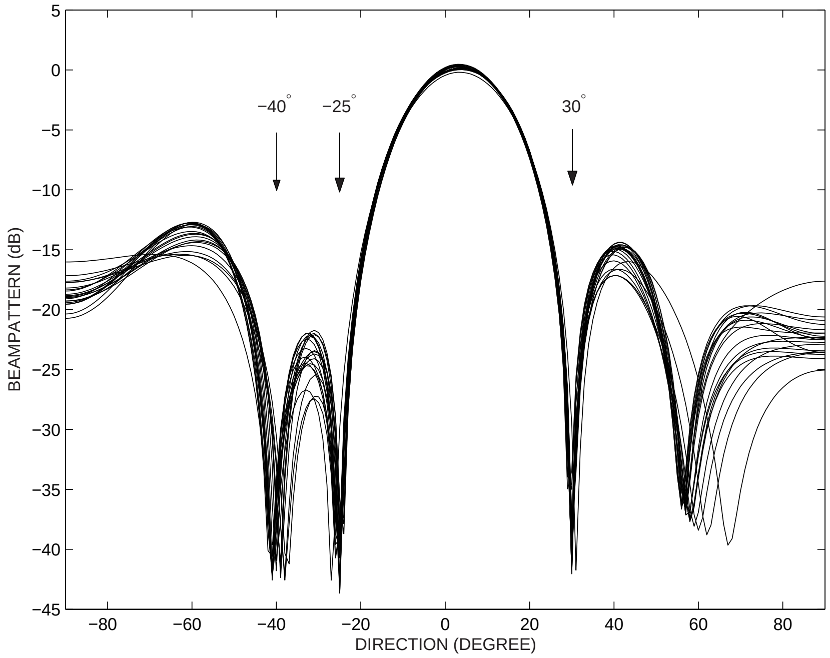

Figure 8.7. Beampatterns of the beamspace adaptive array at 21 frequencies uniformly distributed within $[0.1, 0.3]$, with the multi-beam forming network constructed by the fan-filter method. The interferences come from $-40°$, $-25°$ and $30°$.

improved performance in the above beamspace adaptive array.

Besides the above comparisons, relative to the fan-filter method, the proposed method has the following potential superiorities: First, the array geometry is not limited to uniform arrays. Second, the number of auxiliary beams is not restricted by the number of sensors. With more auxiliary beams, the performance of the beamspace adaptive array can be improved further. Third, the null directions for all the beams can be specified arbitrarily. We do not have to restrict the look direction of each beam to make sure they coincide with the null directions of the other beams.

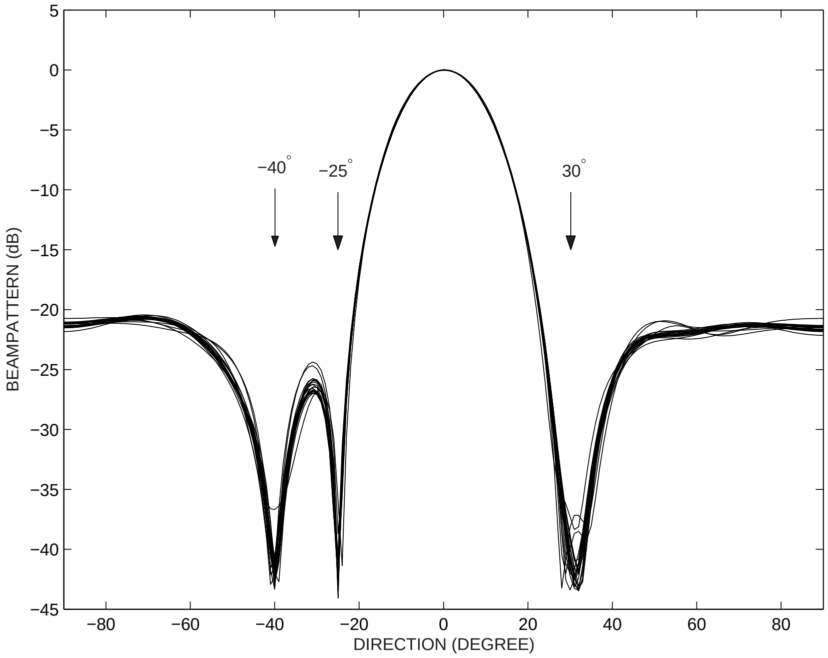

Figure 8.8. Beampatterns of the beamspace adaptive array at 21 frequencies uniformly distributed within $[0.1, 0.3]$, with the multi-beam forming network constructed by the proposed method. The interferences come from $-40°$, $-25°$ and $30°$.

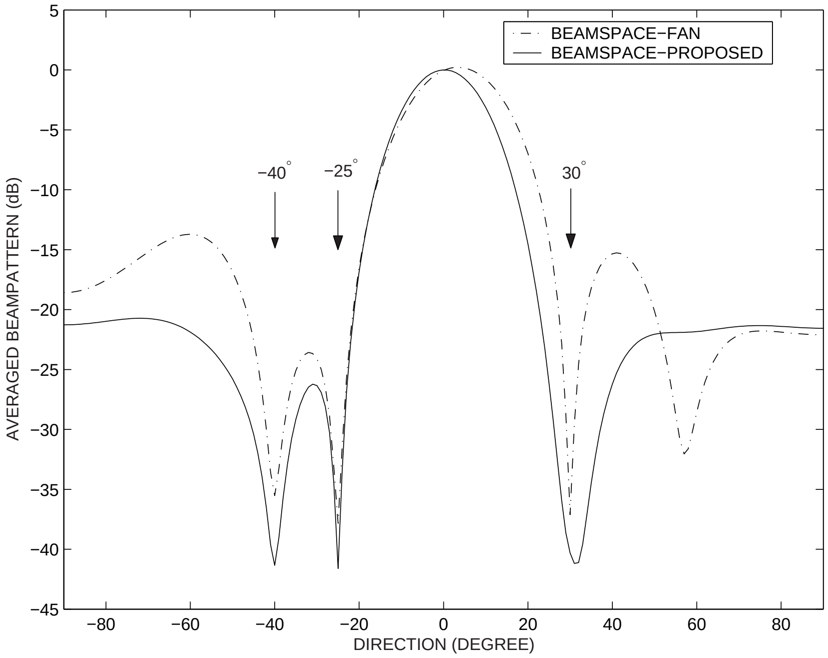

Figure 8.9. Beampatterns averaged over $[0.1, 0.3]$ obtained by the fan-filter method and the proposed method.

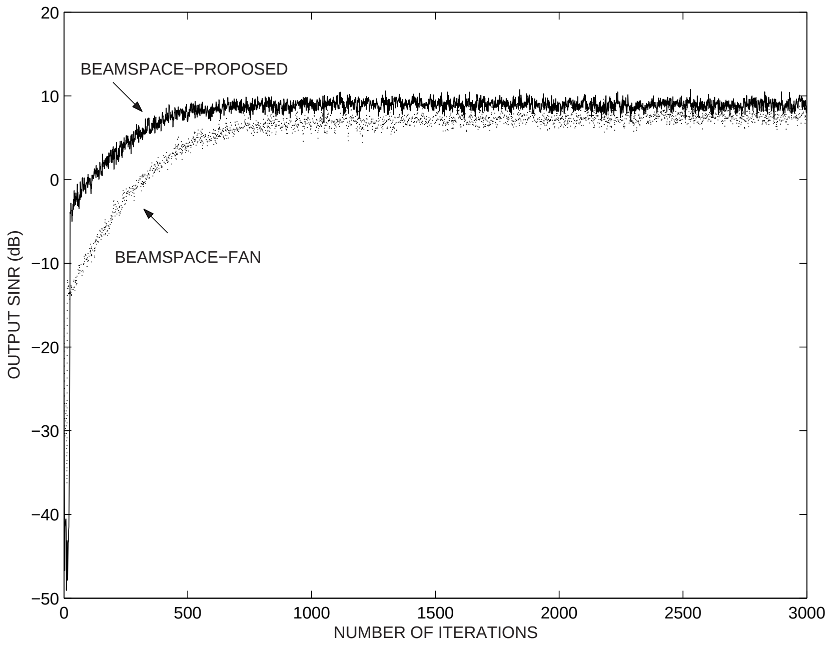

Figure 8.10. Output SINR convergence curves of the beamspace adaptive array averaged over 200 trials. The step size is 0.01 in the normalized LMS algorithm.

8.6 Conclusion

In this chapter, the SRV constraint is defined to restrict the fluctuations of the spatial responses over the desired frequency band for the broadband array. The direct application of the SRV constraint in the optimization formulations of the broadband pattern synthesis problems to produce the FIBP is presented. An efficient approach by using the SRV constraint to simplify broadband array synthesis formulations is investigated. The examples of designing the single-beam FIBP and multi-beam forming network are demonstrated to show the effect of applying the SRV constraint in broadband pattern synthesis. It is found that when the array operating bandwidth is large, especially when lower frequencies are involved in the operating band, the efficient pattern synthesis method using the SRV constraint does not work well. We hope to combine the idea of subband with scaled aperture presented in [127] to solve this problem in the future.

Chapter 9

Conclusions and Future Work

In this chapter, we conclude the studies presented in this thesis and propose some suggestions for the future work.

9.1 Conclusions

In this thesis, we have investigated several topics in broadband array signal processing, including the broadband adaptive beamformer design, performance analysis for broadband beamforming using nonuniform linear arrays and the broadband pattern synthesis techniques.

In Chapter 3, three types of constrained optimization criteria, including the norm-constrained optimization, the frequency-response-constrained optimization and the amplitude-response-constrained optimization, have been proposed to design the look-direction amplitude/phase response to optimize the Frost beamformer. It is shown that the beamformer designed with the new methods can achieve improved interference and noise suppression performance relative to the beamformer with the distortionless constraint.

To reduce the number of weights in broadband time-domain beamformers, the beamforming structure using TDL-form IIR filters has been designed in Chapter 4. The combined LMS algorithm for updating the feedforward and feedback weight vectors has been developed. Moreover, the derivative constraints for obtaining the broadened beamwidth have been derived for the IIR beamformer. The performance improvement of the new IIR beamformer relative to the Frost beamformer is demonstrated by simulation examples.

As an extension of the study in Chapter 4, Chapter 5 has presented the beamformer using second-order IIR sections in place of the first-order IIR sections to allow complex poles. To improve the convergence rate, the combined RGN algorithm has been developed for the Frost-based implementation. The GSC-based implementation has been presented with the unconstrained RGN algorithm designed to compute the weights. Analysis and simulation results show that the new IIR beamformers offer much easier stability monitoring and less sensitivity to the coefficient quantization error than the beamformer using direct-form IIR filters, while comparable SINR improvement over the conventional FIR beamformer is achieved.

Based on the assumption of the ideal continuous-time, infinite-length filters, approximate formulations have been derived in Chapter 6 for computing the 3-dB beamwidth of the broadband LCMV beamformer using MRA and NRA. The accuracy of the derived formulations has been assessed by numerical studies for various scenarios. The comparisons of the beamwidths between MRA, NRA and ULA by these formulations show the superiority of the former two types of geometries in improving the spatial resolution.

In Chapter 7, the broadband interference suppression performance of the MRA has been analyzed. The formulations for computing the optimum power spectra of the beamformer output in different scenarios under the assumption of the ideal temporal filters and the LCMV optimization criterion have been derived to compute the array output power. Several properties about the performance of the MRA compared with that of the ULA have been obtained by mathematical proofs and graphic illustrations. It is proven that for interferences with small FBW, MRA can offer better cancellation performance at angles close to the broadside direction. As the FBW increases, the region of directions where the MRA performs better than the ULA becomes larger. When the FBW is higher than a certain level, MRA can outperform ULA in all directions (except $0°$).

In Chapter 8, the SRV constraint has been defined to reduce the fluctuations of the spatial responses within the desired frequency range for the broadband array. The direct application of the SRV constraint in the optimization formulations for the broadband pattern synthesis problems to produce the FIBP has been studied. It is found that by using the SRV constraint, broadband pattern synthesis problems can be formulated in an efficient way. The effect of applying the SRV constraint in broadband pattern synthesis has been demonstrated by examples of designing the single-beam FIBP and multi-beam forming network.

9.2 Future Work

Based on the studies in this thesis, several suggestions for the future research work are proposed as follows:

The performance improvement of the broadband beamformers proposed in Chapter 3 has been demonstrated by simulation examples. Mathematical analysis for the output SINR in terms of parameters such as the input SNR, finite sample size and so on can be performed in the future studies.

We have developed adaptive algorithms for the broadband beamformer with the structure using TDL-form IIR filters in Chapters 4 - 5. Developing algorithms to synthesize the data-independent IIR beamformer is suggested to be studied in the future. The IIR beamforming structure is expected to provide equivalent performance with less number of weighting coefficients relative to the FIR beamforming structure in the data-independent beamformers as well.

The discussions in Section 5.5 on the convergence and stability have presented the evaluation of the step sizes and the monitoring criteria of the poles in IIR filters. They are based on experiments or empirical values presented in literatures. To get a sufficient condition to guarantee the stability and convergence of the proposed adaptive algorithms, the analysis on the weight error vector should be performed. This is a difficult but important work for the proposed IIR beamformers.

The performance analysis of the broadband beamformer using MRA has been presented in Chapter 7 based on the assumption of using the ideal temporal filters. In real implementations, more factors, like the filter length and the temporal sampling interval, should be considered besides the operating bandwidth. Therefore, performance analysis for the realistic broadband beamformer using MRA is proposed to be one of the future researches.

Our simulation results show that when the array operating bandwidth is large, especially when lower frequencies are involved in the operating band, the efficient pattern synthesis method using the SRV constraint presented in Chapter 8 does not work well. We hope to combine the idea of subband with scaled aperture presented in [127] to solve this problem. A brief description of this scheme is as follows: The array signals are divided into a set of narrower frequency bands. Each sub-array processes one frequency band and has a matched aperture. The SRV-constrained algorithm is used to generate the frequency invariant beampattern within a narrower bandwidth in each sub-array.

Author's Publications

Journal Articles

1. Huiping Duan, Boon Poh Ng and Chong Meng Samson See, "A new broadband beamformer using IIR filters", *IEEE Signal Processing Lett.*, Vol. 12, No. 11, pp. 776-779, Nov. 2005.

2. Huiping Duan, Boon Poh Ng, Chong Meng Samson See and Jun Fang, "Broadband beamforming using TDL-form IIR filters", *IEEE Trans. Signal Processing*, Vol. 55, No. 3, pp. 990-1002, Mar. 2007.

3. Boon Poh Ng and Huiping Duan, "Designing amplitude/phase response of the Frost beamformer", *IEEE Trans. Signal Processing*, Vol. 55, No. 5, Part 1, pp. 1944-1949, May. 2007.

4. Huiping Duan, Boon Poh Ng, Chong Meng Samson See and Jun Fang, "Spatial resolutions of the broadband nonredundant and minimum redundancy arrays", *IEEE Signal Processing Lett.*, Vol. 14, No. 11, pp. 852-855, Nov. 2007.

5. Huiping Duan, Boon Poh Ng, Chong Meng Samson See and Jun Fang, "Broadband interference suppression performance of minimum redundancy arrays", Accepted by *IEEE Trans. Signal Processing.*, 2007.

6. Huiping Duan, Boon Poh Ng, Chong Meng Samson See and Jun Fang, "Applications of the SRV constraint in broadband pattern synthesis", *Signal Processing*, Vol. 88, No. 4, pp. 1035-1045, Apr. 2008.

Bibliography

[1] B. D. V. Veen and K. M. Buckley, “Beamforming: a versatile approach to spatial filtering,” *IEEE ASSP Mag.*, pp. 1–24, Apr. 1988.

[2] H. Krim and M. Viberg, “Two decades of array signal processing research: the parametric approach,” *IEEE Signal Processing Mag.*, pp. 67–94, July 1996.

[3] L. C. Godara, “Application of antenna arrays to mobile communications, part II: beam-forming and direction-of-arrival considerations,” *Proc. IEEE*, vol. 85, no. 8, pp. 1195–1245, Aug. 1997.

[4] H. L. V. Trees, *Optimum Array Processing: Part IV of Detection, Estimation and Modulation Theory*. New York: Wiley, 2002.

[5] L. C. Godara, *Smart Antennas*. CRC Press LLC, 2004.

[6] B. Widrow, P. E. Mantey, L. J. Griffiths, and B. B. Goode, “Adaptive antenna systems,” *Proc. IEEE*, vol. 55, no. 12, pp. 2143–2159, Dec. 1967.

[7] O. L. F. III, “An algorithm for linearly constrained adaptive array processing,” *Proc. IEEE*, vol. 60, no. 8, pp. 926–935, Aug. 1972.

[8] L. J. Griffiths and C. W. Jim, "An alternative approach to linearly constrained adaptive beamforming," *IEEE Trans. Antennas Propagat.*, vol. 30, no. 1, pp. 27–34, Jan. 1982.

[9] K. M. Buckley, "Broad-band beamforming and the generalized sidelobe canceller," *IEEE Trans. Signal Processing*, vol. 34, no. 5, pp. 1322–1323, Oct. 1986.

[10] B. R. Breed and J. Strauss, "A short proof of the equivalence of LCMV and GSC beamforming," *IEEE Signal Processing Lett.*, vol. 9, no. 6, pp. 168–169, June 2002.

[11] S. Werner, J. J. A. Apolinario, and M. L. R. de Campos, "On the equivalence of RLS implementations of LCMV and GSC processors," *IEEE Signal Processing Lett.*, vol. 10, no. 12, pp. 356–359, Dec. 2003.

[12] E. M. Dowling, D. A. Linebarger, Y. Tong, and M. Munoz, "An adaptive microphone array processing system," *Microprocessors and Microsystems*, vol. 16, no. 10, pp. 507–516, Sept. 1992.

[13] M. Strupl and P. Sovka, "Analysis and simulation of Frost's beamformer," *Radioengineering*, vol. 12, no. 2, pp. 1–9, June 2003.

[14] J. T. Mayhan, "Some techniques of evaluating the bandwidth characteristics of adaptive nulling systems," *IEEE Trans. Antennas Propagat.*, vol. 27, no. 3, pp. 363–373, May 1979.

[15] J. T. Mayhan, A. J. Simmons, and W. C. Cummings, "Wide-band adaptive antenna nulling using tapped delay lines," *IEEE Trans. Antennas Propagat.*, vol. 29, no. 6, pp. 923–936, Nov. 1981.

[16] I. J. Gupta, "Effect of jammer power on the performance of adaptive arrays," *IEEE Trans. Antennas Propagat.*, vol. 32, no. 9, pp. 933–938, Sept. 1984.

[17] R. T. C. Jr., “The bandwidth performance of a two-element adaptive array with tapped delay-line processing,” *IEEE Trans. Antennas Propagat.*, vol. 36, no. 1, pp. 5–14, Jan. 1988.

[18] F. W. Vook and R. T. C. Jr., “Bandwidth performance of linear adaptive arrays with tapped delay-line processing,” *IEEE Trans. Aerosp. Electron. Syst.*, vol. 28, no. 3, pp. 901–908, July 1992.

[19] R. P. Gooch and J. J. Shynk, “Wide-band adaptive array processing using pole-zero digital filters,” *IEEE Trans. Antennas Propagat.*, vol. 34, no. 3, pp. 355–367, Mar. 1986.

[20] C. N. Adkins and J. J. Turtora, “A broadband beam former with pole-zero unconstrained jammer rejection in linear arrays,” *IEEE Trans. Signal Processing*, vol. 44, no. 2, pp. 438–441, Feb. 1996.

[21] M. Joho and G. S. Moschytz, “On the design of the target-signal filter in adaptive beamforming,” *IEEE Trans. Circuits Syst. II*, vol. 46, no. 7, pp. 963–966, July 1999.

[22] M. Ghavami and R. Kohno, “Recursive fan filters for a broad-band partially adaptive antenna,” *IEEE Trans. Commun.*, vol. 48, no. 2, pp. 185–188, Feb. 2000.

[23] W. Liu, S. Weiss, and L. Hanzo, “A subband-selective broadband GSC with cosine-modulated blocking matrix,” *IEEE Trans. Antennas Propagat.*, vol. 52, no. 3, pp. 813–820, Mar. 2004.

[24] S. Chandran, “Wideband adaptive beamforming array with improved radiation characteristics,” *IEEE Trans. Wireless Commun.*, vol. 4, no. 5, pp. 1969–1973, Sept. 2005.

[25] D. Korompis, K. Yao, and F. Lorenzlli, "Broadband maximum energy array with user imposed spatial and frequency constraints," *Proc. ICASSP-94*, pp. 529–532, Apr. 1994.

[26] S. Nordebo, I. Claesson, and S. Nordholm, "Adaptive beamforming: spatial filter designed blocking matrix," *IEEE Journal of Oceanic Engineering*, vol. 19, no. 4, pp. 583–590, Oct. 1994.

[27] F. Qian and B. D. V. Veen, "Partially adaptive beamforming for correlated interference rejection," *IEEE Trans. Signal Processing*, vol. 43, no. 2, pp. 506–515, Feb. 1995.

[28] S. J. Chern and C. Y. Sung, "The hybrid Frost's beamforming algorithm for multiple jammers suppression," *Signal Processing*, vol. 43, no. 2, pp. 113–132, May 1995.

[29] O. Hoshuyama, A. Sugiyama, and A. Hirano, "A robust adaptive beamformer for microphone arrays with a blocking matrix using constrained adaptive filters," *IEEE Trans. Signal Processing*, vol. 47, no. 10, pp. 2677–2684, Oct. 1999.

[30] R. L. Fante and J. J. Vaccaro, "Wideband cancellation of interference in a GPS receive array," *IEEE Trans. Aerosp. Electron. Syst.*, vol. 36, no. 2, pp. 549–564, Apr. 2000.

[31] S. Gannot, D. Burshtein, and E. Weinstein, "Signal enhancement using beamforming and nonstationarity with applications to speech," *IEEE Trans. Signal Processing*, vol. 49, no. 8, pp. 1614–1626, Aug. 2001.

[32] M. Koca and B. C. Levy, "Broadband beamforming with power complementary filters," *IEEE Trans. Signal Processing*, vol. 50, no. 7, pp. 1614–1626, July 2002.

[33] Q. Zou, Z. L. Yu, and Z. Lin, “A robust algorithm for linearly constrained adaptive beamforming,” *IEEE Signal Processing Lett.*, vol. 11, no. 1, pp. 26–29, Jan. 2004.

[34] M. E. Weber and R. Heisler, “A frequency-domain beamforming algorithm for wideband, coherent signal processing,” *J. Acoust. Soc. Am.*, vol. 76, no. 4, pp. 1132–1144, Oct. 1984.

[35] J. J. Shynk and R. P. Gooch, “Frequency-domain adaptive pole-zero filtering,” *Proc. IEEE*, vol. 73, no. 10, pp. 1526–1528, Oct. 1985.

[36] R. T. C. Jr., “The relationship between tapped delay-line and FFT processing in adaptive arrays,” *IEEE Trans. Antennas Propagat.*, vol. 36, no. 1, pp. 15–26, Jan. 1988.

[37] L. C. Godara, “Application of the fast Fourier transform to broadband beamforming,” *J. Acoust. Soc. Am.*, vol. 98, no. 1, pp. 230–273, July 1995.

[38] ——, “Limitations and capabilities of frequency domain broadband constrained beamforming schemes,” *IEEE Trans. Signal Processing*, vol. 47, no. 9, pp. 2386–2395, Sept. 1999.

[39] H. Wang and M. Kaveh, “Coherent signal-subspace processing for the detection and estimation of angles of arrival of multiple wide-band sources,” *IEEE Trans. Acoust., Speech, Signal Processing*, vol. 33, no. 4, pp. 823–831, May 1985.

[40] C. J. Tsai and J. F. Yang, “Autofocusing technique for adaptive coherent signal-subspace transformation beamformers,” *IEE Proc. Radar Sonar Navig.*, vol. 141, no. 1, pp. 30–36, Feb. 1994.

[41] H. W. Chen and J. W. Zhao, “Wideband MVDR beamforming for acoustic vector sensor linear array,” *IEE Proc. Radar Sonar Navig.*, vol. 151, no. 3, pp. 158–162, June 2004.

[42] M. H. Er and A. Cantoni, “Derivative constraints for broad-band element space antenna array processors,” *IEEE Trans. Acoust., Speech, Signal Processing*, vol. 31, no. 6, pp. 1378–1393, Dec. 1983.

[43] K. M. Buckley and L. J. Griffiths, “An adaptive generalized sidelobe canceller with derivative constraints,” *IEEE Trans. Antennas Propagat.*, vol. 34, no. 3, pp. 311–319, Mar. 1986.

[44] M. H. Er and B. P. Ng, “The dependency of weight vector on array origin for derivative-constrained broad-band arrays,” *Journal of Electrical and Electronics Engineering*, vol. 10, no. 3, pp. 202–206, June 1991.

[45] ——, “On derivative constrained broad-band beamforming,” *IEEE Trans. Acoust., Speech, Signal Processing*, vol. 38, no. 3, pp. 551–552, Mar. 1990.

[46] M. H. Er, B. P. Ng, and A. Cantoni, “A new set of constraints for derivative-constrained broad-band beam-formers,” *Journal of Electrical and Electronics Engineering*, vol. 11, no. 2, pp. 87–101, June 1991.

[47] I. Thng, A. Cantoni, and Y. H. Leung, “Derivative constrained optimum broad-band antenna arrays,” *IEEE Trans. Signal Processing*, vol. 41, no. 7, pp. 2376–2388, July 1993.

[48] ——, “Constraints for maximally flat optimum broadband antenna arrays,” *IEEE Trans. Signal Processing*, vol. 43, no. 6, pp. 1334–1347, June 1995.

[49] S. Zhang and I. Thng, "Robust presteering derivative constraints for broadband antenna arrays," *IEEE Trans. Signal Processing*, vol. 50, no. 1, pp. 1–10, Jan. 2002.

[50] H. Cox, R. Zeskind, and M. Owen, "Robust adaptive beamforming," *IEEE Trans. Signal Processing*, vol. 35, no. 10, pp. 1365–1376, Oct. 1987.

[51] B. D. V. Veen, "Minimum variance beamforming with soft response constraints," *IEEE Trans. Signal Processing*, vol. 39, no. 9, pp. 1964–1972, Sept. 1991.

[52] M. H. Er, A. Cantoni, and S.Mem, "An alternative formulation for an optimum beamformer with robustness capability," *Proc. IEE*, vol. 132, no. 6, pp. 447–460, Oct. 1985.

[53] C. L. Dolph, "A current distribution for broadside arrays which optimizes the relationship between beam width and side-lobe level," *Proc. IRE*, vol. 34, pp. 335–348, June 1946.

[54] B. P. Ng, M. H. Er, and C. Kot, "A flexible array synthesis method using quadratic programming," *IEEE Trans. Antennas Propagat.*, vol. 41, no. 11, pp. 1541–1550, Nov. 1993.

[55] F. Wang, V. Balakrishman, P. Y. Zhou, J. J. Chen, R. Yang, and C. Frank, "Optimal array pattern synthesis using semidefinite programming," *IEEE Trans. Signal Processing*, vol. 51, no. 5, pp. 1172–1183, May 2003.

[56] C. A. Olen and R. T. C. Jr, "A numerical pattern synthesis algorithm for arrays," *IEEE Trans. Antennas Propagat.*, vol. 38, no. 10, pp. 1666–1676, Oct. 1990.

[57] P. Y. Zhou and M. A. Ingram, "Pattern synthesis for arbitrary arrays using an adaptive array method," *IEEE Trans. Antennas Propagat.*, vol. 47, no. 5, pp. 862–869, May 1999.

[58] C. Y. Tseng and L. J. Griffiths, “A simple algorithm to achieve desired patterns for arbitrary arrays,” *IEEE Trans. Signal Processing*, vol. 40, no. 11, pp. 2737–2746, Nov. 1992.

[59] L. Wu and A. Zielinski, “An iterative method for linear array pattern synthesis,” *IEEE Journal of Oceanic engineering*, vol. 18, no. 3, pp. 280–286, July 1993.

[60] F. Wang, R. Yang, and C. Frank, “A new algorithm for array pattern synthesis using the recursive least squares method,” *IEEE Signal Processing Lett.*, vol. 10, no. 8, pp. 235–238, Aug. 2003.

[61] R. G. Ayestaran and F. L. Heras, “Support vector regression for the design of array antennas,” *Antennas and Wireless Propagat. Lett.*, vol. 4, pp. 414–416, 2005.

[62] S. Haykin and J.Kesler, “Relation between the radiation pattern of an array and the two-dimensional discrete Fourier transform,” *IEEE Trans. Antennas Propagat.*, vol. 23, no. 3, pp. 419–420, May 1975.

[63] S. Nordebo, I. Claesson, and S. Nordholm, “Weighted Chebyshev approximation for the design of broadband beamforming using quadratic programming,” *IEEE Signal Processing Lett.*, vol. 1, no. 7, pp. 103–105, July 1994.

[64] S. Doclo and M. Moonen, “Design of far-field and near-field broadband beamformers using eigenfilters,” *Signal Processing*, vol. 83, pp. 2641–2673, July 2003.

[65] H. Lebret and S. Boyd, “Antenna array pattern synthesis via convex optimization,” *IEEE Trans. Signal Processing*, vol. 45, no. 3, pp. 526–532, Mar. 1997.

[66] D. P. Scholnik and J. O. Coleman, “Formulating wideband array-pattern optimizations,” *Proc. IEEE Phased Array Systems and Technology*, 2000.

[67] ——, “Optimal design of wideband array patterns,” *IEEE International Radar Conference*, 2000.

[68] S. Yan, “Optimal design of FIR beamformer with frequency invariant patterns,” *Applied Acoust.*, vol. 67, no. 6, pp. 511–528, June 2006.

[69] J. Gu, H. Stark, and Y. Yang, “Design of tapped-delay line antenna array using vector space projections,” *IEEE Trans. Antennas Propagat.*, vol. 53, no. 12, pp. 4178–4182, Dec. 2005.

[70] L. J. Griffiths and K. M. Buckley, “Quiescent pattern control in linearly constrained adaptive arrays,” *IEEE Trans. Acoust., Speech, Signal Processing*, vol. 35, no. 7, pp. 917–926, July 1987.

[71] C. Y. Tseng and L. J. Griffiths, “A unified approach to the design of linear constraints in minimum variance adaptive beamformers,” *IEEE Trans. Antennas Propagat.*, vol. 40, no. 12, pp. 1533–1542, Dec. 1992.

[72] B. D. V. Veen, “Optimization of quiescent response in partially adaptive beamformers,” *IEEE Trans. Acoust., Speech, Signal Processing*, vol. 38, no. 3, pp. 471–477, Mar. 1990.

[73] T. P. Guella and R. M. Davis, “Synthesis of notched antenna patterns for wideband processing,” *IEEE Trans. Antennas Propagat.*, vol. 43, no. 12, pp. 1465–1471, Dec. 1995.

[74] P. J. Kootsookos, D. B. Ward, and R. C. Williamson, “Imposing pattern nulls on broadband array responses,” *J. Acoust. Soc. Am.*, vol. 105, no. 6, pp. 3390–3398, June 1999.

[75] M. M. Goodwin and G. W. Elko, “Constant beamwidth beamforming,” *Proc. ICASSP-93*, vol. 1, pp. 27–30, Apr. 1993.

[76] I. J. H. Doles and F. D. Benedict, “Broad-band array design using the asymptotic theory of unequally spaced arrays,” *IEEE Trans. Antennas Propagat.*, vol. 36, no. 1, pp. 27–33, Jan. 1988.

[77] D. B. Ward, R. A. Kennedy, and R. C. Williamson, “Theory and design of broadband sensor arrays with frequency invariant far-field beam patterns,” *J. Acoust. Soc. Am.*, vol. 97, pp. 1023–1034, Feb. 1995.

[78] ——, “FIR filter design for frequency invariant beamformers,” *IEEE Signal Processing Lett.*, vol. 3, no. 3, pp. 69–71, Mar. 1996.

[79] S. Forcellini, “Frequency invariant beamformer using a single set of IIR filter coefficients,” *IEEE Antennas and Propagation Society International Symposium*, vol. 2, pp. 563–566, June 2002.

[80] T. Sekiguchi and Y. Karasawa, “Wideband beamspace adaptive array utilizing FIR fan filters for multibeam forming,” *IEEE Trans. Signal Processing*, vol. 48, no. 1, pp. 277–284, Jan. 2000.

[81] W. Liu and S. Weiss, “A new class of broadband arrays with frequency invariant beam patterns,” *Proc. ICASSP-2004*, vol. 2, pp. 185–188, May 2004.

[82] W. Liu, S. Weiss, and L. Hanzo, “A generalized sidelobe canceller employing two-dimensional frequency invariant filters,” *IEEE Trans. Antennas Propagat.*, vol. 53, no. 7, pp. 2339–2343, July 2005.

[83] W. Liu, R. B. Wu, and R. Langley, “Analysis and a novel design of the beamspace broadband adaptive array,” *Progress in Electromagnetics Research Symposium*, 2006.

[84] Y. Li, K. C. Ho, and C. Kwan, “3-D array pattern synthesis with frequency invariant property for concentric ring array,” *IEEE Trans. Signal Processing*, vol. 54, no. 2, pp. 780–784, Feb. 2006.

[85] M. Ghavami, “Wideband smart antenna theory using rectangular array structures,” *IEEE Trans. Signal Processing*, vol. 50, no. 9, pp. 2143–2151, Sept. 2002.

[86] S. Repetto and A. Trucco, “Designing superdirective microphone arrays with a frequency-invariant beam pattern,” *IEEE Sensors Journal*, vol. 6, no. 3, pp. 737–747, June 2006.

[87] A. Trucco, M. Crocco, and S. Repetto, “A stochastic approach to the synthesis of a robust frequency-invariant filter-and-sum beamformer,” *IEEE Trans. Instru. and Meas.*, vol. 55, no. 4, pp. 1407–1415, Aug. 2006.

[88] S. Doclo and M. Moonen, “Design of broadband beamformers robust against gain and phase errors in the microphone array characteristics,” *IEEE Trans. Signal Processing*, vol. 51, no. 10, pp. 2511–2526, Oct. 2003.

[89] J. F. Sturm, “Using SeDuMi 1.02, a MATLAB toolbox for optimization over symmetric cones,” *Optim. Metho. Softw.*, vol. 11, 1999.

[90] J. Liu, A. B. Gershman, Z. Q. Luo, and K. M. Wong, “Adaptive beamforming with sidelobe control: a second-order cone programming approach,” *IEEE Signal Processing Lett.*, vol. 10, no. 11, pp. 331–334, Nov. 2003.

[91] B. P. Ng and H. Duan, “Designing amplitude/phase response of the Frost beamformer,” *IEEE Trans. Signal Processing*, vol. 55, no. 5, 2007.

[92] H. Duan, B. P. Ng, and C. M. See, “A new broadband beamformer using IIR filters,” *IEEE Signal Processing Lett.*, vol. 12, no. 11, pp. 776–779, Nov. 2005.

[93] H. Duan, B. P. Ng, C. M. See, and J. Fang, “Broadband beamforming using TDL-form IIR filters,” *IEEE Trans. Signal Processing*, vol. 55, no. 3, pp. 990–1002, 2007.

[94] ——, “Spatial resolutions of the broadband nonredundant and minimum redundancy arrays,” *Accepted by IEEE Signal Processing Lett.*, 2007.

[95] ——, “Broadband interference suppression performance of minimum redundancy arrays,” *Submitted to IEEE Trans. Signal Processing.*, 2006.

[96] ——, “Applications of the SRV constraint in broadband pattern synthesis,” *Submitted to Signal Processing.*, 2007.

[97] R. C. Hansen, *Phased Array Antennas*. New York: Wiley, 1998.

[98] T. A. Moffet, “Minimum redundancy linear arrays,” *IEEE Trans. Antennas Propagat.*, vol. 16, no. 2, pp. 172–175, Mar. 1968.

[99] E. Vertatschitsch and S. Haykin, “Nonredundant arrays,” *Proc. IEEE*, vol. 74, no. 1, pp. 217–217, Jan. 1986.

[100] S. Haykin, J. P. Reilly, V. Kezys, and E. Vertatschitsch, “Some aspects of array signal processing,” *Proc. Inst. Elect. Eng. F*, vol. 139, no. 1, pp. 1–26, Feb. 1992.

[101] M. H. Er and A. Cantoni, “A new approach to the design of broad-band element space antenna array processors,” *IEEE Journal of Oceanic Engineering*, vol. OE-10, no. 3, pp. 231–240, July 1985.

[102] Y. Grenier, “A microphone array for car environments,” *Speech Communication*, vol. 12, no. 1, pp. 25–39, Mar. 1993.

[103] W. L. Hsue and C. C. Yeh, “Wideband forward-backward beamforming and its efficient computation methods,” *Signal Processing*, vol. 44, no. 3, pp. 285–297, July 1995.

[104] M. H. Er, B. P. Ng, and A. Cantoni, “A new set of constraints for derivative-constrained broadband beamformers,” *Journal of Electrical and Electronics Engineering*, vol. 11, no. 2, pp. 87–101, June 1991.

[105] C. Y. Tseng, “Minimum variance beamforming with phase-independent derivative constraints,” *IEEE Trans. Signal Processing*, vol. 40, no. 3, pp. 285–294, Mar. 1992.

[106] M. H. Er and C. K. Siew, “Design of FIR filters using quadratic programming approach,” *IEEE Trans. Circuits Syst. II*, vol. 42, no. 3, pp. 217–220, Mar. 1995.

[107] J. R. Mautz and R. F. Harrington, “Computational methods for antenna pattern synthesis,” *IEEE Trans. Antennas Propagat.*, vol. 23, no. 4, pp. 507–512, July 1975.

[108] Z. Shi and Z. Feng, “A new array pattern synthesis algorithm using the two-step least-squares method,” *IEEE Signal Processing Lett.*, vol. 12, no. 3, pp. 250–253, Mar. 2005.

[109] M. Wax and Y. Anu, “Performance analysis of the minimum variance beamformer,” *IEEE Trans. Signal Processing*, vol. 44, no. 4, pp. 928–937, Apr. 1996.

[110] J. J. Shynk, R. P. Gooch, and B. Widrow, "A frequency-domain adaptive pole-zero filter with applications," *Nineteeth Asilomar Conference on Circuits, Systems and Computers*, pp. 299–303, Nov. 1986.

[111] J. J. Shynk, "Adaptive IIR filtering," *IEEE ASSP Mag.*, vol. 6, no. 2, pp. 4–21, Apr. 1989.

[112] J. Li and P. Stoica, *Robust Adaptive Beamforming*. Wiley, 2006.

[113] L. Ljung and T. Soderstrom, *Theory and Practice of Recursive Identification*. Cambridge, MA: M.I.T. Press, 1983.

[114] S. Haykin, *Adaptive Filter Theory, Third Edition*. Englewood Cliffs, NJ: Prentice Hall, 1996.

[115] E. Walach, "On superresolution effects in maximum likelihood adaptive antenna arrays," *IEEE Trans. Signal Processing*, vol. 32, no. 3, pp. 259–263, Mar. 1984.

[116] B. P. Ng, M. H. Er, and C. C. Kot, "A new limit on inter-element spacing for a linear array," *IEEE Antennas Propagat. Mag.*, vol. 40, no. 4, pp. 22–29, Aug. 1998.

[117] ——, "Linear array geometry synthesis with minimum sidelobe level and null control," *Microwaves, antennas and propagat., IEE proceedings*, vol. 141, no. 3, pp. 162–166, June 1994.

[118] S. Nordholdm, I. Claesson, and P. Eriksson, "The broadband Wiener solution for Griffiths-Jim beamformers," *IEEE Trans. Signal Processing*, vol. 40, no. 2, pp. 474–478, Feb. 1992.

[119] R. S. Elliott, *Antenna Theory and Design*. Englewood Cliffs, 1981.

[120] M. B. Jorgenson, M. Fattouche, and S. T. Nichols, “Applications of minimum redundancy arrays in adaptive beamforming,” *Microwaves, antennas and propagat., IEE proceedings. Part H.*, vol. 138, no. 5, pp. 441–447, Oct. 1991.

[121] Y. Bar-Ness, W. L. Chen, and E. Parayirci, “Eigenanalysis for interference cancellation with minimum redundancy array structure,” *IEEE Trans. Aerosp. Electron. Syst.*, vol. 33, no. 3, pp. 977–988, July 1997.

[122] E. Panayirci and W. L. Chen, “Minimum redundancy array structure for interference cancellation,” *Signal Processing*, vol. 42, no. 3, pp. 319–334, Mar. 1995.

[123] G. H. Golub and C. F. V. Loan, *Matrix Computations, Third Edition*. Johns Hopkins University Press, 1996.

[124] M. Abramowitz and I. A. Stegun, *Handbook of Mathematical Functions with Formulas, Graphs, and Mathematical Tables*. New York: Dover, 1972.

[125] S. C. Chan and H. H. Chen, “Uniform concentric circular arrays with frequency-invariant characteristics-theory, design, adaptive beamforming and DOA estimation,” *IEEE Trans. Signal Processing*, vol. 55, no. 1, pp. 165–177, Jan. 2007.

[126] S. Boyd and L. vandenberghe, *Convex Optimization*. Cambridge University Press, 2004.

[127] S. Weiss, R. W. Stewart, and W. Liu, “A broadband adaptive beamformer in subbands with scaled aperture,” *Thirty-Sixth Asilomar Conference on Signals, Systems and Computers*, vol. 2, no. 3-6, pp. 1298–1302, Nov. 2002.